UNIVERSITY OF SOUTHAMPTON

A HYBRID DETERMINISTIC-PROBABILISTIC MODEL FOR VIBROACOUSTIC STUDIES

by

Murilo Weingarten Bonilha

Institute of Sound and Vibration Research
Faculty of Engineering and Applied Science

Thesis submitted for the degree of
Doctor of Philosophy

May, 1996

UNIVERSITY OF SOUTHAMPTON

ABSTRACT

FACULTY OF ENGINEERING AND APPLIED SCIENCE

INSTITUTE OF SOUND AND VIBRATION RESEARCH

Doctor of Philosophy

A HYBRID DETERMINISTIC-PROBABILISTIC MODEL FOR VIBROACOUSTIC STUDIES

by Murilo Weingarten Bonilha

The acoustic field inside a hard-walled acoustic cavity due to the random vibration of one flexible wall is analysed by a novel hybrid deterministic-probabilistic model. This approach implies that the flexible wall is not amenable to a deterministic treatment due to its high modal density and uncertainties concerning its exact geometric and material properties. Thus an original probabilistic treatment based on the vibration field correlation characteristics is proposed for the flexible wall. On the other hand, full information is available for the acoustic cavity making it tractable by deterministic modal techniques. A coupling coefficient between each acoustic mode and the plate bending wave field is employed to represent the vibroacoustic interaction and the response obtained from a modal summation due to contributions from each acoustic mode.

Information concerning the spatial distribution of the plate response is provided by the probabilistic model and expressed in terms of correlation coefficients or normalised cross-power spectral densities of normal acceleration. Expressions for these two coefficients are derived based on an approximate modal representation and on a free wave model. Particular attention is paid to the plate boundary conditions and results are derived for plates with clamped, simply-supported, guided or free edges. A general boundary condition which solely depends on the edge stiffness is employed to model the effect of stiffeners on the plate vibration field. Information about curvature and type of excitation applied to the plate are also incorporated in this model. It is found that the derived correlation coefficients and normalised cross-power spectral densities are valid as frequency average estimates in bands in which more than eight plate modes are available. However, when the plate modal overlap factor is higher than unity they can also be employed in narrow bands.

Comparisons are presented with SEA, FEM and experimental response results on two subsystems which consist of a rigid rectangular box with one flexible wall. It is shown that the hybrid model results approach those from a SEA model as both systems modal density increases and they compare well with FEM results in the lower frequency range in which both systems are modally-sparse. In addition, narrow band and frequency averaged sound pressure levels approach the experimental results as long as more than eight plate modes are available in a frequency band or the plate modal overlap factor is higher than unity. Local and space averaged sound pressure levels are also predicted with this model.

The most significant contribution of the model here proposed is the provision of a new tool for the prediction of narrow band or frequency averaged, local or space averaged sound pressure levels inside acoustic cavities excited by the random vibration of modally-dense plates for whom only the gross properties are available. This type of interaction model is applicable to interior noise control in transportation vehicles.

ACKNOWLEDGEMENTS

The author gratefully acknowledges:

- my supervisor, Prof. F. J. Fahy, for his friendship, guidance, help and extremely valuable orientation throughout this work;

- CAPES (Brazilian Government Agency for Post-Graduate Education), for the financial support;

- the members of my review board, Prof. R. S. Langley, Dr. N. Lalor and Dr. D. Anderton, for their suggestions and criticisms;

- Gordon Stimpson, for allowing me to share his office and for the insight into the 'impractical' aspects of SEA;

- the ISVR staff, technical and clerical, and the colleagues and friends I made at ISVR, which names can easily occupy this whole page, for the help and illuminating ideas;

- my wife, Andréa, for her love and constant dedication;

- my parents and sisters, '*pelo amor à mim dedicado e pelo apoio recebido que permitiu que eu completasse a minha educação acadêmica*'.

LIST OF CONTENTS

LIST OF FIGURES

Chapter 4

Chapter 5

Appendices

LIST OF SYMBOLS

a	normal vibration acceleration
A	Fourier transform of a
A_{ref}^{B}	complex amplitude of the wave reflected at the bottom edge
A_{in}^{B}	complex amplitude of the wave incident on the bottom edge
A_{e}^{B}	complex amplitude of the evanescent field component (bottom edge)
A_t	complex amplitude of the transmitted wave
B_e	resolution bandwidth
$B_r \approx 2\zeta f_d$	system half-power bandwidth
c_o	fluid sound speed
C_{np}	modal coupling coefficient (Chapter 1)
$C_{nn}^{2}(\omega)$	direct coupling coefficient
$C_{nm}^{2}(\omega)$	cross coupling coefficient
D	flexural rigidity, $D=Eh^3/12(1-\nu^2)$
$E[\ ]$	ensemble-average value
E_B	complex evanescent field component coefficient (bottom edge)
E_p, E_n	time-averaged modal energies
E	Young's modulus
EI_1, EI_2, EI_{12}	flexural rigidities of the stiffener
$E\Gamma$ and GJ	torsional rigidities
f_{crit}	lowest coincidence frequency, or critical frequency
f_d	damped natural frequency (Chapter 4)
f_x, f_y	'plane stress' ring frequencies of the shell (Appendix F)
f_r	'plane stress' ring frequency of singly-curved shell
F^2	mean-square force
F_p, F_n	modal generalised sources
$F_n(\omega)$	Fourier transform of $F_n(t)$
G	shear modulus (Appendix F)
$G(\mathbf{r},\mathbf{r}_s)$	Green's function
$G_{12}(\mathbf{x}_1,\mathbf{x}_2,f)$	one-sided cross-power spectral density
$G_1(f)$	one-sided auto-power spectral density

G_{np}	modal power flow coefficient
h	shell or plate thickness
$H_p = (\omega_p^2 - \omega^2)$, $W_p = \eta_p \omega \omega_p$	modal functions for plate
Im[ ]	imaginary part
$J_o(w)$	zero-order Bessel function of argument w
$J_1(w)$	first-order Bessel function of argument w
k	acoustic wavenumber
k_x, k_y	wavenumbers in x and y directions, respectively
k_B	generic bending wavenumber
k_b	band centre frequency bending wavenumber
k_n	modal wavenumber
k_{zz}	stiffener translational stiffness
$k_{\theta\theta}$	stiffener rotational stiffness
$k_{z\theta}$	stiffener coupling stiffness
l	average distance a wave front travels between successive reflections
l_o	averaged distance to the boundary of the plate
L_x, L_y, L_z	internal dimensions of the acoustic cavity
L_{st}	stiffener length
m	mass per unit area
M	Bending moment (Appendix C)
M	plate mass
n(f)	modal density
n_d	number of non-overlapping averages
N	number of modes in a frequency band of width $\Delta\omega$
$p(\mathbf{r}_s)$	surface pressure acting on the structure
P	Fourier transform of p
P	plate perimeter
P_{np}	time-averaged modal power flow
$q(\mathbf{r}_o)$	distribution of volume velocity source strength per unit volume
Q_n	strength of acoustic sources located within the fluid volume
r	singly-curved shell radius
r_x, r_y, r_z	modal numbers (positive integers)

r_x, r_y	principal radii of curvature of the surface, $X=r_x/r_y$, (Appendix F)
$\mathbf{r}$	vector at the receiver point
$\mathbf{r}_s$	position vector on the vibrating surface
R_B	complex reflection coefficient of bottom edge
$R_{12}(\mathbf{x}_1,\mathbf{x}_2,\tau)$	spatial cross-correlation function
Re[ ]	real part
S	area
$\sin k_x\xi_x$, $\cos k_x\xi_x$, C_x	dynamic edge parameters
$S_p(x,y,z,\omega)$	double-sided auto-power spectral density of pressure
$S_a(\mathbf{x}_1,\mathbf{x}_2,\omega)$	cross-power spectral density of normal plate acceleration
S_{pv}	double-sided cross-power spectral density of acoustic pressure and plate velocity
T	complex transmission coefficient
T_t	total duration of the record data
V	volume
v^2	mean-square plate normal vibration velocity
$v_N(\mathbf{r}_s)$	structure normal vibration velocity
$\mathbf{x}_1,\mathbf{x}_2$	spatial points
$X_n=(\omega_n^2-\omega^2)$, $Y_n=\eta_n\omega\omega_n$	modal functions for acoustic cavity
Y	mobility
z_p	modal structural displacement
$z_{1M}(t)$	instantaneous modal displacements
δ	Dirac delta function
ε_r	normalised random error
ε_b	normalised bias error
$\varepsilon=\sqrt{\varepsilon_r^2+\varepsilon_b^2}$	normalised r.m.s. error
$\phi_p(x,y)$	mode shape of the pth plate mode
$\gamma_a(\mathbf{x}_1,\mathbf{x}_2,\omega)$	normalised cross-power spectral density of acceleration
$\gamma_{12}(\mathbf{x}_1,\mathbf{x}_2,\tau)$	spatial cross-correlation coefficient or normalised covariance
$\gamma_{12}(\mathbf{x}_1,\mathbf{x}_2,f_c)$	zero-time-delay spatial correlation coefficient or band-limited spatial correlation coefficient

γ_{xy}^2 ordinary coherence function (Chapter 4)

η frequency-averaged plate loss factor (Chapter 3)

η_n, η_p modal loss factors (Chapter 1)

η_p frequency-averaged plate loss factor (Chapter 2)

η_a frequency-averaged acoustic loss factor (Chapter 5)

η_{ap} coupling loss factor between plate and acoustic cavity

η_{ij} coupling loss factor between subsystems i and j

κ number of degrees of freedom of the chi-square distribution

κ^2 shear coefficient, $G' = \kappa^2 G$, (Appendix F)

λ bending wavelength

$\mu_x = \sqrt{k_x^2 + 2k_y^2}$ and $\mu_y = \sqrt{k_y^2 + 2k_x^2}$

ν Poisson ratio

θ propagation angle or angle defined by $\arctan(k_y/k_x)$

ρ material density

ρ_o fluid mean density

ρA mass and polar moment of inertia per unit length

$\rho_B = |R_B|^2$ reflection efficiency of bottom edge

σ standard deviation of the measurement of average m (Chapter 4)

σ_{rad} frequency-averaged plate radiation efficiency

ω frequency of analysis

ω frequency of the free oscillation of the shell (Appendix F)

ω_n, ω_p modal natural frequencies

ψ_n acoustic pressure mode shape

ζ damping ratio (Chapter 4)

$\Delta\omega = \omega_2 - \omega_1$ frequency bandwidth

$\Delta k = k_2 - k_1$

Φ_n modal acoustic-field velocity potential related to acoustic pressure by $p = -\rho_o \partial\Phi / \partial t$

Λ_n, Λ_p modal-generalised volume and mass, respectively

Π_{in} steady-state input power in a finite frequency band $\Delta\omega$

Π_{diss} power absorbed on the walls of the cavity in a finite frequency band

Π_{in}^{i}	total real power input to plate i from an external source (Appendix A)
Π_{diss}^{i}	power dissipated by subsystem i due to its internal damping (App. A)
Π_{ij}	power transferred between subsystems i and j (Appendix A)
*	complex conjugate
$< >$	spatial average
$< >_t$	time average

CHAPTER 1

INTRODUCTION

1.1 The aim of the research

The purpose of the research is to develop means of modelling and analysing the vibroacoustic interaction of modally-dense structures and modally-sparse acoustic cavities applicable to interior noise control in transportation vehicles. A probabilistic description of the correlation characteristics of the structural system is employed to account for effects of boundary conditions, curvature, type of excitation and presence of stiffeners on the structural dynamic behaviour. The acoustic modes of the enclosed air space are assumed to be obtainable by a deterministic approach and the vibroacoustic interaction is expressed in terms of a coupling coefficient. The features of the proposed model are illustrated by applying it to the response analysis of a rectangular box which is randomly excited by one non-rigid wall.

1.2 Importance of interior noise control in transportation vehicles

Noise levels inside transportation vehicles constitute an important element in the subjective assessment of the vehicle quality and are one of the key factors in enhancing the competitiveness of the vehicle as a commercial product. Together with quality, noise-related factors such as the ease of spoken communication and/or listening to sound systems, association with comfort, fatigue of occupants when taking long journeys, and product cost, form the main concerns of the noise control engineer when tackling interior noise problems in vehicles. Furthermore, excessive interior noise levels can cause delay in the launching of a new product, leading to increase in development costs and contract penalties (e.g. ref. [1]).

The noise control problem in vehicles may be qualitatively described in terms of a source-path-receiver model [2,3]. The characteristics of noise sources which

operate in different types of vehicle vary, but they usually have a broad-band random content (e.g. wind and road noise in cars, turbulent flow in aircraft, rail-wheel interaction in trains) together with substantial tonal and harmonic components (e.g. engine and transmission noise in cars, propeller, compressor and engine exhaust noise in aircraft). Noise excitation mechanisms in vehicles have been extensively studied and, in general, an adequate physical understanding of their causes and effects has been achieved (see for instance the reviews presented in refs. [3,4]).

The disturbances generated by source mechanisms are transmitted via structure and airborne paths to the vehicle interior. These transmission paths are geometrically and materially complex and are influenced by operating conditions and manufacturing tolerances. The vibroacoustic interaction between structures and the contained air can involve resonant and/or non-resonant response of the modes of the individual components. The irregular shape of the vehicle interior, together with inhomogeneous distribution of absorptive areas (carpets, seats and soft trim) and reflective surfaces (hard trim and glass), contribute to the complexity of the interior noise control problem in transportation vehicles.

Numerous strategies have been employed to improve the interior noise characteristics of transportation vehicles. They can be roughly divided into corrective and predictive strategies. Active and passive noise and vibration control can be classified as corrective, while predictive techniques such as the Boundary Element Method (BEM), Finite Element Method (FEM) and Statistical Energy Analysis (SEA) are most commonly employed at the design stage. In order to reduce costs, predictive techniques based on computer simulation are preferred and much effort has been put in their development. These predictive approaches are complemented by experimental techniques developed as means of assessing the reliability of such approaches.

1.3 Statement of the Problem

As a result of geometric characteristics of different vehicles, combined with the complexity of the propagation paths, a tendency exists to divide the analysis of interior noise problems into separate frequency ranges [5]. In each frequency range, normally termed 'low', 'medium' and 'high', different analytical and numerical

procedures are employed according to typical vibration and acoustic wavelengths and the vibrational behaviour of the structure. Low frequencies are characterised by a sparsity of low-order natural modes which are rather insensitive to variations in the model details. As a result, one can use a deterministic model to tackle noise problems in this frequency range. On the other hand, when the natural modes are of high order, the response is extremely dependent on the model details and minor variations of the model can cause significant differences in the predicted response. Therefore, probabilistic models are more relevant to the analytical treatment of the system response in this frequency range which is termed 'high'. The transition region is termed mid-frequency range. Typical frequency responses in high and low frequencies are illustrated in fig. 1.1. As shown in this figure, in the frequency region below 1000 Hz the natural modes in the acoustic system are sparsely distributed while the natural modes are more densely concentrated in the structural system.

Deterministic techniques such as the Finite Element Method (FEM) and the Boundary Element Method (BEM) are well established for the prediction of low frequency noise inside vehicles (e.g. refs. [6-9]). Nevertheless, as discussed by Fahy [10], the application of such techniques to the prediction of high frequency noise is problematic. This stems from the fact that the sensitivities of modal resonance frequencies and relative modal phase response to small variations in structural detail increase with modal order. Therefore, the confidence in the validity of the model decreases with frequency. Moreover, vibrational/acoustic energy sources and the propagation of structure-borne noise can be strongly affected by the vehicle operating conditions, quality of components and manufacturing processes [2,10]. The extent of the variation of the dynamic response of identical systems can be illustrated by the results presented by Kompella and Bernhard in ref. [11]. They show that the acoustic pressure response at the driver's ear position in individual examples of nominally identical production cars (57 in total) can differ by as much as 20 dB at individual frequencies.

The large amount of input data required by deterministic numerical models in a frequency region in which the vibration wavenumber is large is another factor that contributes to making the application of such approaches to high frequency studies laborious. This is because the size of the discrete elements necessary to achieve a certain precision in a given frequency decreases with increasing frequency. Sung and

Nefske [8] applied FEM to the analysis of interior noise of a van and as a result they point out that the frequency range of accurate prediction of interior sound pressure levels is limited by the upper frequency limit of acceptable accuracy of the structural model, which they demonstrated to be about 100 Hz for the van. As observed by Lalor [12], this is because vehicle structures are highly non-uniform and have rather high modal density, making modal representation imprecise beyond about the 10th to 20th mode (around 100 to 120 Hz). However, above this frequency, the acoustic frequencies are still fairly sparse and a FEM model can give reasonable estimates of the dynamic behaviour (natural frequencies and associated mode shapes) of the air space inside a passenger compartment. This suggests that the structure, and not the acoustic cavity, complicates the numerical modelling of vibroacoustic problems.

As an alternative to deterministic techniques, a probabilistic approach has been developed in the last 30 years [14]. This approach, Statistical Energy Analysis (SEA), has been successfully applied to the study of high frequency structure-borne sound transmission in road vehicles [15] and helicopters [16]. However, as pointed out by Fahy [10], SEA is at the moment relegated to the 'high frequency' rank as no formal procedure is yet available to evaluate the predictive confidence of SEA when it is applied to typical structures, particularly when the response is determined by coupling between a rather small number of modes which have low modal overlap (i.e. their average resonance frequency separation is much larger than their average half-power bandwidths). The present weakness of SEA in dealing with low modal density subsystems, which is associated with the lack of confidence data, precludes the application of this approach to the analysis of interior noise in motor cars in frequency ranges below 200 Hz because, as already discussed, few acoustic modes have natural frequencies in this frequency range. Furthermore, only frequency-averaged, spatially-averaged response quantities are available in SEA, excluding the estimation of response values at specific points, such as passenger head positions, and in narrow bands.

1.4 An alternative approach

In summary, some practical systems involve, in certain frequency ranges, interaction between a large number of structural modes with a few, or even no, resonant acoustic modes. In these frequency bands neither SEA nor modal-interaction (described in section 1.5.1) models are optimum. Furthermore, the structural modes may be excited by broad-band sources, causing both resonant and non-resonant acoustic response. In particular, this situation is encountered in medium-sized cars in the 100-200 Hz frequency range [12]. As previously explained, in this frequency range the structural modal density is high enough to justify an SEA model and FEM can be efficiently applied to the air volume inside the car interior as the acoustic modes are reasonably sparse. Similar conditions apply, to a lesser extent, in trains and aircraft.

A number of approaches [17] have been suggested for analysing cases in which neither SEA nor modal-interaction models are optimum, a situation sometimes referred to informally as 'the mid-frequency crisis'. These approaches are based variously upon a heat conduction analogy to structural energy flow and smoothing of frequency response functions. However, they usually assume that both structural and acoustic systems have a similar modal density and do not take advantage of the situation described in the previous paragraph.

In order to tackle the problem here presented, a hybrid deterministic-probabilistic model is proposed as means of modelling the vibroacoustic coupling. The assessment of the limitations of this hybrid model in representing a general vibroacoustic coupling is based on the study of its application to the interaction between an acoustic volume and a thin plate. A rather extensive literature exists concerning the interaction between a plate and an enclosed volume of fluid, and in what follows the works which are most relevant to the present research are reviewed. The inclusion of some equations in the review is an attempt to introduce some of the basic mathematical concepts together with the development of the physical understanding. This hybrid model can be considered a first step to a combined SEA-FEM model suggested by Lalor [12] as an option for studying interior noise inside motor cars in the medium frequency range.

1.5 Plate/acoustic volume interaction: a literature review

1.5.1 Modal-interaction model

In the modal-interaction model, the differential equations that govern the behaviour of enclosed fluid and structure are expanded directly in terms of the uncoupled natural modes. A differential equation is written for each subsystem mode and the subsystem response is obtained from modal summation truncated to the desired degree of precision. Normal structural surface acceleration is the agent by which the structure generates the fluid field and the fluid pressure on the surface of the structure excites the structural wave field. For an enclosed volume of fluid interacting with a plane structure the differential equations of motion expanded in terms of the uncoupled normal modes are [19],

$$\ddot{z}_p + \omega_p \eta_p \dot{z}_p + \omega_p^2 z_p = -\frac{\rho_o}{\Lambda_p} \sum_n \dot{\Phi}_n C_{np} + \frac{F_p}{S\Lambda_p}, \tag{1.1}$$

$$\ddot{\Phi}_n + \omega_n \eta_n \dot{\Phi}_n + \omega_n^2 \Phi_n = \left(\frac{c_o^2 S}{V\Lambda_n}\right) \sum_p \dot{z}_p C_{np} - \left(\frac{c_o^2}{V\Lambda_n}\right) Q_n, \tag{1.2}$$

where z_p is a modal structural displacement, Φ_n is a modal acoustic-field velocity potential related to the internal pressure by $p = -\rho_o \partial\Phi / \partial t$, ω_n and ω_p are the modal natural frequencies, C_{np} is a coupling coefficient obtained from the integration of fluid and structure mode shapes over the contact area S, F_p is a generalised force acting on the structure, η_n,η_p are modal loss factors, Λ_n and Λ_p are modal-generalised volume and mass, respectively, and Q_n is the strength of acoustic sources located within the fluid volume.

Analytical approaches based on modal representation have been used as a means of studying stress and low-frequency sound transmission in plates backed by rectangular cavities [20-22]. The inhomogeneous wave equation that governs the acoustic pressure inside the enclosure is solved for specific boundary conditions: five walls are assumed acoustically hard (perfect acoustic reflectors) and one is assumed flexible. This solution is normally expressed as a separable function of the three space

variables. The space variable that corresponds to the deflection of the flexible wall is approximated in terms of an infinite Fourier series. The backing pressure acting on the flexible wall is then estimated from the velocity potential and its influence on the plate vibration computed as a generalised force for the mode concerned (first term on the left of equation (1.1)).

This procedure was employed by Dowell and Voss [20] to study the effect of an underlying cavity on the plate vibration. They assumed the deflection of the flexible wall to be expanded in double cosine functions and used a Galerkin method to solve the equation of motion of the plate (equation (1.1)). They concluded that only the fundamental plate mode is strongly affected by the presence of the cavity and presented a semi-empirical expression to estimate the change in the resonance frequency of this mode.

Pretlove [21,22] used exactly the same procedure but assumed the flexible wall to vibrate in double-sine modes. The plate modes, modified by the acoustic cavity effects, are obtained from an eigenproblem (equation (1.1) in matrix form) in which the term that involves the acoustic velocity potential is included. This leads to the concept of cavity- and plate-controlled modes of the coupled system, which depends on the relative energy contribution of each subsystem. The influence of the cavity on the plate vibration was then discussed in terms of the relative plate and acoustic cavity stiffness in which the coupled modes were obtained from the uncoupled *in vacuo* plate and cavity modes. For the case in which the walls are much stiffer than the room cavity the acoustic field inside the cavity can be calculated directly from the uncoupled plate vibrations. However, for light plates that enclose shallow cavities, the relative stiffness of both systems is similar and therefore they must be analysed as a single coupled system.

A general treatment of the panel-cavity coupling problem has been presented by Dowell, Gorman and Smith [23]. They derived equations similar to equations (1.1) and (1.2), the only difference being the use of an impedance to model the absorption characteristics of the cavity. The direct effect of this impedance is to couple the (rigid wall) acoustic modes. The coupled differential equations are used to form a matrix equation with stiffness, mass, damping and coupling terms and, as the coupling between the panel and the room is of gyrostatic type, a numerical procedure due to

Meirovitch [24] is suggested for the solution of the associated eigenproblem (without the damping). Simplifications are carried out in the general solution in order to form the eigenproblem of two cavities joined by an opening. This simplified eigenproblem is solved and a good agreement was reported between experimental and analytical results.

Another interesting discussion was presented in ref. [23] for the case in which the plate is the only source of excitation in the system. Simplifications were given for the cases in which the forcing frequency is equal to the *in vacuo* plate resonance frequency, or equal to the cavity resonance frequency, or yet, when the three frequencies are very similar. Generally, observations similar to ones already presented in earlier works [20-22] are reported. Most importantly, they have suggested that when the excitation frequency is well separated from all panel and room natural frequencies the interaction between the panel and the room can be neglected. This means ignoring the first term on the right side of equation (1.1). In this situation one only needs to obtain the panel response from equation (1.1) and then use this result to estimate the pressure response using equation (1.2).

1.5.2 Green's function approach

Alternatively, the radiation of sound from a vibrating structure into a surrounding fluid can be formulated in terms of an integral equation, the Kirchhoff-Helmholtz integral equation. This equation comprises Green's functions, which represent solutions to the inhomogeneous wave equation, with an imposed radiation condition that ensures outward travelling waves. It relates the harmonic surface vibrational motion on the structure to the radiated pressure field and it is normally expressed as [25]

$$p(\mathbf{r}) = \int_S [p(\mathbf{r}_s)\partial G(\mathbf{r},\mathbf{r}_s)/\partial n + i\omega\rho_o v_N(\mathbf{r}_s)G(\mathbf{r},\mathbf{r}_s)]dS + i\omega\rho_o \int_V q(\mathbf{r}_o)G(\mathbf{r},\mathbf{r}_o)dV, \quad (1.3)$$

where $G(\mathbf{r},\mathbf{r}_s)$ is the Green's function, $\mathbf{r}$ is the vector at the receiver point, $\mathbf{r}_s$ is the position vector on the vibrating surface, $p(\mathbf{r}_s)$ is the surface pressure on the structure, $v_N(\mathbf{r}_s)$ is the structure normal vibration velocity, $\partial G/\partial n$ is the derivative of the Green's function with respect to the outward-going normal to the local surface, and $q(\mathbf{r}_o)$ is the distribution of volume velocity source strength per unit volume. The derivation of the

above equation is presented in ref. [26] and its application for sound radiation on unbounded fluid is extensively discussed in the acoustics literature (e.g. refs. [19,25,26]). Explicit expressions for the Green's function are available only for very simplified and regular geometries and in the case of more complicated structures numerical techniques are necessary to solve this integral equation [25,27].

The integral equation is applicable to either a vibrating body radiating in an unbounded medium or a bounded volume of fluid in which part of its boundaries vibrate. In the latter, the presence of physical boundaries causes natural modes of vibration and associated natural frequencies to appear in the fluid. The normal motion of the vibrating flexible boundaries excites the acoustic modes causing the enclosed fluid to exhibit resonant acoustic behaviour. The volume integral in the above equation represents the pressure generated by sources within the fluid volume and, as it is assumed that the vibrating surface is the only source of disturbance in the fluid, this term can be ignored. For the case of an enclosure with rigid walls ($\partial p/\partial n = 0$ on the boundaries) a Green's function that satisfies the wave equation with this boundary condition is given by [19,25]

$$G(\mathbf{r},\mathbf{r}_o,\omega) = \sum_n \frac{\psi_n(\mathbf{r})\psi_n(\mathbf{r}_o)}{V\Lambda_n(k_n^2 - k^2)}, \tag{1.4}$$

where ψ_n is the acoustic-pressure mode shape corresponding to the natural frequency ω_n of the enclosed space, k_n is the complex wavenumber of mode n, and $k=\omega/c$ is the analysis wavenumber. The harmonic surface vibration velocity can be obtained from the solution of the equation of motion of the vibrating body. For instance, Fahy [19] suggests the use of equation (1.1) to solve for the normal surface vibration velocity in terms of the *in vacuo* plate modes. As already presented (eg. [20-23]), for enclosed volumes of air at static pressure close to atmospheric the fluid loading in the structure can be neglected (neglect the first term on the right-hand side of equation (1.1)) and the structure is said to be weakly coupled to the fluid.

This integro-differential representation was applied by Pan and Bies [28-30] to study the effect of a flexible panel in the modal properties of a room and associated forced response to acoustic and structural sources. The plate and acoustic cavity Green's function were obtained from uncoupled plate and cavity natural modes (expression (1.3)) and used as base functions to obtain the room (coupled rectangular

acoustic cavity and simply-supported flat plate) modal reverberation times and resonance frequencies. Two different methods, orthogonal expansion [23] and successive substitutions, were employed in the solution of the integral equations. Modal coupling and exterior radiation were incorporated in the solution and their influence in the properties of the coupled system discussed.

A transfer factor was defined as a means of deciding the relative importance of the energy transfer between two coupled modes. This factor depends on the difference between the natural frequencies and on the spatial matching given by the integral of the mode shapes over the contacting area (coupling coefficient, C_{np}). They observed that if the transfer factor is close to unity for a structural/acoustic mode pair, the transfer of energy in this frequency region is almost entirely governed by this pair. However, if a cavity mode is not strongly coupled to any plate mode, then the energy transfer from this cavity mode is distributed over many plate modes. When the modal density of the plate is low, the energy transfer between plate and cavity tend to be dominated by one pair; but as the plate modal density increases this dominance tends to decrease. Pan and Bies also observed that, on average, the decay time (damping) decreases as the plate modal density increases. Another observation, associated with the forced sound transmission, is that as the panel gets thinner and its damping is low, radiation into the external space is an important component of the acoustic energy loss from the cavity.

An advantage of the procedures reported in refs. [23,28-30] is that they can be applied to any geometry of plate and acoustic cavity for which uncoupled natural modes are available. Natural modes of dynamic systems can be obtained using numerical methods such as the Finite Element Method or the Boundary Element Method. Since a discussion of these numerical methods in a literature review would be quite involved, it is omitted in the present work. Suffice to say that reliable procedures are available to obtain the natural frequencies and mode shapes of odd-shaped acoustic enclosures, using either FEM [31] or BEM [32].

The importance of the plate boundary conditions on the internal pressure response has been studied by Cheng and Nicolas [33] for the case of a cylindrical hard-walled cavity with a point-driven circular plate. The Green's function approach was used to describe the pressure inside the enclosure (equations (1.3) and

(1.4)) and a variational formulation associated with a Rayleigh-Ritz approach was employed in the plate analysis. The plate was elastically supported by rotational and translational springs enabling classical and intermediate boundary conditions to be simulated. A 'radiation efficiency into cavity' was defined as the ratio of the acoustic energy in the cavity to the kinetic energy of the plate. They observed that free and guided plates radiate much less sound into the cavity than simply-supported and clamped ones, which shows the significance of the deflection of the plate boundaries in the plate radiation. This study suggests that the sound pressure inside the enclosure can be reduced if the rigidity of the edges fixation is decreased.

1.5.3 Power flow approach

Statistical Energy Analysis (SEA)

The works reviewed in the two previous sections model the plate and acoustic cavity interaction by expressing the dynamic behaviour of both systems in terms of their natural modes. However, as the frequency increases, the number of natural modes to be included in the analysis increases and a modal representation is no longer practicable. As already indicated, approximate treatments based on energy balance equations are a popular alternative in the high frequency regime.

In the so-called 'predictive mode' [10] of Statistical Energy Analysis, the studied system is divided in subsystems, separated from each other by significant dynamic discontinuities (barriers to the transmission of vibrational energy from the source(s) of excitation), the parameters of which are probabilistically defined in terms of gross properties. The total time-averaged energy of vibration of each subsystem and the time-averaged vibratory input are used to write steady-state power balance equations. Hence, parameters that control the rate of net energy exchange between the subsystems, the rate of vibrational energy decay (damping) and the capacity for storing vibrational energy (modal density) need to be estimated, either analytically or, as in present common practice, empirically. From the solution of the system of power balance equations, an estimate of the subsystems response is obtained in terms of frequency- and spatial-average quantities.

This approach is based on the exact power flow proportionality relationship that exists between two coupled resonators (modes) randomly excited by statistically independent forces [34],

$$P_{np} = G_{np}(E_p - E_n), \tag{1.5}$$

where P_{np} is the time-averaged power flow between modes n and p, E_p and E_n are the time-averaged modal energies, and G_{np} is a power flow coefficient. In the case of gyrostatic coupling, this coefficient can be derived from equations (1.1) and (1.2) and it depends only on the modal parameters [35]. By assuming there is equipartition of energy between the modes of individual subsystems, that the modal responses of individual subsystems are uncorrelated, and that the exciting forces are uncorrelated in space and time, this relation can be extended to express the time-averaged power flow between two sets of subsystem modes. This extension proves to be a good practical approximation for the band-limited power flow between weakly coupled subsystems with high modal density.

Noise transmission from a reverberant field through a flexible panel into a small enclosure has been investigated by Lyon [36]. In the frequency regime above the first acoustic resonance, he employed SEA to model the resonant transmission. Forced (non-resonant) and free (resonant) sound transmission were compared, and he suggested that noise reduction due to resonant transmission are generally less important than forced waves noise reduction for panels in which the damping loss factor is smaller than 0.3. The power flow coefficient (G_{np}) between panel and cavity subsystems in one-third octave bands was estimated from the band-averaged radiation resistance of a single panel into a free field [37]. However, no criterion was given for the limits of applicability of this approximation to the power flow coefficient.

Two important terms in the power flow coefficient are the coupling coefficient (C_{np}) and a term given by square of the difference between the squares of the natural frequencies of the interacting modes ($(\omega_n^2 - \omega_p^2)^2$). This coefficient has been extensively studied by Fahy [35] who concluded that the power flow between a mode pair is only appreciable if it satisfies a proximity requirement (proximate mode coupling). This proximity requirement is based on the relative value of the modal loss factors and natural frequencies. Uncoupled *in vacuo* plate and acoustic volume modal

parameters were used by Fahy to estimate the coupling coefficient (C_{np}) and associated power flow coefficient between a flexible panel and a rectangular acoustic cavity. The radiation resistance of the panel into the enclosed space was estimated from the individual mode pairs power flow coefficients; a comparison made with the band-averaged baffled panel radiation efficiency into a diffuse field [37] suggested that both results are coincident above a certain frequency. This frequency corresponds to a low frequency limit below which proximate coupling no longer dominates; he named this frequency the 'lower limiting frequency' for maximum proximate mode coupling. In the frequency range below this frequency all mode pairs must be taken into account in the computation of the coupling. He also pointed out that below this frequency the coupling can be strongly affected by the introduction of a perturbation in the geometry of the enclosure which is not the case when proximate mode coupling is present. Therefore, if the modal density of each component is sufficiently high, the power exchanged between a structure and a enclosed volume of fluid can be evaluated from the modal-average free-space radiation properties of the structure. This fact has been extensively employed in applications of SEA to the study of response of enclosed volumes of fluid to random structural vibration [14,19,38,39].

As already explained, a thin plate and an enclosed volume of air can generally be considered to be weakly coupled. In other words, neither *in* vacuo plate nor uncoupled acoustic cavity natural frequencies differ greatly from the natural frequencies of the coupled plate-cavity system, with the exception of the fundamental plate mode. This situation appears to be an important condition for the successful application of SEA and it is normally known as the weak coupling assumption in SEA. A formal analysis of the degree of coupling between plate and acoustic cavity subsystems in terms of power flow has been presented by Gulizia and Price [40]. They modified the approach originally employed by Lyon [36] and Fahy [35] to account explicitly for arbitrary coupling strength in the power flow coefficient and concluded that the equation for the radiation resistance (which is a measure of the rate at which the plate does work on the fluid) is independent of the coupling strength provided the structural modes are considered independent and there are many modes coupling the acoustic and the structural field. They compared their theoretical findings with experiments in which a plate is point excited and radiates into water, a classical strong coupling situation. A

reasonably good agreement was obtained in the frequency range in which both components have high modal density but differences of nearly 10 dB between theoretical and experimental coupling coefficient were observed in the frequency region in which the modal density is not sufficiently high.

Howlett [41] also tackled the case of the strong coupling between an enclosed water-filled box and a thin plate. He employed a statistical modal analysis based on the *in vacuo* plate modes and uncoupled hard-walled acoustic modes to account for the strong interaction between both systems. Substantial difference between theoretical and experimental results was observed, generally at low frequencies, when the steel panel was excited by an acoustic field generated within the water-filled box. He concluded that such differences are related to the neglect of panel radiation coupling effects in his model while Gulizia and Price [40] pointed out that such discrepancy was probably related to the low modal density in the low frequency range. However, Howlett [41] observed that his theoretical results represented a useful improvement over weak-coupling theory.

Uncertainty in SEA

The usual application of SEA to the study of the dynamic behaviour of coupled systems only provides an ensemble average of subsystem response with no (or relatively little) information provided about the uncertainty of the response estimate in relation to any single realisation. Some scattered works have addressed this important issue in the case of plate/acoustic cavity coupling [42,43] but they tend to concentrate on results that are specific to the case analysed. Generic expressions of lower and upper limits of power flow have been suggested by Scharton and Lyon [34] and Hodges and Woodhouse [44] in application to high modal density systems.

The sensitivity of the coupling between a flat plate and an enclosed volume of fluid has been numerically investigated by Mohammed [45] using a Monte Carlo method. The coupled oscillator theory was used to model the dynamic behaviour of the coupled system with the proximate coupling treatment [35] used in the estimation of the plate radiation efficiency (or radiation resistance). The thickness of the plate was randomly perturbed around 10 % of its average value with thickness values drawn from

a normal distribution and the radiation efficiency obtained for a range of modal bandwidth values. It was found that the fluctuation of the radiation resistance about the mean diminishes as the number of interacting mode pairs increases (characterised by an increase in modal density) and as the sum of the half-power bandwidths of the plate and cavity modes gets larger. Moreover, the distribution of the computed radiation efficiency approaches that of the normal distribution as the plate/cavity average modal overlap factor increases (modal overlap factor = $\eta n(f) f$, where $n(f)$ is the modal density).

Works related to SEA

Pope [46] and Pope and Wilby [18,47] presented a low frequency treatment of the noise transmission into an enclosed space based on an energy balance between the power radiated into the cavity and the power dissipated by the enclosed volume of fluid. As in previous approaches they assumed the coupling to be weak and used *in vacuo* structural modes and rigid wall acoustic modes. They considered the interaction of the structure with the inside and outside fluid, and used a joint acceptance function to model the structural excitation due to an arbitrary form of acoustic field. Simplifications were presented for summations of plate modes resonating below, within, and above the frequency band which interact with acoustic modes resonating in the band, or outside the band. The expressions were also simplified for the special case in which the acoustic modal density is high and the sound field inside the enclosure approaches the diffuse state. The interior space-averaged mean-square pressure was obtained by equating the expressions for the power dissipated on the inner cavity walls to the power radiated by the vibrating structure into the cavity in limited frequency bands. This treatment of the energy balance is considered to be a complement to SEA in frequencies in which there is a sparsity of acoustic and structural modes and was successfully employed to model noise transmission in cylinder-like structures [48,49].

By studying the asymptotic behaviour of the modal equations that govern the dynamics of plate and acoustic cavity coupling, Kubota, Dionne and Dowell [50] formally demonstrated the relation between modal analysis and SEA. Their expressions are based in results derived from deterministic equations (equations (1.1)

and (1.2)) in which the number of interacting modes are made very large in order to allow the modal summations to be substituted by integrations and wildly fluctuating functions to be smoothed out. This artifice permits modal parameters to be replaced by their spatially and frequency averaged values. Moreover, it manages to retain the capability of predicting spatial variations of the responses involved. This capability of predicting spatial variations in the pressure response was used to show the existence of intensification zones near the corner, edges and walls of a reverberant room [51,52]. Their results are interesting *per se* but they fail to address important points related to intermediate cases, i.e. the ones in which the number of natural modes are not sufficiently high to allow a reasonable approximation to be achieved by the asymptotic limits of the system parameters. For instance, they assume the structural response to be delta-correlated in space. This is certainly true in the very high frequency limit or for very wide frequency bands but experimental results collected in real structures [53,54,78] and presented in this thesis suggests a different situation.

1.6 Summary of the present study

The novel hybrid deterministic-probabilistic model here presented presupposes a knowledge of the acoustic enclosure modal characteristics, and that the structure is defined by its gross properties and has high modal density. The former implies that the representation adopted for the acoustic cavity is deterministic while the structural system may be only probabilistically represented. Its gross properties will suffice for the estimation of its average response values. We assume that the high modal density subsystem is directly excited and the response in the receiving system needs to be estimated in specific points in three-dimensional space. Moreover, the excitation is of the broad-band random type and all the plate modes are assumed to be excited.

As a result of the exact modal characteristics of the structural system being unpredictable, a bending wave field representation is adopted for this system. This analysis is similar to the one employed in rooms in which the reverberant field predominates over the direct field. In such rooms, interference patterns are created near

the edges and their importance in the acoustic response increases as the wavelength increases. The influence of the boundaries in the structural wave field are taken into account using a free travelling wave model [55] to estimate band-limited spatial correlation of the vibrational response. The correlation characteristics of flat plates are represented by a correlation coefficient which approaches that of a diffuse bending wave field [53] as the structural wavelength decreases and for situations in which the field points are far from the boundaries.

Similar results are presented for cases in which an approximate modal representation based on Bolotin's dynamic edge effect method [56] is employed to represent the vibration field. By taking advantage of the high modal density of the structural subsystem, the modal summation is substituted by an integration in wavenumber space in a manner similar to Bolotin's integral method [56]. New results are presented for cases in which the structural systems have a range of ideal boundary conditions, are plane, singly- or doubly-curved, and may be reinforced by ribs.

These analytical estimates of band-limited spatial correlation of structural response are compared with experimental results obtained on various flat plates and on a road vehicle body shell. These experiments were carried out using a procedure suggested by Stearn [53] based upon the measurement of structural acceleration on a number of points placed along a line due to random excitation. Both acoustic and structural sources were used to excite the measured system.

The coupling coefficients between the structural field and each acoustic mode are computed using numerical integration techniques. These coupling coefficients are used to obtain the theoretical value of acoustic pressure inside a hard-walled acoustic cavity excited by vibration of one flexible wall. The theoretical response results are compared with measurements of acoustic pressure made in an acoustic enclosure with rectangular boundaries of which one flexible wall is mechanically driven by random noise. The advantage of such a geometric configuration is that it permits the use of closed form expressions for acoustic mode shapes and associated natural frequencies.

The novel procedure and basic concepts presented in this work can in principle be extended to irregular cavity geometries and various forms of structural systems. FEM can be used to obtain the acoustic space modal characteristics and SEA can be employed to obtain the vibration levels of the structural components. The

contribution of each structural component to the internal sound pressure is obtained from the coupling coefficients between each structural component and a particular acoustic mode. The overall sound pressure level is obtained by modal summation.

1.7 Thesis arrangement

The chapters of the present work are arranged as follows.

Chapter 2 presents equations of a deterministic-probabilistic description of vibroacoustic coupling.

The spatial correlation characteristics of multimodal bending wave fields are analysed in Chapter 3. This original analysis is directed towards the case in which a perfectly diffuse wave field is not set up in the structure. Particular attention is paid to the effect of boundary conditions on the edge nearfield of such systems.

Chapter 4 presents a comparison between the expressions derived in Chapter 3 and correlation measurements carried out on a number of simple structures and on the bodyshell of a passenger car.

Experimental studies of vibroacoustic interaction are presented in Chapter 5. The pressure inside an acoustic enclosure due to point excitation of the flexible plate is measured and the results compared with estimates obtained from the hybrid deterministic-probabilistic model.

The last chapter is dedicated to a general discussion of the present work and in making recommendations for future work.

A number of appendices is also included in this work in order to complement the main text. In particular, a novel representation of plate radiation efficiency in terms of the present model is compared to classical results of radiation efficiency as given by Maidanik [37] and Leppington et al. [93].

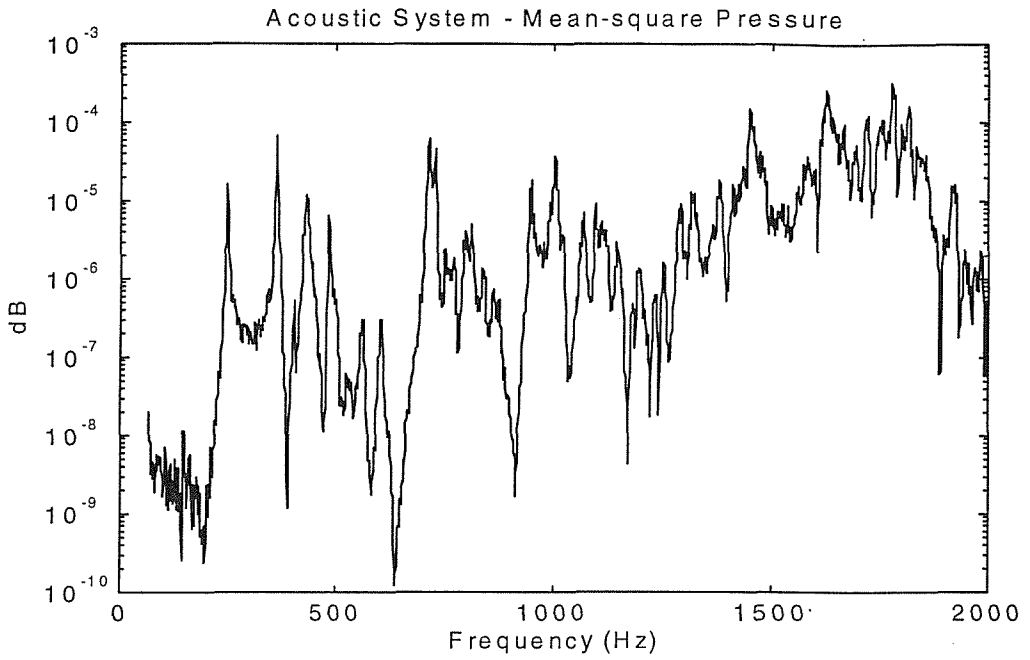

Fig. 1.1.a - Pressure response inside an acoustic cavity due to a point acoustic source

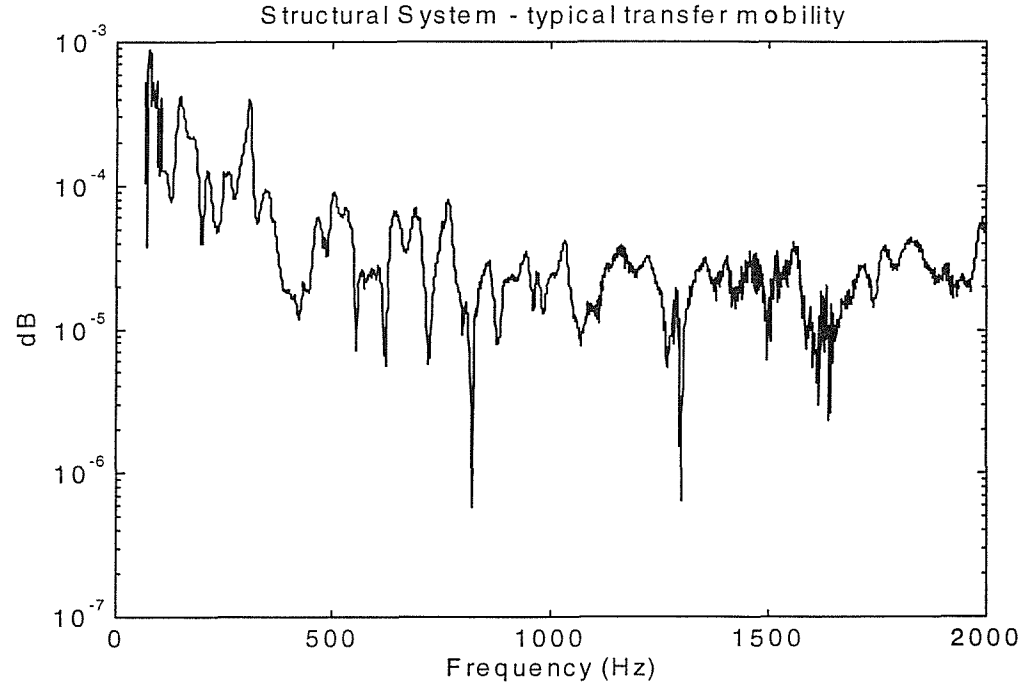

Fig. 1.1.b - Typical transfer mobility of a flat plate.

CHAPTER 2

HYBRID MODEL: BASIC EQUATIONS

2.1 Derivation of hybrid model for a plate coupled to an acoustic cavity based upon modal-interaction

Various procedures for modelling the vibroacoustic interaction between enclosed fluids and flexible plates have been discussed in the previous chapter. One of these, the modal-interaction model, is used when both uncoupled acoustic and structural modes are known. These uncoupled modes are employed in a modal expansion of the response variables and the coefficients of this expansion are used to write a set of differential equations (equations (1.1) and (1.2)) that can be solved to obtain the coupled response. However, if the plate modes are not individually predictable the modal expansion (equation (1.1)) can not be applied to represent the plate wave equation. Therefore, a different procedure needs to be employed to represent the dynamic behaviour of the plate.

Assuming that the only source of excitation for the acoustic cavity is the plate vibration, this excitation can be represented by a generalised modal source ($F_n(t)$) and the acoustic modal equation can be written as [23]

$$\frac{\partial^2 p_n(t)}{\partial t^2} + \eta_n \omega_n \frac{\partial p_n(t)}{\partial t} + \omega_n^2 p_n(t) = \frac{F_n(t)}{\Lambda_n}, \tag{2.1}$$

where the normalisation constant is expressed as

$$\Lambda_n = \frac{1}{V}\int_V \psi_n^2(x,y,z)dV, \tag{2.2}$$

the generalised source due to wall vibration is given by

$$F_n(t) = -\frac{1}{V}\int_S a(x,y,t)\psi_n(x,y,z_o)dxdy, \tag{2.3}$$

$p_n(t)$ are the coefficients in an acoustic normal mode expansion for the pressure (equation (2.4)), ω_n is the n-th acoustic natural frequency with an associated mode shape ψ_n, η_n represents an equivalent damping ratio which can be expressed in terms of the specific normal impedance of the cavity walls (section 5.2.4, ref.[23]), V is the cavity volume, S is the interface area (normally the plate area) and a(x,y,t) represents the normal acceleration of the plate vibration field. A sketch of the plate/acoustic cavity configuration is presented in figure 2.1.

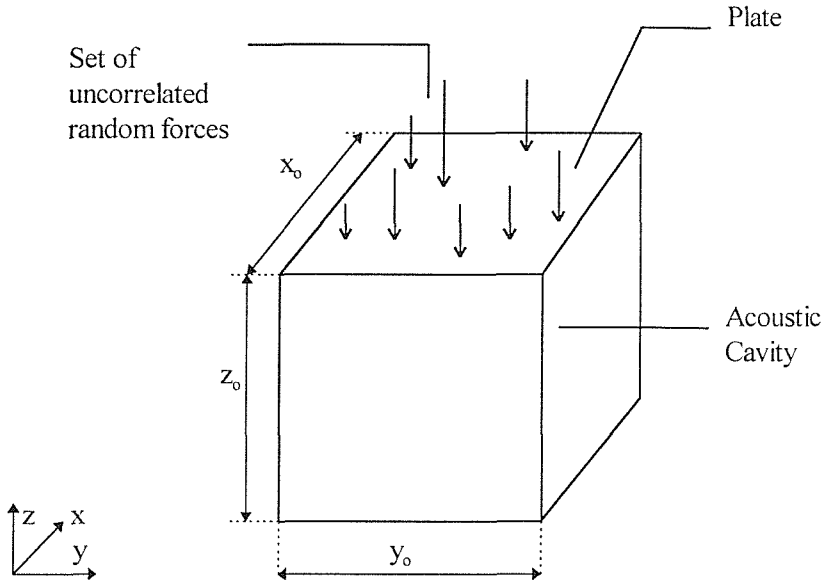

Fig. 2.1 - Acoustic Cavity excited by a random vibrating plate

Using this description the pressure inside the cavity can be obtained using a normal mode expansion

$$p(x,y,z,t) = \rho_o c_o^2 \sum_n p_n(t)\psi_n(x,y,z) \qquad (2.4)$$

where the coefficients $p_n(t)$ are available from solutions of equation (2.1).

In the present analysis, the plate is assumed to be randomly excited by a spatially-uncorrelated time-stationary source. As a result, a vibration field is set up in the plate with an assumed smoothly-varying spectrum in finite bands and known

spatial correlation characteristics; the plate is an excitation field to the acoustic modes. Consequently, the normal-mode approach suggested by Powell [57,58] to study the response of continuous structures under random loading can be employed to estimate the mean-square pressure inside the cavity. In this treatment, the set of acoustic equations (equation (2.1)) is Fourier transformed as a means of obtaining the description of the air enclosure dynamics in the frequency domain. The frequency domain representation of equation (2.1) is

$$\Lambda_n\left[\left(\omega_n^2-\omega^2\right)+i\eta_n\omega\omega_n\right]P_n(\omega)=F_n(\omega), \tag{2.5}$$

where

$$F_n(\omega)=-\frac{1}{V}\int_S A(x_1,y_1,\omega)\psi_n(x_1,y_1,z_o)dx_1dy_1$$

and $A(x_1,y_1,\omega)$ is the Fourier transform of $a(x_1,y_1)$.

The associated Fourier transform of p(t) is

$$P(x,y,z,\omega)=\rho_o c_o^2\sum_n P_n(\omega)\psi_n(x,y,z). \tag{2.6}$$

From equations (2.5) and (2.6) we have

$$P(x,y,z,\omega)=\rho_o c_o^2\sum_n \frac{F_n(\omega)\psi_n(x,y,z)}{\Lambda_n}\frac{\left[X_n-iY_n\right]}{\left[X_n^2+Y_n^2\right]}, \tag{2.7}$$

and its complex conjugate is

$$P^*(x,y,z,\omega)=\rho_o c_o^2\sum_m \frac{F_m^*(\omega)\psi_m(x,y,z)}{\Lambda_m}\frac{\left[X_m+iY_m\right]}{\left[X_m^2+Y_m^2\right]}, \tag{2.8}$$

with

$$F_m^*(\omega)=-\frac{1}{V}\int_S A^*(x_2,y_2,\omega)\psi_m(x_2,y_2,z_o)dx_2dy_2,$$

$$X_n=(\omega_n^2-\omega^2) \qquad \text{and} \qquad Y_n=\eta_n\omega\omega_n$$

The (double-sided) auto-power spectral density of the total pressure is obtained from

$$S_p(x,y,z,\omega)=\lim_{T\to\infty}\frac{\pi}{T}\left[P(x,y,z,\omega)P^*(x,y,z,\omega)\right] \tag{2.9}$$

Substituting equations (2.7) and (2.8) in (2.9) we obtain

$$S_p(x,y,z,\omega) = \frac{(\rho_o c_o^2)^2}{V^2} \sum_n \sum_m \frac{\psi_n(x,y,z)\psi_m(x,y,z)}{\Lambda_n \Lambda_m} \frac{[X_n - iY_n][X_m + iY_m]}{[X_n^2 + Y_n^2][X_m^2 + Y_m^2]} \times$$
$$\times \int_S \int_S S_a(x_1,y_1,x_2,y_2,\omega)\psi_n(x_1,y_1,z_o)\psi_m(x_2,y_2,z_o)dx_1 dx_2 dy_1 dy_2, \quad (2.10)$$

where $S_a(x_1,y_1,x_2,y_2,\omega)$ is the cross-power spectral density of the normal plate acceleration at points $X_1 = (x_1,y_1)$ and $X_2 = (x_2,y_2)$. As the vibration field is not necessarily homogeneous in space, the cross-power spectral density is normalised by the power spectral density of the space-averaged acceleration ($S_a(\omega)$) of the vibration field,

$$\gamma_a(x_1,y_1,x_2,y_2,\omega) = \frac{S_a(x_1,y_1,x_2,y_2,\omega)}{S_a(\omega)}, \quad (2.11)$$

where $\gamma_a(x_1,y_1,x_2,y_2,\omega)$ is here named the normalised cross-power spectral density between the acceleration at two points in the vibration field. The cross-power spectral density can also be normalised by the power spectral density of the acceleration at any single point in the vibration field or by the product of the square root of the power spectral density at points 1 and 2. The former will give the zero-time-delay correlation coefficient of the vibration acceleration between points 1 and 2. All these functions can be derived from the cross-power spectral density simply by manipulating the points coordinates. The formalism related to the study of this quantity is presented in the next chapter together with some simplified expressions for the case of simple modally-dense structural components subjected to spatially-uncorrelated time-stationary random excitation. An experimental investigation of the correlation coefficient on different plates is presented in Chapter 4, together with some results for the cross-power spectral density normalised by the power spectral density of the space-averaged plate acceleration (equation (2.11)).

Introducing equation (2.11) in equation (2.10) we obtain,

$$S_p(x,y,z,\omega) = \frac{(\rho_o c_o^2)^2}{V^2} \sum_n \sum_m \frac{\psi_n(x,y,z)\psi_m(x,y,z)}{\Lambda_n \Lambda_m} S_a(\omega) \frac{[X_n - iY_n][X_m + iY_m]}{[X_n^2 + Y_n^2][X_m^2 + Y_m^2]} \times$$
$$\times \int_S \int_S \gamma_a(x_1,y_1,x_2,y_2,\omega)\psi_n(x_1,y_1,z_o)\psi_m(x_2,y_2,z_o)dx_1 dx_2 dy_1 dy_2, \quad (2.12)$$

The double integral over the plate area in equation (2.12) is a measure of the effectiveness of the random vibration field in exciting a particular

acoustic mode. It represents a coupling coefficient between the vibration field and the acoustic mode.

Equation (2.12) can be separated in direct (m=n) and cross (m≠n) terms. Following this representation the direct coupling coefficient is defined as

$$C_{nn}^2(\omega) = \frac{1}{S^2}\int_S\int_S \gamma_a(x_1,y_1,x_2,y_2,\omega)\psi_n(x_1,y_1,z_o)\psi_n(x_2,y_2,z_o)dx_1dx_2dy_1dy_2. \quad (2.13)$$

and the cross coupling coefficient is given by

$$C_{nm}^2(\omega) = \frac{1}{S^2}\int_S\int_S \gamma_a(x_1,y_1,x_2,y_2,\omega)\psi_n(x_1,y_1,z_o)\psi_m(x_2,y_2,z_o)dx_1dx_2dy_1dy_2. \quad (2.14)$$

Using these definitions of cross and direct coupling coefficients we have

$$S_p(x,y,z,\omega) = \frac{(\rho_o c_o^2)^2 S^2}{V^2} S_a(\omega)\left[\sum_n \frac{\psi_n^2(x,y,z)}{\Lambda_n^2}\frac{1}{[X_n^2+Y_n^2]}C_{nn}^2(\omega) + \sum_n\sum_{\substack{m\\ m\neq n}} \frac{\psi_n(x,y,z)\psi_m(x,y,z)}{\Lambda_n\Lambda_m}\frac{[X_n-iY_n][X_m+iY_m]}{[X_n^2+Y_n^2][X_m^2+Y_m^2]}C_{nm}^2(\omega)\right]. \quad (2.15)$$

The second series in the above equation is normally neglected in cases in which the resonant acoustic modes that participate in the response are lightly damped and well separated. This assumption is not formally correct, though it is widely employed in the literature concerning the dynamic response of lightly damped systems [39,59,60]. For the case in which the summation involves acoustic modes, Chu [60] performed a numerical computation of the values of an equation similar to equation (2.15) to assess the importance of the terms involving n≠m. He observed that when this equation is integrated over frequency (or over wavenumber, as in his case) the main contribution comes for terms in which n=m, because the values of the integral are large for these terms. Moreover, he verified that the numerical value of the modal displacements (ψ's) are always positive for n=m and those for n≠m can be positive or negative and tend to average out to very small contributions. Therefore, for the case of an approximate computation of the response, it is reasonable to neglect the second series in equation (2.15). In this case, the spectral density of the mean-square pressure can be approximated as

$$S_p(x,y,z,\omega) \approx \frac{(\rho_o c_o^2)^2 S^2}{V^2} S_a(\omega)\sum_n \frac{\psi_n^2(x,y,z)}{\Lambda_n^2}\frac{1}{[X_n^2+Y_n^2]}C_{nn}^2(\omega). \quad (2.16)$$

This is the basic equation used to express the ratio between the mean-square acoustic pressure inside an acoustic cavity and the space-averaged mean square acceleration of the random excited flexible wall. It is expected that this expression will be a good approximation to the true response ratio for frequencies in which the plate modal density is high and the acoustic modal density is low. The scope of validity of this result is discussed in Chapter 5. Similar results can be obtained using Green's function (section 2.2) or power balance models (section 2.3). These alternative derivations are presented in the next two sections.

The above results can be extended to represent the acoustic pressure response in terms of the spatially-uncorrelated random forces by considering the response of the plate to these forces. The plate response is described by the spatial average of the mean-square value of its normal acceleration ($< a^2 >$) which can be estimated using power balance considerations. The steady-state input power to a plate in a finite frequency band is given by [14]

$$\Pi_{in} = M\langle v^2 \rangle \eta_p \omega_c = \frac{M\langle a^2 \rangle \eta_p}{\omega_c}, \tag{2.17}$$

where ω_c is the band centre frequency, M is the plate mass, η_p is the frequency-averaged plate loss factor, v^2 is the mean-square plate normal velocity and $< >$ denotes spatial average.

The steady-state input power of a point force is equal to the zero-time-delay cross-correlation between the force and the velocity at the input point. This quantity is normally expressed as a function of the mean-square force [39]

$$\Pi_{in} = \langle F^2 \rangle \mathrm{Re}[Y], \tag{2.18}$$

where Re [Y] is the real part of the point mobility. The point mobility, when space-averaged and integrated over the frequency band, is a function of the modal density (n(f)) of the structure [38]

$$n(f) = 4M\,\mathrm{Re}[Y], \tag{2.19}$$

where the above equation has been obtained from energy balance considerations of a point excited structure [38].

Expressing the space-averaged mean square plate acceleration and force in terms of power spectral densities we obtain from equations (2.17), (2.18) and (2.19)

$$S_a(\omega_c) = \frac{\omega_c n(f) S_F(\omega_c)}{4M^2 \eta_p}. \qquad (2.20)$$

The above equation is valid in finite frequency bands in which a large number of plate modes are resonating. It is a standard result for structural response that is normally used in SEA. Dowell and Kubota [61] have presented a derivation of this equation based on the plate modal equation (equation (1.1)) using asymptotic reasoning. This asymptotic analysis also implies that a large number of plate modes are resonating in each frequency interval, the plate modal parameters (modal mass, modal loss factor, natural frequency and mode shape) vary slowly with mode number and the mean-square force is slowly varying with respect to frequency.

When equation (2.20) is substituted in equations (2.15) or (2.16), the parameters, M, n(f) and η_p, represents the probabilistic part of the hybrid model. The deterministic part is represented by the modal characteristics (F_n, ω_n, η_n, Λ_n) of the acoustic space. The coupling coefficient represents the interaction between these two parts and it is extensively discussed in Chapter 5. From equations (2.16) and (2.20) we can obtain an estimate for the auto-power spectral density of the internal pressure due to smoothly varying random forces which is valid in a frequency interval which centre frequency is ω_c ,

$$S_p(x,y,z,\omega_c) \approx \frac{(\rho_o c_o^2)^2 S^2}{V^2} \frac{\omega_c n(f) S_F(\omega_c)}{4M^2 \eta_p} \sum_n \frac{\psi_n^2(x,y,z)}{\Lambda_n^2} \frac{1}{\Delta\omega} \int_{\Delta\omega} \frac{C_{nn}^2(\omega_c)}{[X_n^2 + Y_n^2]} d\omega. \qquad (2.21)$$

The application of equation (2.21) to the analysis of practical systems presupposes that the acoustic modes are estimated by numerical or analytical procedures and that the plate and acoustic loss factors are, either 'guessed' or estimated using experimental procedures.

We should point out that the present analysis resembles the one presented by Kubota, Dionne and Dowell in ref. [50]. However, their main concern was to derive an expression for the coupling between two modally-dense subsystems based on the modal-interaction model. Other main differences from their work are the use of a more realistic model for the vibration field correlation characteristics and the

introduction of the coupling coefficient between acoustic modes and a vibration field to represent the interaction between modally-sparse and modally-dense subsystems.

2.2 Derivation of hybrid model for a plate coupled to an acoustic cavity based upon the Green's function approach

As presented in Chapter 1, the Kirchhoff-Helmholtz integral equation (equation (1.3)) represents the radiation of sound from a vibrating structure into a surrounding medium. When no acoustic source is present the volume integral in equation (1.3) can be neglected. Moreover, if the Green's function is chosen in order to have zero normal derivative at the boundaries, then the first term on the right-hand side of equation (1.3) can also be neglected. Therefore, for the case of a vibrating structure that encloses a volume of air, the pressure inside the acoustic cavity is related to the normal velocity acceleration of the vibrating structure by

$$p(\mathbf{r}) = \int_S i\omega\rho_o v_N(\mathbf{r}_s) G(\mathbf{r},\mathbf{r}_s) dS. \tag{2.22}$$

When random excitation is applied to the plate/acoustic cavity system the above harmonic formulation can be transformed into a frequency representation by means of a Fourier transformation. This can be done by following the procedure presented in section 2.1. Hence, using the same notation as in section 2.1 we obtain [46]

$$S_p(\mathbf{r},\omega) = \rho_o^2 \int_S \int_S G^*(\mathbf{r},\mathbf{r}_1,\omega) G(\mathbf{r},\mathbf{r}_2,\omega) S_a(\mathbf{r}_2,\mathbf{r}_1,\omega) dS' dS, \tag{2.23}$$

where $\mathbf{r} = (x,y,z)$ is a point inside the acoustic cavity, $\mathbf{r}_1 = (x_1,y_1,z_o)$ and $\mathbf{r}_2 = (x_2,y_2,z_o)$ are two points placed on the interface area (plate). For the case of an acoustic cavity the Green's function can be expanded in terms of the acoustic normal modes in the form presented in equation (1.4). Following the notation presented in section 2.1 the Green's function for the acoustic cavity can be written as

$$G(\mathbf{X},\mathbf{Y},\omega) = \sum_n \frac{c_o^2}{V\Lambda_n} \frac{\psi_n(\mathbf{X})\psi_n(\mathbf{Y})}{(X_n - iY_n)} \tag{2.24}$$

The cross-power spectral density of the plate acceleration can be normalised as proposed in equation (2.11). Substituting equations (2.24) and (2.11) in equation (2.23) we obtain

$$S_p(x,y,z,\omega) = \frac{\rho_o^2 c_o^4}{V^2} S_a(\omega) \sum_n \sum_m \frac{\psi_n(x,y,z)\psi_m(x,y,z)}{\Lambda_n \Lambda_m} \frac{(X_n + iY_n)}{(X_n^2 + Y_n^2)} \times$$
$$\times \frac{(X_m - iY_m)}{(X_m^2 + Y_m^2)} \int_S \int_S \psi_n(x_1,y_1,z_o)\psi_m(x_2,y_2,z_o)\gamma_a(x_1,y_1,x_2,y_2,\omega) dS' dS. \quad (2.25)$$

If the above equation is written in terms of direct and cross terms and the expression for the coupling coefficient (equations (2.13) and (2.14)) is substituted in this equation, equation (2.15) is obtained.

2.3 Derivation of hybrid model for a plate coupled to an acoustic cavity based upon the power balance approach

The total real power radiated by a random vibrating flexible plate into a closed cavity in band $\Delta\omega$ is given by [18]

$$\Pi_{in} = \int_{\Delta\omega} \mathrm{Re}[\int_S S_{pv}(\mathbf{r}_s,\omega) dS] d\omega, \quad (2.26)$$

where $\mathbf{r}_s$ is a point situated on the radiating surface.

The (double-sided) cross-power spectral density of the acoustic pressure and plate velocity over the radiating area (S) is expressed as [18]

$$S_{pv}(\mathbf{r}_s,\mathbf{r}_1,\omega) = \lim_{T\to\infty} \frac{\pi}{T} \left[P(\mathbf{r}_s,\omega) V^*(\mathbf{r}_1,\omega)\right], \quad (2.27)$$

where $\mathbf{r}_1$ is a point situated on the radiating surface.

The Fourier Tranform of equation (2.22) can be expressed as

$$P(\mathbf{r}_s,\omega) = \rho_o \int_S G(\mathbf{r}_S,\mathbf{r}_2,\omega) A(\mathbf{r}_2,\omega) dS', \quad (2.28)$$

where $\mathbf{r}_2$ is a point situated on the radiating surface and equation (2.29) was used in the derivation of equation (2.28),

$$V(\mathbf{r}_2,\omega) = \frac{i}{\omega} A(\mathbf{r}_2,\omega). \quad (2.29)$$

Substituting (2.28) in (2.27) and using the relation (2.29) we can write that,

$$S_{pv}(\mathbf{r}_s,\mathbf{r}_1,\omega)=\lim_{T\to\infty}\frac{\pi}{T}\left[\rho_o\int_S G(\mathbf{r}_s,\mathbf{r}_2,\omega)A(\mathbf{r}_2,\omega)dS'\frac{i}{\omega}A^*(\mathbf{r}_1,\omega)\right],$$

and rearranging the terms of the above equation we obtain,

$$S_{pv}(\mathbf{r}_s,\mathbf{r}_1,\omega)=\frac{i\rho_o}{\omega}\left[\int_S G(\mathbf{r}_s,\mathbf{r}_2,\omega)\lim_{T\to\infty}\frac{\pi}{T}A(\mathbf{r}_2,\omega)A^*(\mathbf{r}_1,\omega)dS'\right].$$

From equation (2.9) we can substitute the cross-spectral density of the plate acceleration on the above equation to write,

$$S_{pv}(\mathbf{r}_s,\mathbf{r}_1,\omega)=\frac{i\rho_o}{\omega}\left[\int_S G(\mathbf{r}_s,\mathbf{r}_2,\omega)S_a(\mathbf{r}_2,\mathbf{r}_1,\omega)dS'\right],$$

where the above integral is evaluated on $\mathbf{r}_2$. The integral over the radiating area of the autospectral density of the acoustic pressure and plate velocity can be obtained from the above expression by setting $\mathbf{r}_s \equiv \mathbf{r}_1$,

$$\int_S S_{pv}(\mathbf{r}_s,\omega)dS=\frac{i\rho_o}{\omega}\int_S\int_S G(\mathbf{r}_2,\mathbf{r}_1,\omega)S_a(\mathbf{r}_2,\mathbf{r}_1,\omega)dS'dS. \qquad (2.30)$$

As in the previous section, the Green's function for the acoustic cavity can be expressed in terms of the acoustic modes (equation (2.24)). Moreover, the normalisation for the cross-power spectral density of the plate acceleration (equation (2.11)) can be applied to equation (2.30). With these modifications we have

$$\int_S S_{pv}(\mathbf{r}_s,\omega)dS=\frac{i\rho_o}{\omega}\sum_n\frac{c_o^2}{V\Lambda_n}\frac{(X_n+iY_n)}{(X_n^2+Y_n^2)}S_a(\omega)\int_S\int_S\psi_n(\mathbf{r}_1)\psi_n(\mathbf{r}_2)\gamma_a(\mathbf{r}_2,\mathbf{r}_1,\omega)dS'dS.$$

The real part of the above expression is given by

$$\mathrm{Re}\left[\int_S S_{pv}(\mathbf{r}_s,\omega)dS\right]=-\frac{\rho_o c_o^2 S^2}{V\omega}S_a(\omega)\sum_n\frac{Y_n}{\Lambda_n(X_n^2+Y_n^2)}C_{nn}^2(\omega). \qquad (2.31)$$

where $C_{nn}^2(\omega)$ is defined in equation (2.13) and $Y_n=\omega_n\omega\eta_n$. Finally, substituting equation (2.31) into equation (2.26) we obtain the total real power radiated by a plate into a closed cavity in a band $\Delta\omega$,

$$\Pi_{in}=\frac{\rho_o c_o^2 S^2}{V}\sum_n\frac{1}{\Lambda_n}\int_{\Delta\omega}\frac{S_a(\omega)\eta_n\omega_n C_{nn}^2(\omega)}{(X_n^2+Y_n^2)}d\omega, \qquad (2.32)$$

where the power spectrum of the plate acceleration is assumed to be smoothly varying over the frequency interval $\Delta\omega$.

The total time-average power absorbed on the walls of the cavity in band $\Delta\omega$ has been derived by Pope and Wilby [47] and it is equal to

$$\Pi_{diss} = \frac{V}{\rho_o c_o^2} \sum_n \eta_n \omega_n \langle p_n^2 \rangle, \tag{2.33}$$

where $< p_n^2 >$ is space-average of the nth term modal pressure.

The total power radiated into the enclosure must equal the total power absorbed on the inner walls of the enclosure. So, in order to obtain the power radiated to acoustic modes resonant in the band $\Delta\omega$, the nth term of equation (2.32) must equal the nth term of equation (2.33). This equality gives the individual modal pressures and their summation gives the frequency- and space-averaged mean square pressure inside the cavity. Then,

$$\langle p_n^2 \rangle = \frac{(\rho_o c_o^2)^2 S^2}{V^2} \int_{\Delta\omega} S_a(\omega) \frac{C_{nn}^2(\omega)}{\Lambda_n (X_n^2 + Y_n^2)} d\omega. \tag{2.34}$$

From ref. [47] we have that

$$\langle p_n^2 \rangle = \int_{\Delta\omega} S_{p_n}(\omega) d\omega,$$

where $S_{pn}(\omega)$is the amplitude of the spectral component associated with the nth acoustic mode. Finally, we can write that

$$S_p(\omega) = \frac{(\rho_o c_o^2)^2 S^2}{V^2} \sum_n \frac{S_a(\omega) C_{nn}^2(\omega)}{\Lambda_n (X_n^2 + Y_n^2)}. \tag{2.35}$$

Equation (2.35) is the result for the auto-spectrum of the space-averaged pressure inside the cavity obtained from equation (2.16) by averaging the square of the acoustic mode shape over the enclosure volume. This result is also presented in equation (5.2).

CHAPTER 3

CHARACTERISATION OF MODALLY-DENSE VIBRATION WAVE FIELDS

This chapter introduces an approximate model of the bending wave field generated by the random vibration of thin plate-like components. Only bending waves are considered because these are the types of structural waves in thin plates or shells which couple most effectively with a sound field. This approximate model is employed as a means of obtaining theoretical expressions for the normalised cross-power spectral density of normal plate vibration acceleration averaged in frequency bands, which was introduced in the previous chapter. The expressions here derived are valid for uniform, homogeneous thin plates with ideal boundary conditions excited by spatially-uncorrelated random forces. Corrections are presented to account for effects of curvature, stiffeners and various types of random excitation.

3.1 Rationale of the suggested procedure

The use of this approximate description is an artifice employed in an attempt to avoid the necessity of the precise determination of the structural modes by making use of the very condition that militates against deterministic computation . In other words, it is assumed that many high-order plate modes resonate in each frequency band of analysis, so that computational analysis by the currently available deterministic methods will produce unreliable results. This stems from the fact that it is impossible to compute the precise spatial distribution of amplitude and phase of a vibrational field involving high order modes because these modes are very sensitive to damping distributions, joints and other boundary conditions, about which there is always significant uncertainty. Moreover, deterministic computation must be carried out frequency by frequency, and the response results are then normally compiled in frequency bands, which implies that a large amount of data is unnecessarily

processed. Therefore, it seems natural to seek a representation that avoids this unrealistic approach.

The representation here proposed is based on the computation of the spatial correlation characteristics of the vibration field, which are described by a frequency-averaged parameter, the zero-time-delay correlation coefficient of the plate response (defined in equation (3.6)). Expressions are also presented for the normalised cross-power spectral density (defined in equation (2.11)). The main reason for concentrating the present study on zero-time-delay correlation coefficient is to enable the comparison of some of the results derived herein to others available in the literature. For the moment, it suffices to say that because both quantities are derived from the cross-power spectral density of the plate response it is expected that when one is shown to be applicable to a certain situation, the other will also apply.

Both free-wave and approximate modal models are employed in the derivation of theoretical values for the correlation coefficient. In the modal model, due to the assumed high modal density of the structural components, the summation over the structural modes is substituted by an integration in wavenumber space. Only approximate mode shapes as a function of the boundary conditions are required. Bolotin's dynamic edge effect method [56] is employed to provide an expression for the mode shapes represented as a continuous function of the wavenumber amplitude and phase. As only those modes whose resonance frequencies lie in the band of interest are considered in the summation, the corresponding limits of integration over wavenumber space are for an interval Δk around k_c, the wavenumber of the band centre frequency. The main advantage of this substitution is that the precise determination of the individual mode shapes as a function of individual wavenumbers and resonance frequencies is not necessary. This procedure is only strictly valid for uniform, flat, simply-supported plates. However, for other boundary conditions the mode shapes are represented by sine functions, with a correction to account for the influence of the boundaries (phase shift), and an exponentially decaying term which is only appreciable in a region one wavelength from the edges.

A similar approximate procedure is employed in the derivation based upon a free travelling wave model [55]. In this case, the correlation coefficient is written for only one wave direction and the average result computed from an

integration in wave direction assuming that all directions of propagation are equally probable. The two models give similar results, since the average in terms of waves coming from all directions is equivalent to the average in wavenumber space [60]. The resultant correlation coefficients averaged in frequency bands approach that of a two-dimensional diffuse field in regions remote from the edges, irrespective of the assumed boundary conditions. However, near the edges these correlation coefficients depart considerably from diffuse field form. A brief discussion of the diffuse wave concept is presented in the next section.

3.2 Diffuse wave fields and correlation: a literature review

The concept of diffuseness is widely used in geometrical acoustics to model enclosed spaces when many acoustic modes are simultaneously excited, and also to facilitate the mathematical description of the acoustic field in order to specify standardised acoustic performance tests, such as transmission loss determination and absorption measurements in reverberation chambers. There is no commonly agreed definition of a diffuse sound field; however, two equivalent definitions that appear to be reasonable were presented by Jacobsen [63]. They read :

- *In a diffuse sound field there is equal probability of energy flow in all directions.*
- *A diffuse sound field comprises an infinite number of plane propagating waves with random phase relations, arriving from uniformly distributed directions.*

A diffuse sound field may be approximated in practice in the central region of a reverberant enclosure, at least half a wavelength away from any boundary, at frequencies above the Schroeder cut-off frequency, in cases of pure-tone excitation [26]. When the excitation is of a random nature, the diffuse sound field approximation may be achieved in finite frequency bands below the Schroeder cut-off frequency. Close to the boundaries or any reflecting surface large compared to the wavelength, a sound field departs considerably from the diffuse state. The incident and reflected (or scattered) wave components can interact constructively or destructively, giving rise to interference patterns that are created by the reduction of the number of waves with uncorrelated random phase which contribute to the total pressure at a field point near the edges. In other words, waves within the incident and reflected sets may be

uncorrelated with each other, but individual waves of the incident set are correlated with the corresponding waves of the reflected (or scattered) set. As a result of this interference, the sound energy is not uniformly distributed over the entire volume of a reverberant sound field.

Interference patterns in reverberant sound fields have been studied by Waterhouse [64], Waterhouse and Cook [65], Chu [60,66] and a number of other researchers. Expressions were derived for interference patterns created by plane reflectors intersecting at right angles, whose surfaces are either hard (rigid reflecting; normal velocity component equal to zero) or soft (pressure release; pressure equal to zero) [64,65]. Chu [60,66] demonstrated that these expressions apply to a reverberant space excited either by a band-limited random noise source located at a single position or by a pure-tone excitation averaged over many source positions. The same author [66] also presented expressions for the cross-correlation function of the pressure near and remote from the boundaries of a reverberant acoustic space.

The concept of a diffuse field was extended by Stearn [53] to the case of two-dimensional structural wave fields. He observed that a close approximation to a diffuse bending wave field can be set up in a plate when more than ten modes are simultaneously excited. He also showed that the band-limited, zero-time-delay, correlation coefficient of acceleration of diffuse bending wave fields is equal to a zero-order Bessel function, with the argument given by the product of the measurement points separation distance and the band centre-frequency wavenumber. In real, bounded flat plates, an approximation to this form of correlation coefficient was experimentally observed in regions far from the edges and far from the excitation points [53]. Lyon [14] presented an expression for the ratio between the mean-square acceleration near and remote from the boundaries of a randomly vibrating, simply-supported rectangular plate. However, no information is available in the literature on the influence of the boundary conditions on the correlation function near the boundaries of structural systems.

3.3 Correlation coefficients of random processes

Consider a continuous, time-invariant, linear system subjected to stationary random excitation. The displacements, ($z_1(\mathbf{x}_1,t)$ and $z_2(\mathbf{x}_2,t)$), at two different positions in this system can be considered to be stationary random processes. Thus, the cross-correlation function between the system displacements at points 1 and 2 is defined as [67]

$$R_{12}(\mathbf{x}_1,\mathbf{x}_2,\tau) = E\left[z_1(\mathbf{x}_1,t)z_2(\mathbf{x}_2,t+\tau)\right] \tag{3.1}$$

where E[ ] represents the expected value, or the ensemble-averaged value, of the quantity in square brackets, τ is the time delay between the two-signals.

Assuming that the random processes z_1 and z_2 have zero mean value, the cross-correlation coefficient (or normalized covariance), $\gamma_{12}(\mathbf{x}_1,\mathbf{x}_2,\tau)$, for these random processes can be written as [67]

$$\gamma_{12}(\mathbf{x}_1,\mathbf{x}_2,\tau) = \frac{R_{12}(\mathbf{x}_1,\mathbf{x}_2,\tau)}{\left(E\left[z_1^2(\mathbf{x}_1,t)\right]\right)^{1/2}\left(E\left[z_2^2(\mathbf{x}_2,t)\right]\right)^{1/2}}, \tag{3.2}$$

where $E[z_1^2]$ and $E[z_2^2]$ are the mean square values of the random processes z_1 and z_2, respectively.

Using the Wiener-Khinchin relationships we can relate the cross-correlation function with the cross-power spectral density

$$R_{12}(\mathbf{x}_1,\mathbf{x}_2,\tau) = \mathrm{Re}\left[\int_0^\infty G_{12}(\mathbf{x}_1,\mathbf{x}_2,f)\exp(i2\pi f\tau)df\right], \tag{3.3}$$

where $G_{12}(\mathbf{x}_1,\mathbf{x}_2,f)$ is the one-sided cross-power spectral density of random variable z at positions 1 and 2.

This cross-power spectral density is a complex function because $R_{12}(\mathbf{x}_1,\mathbf{x}_2,\tau)$ is an odd function of τ. So, for $\tau = 0$, equation (3.3) yields

$$R_{12}(\mathbf{x}_1,\mathbf{x}_2,\tau=0) = \int_0^\infty \mathrm{Re}[G_{12}(\mathbf{x}_1,\mathbf{x}_2,f)]df. \tag{3.4}$$

The contribution of frequency components of $G_{12}(\mathbf{x}_1,\mathbf{x}_2,f)$ in a finite frequency band Δf is obtained by the integration of this function between f_2 and f_1, where f_2 and f_1 are the upper and lower frequency limits of the band Δf. Hence, in a frequency band the corresponding zero-time-delay correlation coefficient can be termed

the band-limited correlation coefficient ($\gamma_{12}(\mathbf{x}_1, \mathbf{x}_2, f_c)$), where f_c is the band centre frequency and the explicit indication of zero time delay is dropped for convenience. The mean-square value of the random processes z_1 and z_2 in a frequency band (f_1-f_2) can be obtained from

$$E\left[z_1^2(\mathbf{x}_1, t)\right] = \int_{f_1}^{f_2} G_1(f)\,df, \qquad \text{and} \qquad E\left[z_2^2(\mathbf{x}_2, t)\right] = \int_{f_1}^{f_2} G_2(f)\,df, \tag{3.5}$$

where $G_1(f)$ and $G_2(f)$ are the auto-spectral densities of the random processes z_1 and z_2 at positions 1 and 2, respectively.

Thus, from equations (3.5), (3.4) and (3.2), in a given frequency band, we have

$$\gamma_{12}(\mathbf{x}_1, \mathbf{x}_2, f_c) = \frac{\int_{f_1}^{f_2} \mathrm{Re}\left[G_{12}(\mathbf{x}_1, \mathbf{x}_2, f)\right] df}{\left[\int_{f_1}^{f_2} G_1(f)\,df\right]^{1/2} \left[\int_{f_1}^{f_2} G_2(f)\,df\right]^{1/2}}. \tag{3.6}$$

The above equation is convenient for experimental computation of correlation coefficient values and it was extensively utilised in the experimental work reported in Chapter 4. Moreover, this equation is equivalent to the correlation density coefficient as defined by Morrow [68] and employed in the analysis of correlation of sound pressures in reverberant sound fields. In the same paper, Morrow also defined another coefficient in which the real part of the cross-power spectral density is substituted by the imaginary part of the cross-power spectral density. This coefficient was termed the quadrature density coefficient and experimental values of this coefficient measured on a flat plate are presented in fig. 4.38.

Equation (3.6) can also be employed in the theoretical derivation of frequency-averaged correlation coefficients based on a modal model as described in section 3.6. Alternatively, a different procedure can be employed in the computation of the correlation coefficient using a modal model. The modal correlation coefficient when one single undamped mode is present is given by [68]

$$\gamma_{12M}(\mathbf{x}_1, \mathbf{x}_2) = \frac{\left\langle z_{1M}(t) z_{2M}(t) \right\rangle_t}{\left[\left\langle z_{1M}^2(t) \right\rangle_t\right]^{1/2} \left[\left\langle z_{2M}^2(t) \right\rangle_t\right]^{1/2}},$$

where $z_{1M}(t)$ and $z_{2M}(t)$ are the instantaneous modal displacements at positions 1 and 2, and $<>_t$ represents time average of the quantity inside brackets. In the above coefficient, the specific mode numbers k_x and k_y are represented by an intersection of the lines of the grid shown in fig. 3.1 As the time dependence of an undamped vibration mode is expressed by a sinusoidal factor the modal correlation coefficient equals ± 1 [68].

In a frequency band in which more than one mode is present, the frequency-averaged correlation coefficient can be obtained by summing the contribution from all modes that have resonance frequencies in this band. In addition, assuming that these modes are uncorrelated we can write the frequency-averaged correlation coefficient as

$$\gamma_{12}(\mathbf{x}_1,\mathbf{x}_2,f_c)=\frac{\sum_N \langle z_{1M}(t)z_{2M}(t)\rangle_t}{\left[\sum_N \langle z_{1M}^2(t)\rangle_t\right]^{1/2}\left[\sum_N \langle z_{2M}^2(t)\rangle_t\right]^{1/2}}. \tag{3.7}$$

Alternatively, if the density of modal frequencies is high, the number of modes summed in equation (3.7) is large and the summation can be converted into integration over wavenumber space [25,56]. The limits of integration are for an interval Δk around k_b, the bending wavenumber of the centre frequency of the band (fig. 3.1). Equation (3.7) is then changed to

$$\gamma_{12}(\mathbf{x}_1,\mathbf{x}_2,f_c)=\frac{\int_{\Delta k}\langle\langle z_{1M}(t)z_{2M}(t)\rangle_t\rangle dk_B}{\left[\int_{\Delta k}\langle\langle z_{1M}^2(t)\rangle_t\rangle dk_B\right]^{1/2}\left[\int_{\Delta k}\langle\langle z_{2M}^2(t)\rangle_t\rangle dk_B\right]^{1/2}},$$

where $<>$ denotes an average over a quarter circle of radius k_B in the wavenumber space. Changing from rectangular to cylindrical coordinates it follows that $k_x = k_B\cos\theta$ and $k_y = k_B\sin\theta$ (fig. 3.1). As a result, the frequency-averaged correlation coefficient can be obtained from

$$\gamma_{12}(\mathbf{x}_1,\mathbf{x}_2,f_c)=\frac{\int_{\Delta k}\int_0^{\pi/2}\left[\langle z_{1M}(t)z_{2M}(t)\rangle_t\right]d\theta dk_B}{\left[\int_{\Delta k}\int_0^{\pi/2}\langle z_{1M}^2(t)\rangle_t\, d\theta dk_B\right]^{1/2}\left[\int_{\Delta k}\int_0^{\pi/2}\langle z_{2M}^2(t)\rangle_t\, d\theta dk_B\right]^{1/2}}. \tag{3.8}$$

For the case in which a wave model is used, it is assumed that the amplitude and direction of each propagating wave are indepedent random functions. The

contribution from waves coming from all directions is obtained by choosing, for each wave, one direction and one wavespeed (frequency). This wavespeed is chosen to be inside the interval Δk corresponding to the band of analysis and the wave direction varies from 0 to $\pi/2$. Therefore, when the amplitude of the propagating waves are real, the frequency-averaged correlation coefficient, based on a wave model, is given by equation (3.8). A wave model was employed by Waterhouse [64] and Waterhouse and Cook [65] in the study of interference patterns, and by Cook et al [69] and Stearn [53] in the derivation of correlation coefficients on acoustic and vibration fields. Assuming the amplitude of each propagating wave to be complex, a slightly different equation can be written for the frequency-averaged correlation coefficient

$$\gamma_{12}(\mathbf{x}_1,\mathbf{x}_2,f_c)=\frac{\int_{\Delta k}\int_{0}^{\pi/2}\mathrm{Re}\left[\left\langle z_1(t)z_2^*(t)\right\rangle_t\right]\mathrm{d}\theta\mathrm{d}k_B}{\left[\int_{\Delta k}\int_{0}^{\pi/2}\left\langle z_1^2(t)\right\rangle_t\mathrm{d}\theta\mathrm{d}k_B\right]^{1/2}\left[\int_{\Delta k}\int_{0}^{\pi/2}\left\langle z_2^2(t)\right\rangle_t\mathrm{d}\theta\mathrm{d}k_B\right]^{1/2}} \tag{3.9}$$

where $z_2^*(t)$ represents the complex conjugate of a wave fluctuation given by a complex amplitude component and a component that represents time variation.

The normalised cross-power spectral density (eq. (2.11)) can be obtained by means of a derivation similar to the one presented for the correlation coefficient. The frequency-averaged expression for the real part of this function is then given by

$$\mathrm{Re}\left[\gamma_a(\mathbf{x}_1,\mathbf{x}_2,f_c)\right]=\frac{\int_{f_1}^{f_2}\mathrm{Re}\left[G_{12}(\mathbf{x}_1,\mathbf{x}_2,f)\right]\mathrm{d}f}{\frac{1}{S}\int_{S}\int_{f_1}^{f_2}G(\mathbf{x},f)\mathrm{d}f\mathrm{d}S}=\frac{\int_{\Delta k}\int_{0}^{\pi/2}\left[\left\langle z_{1M}(t)z_{2M}(t)\right\rangle_t\right]\mathrm{d}\theta\mathrm{d}k_B}{\frac{1}{S}\int_{S}\int_{\Delta k}\int_{0}^{\pi/2}\left\langle z_{1M}^2(\mathbf{x},\theta,t)\right\rangle_t\mathrm{d}\theta\mathrm{d}k_B\mathrm{d}S}, \tag{3.10}$$

where the first coefficient is employed in the experimental investigation and the second coefficient is used in theoretical study of normalised cross-power spectral density.

3.4 Derivation of correlation coefficients based on a modal description

3.4.1 Correlation coefficients on modally-dense simply-supported flat plates

The contribution of N vibration modes to transverse displacement response of a simply-supported flat plate is given by

$$z(x,y,t) = \sum_{M=1}^{N} \sin(k_x x)\sin(k_y y) Z_M(t), \tag{3.11}$$

where k_x and k_y are the modal bending wavenumbers in the x and y directions and $Z_M(t)$ represents the modal time dependence. The displacements at points 1 and 2 for one particular mode are

$$\begin{aligned} z_{1M}(t) &= Z_M(t)\sin(k_x x_1)\sin(k_y y_1), \\ z_{2M}(t) &= Z_M(t)\sin(k_x x_2)\sin(k_y y_2), \end{aligned} \tag{3.12}$$

where (x_1,y_1) and (x_2,y_2) are coordinates of points 1 and 2.

Multiplying and time averaging the displacements at points 1 and 2 we have

$$\langle z_{1M}(t) z_{2M}(t)\rangle_t = \overline{Z_M^2}\sin(k_x x_1)\sin(k_x x_2)\sin(k_y y_1)\sin(k_y y_2), \tag{3.13}$$

where $\overline{Z_M^2}$ is the mean square value of $Z_M(t)$. Using standard trigonometric transformations it follows from equation (3.13) that

$$\begin{aligned} \langle z_{1M}(t) z_{2M}(t)\rangle_t = \overline{Z_M^2}\Big[1/2\left(\cos(k_x(x_1 - x_2)) - \cos(k_x(x_1 + x_2))\right)\Big]\times \\ \times\Big[1/2\left(\cos(k_y(y_1 - y_2)) - \cos(k_y(y_1 + y_2))\right)\Big] . \end{aligned} \tag{3.14}$$

Following the procedure suggested in section (3.3) we can express k_x and k_y in terms of the bending wavenumber (k_B) and angle θ. The sum over the individual modes is then substituted by an integration carried out in a strip of width Δk much smaller than the band-centre-frequency wavenumber (k_b) (illustration in fig. 3.1). This substitution is the basis of the method of integral estimates as proposed by Bolotin [56]. The result of this operation is

$$\sum_{M\in\Delta k}\langle z_{1M}(t)z_{2M}(t)\rangle_t = \int_{\Delta k}\int_0^{\pi/2}\langle z_{1M}(t)z_{2M}(t)\rangle_t d\theta dk_B = \frac{N\overline{Z_M^2}}{4}\int_{\Delta k}\Big[\int_0^{\pi/2}\cos(k_B(x_1-x_2)\cos\theta)\cos(k_B(y_1-y_2)\sin\theta)d\theta -$$
$$\int_0^{\pi/2}\cos(k_B(x_1-x_2)\cos\theta)\cos(k_B(y_1+y_2)\sin\theta)d\theta - \int_0^{\pi/2}\cos(k_B(x_1+x_2)\cos\theta)\cos(k_B(y_1-y_2)\sin\theta)d\theta$$
$$+\int_0^{\pi/2}\cos(k_B(x_1+x_2)\cos\theta)\cos(k_B(y_1+y_2)\sin\theta)d\theta\Big]dk_B, \qquad (3.15)$$

where N modes are assumed to be excited in the band Δk and $\overline{Z_M^2}$ is assumed equal for all modes. The four integrals inside the brackets in the above equation can be solved using equation (D.6) presented in Appendix D. The solution is

$$\frac{\pi}{2}\Big[J_0\Big(k_B\sqrt{(x_1-x_2)^2+(y_1-y_2)^2}\Big)+J_0\Big(k_B\sqrt{(x_1-x_2)^2+(y_1+y_2)^2}\Big)$$
$$-J_0\Big(k_B\sqrt{(x_1+x_2)^2+(y_1-y_2)^2}\Big)+J_0\Big(k_B\sqrt{(x_1+x_2)^2+(y_1+y_2)^2}\Big)\Big]. \qquad (3.15')$$

The expressions for $\int_0^{\pi/2}\langle z_{1M}^2(t)\rangle_t d\theta$ and $\int_0^{\pi/2}\langle z_{2M}^2(t)\rangle_t d\theta$ can be obtained from equations (3.15) and (3.15') by making $x_1 = x_2$ and $y_1 = y_2$. The resulting integrals can then be solved using expressions (D.1), (D.2) and (D.6) from Appendix D. For point 1 the result is

$$\int_0^{\pi/2}\langle z_{1M}^2(t)\rangle_t d\theta = \frac{N\pi\overline{Z_M^2}}{8}\Big[1-J_0(2k_Bx_1)-J_0(2k_By_1)+J_0\Big(2k_B\sqrt{x_1^2+y_1^2}\Big)\Big]. \qquad (3.16)$$

When divided by $N\pi\overline{Z_M^2}/8$, the above expression gives the interference patterns near the boundaries of the plate as originally derived by Lyon [14]. It expresses the relation between the mean-square acceleration near the boundaries and its equivalent in a position far from the boundaries. A sketch of such interference patterns near the corner of a plate are presented in fig. 3.3 and 3.4. They are sketched as a function of a typical wavelength (λ) and it can be noted from the contour plot of fig. 3.4 that when $x_1, y_1 \geq \lambda$ and $x_2, y_2 \geq \lambda$ the mean-square values of the response variable do not depart considerably from the spatial average ($\langle v^2\rangle$).

The integral of the type

$$\int_{k_1}^{k_2} J_0(k_Br)dk_B,$$

required when the terms of equation (3.15), (3.15') and (3.16) are summed in the strip $\Delta k = k_1 - k_2$ has been shown by Cook et al [69] to be given by

$$J_0(k_b r)\Delta k \quad + \text{terms of the order } \left(\frac{k_2 - k_1}{k_b}\right)^2 \Delta k \qquad (3.16')$$

where $k_b=(k_2+k_1)/2$. Assuming that the width of the strip is small enough in order that the second terms in equation (3.16') are neglected we obtain from equations (3.15), (3.15'), (3.16) and (3.8) an approximate expression for the frequency-averaged correlation coefficient of acceleration between two points on a simply-supported homogenous flat plate. This expression is,

$$\gamma_{12}(\mathbf{x_1},\mathbf{x_2},f_c) = \frac{\left[J_0\left(k_b\sqrt{(x_1-x_2)^2+(y_1-y_2)^2}\right)-J_0\left(k_b\sqrt{(x_1-x_2)^2+(y_1+y_2)^2}\right)\right.}{\left.-J_0\left(k_b\sqrt{(x_1+x_2)^2+(y_1-y_2)^2}\right)+J_0\left(k_b\sqrt{(x_1+x_2)^2+(y_1+y_2)^2}\right)\right]} \qquad (3.17)$$
$$\left[1-J_0(2k_bx_1)-J_0(2k_by_1)+J_0\left(2k_b\sqrt{x_1^2+y_1^2}\right)\right]^{1/2}$$
$$\times\left[1-J_0(2k_bx_2)-J_0(2k_by_2)+J_0\left(2k_b\sqrt{x_2^2+y_2^2}\right)\right]^{1/2}$$

The above result is valid in frequency bands whose centre frequency is f_c (with corresponding bending wavenumber k_b) in which a random source excites a large number of plate modes. As the bandwidth of the frequency band increases beyond a certain limit the frequency-averaged coefficient presented in equation (3.17) is no longer valid.

All the results presented in this section presuppose that points 1 and 2 are situated in the quarter space bounded by $0 \le x \le a/2$ and $0 \le y \le b/2$, where a and b are the plate dimensions (fig. 3.2). However, they are unaffected by the substitution $x \rightarrow a-x$, $y \rightarrow b-y$ (pag.121, ref. [14]) and, therefore, they can be used to represent the interference patterns and correlation coefficients in other sections of the plate.

A number of simplifications can be carried out in equation (3.17) but the most important one is for the case in which points 1 and 2 are far from the edges. In this situation, the three last terms on the left of equation (3.15') and on the left of equation (3.16) approach zero and are much smaller than the first term. For this reason, these terms can be neglected. As a result, we obtain equation (3.18) that gives the frequency-averaged correlation coefficient in points remote from the edges on a simply-supported flat plate. However, this approximation is not valid for some specific lines in which there is superposition of nodal lines.

$$\gamma_{12}(\mathbf{x}_1, \mathbf{x}_2, f_c) = J_0(k_b r), \tag{3.18}$$

where r is the distance between points 1 and 2. This is the result derived by Cook et al [69] and by Morrow [68] for a two-dimensional reverberant sound field. Similarly, as already mentioned in section 3.2, Stearn [53] has shown that this result also applies to a diffuse bending wave field as long as the frequency band is restricted to a one-third octave and $k_b r$ is less than ten. Even though the present analysis has been restricted to simply-supported edges, equation (3.18) is valid for any type of boundary condition because, as shown by Bolotin [56], flat structures behave like simply-supported plates at points remote from their boundaries at frequencies high compared with the fundamental resonance frequency. Experimental results presented in the following chapter confirm this statement.

For the case of diffuse bending wave fields it can be shown that the frequency-averaged normalised cross-power spectral density is equal to the correlation coefficient (equation (3.18)). However, for simply-supported plates the normalised cross-power spectral density is given by

$$\mathrm{Re}[\gamma_a(\mathbf{x}_1, \mathbf{x}_2, f_c)] = \frac{\left[J_0\left(k_b\sqrt{(x_1-x_2)^2+(y_1-y_2)^2}\right)+J_0\left(k_b\sqrt{(x_1-x_2)^2+(y_1+y_2)^2}\right)\right.}{\left.-J_0\left(k_b\sqrt{(x_1+x_2)^2+(y_1-y_2)^2}\right)+J_0\left(k_b\sqrt{(x_1+x_2)^2+(y_1+y_2)^2}\right)\right]} \cdot (3.19)$$
$$\frac{1}{S}\int_s\left[1-J_0(2k_b x)-J_0(2k_b y)+J_0\left(2k_b\sqrt{x^2+y^2}\right)\right]dS$$

3.4.2 Correlation coefficients on modally-dense flat plates with generic boundary conditions.

In order to derive an expression for the correlation coefficients of random excited flat plates with arbitrary boundary conditions, the dynamic response of a rectangular plate is represented using Bolotin's dynamic edge effect method [56]. This method involves using a generating (inner) solution in the form of a sinusoidal function and an exponential term (outer solution) that accounts for the dynamic boundary effect in the boundary zone. For the case of a rectangular plate in which the edges generate an evanescent near field, an approximate representation for the normal

displacements at points 1 and 2 for one particular resonant mode can be written as [56]

$$\begin{aligned} z_{1M}(t) &= Z_M(t)X(x_1)Y(y_1), \\ z_{2M}(t) &= Z_M(t)X(x_2)Y(y_2), \end{aligned} \tag{3.19'}$$

where,

$$\begin{aligned} X(x) &= \sin k_x(x-\xi_x) + C_x \exp(-\mu_x x), \\ Y(y) &= \sin k_y(y-\xi_y) + C_y \exp(-\mu_y y), \\ \mu_x &= \sqrt{k_x^2 + 2k_y^2}, \quad \mu_y = \sqrt{k_y^2 + 2k_x^2}. \end{aligned}$$

Multiplying and time averaging the displacements at points 1 and 2 we obtain expressions for $\langle z_{1M}(t)z_{2M}(t)\rangle_t$, $\langle z_{1M}^2(t)\rangle_t$ and $\langle z_{2M}^2(t)\rangle_t$. These expressions are valid for a single mode with modal wavenumbers k_x and k_y. The dynamic edge parameters, $\sin k_x\xi_x$, $\cos k_x\xi_x$, C_x, $\cos k_y\xi_y$, $\sin k_y\xi_y$, C_y, are obtained from the plate boundary conditions. The dynamic edge parameters for simply-supported, clamped, free, guided or spring-supported edges are presented in Appendix B. As already presented, a frequency-averaged value for these expressions can be obtained by summing the contribution from each mode that is excited in the band. Alternatively, when the structure has a high modal density the discrete wavenumbers (k_x,k_y) can be substituted by the continuous functions $k_B\cos\theta$ and $k_B\sin\theta$ and the modal summation substituted by an integration over wavenumber space (fig. 3.1). In addition, the dynamic edge parameters will also be function of k_B and θ, though this dependence is omitted in equations (3.20) and (3.21).

Performing this substitution we have that

$$\sum_{M\in\Delta k}\langle z_{1M}(t)z_{2M}(t)\rangle_t = \int_{\Delta k}\int_0^{\pi/2}\langle z_{1M}(t)z_{2M}(t)\rangle_t d\theta dk_B = N\overline{Z_M^2}\int_{\Delta k}\int_0^{\pi/2} X(x_1)X(x_2)Y(y_1)Y(y_2)d\theta dk_B, \tag{3.20}$$

where,

$$\begin{aligned} X(x_1)X(x_2) = \frac{1}{2}\Big[&\cos\big(k_B(x_1-x_2)\cos\theta\big) - \cos\big(k_B(x_1+x_2)\cos\theta\big)\cos\big(2\xi_x k_B\cos\theta\big) \\ &- \sin\big(k_B(x_1+x_2)\cos\theta\big)\sin\big(2\xi_x k_B\cos\theta\big)\Big] + C_x^2\exp\big(-\mu_x(x_1+x_2)\big) \\ &+ C_x\exp(-\mu_x x_2)\Big[\cos\big(\xi_x k_B\cos\theta\big)\sin\big(k_B x_1\cos\theta\big) + \sin\big(\xi_x k_B\cos\theta\big)\cos\big(k_B x_1\cos\theta\big)\Big] \\ &+ C_x\exp(-\mu_x x_1)\Big[\cos\big(\xi_x k_B\cos\theta\big)\sin\big(k_B x_2\cos\theta\big) + \sin\big(\xi_x k_B\cos\theta\big)\cos\big(k_B x_2\cos\theta\big)\Big], \end{aligned} \tag{3.20a}$$

and,

$$
\begin{aligned}
Y(y_1)Y(y_2) = \frac{1}{2}\Big[&\cos\big(k_B(y_1-y_2)\sin\theta\big) - \cos\big(k_B(y_1+y_2)\sin\theta\big)\cos\big(2\xi_y k_B \sin\theta\big) \\
&-\sin\big(k_B(y_1+y_2)\sin\theta\big)\sin\big(2\xi_y k_B \sin\theta\big)\Big] + C_y^2 \exp\big(-\mu_y(y_1+y_2)\big) \\
&+C_y \exp\big(-\mu_y y_2\big)\Big[\cos\big(\xi_y k_B \sin\theta\big)\sin\big(k_B y_1 \sin\theta\big) + \sin\big(\xi_y k_B \sin\theta\big)\cos\big(k_B y_1 \sin\theta\big)\Big] \\
&+C_y \exp\big(-\mu_y y_1\big)\Big[\cos\big(\xi_y k_B \sin\theta\big)\sin\big(k_B y_2 \sin\theta\big) + \sin\big(\xi_y k_B \sin\theta\big)\cos\big(k_B y_2 \sin\theta\big)\Big].
\end{aligned}
\tag{3.20b}
$$

and N modes are assumed to be excited in the band Δk. In order to estimate the correlation coefficient we also need analytical expressions for $\sum_{M\in\Delta k}\langle z_{1M}^2(t)\rangle_t$ and $\sum_{M\in\Delta k}\langle z_{2M}^2(t)\rangle_t$. These expressions are obtained from (3.20) by setting $x_1 = x_2$ and $y_1 = y_2$. For point 1 we have that

$$
\sum_{M\in\Delta k}\langle z_{1M}^2(t)\rangle_t = \int_{\Delta k}\int_0^{\pi/2}\langle z_{1M}^2(t)\rangle_t \, d\theta dk_B = N\overline{Z_M^2}\int_{\Delta k}\int_0^{\pi/2} W(x_1)W(x_2)\,d\theta dk_B, \tag{3.21}
$$

where,

$$
\begin{aligned}
W(x_1) = \frac{1}{2}\Big[&1-\cos\big(2k_B x_1\cos\theta\big)\cos\big(2\xi_x k_B\cos\theta\big) - \sin\big(2k_B x_1\cos\theta\big)\sin\big(2\xi_x k_B\cos\theta\big)\Big] \\
&+2C_x\exp\big(-\mu_x x_1\big)\Big[\cos\big(\xi_x k_B\cos\theta\big)\sin\big(k_B x_1\cos\theta\big) + \sin\big(\xi_x k_B\cos\theta\big)\cos\big(k_B x_1\cos\theta\big)\Big] \\
&+C_x^2\exp\big(-2\mu_x x_1\big), \qquad (3.21a)
\end{aligned}
$$

and,

$$
\begin{aligned}
W(y_1) = \frac{1}{2}\Big[&1-\cos\big(2k_B y_1\sin\theta\big)\cos\big(2\xi_y k_B\sin\theta\big) - \sin\big(2k_B y_1\sin\theta\big)\sin\big(2\xi_y k_B\sin\theta\big)\Big] \\
&+2C_y\exp\big(-\mu_y y_1\big)\Big[\cos\big(\xi_y k_B\sin\theta\big)\sin\big(k_B y_1\sin\theta\big) + \sin\big(\xi_y k_B\sin\theta\big)\cos\big(k_B y_1\sin\theta\big)\Big] \\
&+C_y^2\exp\big(-2\mu_y y_1\big). \qquad (3.21b)
\end{aligned}
$$

The expression for $\sum_{M\in\Delta k}\langle z_{2M}^2(t)\rangle_t$ is analogous to (3.21) with the index 1 substituted by 2 in expressions (3.21a) and (3.21b). In the above expressions we have that,

$$
\mu_x = k_B\sqrt{1+\sin^2\theta}, \quad \text{and} \quad \mu_y = k_B\sqrt{1+\cos^2\theta}. \tag{3.22}
$$

Finally, from (3.8), (3.20) and (3.21) we obtain an expression for the frequency-averaged correlation coefficient at points $\mathbf{x}_1=(x_1,y_1)$ and $\mathbf{x}_2=(x_2,y_2)$,

$$\gamma_{12}(\mathbf{x}_1,\mathbf{x}_2,f_c)=\frac{\int_{\Delta k}\int_{0}^{\pi/2}X(x_1)X(x_2)Y(y_1)Y(y_2)\,d\theta dk_B}{\left[\int_{\Delta k}\int_{0}^{\pi/2}W(x_1)W(y_1)\,d\theta dk_B\right]^{1/2}\left[\int_{\Delta k}\int_{0}^{\pi/2}W(x_2)W(y_2)\,d\theta dk_B\right]^{1/2}}, \quad (3.23)$$

where $X(x_1)X(x_2)$, $Y(y_1)Y(y_2)$, $W(x_1)$, $W(y_1)$, $W(x_2)$ and $W(y_2)$ are given by equations (3.20a), (3.20b), (3.21a), (3.21b).

The above result allows the computation of correlation coefficients for different types of boundary conditions by using the relevant dynamic edge parameters presented in Appendix B. For the majority of these boundary conditions the integration in wavenumber space has to be performed numerically as no closed form solutions have been found for these integrals. Attempts were made to obtain closed form expressions using a different number of integration procedures, results from tables of integrals [70,71,72] and symbolic languages like Maple V. However, no computationally convenient expressions were found for the correlation coefficient of plates with clamped, free or spring supported edges. Therefore, we had to resort to numerical integration as a means of computing the correlation coefficient of plates with these boundary conditions. Nevertheless, as the integration in angle θ is performed in only one variable the computing time involved is not critical. The numerical efficiency and precision aspects of the integration routines employed are discussed in Chapter 5.

A general expression for the frequency average of the normalised cross-power spectral density can be obtained in a derivation similar to the one presented for the correlation coefficient. The final result, which is employed in the response computation (Chapter 5) and on the verification of the experimental results (Chapter 4), is

$$\mathrm{Re}\left[\gamma_a(\mathbf{x}_1,\mathbf{x}_2,f_c)\right]=\frac{\int_{\Delta k}\int_{0}^{\pi/2}X(x_1)X(x_2)Y(y_1)Y(y_2)\,d\theta dk_B}{\frac{1}{S}\int_{S}\int_{\Delta k}\int_{0}^{\pi/2}W(x)W(y)\,d\theta dk_B dxdy}. \quad (3.23')$$

where $X(x_1)X(x_2)$, $Y(y_1)Y(y_2)$, $W(x)$, $W(y)$ are given by equations (3.20a), (3.20b), (3.21a), (3.21b).

The theoretical results for clamped and free edges were validated against experimental observations on flat plates. As reported in Chapter 4, the agreement between theory and experiments is reasonable and so, the expressions here presented can be employed on analytical models based on the theory presented in Chapter 2. Moreover, corrections are presented to account for the influence of the curvature on doubly- and singly-curved flat shells (Appendix F).

Correlation coefficients near the corner of a plate with guided edges are plotted as a function of the wavelength (λ) in fig. 3.5. This illustration assumes that one of the points is fixed at $x_1 = y_1 = 1.05/\lambda$ and the other one varies over the area sketched. It is verified that far from the edges the correlation coefficient approaches zero very quickly. From figs. 3.3 and 3.5 we can say that the edges are important in the mean-square response estimation in a region one wavelength from them and for points that depart from the boundaries the response is uncorrelated for points two wavelengths apart.

By comparing expression (3.16) with the interference patterns presented in ref. [65] it is verified that this expression is equivalent to that for the interference patterns of the pressure near a two-plane edge in a room whose walls are acoustically soft (pressure release boundary condition). The only difference is that for 3-dimensional wave fields the zero-order Bessel function is replaced by the sinc function, (sin x)/x. It can be also shown that a guided edge in a modally-dense 2-dimensional vibration field generates interference patterns similar to those generated by an acoustically hard wall (rigid reflecting, normal velocity component equal to zero) in a 2-dimensional reverberant acoustic field. Furthermore, when the zero-order Bessel functions are replaced by sinc functions, expression (3.17) gives the correlation coefficient of the pressure near a two-plane edge in reverberation chambers whose walls are soft. The interference patterns near a three-plane corner can be obtained following a similar procedure as the one presented in this chapter. Such results have been employed in the study of zones of quiet in diffuse acoustic fields. They have also been checked against numerical simulation of diffuse sound fields [88].

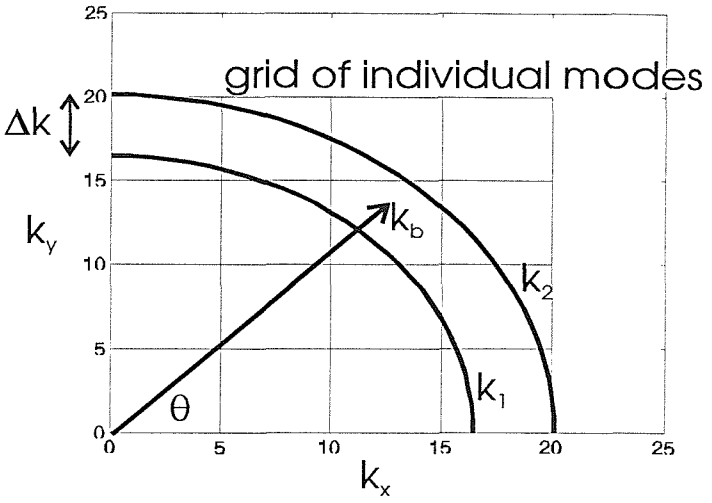

Fig. 3.1 - Grid of discrete modes compared to continuous function representation in terms of k_b and θ.

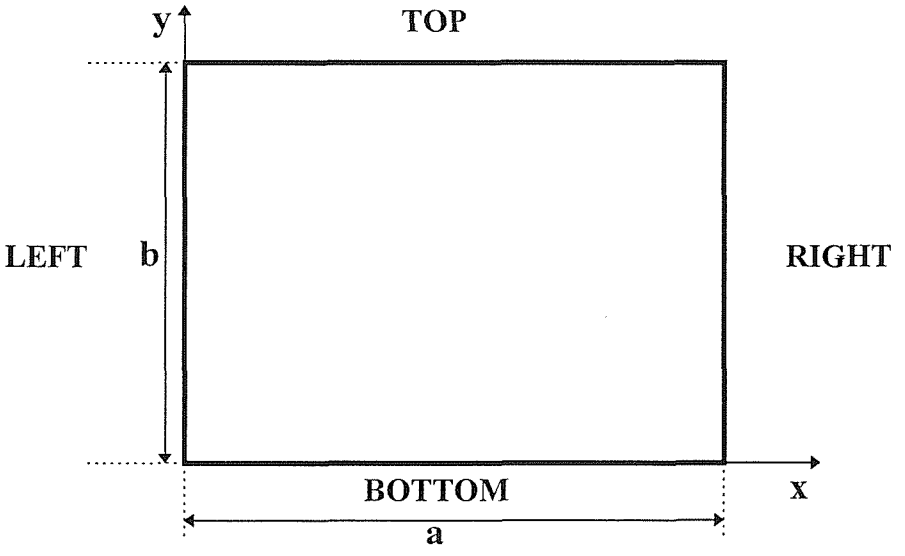

Fig. 3.2 - Sketch of plate used in the derivation of the correlation coefficient

fig. 3.3 - Interference patterns near the corner of a simply-supported plate

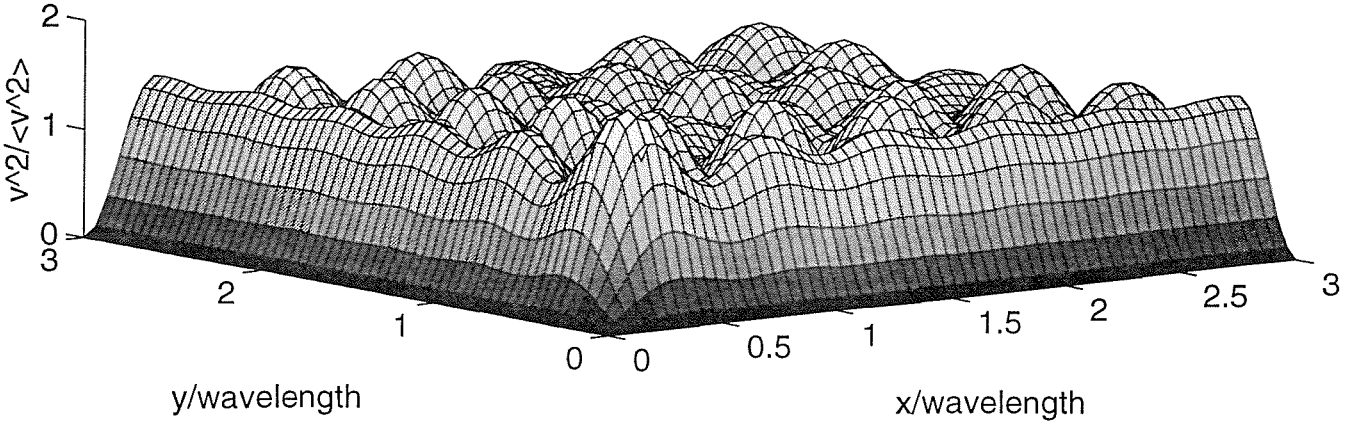

fig. 3.4 - Contour plot for the interference patterns of fig. 3.3

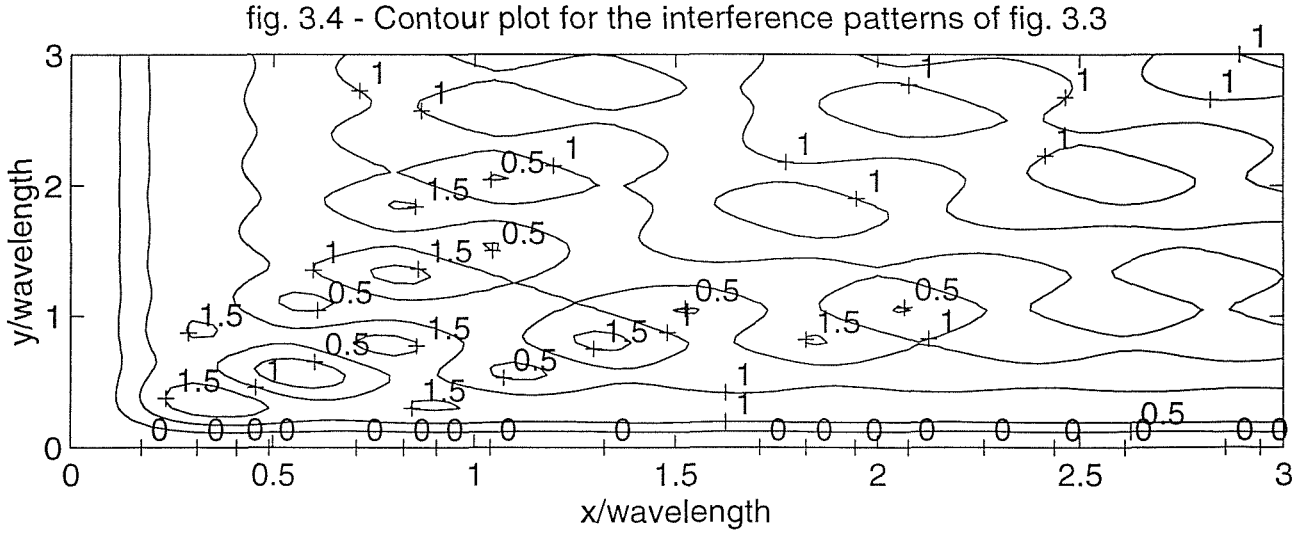

fig. 3.5 - Correlation coefficient near the corner of a guided plate - fixed point=1.05/wav.,1.05/wa

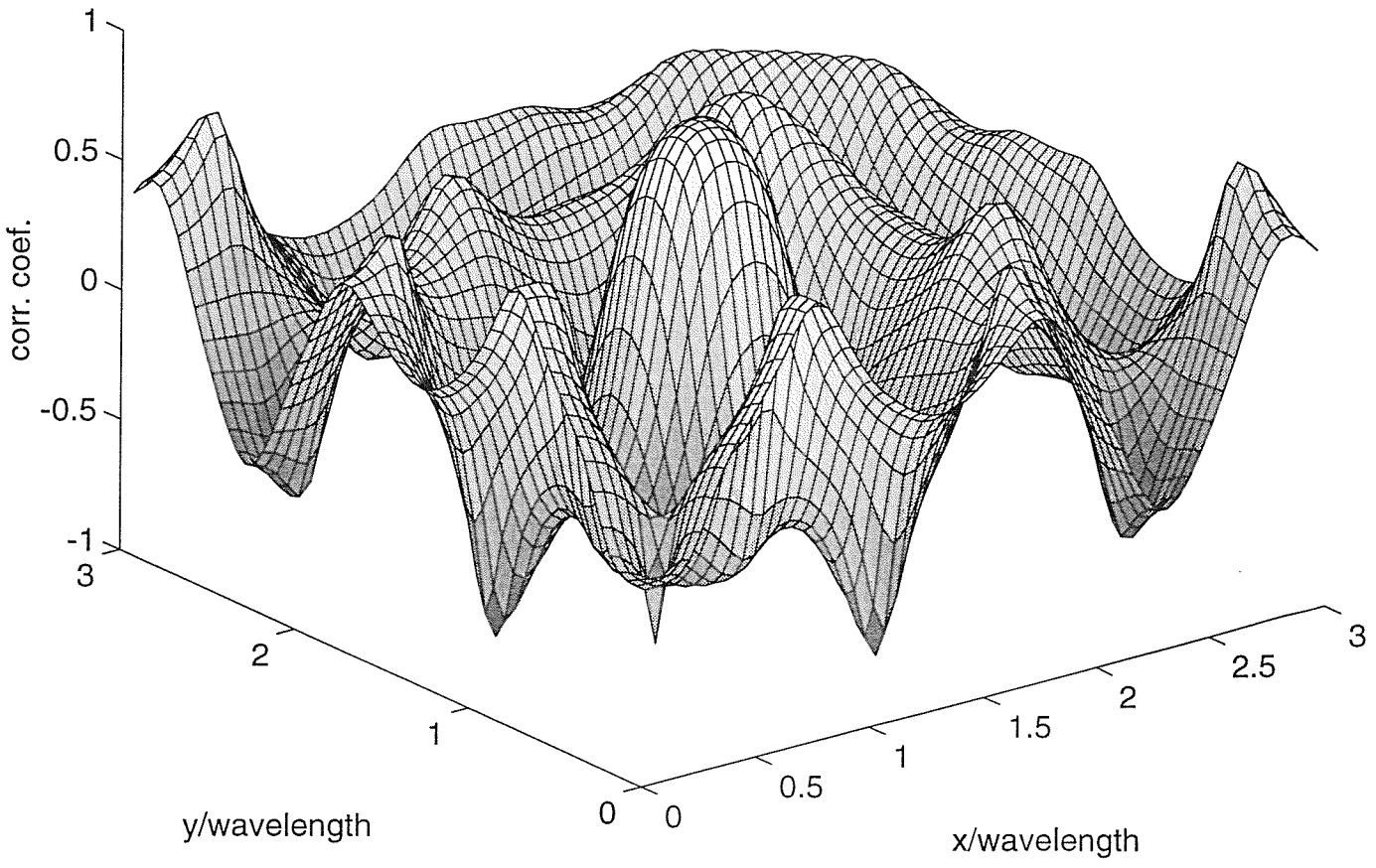

3.5 Derivation of correlation coefficients based on a free-wave description

A free travelling wave model [55] is here employed to derive theoretical correlation coefficient expressions for 2-dimensional structural wave fields. This approach is based on the analysis of the free bending wave propagation through the structure with the application of the relevant reflection coefficients at the structure boundaries. The expressions derived in section 3.5.1 are valid in any region of structures with boundaries that do not generate evanescent field components or far from the edges in plates with any type of boundary conditions. In section 3.5.2, bending evanescent field components are included in the analysis enabling the derivation of results for structures with any type of boundary conditions. This is achieved by including the evanescent field components' reflection coefficients in the solution of the structure's equation of motion.

3.5.1 Rectangular flat plate with generic boundary conditions excluding evanescent field components

The differential equation of motion which governs the out of plane displacement, z(x,y,t), of a thin plate takes the form [38]

$$D\left[\frac{\partial^2}{\partial x^2}+\frac{\partial^2}{\partial y^2}\right]^2 z+m\ddot{z}=0, \tag{3.24}$$

where D is the flexural rigidity and m is the mass per unit area. One possible harmonic plane wave solution to this equation is composed of four free bending wave components which are reflected and transmitted at the boundaries so that [55]

$$z(x,y,t)=\left[A_1e^{-ik_x x-ik_y y}+A_2e^{ik_x x-ik_y y}+A_3e^{ik_x x+ik_y y}+A_4e^{-ik_x x+ik_y y}\right]e^{i\omega t}, \tag{3.25}$$

where A_1, A_2, A_3, A_4 are complex amplitudes.

The above equation presupposes that no free in-plane waves are generated at the boundaries and that evanescent bending and in-plane field components decay rapidly with distance from the boundaries. According to the

illustration in fig. 3.6, the reflection conditions at the lower left corner of the plate require that

$$\frac{A_1}{A_2}=\frac{A_4}{A_3}=R_L, \qquad \text{and} \qquad \frac{A_2}{A_3}=\frac{A_1}{A_4}=R_B, \tag{3.26}$$

where R_L and R_B are the complex reflection coefficients at the left and bottom edges of the plate. Using expression (3.26) to express A_2, A_3, A_4 in terms of A_1, R_L and R_B and substituting these results in (3.25) we obtain

$$z(x,y,t)=A_1\left[e^{-ik_x x-ik_y y}+\frac{R_L^*}{\rho_L}e^{ik_x x-ik_y y}+\frac{R_L^*R_B^*}{\rho_L\rho_B}e^{ik_x x+ik_y y}+\frac{R_B^*}{\rho_B}e^{-ik_x x+ik_y y}\right]e^{i\omega t}, \tag{3.27}$$

where * denotes the complex conjugate and, as defined in ref. [38], $\rho_L=|R_L|^2$ and $\rho_B=|R_B|^2$ are the reflection efficiencies of the left and bottom edges, respectively. For cases in which no wave is transmitted through the boundaries the reflection efficiencies are equal to unity and the expressions here presented can be greatly simplified.

Multiplying and time averaging the displacement at point 1 and the complex conjugate of the displacement at point 2 we can express the spatial correlation of the displacement as

$$\begin{aligned}\left\langle z_1(t)z_2^*(t)\right\rangle_t=|A_1|^2\Bigg[&e^{-ik_x(x_1-x_2)-ik_y(y_1-y_2)}+\frac{R_L}{\rho_L}e^{-ik_x(x_1+x_2)-ik_y(y_1-y_2)}\\
&+\frac{R_LR_B}{\rho_L\rho_B}e^{-ik_x(x_1+x_2)-ik_y(y_1+y_2)}+\frac{R_B}{\rho_B}e^{-ik_x(x_1-x_2)-ik_y(y_1+y_2)}+\frac{R_L^*}{\rho_L}e^{ik_x(x_1+x_2)-ik_y(y_1-y_2)}\\
&+\frac{1}{\rho_L}e^{ik_x(x_1-x_2)-ik_y(y_1-y_2)}+\frac{R_B}{\rho_L\rho_B}e^{ik_x(x_1-x_2)-ik_y(y_1+y_2)}+\frac{R_L^*R_B}{\rho_L\rho_B}e^{ik_x(x_1+x_2)-ik_y(y_1+y_2)}\\
&+\frac{R_L^*R_B^*}{\rho_L\rho_B}e^{ik_x(x_1+x_2)+ik_y(y_1+y_2)}+\frac{R_B^*}{\rho_L\rho_B}e^{ik_x(x_1-x_2)+ik_y(y_1+y_2)}+\frac{1}{\rho_L\rho_B}e^{ik_x(x_1-x_2)+ik_y(y_1-y_2)}\\
&+\frac{R_L^*}{\rho_L\rho_B}e^{ik_x(x_1+x_2)+ik_y(y_1-y_2)}+\frac{R_B^*}{\rho_B}e^{-ik_x(x_1-x_2)+ik_y(y_1+y_2)}+\frac{R_B^*R_L}{\rho_L\rho_B}e^{-ik_x(x_1+x_2)+ik_y(y_1+y_2)}\\
&+\frac{R_L}{\rho_L\rho_B}e^{-ik_x(x_1+x_2)+ik_y(y_1-y_2)}+\frac{1}{\rho_B}e^{-ik_x(x_1-x_2)+ik_y(y_1-y_2)}\Bigg].\end{aligned} \tag{3.28}$$

As discussed in section 3.3 only the real part of $\left\langle z_1(t)z_2^*(t)\right\rangle_t$ is necessary in the computation of the correlation coefficient. In addition, expression (3.28) can be

simplified by writing the exponential terms in terms of sines and cosines. Thus, after some mathematical manipulation we obtain that

$$\begin{aligned}
\mathrm{Re}\left[\left\langle z_1(t)z_2^*(t)\right\rangle_t\right] = \frac{|A_1|^2}{\rho_L\rho_B}\Big[&(1+\rho_L)(1+\rho_B)\cos(k_x(x_1-x_2))\cos(k_y(y_1-y_2)) \\
&-(1-\rho_L)(1-\rho_B)\sin(k_x(x_1-x_2))\sin(k_y(y_1-y_2)) + 2(1+\rho_B)\mathrm{Re}[R_L]\times \\
&\times\cos(k_x(x_1+x_2))\cos(k_y(y_1-y_2)) + 2(1+\rho_B)\mathrm{Im}[R_L]\sin(k_x(x_1+x_2))\times \\
&\times\cos(k_y(y_1-y_2)) + 2(1+\rho_L)\mathrm{Re}[R_B]\cos(k_x(x_1-x_2))\cos(k_y(y_1+y_2)) \\
&+2(1+\rho_L)\mathrm{Im}[R_B]\cos(k_x(x_1-x_2))\sin(k_y(y_1+y_2)) + 4\,\mathrm{Re}[R_L]\mathrm{Re}[R_B]\times \\
&\times\cos(k_x(x_1+x_2))\cos(k_y(y_1+y_2)) + 4\,\mathrm{Re}[R_L]\mathrm{Im}[R_B]\cos(k_x(x_1+x_2))\times \\
&\times\sin(k_y(y_1+y_2)) + 4\,\mathrm{Im}[R_L]\mathrm{Re}[R_B]\sin(k_x(x_1+x_2))\cos(k_y(y_1+y_2)) \\
&+4\,\mathrm{Im}[R_L]\mathrm{Im}[R_B]\sin(k_x(x_1+x_2))\sin(k_y(y_1+y_2))\Big].
\end{aligned} \tag{3.29}$$

Equation (3.29) gives the real part of the spatial correlation of the displacement between points 1 and 2 for a wave whose frequency ω is related to the wavenumbers k_x and k_y by the bending wave dispersion relation [38]

$$\left(k_x^2+k_y^2\right)^2 = \frac{\omega^2 m}{D}.$$

Expressions for $\left\langle z_1^2(t)\right\rangle_t$ and $\left\langle z_2^2(t)\right\rangle_t$ are also necessary in the computation of equation (3.9). As shown in the previous section they can be derived from the expression for $\left\langle z_1(t)z_2^*(t)\right\rangle_t$ by setting $x_1 = x_2$ and $y_1 = y_2$. When this substitution is carried out the imaginary part of $\left\langle z_1(t)z_2^*(t)\right\rangle_t$ disappears.

Assuming the boundary conditions are known, appropriate reflection coefficients can be obtained from the expressions presented in Appendix C. Since the resultant expression for the correlation coefficient needs to be integrated over wave direction, the individual wavenumbers k_x and k_y have to be replaced by the continuous functions $k_B\cos\theta$ and $k_B\sin\theta$, respectively. As discussed in section 3.1, this substitution implies that the flat plate has a reasonably high modal density in the band of analysis, or that a large number of wave directions are available. Thus, the frequency-averaged correlation coefficient of a flat plate based on an elastic wave representation is given by

$$\gamma_{12}(\mathbf{x}_1,\mathbf{x}_2,f_c)=\frac{\int_{\Delta k}\int_{0}^{\pi/2}\mathrm{Re}\left[\left\langle z_1(t)z_2^*(t)\right\rangle_t\right]\mathrm{d}\theta\mathrm{d}k_B}{\left[\int_{\Delta k}\int_{0}^{\pi/2}\left\langle z_1^2(t)\right\rangle_t\mathrm{d}\theta\mathrm{d}k_B\right]^{1/2}\left[\int_{\Delta k}\int_{0}^{\pi/2}\left\langle z_2^2(t)\right\rangle_t\mathrm{d}\theta\mathrm{d}k_B\right]^{1/2}},\tag{3.30}$$

where

$$\begin{aligned}\mathrm{Re}\left[\left\langle z_1(t)z_2^*(t)\right\rangle_t\right]=\frac{|A_1|^2}{\rho_L\rho_B}\Big[&(1+\rho_L)(1+\rho_B)\cos(k_B(x_1-x_2)\cos\theta)\cos(k_B(y_1-y_2)\sin\theta)\\&-(1-\rho_L)(1-\rho_B)\sin(k_B(x_1-x_2)\cos\theta)\sin(k_B(y_1-y_2)\sin\theta)\\&+2(1+\rho_B)\mathrm{Re}[R_L]\cos(k_B(x_1+x_2)\cos\theta)\cos(k_B(y_1-y_2)\sin\theta)\\&+2(1+\rho_B)\mathrm{Im}[R_L]\sin(k_B(x_1+x_2)\cos\theta)\cos(k_B(y_1-y_2)\sin\theta)\\&+2(1+\rho_L)\mathrm{Re}[R_B]\cos(k_B(x_1-x_2)\cos\theta)\cos(k_B(y_1+y_2)\sin\theta)\\&+2(1+\rho_L)\mathrm{Im}[R_B]\cos(k_B(x_1-x_2)\cos\theta)\sin(k_B(y_1+y_2)\sin\theta)\\&+4\,\mathrm{Re}[R_L]\mathrm{Re}[R_B]\cos(k_B(x_1+x_2)\cos\theta)\cos(k_B(y_1+y_2)\sin\theta)\\&+4\,\mathrm{Re}[R_L]\mathrm{Im}[R_B]\cos(k_B(x_1+x_2)\cos\theta)\sin(k_B(y_1+y_2)\sin\theta)\\&+4\,\mathrm{Im}[R_L]\mathrm{Re}[R_B]\sin(k_B(x_1+x_2)\cos\theta)\cos(k_B(y_1+y_2)\sin\theta)\\&+4\,\mathrm{Im}[R_L]\mathrm{Im}[R_B]\sin(k_B(x_1+x_2)\cos\theta)\sin(k_B(y_1+y_2)\sin\theta)\Big],\end{aligned}\tag{3.31}$$

and

$$\begin{aligned}\left\langle z_1^2(t)\right\rangle_t=\frac{|A_1|^2}{\rho_L\rho_B}\Big[&(1+\rho_L)(1+\rho_B)\\&+2(1+\rho_B)(\mathrm{Re}[R_L]\cos(2k_Bx_1\cos\theta)+\mathrm{Im}[R_L]\sin(2k_Bx_1\cos\theta))\\&+2(1+\rho_L)(\mathrm{Re}[R_B]\cos(2k_By_1\sin\theta)+\mathrm{Im}[R_B]\sin(2k_By_1\sin\theta))\\&+4\,\mathrm{Re}[R_L]\mathrm{Re}[R_B]\cos(2k_Bx_1\cos\theta)\cos(2k_By_1\sin\theta)\\&+4\,\mathrm{Re}[R_L]\mathrm{Im}[R_B]\cos(2k_Bx_1\cos\theta)\sin(2k_By_1\sin\theta)\\&+4\,\mathrm{Im}[R_L]\mathrm{Re}[R_B]\sin(2k_Bx_1\cos\theta)\cos(2k_By_1\sin\theta)\\&+4\,\mathrm{Im}[R_L]\mathrm{Im}[R_B]\sin(2k_Bx_1\cos\theta)\sin(2k_By_1\sin\theta)\Big],\end{aligned}\tag{3.32}$$

and the expression for $\left\langle z_2^2(t)\right\rangle_t$ is equal to the one for $\left\langle z_1^2(t)\right\rangle_t$ with the index 1 changed to 2.

Expressions (3.30), (3.31) and (3.32) and the reflection coefficients presented in Appendix C enable the correlation coefficient of plates to be evaluated with various boundary conditions. The limitation is that no evanescent field components are included in this analysis and considerable errors between experiments

and theory are expected in a region one wavelength near the boundary of plates with edges which generate evanescent field components. The same procedure here presented can be employed to derive results for the normalised cross-power spectral density.

In agreement with the modal representation results (section 3.4), closed form solutions for the integration in wave direction were only obtained for simply-supported and guided edges. For instance, consider that the plate illustrated in fig. 3.2 has a left edge with guided boundary conditions and a bottom edge with simply-supported boundary conditions. Then, the reflection coefficients in this case are real and equal to $R_L = 1$ and $R_B = -1$. Substituting these parameters in equation (3.30) we have, after some mathematical manipulation, that the frequency-averaged correlation coefficient for this plate under random excitation is

$$\gamma_{12}(\mathbf{x_1},\mathbf{x_2},f_c) = \frac{\left[J_0\left(k_b\sqrt{(x_1-x_2)^2+(y_1-y_2)^2}\right)-J_0\left(k_b\sqrt{(x_1-x_2)^2+(y_1+y_2)^2}\right)\right.}{\left.+J_0\left(k_b\sqrt{(x_1+x_2)^2+(y_1-y_2)^2}\right)-J_0\left(k_b\sqrt{(x_1+x_2)^2+(y_1+y_2)^2}\right)\right]} \cdot (3.33)$$
$$\left[1+J_0(2k_bx_1)-J_0(2k_by_1)-J_0\left(2k_b\sqrt{x_1^2+y_1^2}\right)\right]^{1/2}$$
$$\times\left[1+J_0(2k_bx_2)-J_0(2k_by_2)-J_0\left(2k_b\sqrt{x_2^2+y_2^2}\right)\right]^{1/2}$$

The interference patterns for a plate corner with these boundary conditions are illustrated in fig. 3.8 and 3.9 as a function of the system wavelength. It is observed that such interference patterns are coincident with the ones illustrated in fig. 5 of ref. [65]. Finally, it is important to point out that for cases in which the edges generate evanescent field components the results obtained with the expressions presented in this section are not valid in a region within one wavelength from the edges. The evanescent field components have to be explicitly included in the correlation model. This type of analysis is presented in the next section.

3.5.2 Rectangular flat plate with generic boundary conditions including evanescent field components due to reflection at the edges.

The general harmonic solution to equation (3.24) near the bottom and left edges of a flat plate, as illustrated in fig. 3.7, is given by [38,55]

$$z(x,y,t) = \left(A^{B}_{ref}e^{-ik_y y} + A^{B}_{in}e^{ik_y y} + A^{B}_{e}e^{-\mu_y y}\right)\left(A^{L}_{ref}e^{-ik_x x} + A^{L}_{in}e^{ik_x x} + A^{L}_{e}e^{-\mu_x x}\right)e^{i\omega t}, \quad (3.34)$$

where the index B refers to the bottom edge, L to the left edge, *ref* means reflected, *in* means incident, *e* means evanescent field component, $\mu_y = \sqrt{k_y^2 + 2k_x^2}$ and $\mu_x = \sqrt{k_x^2 + 2k_y^2}$. Following the same procedure as the one used in section 3.5.1, we have to derive an expression for $\langle z_1(t)z_2^*(t)\rangle_t$ as function of the points coordinates, bending wavenumber, propagation angle and reflection conditions at the edges. In order to facilitate this derivation we can treat this expression in terms of two separate functions of x and y, namely

$$\langle z_1(t)z_2^*(t)\rangle_t = I_x I_y = W(x_1)W(x_2)Q(y_1)Q(y_2). \quad (3.35)$$

Using this representation, an initial expression for I_x can be derived as

$$\begin{aligned} I_x = \left|A^{L}_{in}\right|^2 \Big[& |R_L|^2 e^{-ik_x(x_1-x_2)} + R_L e^{-ik_x(x_1+x_2)} + R_L E_L^* e^{-ik_x x_1 - \mu_x x_2} + R_L^* e^{+ik_x(x_1+x_2)} \\ & + e^{+ik_x(x_1-x_2)} + E_L^* e^{ik_x x_1 - \mu_x x_2} + R_L^* E_L e^{-\mu_x x_1 + ik_x x_2} + E_L e^{-\mu_x x_1 - ik_x x_2} + E_L E_L^* e^{-\mu_x(x_1+x_2)} \Big] \end{aligned} \quad (3.36)$$

where R is the reflection coefficient of the edge, E is the coefficient of the evanescent field component defined as $E=A_e/A_{in}$ and the symbol * represents the complex conjugate of the complex variable. Equation (3.36) can be simplified and expressed in real and imaginary parts. They are

$$
\begin{aligned}
\mathrm{Re}[I_x] = \left|A_{in}^{L}\right|^2 \Big[& (1+\rho_L)\cos(k_x(x_1-x_2)) + 2\,\mathrm{Re}[R_L]\cos(k_x(x_1+x_2)) \\
& + 2\,\mathrm{Im}[R_L]\sin(k_x(x_1+x_2)) \\
& + \begin{pmatrix} (\mathrm{Re}[R_L]\mathrm{Re}[E_L] + \mathrm{Im}[R_L]\mathrm{Im}[E_L])\cos(k_x x_1) \\ -(-\mathrm{Im}[R_L]\mathrm{Re}[E_L] + \mathrm{Re}[R_L]\mathrm{Im}[E_L])\sin(k_x x_1) \end{pmatrix} e^{-\mu_x x_2} \\
& + (\mathrm{Re}[E_L]\cos(k_x x_1) + \mathrm{Im}[E_L]\sin(k_x x_1)) e^{-\mu_x x_2} \\
& + \begin{pmatrix} (\mathrm{Re}[R_L]\mathrm{Re}[E_L] + \mathrm{Im}[R_L]\mathrm{Im}[E_L])\cos(k_x x_2) \\ -(\mathrm{Re}[R_L]\mathrm{Im}[E_L] - \mathrm{Im}[R_L]\mathrm{Re}[E_L])\sin(k_x x_2) \end{pmatrix} e^{-\mu_x x_1} \\
& + (\mathrm{Re}[E_L]\cos(k_x x_2) + \mathrm{Im}[E_L]\sin(k_x x_2)) e^{-\mu_x x_1} + \left|E_L\right|^2 e^{-\mu_x (x_1+x_2)} \Big],
\end{aligned}
\tag{3.37}
$$

and

$$
\begin{aligned}
\mathrm{Im}[I_x] = \left|A_{in}^{L}\right|^2 \Big[& (1-\rho_L)\sin(k_x(x_1-x_2)) \\
& + (\mathrm{Re}[E_L]\sin(k_x x_1) - \mathrm{Im}[E_L]\cos(k_x x_1)) e^{-\mu_x x_2} \\
& + \begin{pmatrix} (\mathrm{Im}[R_L]\mathrm{Re}[E_L] - \mathrm{Re}[R_L]\mathrm{Im}[E_L])\cos(k_x x_1) \\ -(\mathrm{Re}[R_L]\mathrm{Re}[E_L] + \mathrm{Im}[R_L]\mathrm{Im}[E_L])\sin(k_x x_1) \end{pmatrix} e^{-\mu_x x_2} \\
& + \begin{pmatrix} (\mathrm{Re}[R_L]\mathrm{Re}[E_L] + \mathrm{Im}[R_L]\mathrm{Im}[E_L])\sin(k_x x_2) \\ +(\mathrm{Re}[R_L]\mathrm{Im}[E_L] - \mathrm{Im}[R_L]\mathrm{Re}[E_L])\cos(k_x x_2) \end{pmatrix} e^{-\mu_x x_1} \\
& + (\mathrm{Im}[E_L]\cos(k_x x_2) - \mathrm{Re}[E_L]\sin(k_x x_2)) e^{-\mu_x x_1} \Big].
\end{aligned}
\tag{3.38}
$$

Similar results As that for I_x were obtained for the real and imaginary parts of I_y, the only difference being that the index L has to be replaced by B and where we have x in I_x we have to replace it by y in I_y. From equation (3.35) we can then write

$$
\begin{aligned}
\mathrm{Re}\left[\left\langle z_1(t) z_2^*(t)\right\rangle_t\right] &= \mathrm{Re}[I_x]\mathrm{Re}[I_y] - \mathrm{Im}[I_x]\mathrm{Im}[I_y], \\
\mathrm{Im}\left[\left\langle z_1(t) z_2^*(t)\right\rangle_t\right] &= \mathrm{Re}[I_y]\mathrm{Im}[I_x] + \mathrm{Re}[I_x]\mathrm{Im}[I_y],
\end{aligned}
\tag{3.39}
$$

where equations (3.37) and (3.38), plus the equivalent expressions for the real and imaginary parts of I_y have to be substituted in the above equations. The equations for $\left\langle z_1^2(t)\right\rangle_t$ and $\left\langle z_2^2(t)\right\rangle_t$ can be derived from (3.39). Performing this derivation we obtain a general expression for $\left\langle z_1^2(t)\right\rangle_t$

$$\begin{aligned}\left\langle z_1^2(t)\right\rangle_t = &\left|A_{in}^B\right|^2\left|A_{in}^L\right|^2\Big[(1+\rho_L)+2\,\mathrm{Re}[R_L]\cos(2k_x x_1)+2\,\mathrm{Im}[R_L]\sin(2k_x x_1)\\ &+2\begin{pmatrix}(\mathrm{Re}[R_L]\mathrm{Re}[E_L]+\mathrm{Im}[R_L]\mathrm{Im}[E_L])\cos(k_x x_1)\\ -(\mathrm{Re}[R_L]\mathrm{Im}[E_L]-\mathrm{Im}[R_L]\mathrm{Re}[E_L])\sin(k_x x_1)\end{pmatrix}e^{-\mu_x x_1}\\ &+2(\mathrm{Re}[E_L]\cos(k_x x_1)+\mathrm{Im}[E_L]\sin(k_x x_1))e^{-\mu_x x_1}+|E_L|^2 e^{-2\mu_x x_1}\Big]\times\\ &\times\Big[(1+\rho_B)+2\,\mathrm{Re}[R_B]\cos(2k_y y_1)+2\,\mathrm{Im}[R_B]\sin(2k_y y_1)\\ &+2\begin{pmatrix}(\mathrm{Re}[R_B]\mathrm{Re}[E_B]+\mathrm{Im}[R_B]\mathrm{Im}[E_B])\cos(k_y y_1)\\ -(\mathrm{Re}[R_B]\mathrm{Im}[E_B]-\mathrm{Im}[R_B]\mathrm{Re}[E_B])\sin(k_y y_1)\end{pmatrix}e^{-\mu_y y_1}\\ &+2(\mathrm{Re}[E_B]\cos(k_y y_1)+\mathrm{Im}[E_B]\sin(k_y y_1))e^{-\mu_y y_1}+|E_B|^2 e^{-2\mu_y y_1}\Big].\end{aligned} \tag{3.40}$$

Following the procedure presented in the previous section we can then derive the frequency-averaged correlation coefficient by substituting equations (3.37), (3.38), (3.39) and (3.40) in equation (3.9). The result is

$$\gamma_{12}(\mathbf{x}_1,\mathbf{x}_2,f_c)=\frac{\int_{\Delta k}\int_0^{\pi/2}(\mathrm{Re}[I_x]\mathrm{Re}[I_y]-\mathrm{Im}[I_x]\mathrm{Im}[I_y])\,d\theta\,dk_B}{\left[\int_{\Delta k}\int_0^{\pi/2}Q(x_1)R(y_1)\,d\theta\,dk_B\right]^{1/2}\left[\int_{\Delta k}\int_0^{\pi/2}Q(x_2)R(y_2)\,d\theta\,dk_B\right]^{1/2}}, \tag{3.41}$$

where

$$\begin{aligned}\mathrm{Re}[I_x]=&\Big[(1+\rho_L)\cos(k_B(x_1-x_2)\cos\theta)+2\,\mathrm{Re}[R_L]\cos(k_B(x_1+x_2)\cos\theta)\\ &+2\,\mathrm{Im}[R_L]\sin(k_B(x_1+x_2)\cos\theta)\\ &+\begin{pmatrix}(\mathrm{Re}[R_L]\mathrm{Re}[E_L]+\mathrm{Im}[R_L]\mathrm{Im}[E_L])\cos(k_B x_1\cos\theta)\\ -(-\mathrm{Im}[R_L]\mathrm{Re}[E_L]+\mathrm{Re}[R_L]\mathrm{Im}[E_L])\sin(k_B x_1\cos\theta)\end{pmatrix}e^{-\mu_x x_2}\\ &+(\mathrm{Re}[E_L]\cos(k_b x_1\cos\theta)+\mathrm{Im}[E_L]\sin(k_B x_1\cos\theta))e^{-\mu_x x_2}\\ &+\begin{pmatrix}(\mathrm{Re}[R_L]\mathrm{Re}[E_L]+\mathrm{Im}[R_L]\mathrm{Im}[E_L])\cos(k_B x_2\cos\theta)\\ -(\mathrm{Re}[R_L]\mathrm{Im}[E_L]-\mathrm{Im}[R_L]\mathrm{Re}[E_L])\sin(k_B x_2\cos\theta)\end{pmatrix}e^{-\mu_x x_1}\\ &+(\mathrm{Re}[E_L]\cos(k_B x_2\cos\theta)+\mathrm{Im}[E_L]\sin(k_B x_2\cos\theta))e^{-\mu_x x_1}+|E_L|^2 e^{-\mu_x(x_1+x_2)}\Big],\end{aligned} \tag{3.42}$$

$$
\begin{aligned}
\mathrm{Im}[I_x] = \Big[& (1-\rho_L)\sin(k_B(x_1-x_2)\cos\theta) \\
& + (\mathrm{Re}[E_L]\sin(k_B x_1\cos\theta) - \mathrm{Im}[E_L]\cos(k_B x_1\cos\theta))e^{-\mu_x x_2} \\
& + \begin{pmatrix} (\mathrm{Im}[R_L]\mathrm{Re}[E_L] - \mathrm{Re}[R_L]\mathrm{Im}[E_L])\cos(k_B x_1\cos\theta) \\ -(\mathrm{Re}[R_L]\mathrm{Re}[E_L] + \mathrm{Im}[R_L]\mathrm{Im}[E_L])\sin(k_B x_1\cos\theta) \end{pmatrix} e^{-\mu_x x_2} \\
& + \begin{pmatrix} (\mathrm{Re}[R_L]\mathrm{Re}[E_L] + \mathrm{Im}[R_L]\mathrm{Im}[E_L])\sin(k_B x_2\cos\theta) \\ +(\mathrm{Re}[R_L]\mathrm{Im}[E_L] - \mathrm{Im}[R_L]\mathrm{Re}[E_L])\cos(k_B x_2\cos\theta) \end{pmatrix} e^{-\mu_x x_1} \\
& + (\mathrm{Im}[E_L]\cos(k_B x_2\cos\theta) - \mathrm{Re}[E_L]\sin(k_B x_2\cos\theta))e^{-\mu_x x_1} \Big],
\end{aligned}
\tag{3.43}
$$

$$
\begin{aligned}
\mathrm{Re}[I_y] = \Big[& (1+\rho_B)\cos(k_B(y_1-y_2)\sin\theta) + 2\,\mathrm{Re}[R_B]\cos(k_B(y_1+y_2)\sin\theta) \\
& + 2\,\mathrm{Im}[R_B]\sin(k_B(y_1+y_2)\sin\theta) \\
& + \begin{pmatrix} (\mathrm{Re}[R_B]\mathrm{Re}[E_B] + \mathrm{Im}[R_B]\mathrm{Im}[E_B])\cos(k_B y_1\sin\theta) \\ -(-\mathrm{Im}[R_B]\mathrm{Re}[E_B] + \mathrm{Re}[R_B]\mathrm{Im}[E_B])\sin(k_B y_1\sin\theta) \end{pmatrix} e^{-\mu_y y_2} \\
& + (\mathrm{Re}[E_B]\cos(k_B y_1\sin\theta) + \mathrm{Im}[E_B]\sin(k_B y_1\sin\theta))e^{-\mu_y y_2} \\
& + \begin{pmatrix} (\mathrm{Re}[R_B]\mathrm{Re}[E_B] + \mathrm{Im}[R_B]\mathrm{Im}[E_B])\cos(k_B y_2\sin\theta) \\ -(\mathrm{Re}[R_B]\mathrm{Im}[E_B] - \mathrm{Im}[R_B]\mathrm{Re}[E_B])\sin(k_B y_2\sin\theta) \end{pmatrix} e^{-\mu_y y_1} \\
& + (\mathrm{Re}[E_B]\cos(k_B y_2\sin\theta) + \mathrm{Im}[E_B]\sin(k_B y_2\sin\theta))e^{-\mu_y y_1} + |E_B|^2 e^{-\mu_y(y_1+y_2)} \Big],
\end{aligned}
\tag{3.44}
$$

$$
\begin{aligned}
\mathrm{Im}[I_y] = \Big[& (1-\rho_B)\sin(k_B(y_1-y_2)\sin\theta) \\
& + (\mathrm{Re}[E_B]\sin(k_B y_1\sin\theta) - \mathrm{Im}[E_B]\cos(k_B y_1\sin\theta))e^{-\mu_y y_2} \\
& + \begin{pmatrix} (\mathrm{Im}[R_B]\mathrm{Re}[E_B] - \mathrm{Re}[R_B]\mathrm{Im}[E_B])\cos(k_B y_1\sin\theta) \\ -(\mathrm{Re}[R_B]\mathrm{Re}[E_B] + \mathrm{Im}[R_B]\mathrm{Im}[E_B])\sin(k_B y_1\sin\theta) \end{pmatrix} e^{-\mu_y y_2} \\
& + \begin{pmatrix} (\mathrm{Re}[R_B]\mathrm{Re}[E_B] + \mathrm{Im}[R_B]\mathrm{Im}[E_B])\sin(k_B y_2\sin\theta) \\ +(\mathrm{Re}[R_B]\mathrm{Im}[E_B] - \mathrm{Im}[R_B]\mathrm{Re}[E_B])\cos(k_B y_2\sin\theta) \end{pmatrix} e^{-\mu_y y_1} \\
& + (\mathrm{Im}[E_B]\cos(k_B y_2\sin\theta) - \mathrm{Re}[E_B]\sin(k_B y_2\sin\theta))e^{-\mu_y y_1} \Big],
\end{aligned}
\tag{3.45}
$$

$$Q(x_1)=\Big[(1+\rho_L)+2\,\mathrm{Re}[R_L]\cos(2k_Bx_1\cos\theta)+2\,\mathrm{Im}[R_L]\sin(2k_Bx_1\cos\theta)$$
$$+2\begin{pmatrix}(\mathrm{Re}[R_L]\mathrm{Re}[E_L]+\mathrm{Im}[R_L]\mathrm{Im}[E_L])\cos(k_Bx_1\cos\theta)\\-(\mathrm{Re}[R_L]\mathrm{Im}[E_L]-\mathrm{Im}[R_L]\mathrm{Re}[E_L])\sin(k_Bx_1\cos\theta)\end{pmatrix}e^{-\mu_x x_1} \qquad (3.46)$$
$$+2(\mathrm{Re}[E_L]\cos(k_Bx_1\cos\theta)+\mathrm{Im}[E_L]\sin(k_Bx_1\cos\theta))e^{-\mu_x x_1}+|E_L|^2e^{-2\mu_x x_1}\Big],$$

and

$$R(y_1)=\Big[(1+\rho_B)+2\,\mathrm{Re}[R_B]\cos(2k_By_1\sin\theta)+2\,\mathrm{Im}[R_B]\sin(2k_By_1\sin\theta)$$
$$+2\begin{pmatrix}(\mathrm{Re}[R_B]\mathrm{Re}[E_B]+\mathrm{Im}[R_B]\mathrm{Im}[E_B])\cos(k_By_1\sin\theta)\\-(\mathrm{Re}[R_B]\mathrm{Im}[E_B]-\mathrm{Im}[R_B]\mathrm{Re}[E_B])\sin(k_By_1\sin\theta)\end{pmatrix}e^{-\mu_y y_1} \qquad (3.47)$$
$$+2(\mathrm{Re}[E_B]\cos(k_By_1\sin\theta)+\mathrm{Im}[E_B]\sin(k_By_1\sin\theta))e^{-\mu_y y_1}+|E_B|^2e^{-2\mu_y y_1}\Big].$$

Expressions for μ_x and μ_y are given by (3.22), and $Q(x_2)$ and $R(y_2)$ can be obtained from (3.46) and (3.47) by replacing the index 1 with 2. As already mentioned, the correlation coefficient can then be obtained from (3.41) by substituting suitable reflection and evanescent field coefficients (Appendix C) in this equation and performing the integration in wave direction. Assuming that the width of the strip $\Delta k = k_2 - k_1$ is small enough in order that the second order terms in (3.16') are neglected, the result of the integration in wave direction is a good approximation of the frequency-averaged correlation coefficient with the bending wavenumber, k_B, substituted by the band centre frequency bending wavenumber, k_b.

The computed correlation coefficient results are valid near and far from the edges. However, they give exactly the same results as those derived in the previous section when the points are situated in a region more than one wavelength far from the edges. This happens because the evanescent term contribution will have died out and it will be no longer relevant. However, if both points are in a region less than one wavelength far from the edges then results with and without evanescent terms will differ considerably. This difference was verified experimentally on clamped rectangular plates as described in the next chapter.

If the analysis presented in this chapter were restricted to real wave components, then the final correlation coefficient expressions would have been exactly the same as the ones derived using the approximate modal model based upon

Bolotin's dynamic edge effect method (section 3.4.2). Nevertheless, the inclusion of imaginary terms does not affect the results greatly, and when overlaid one can barely note the difference between them. Moreover, if only the inner solution of Bolotin's dynamic edge effect method were considered in the derivation of section 3.4.2, then the correlation coefficients would have been very similar to the derivation presented in the previous section (wave approach without evanescent terms). Therefore, it can be concluded that the correlation coefficients derived using wave or modal models are coincident. This conclusion supports the analysis presented by Waterhouse and Cook [73] on the equivalence of modal and wave methods for description of reverberant fields. In addition, Langley [55] has shown that the free travelling wave model is simply a reformulation of Bolotin's dynamic edge effect method.

The correlation coefficient expressions derived in this chapter are strictly valid in the lower left quarter of the plate. However, if appropriate reflection coefficients and coordinate systems are used these results can be extended for the other plate quarters. This means that the origin of the coordinates that defines points 1 and 2 ($\mathbf{x}_1$ and $\mathbf{x}_2$) are always situated at the corner which point 1 is closer. Moreover, it is verified that in the middle of the plate (far from the edges) the expression for the correlation coefficient approaches that of a diffuse bending wave field.

The usefulness and validity of the theoretical results derived in this chapter are analysed in Chapter 4. The analysis is based on information obtained from an experimental investigation carried out on flat plates and in a passenger car bodyshell.

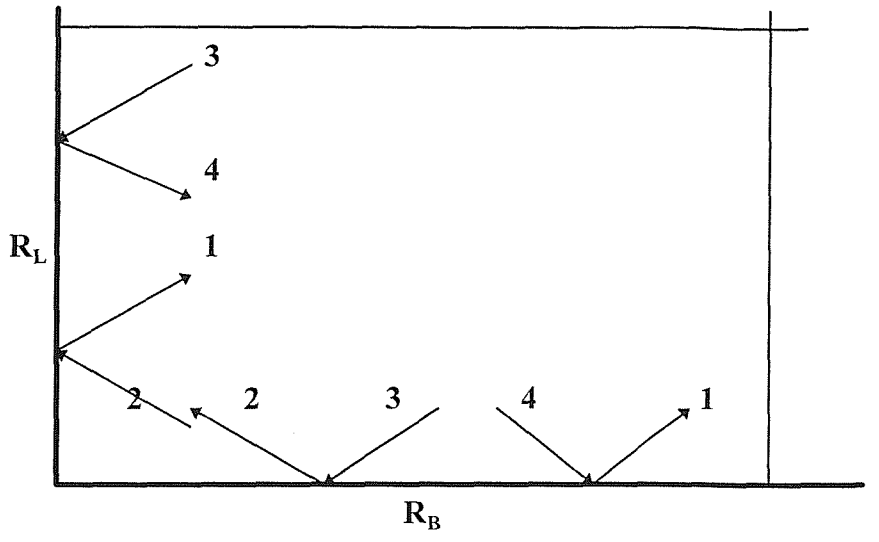

Fig. 3.6 - Boundary reflections on the lower left corner

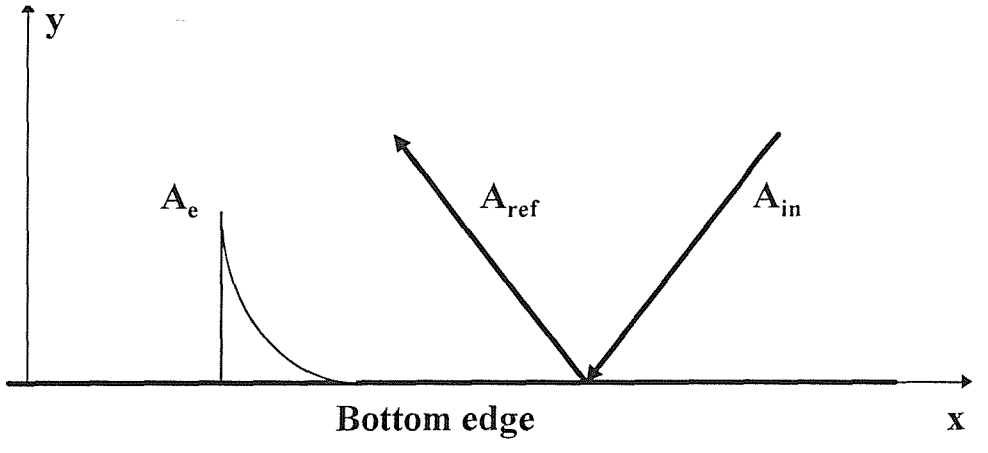

Fig. 3.7 - Sketch of incident, reflected and evanescent waves for the bottom edge

fig. 3.8 - Interference patterns near the junction of a simply-supported and a guided edge

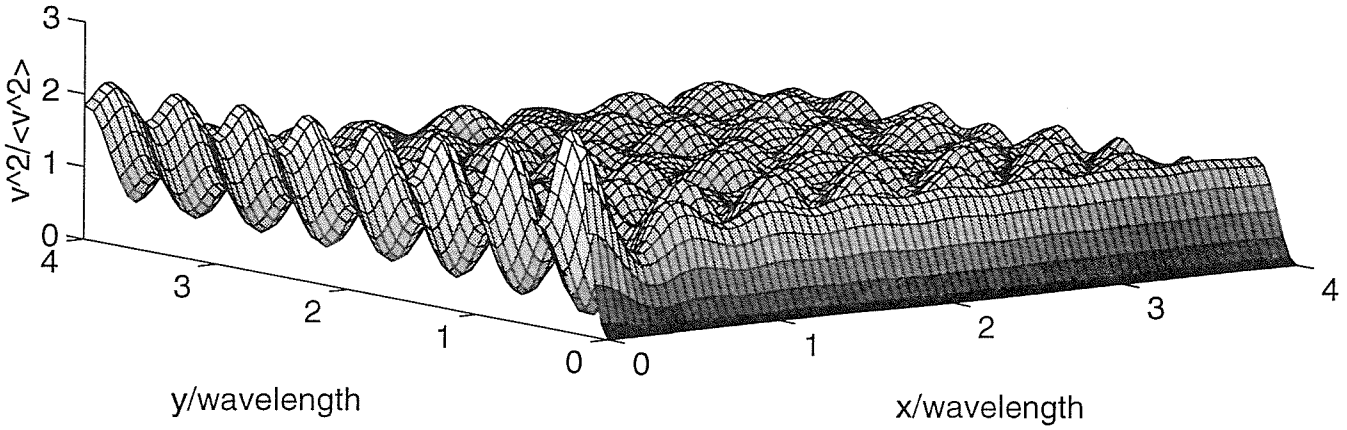

fig. 3.9 - Contour plot for the interference patterns of fig. 3.8

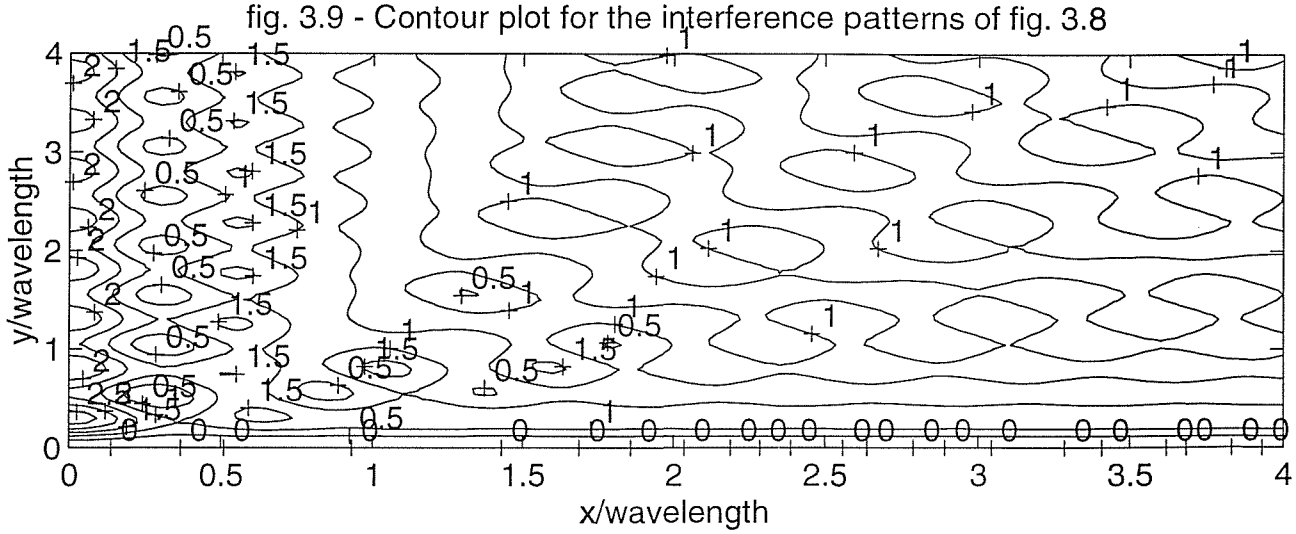

3.6 INFLUENCE OF ACOUSTIC AND MECHANICAL EXCITATION ON CORRELATION COEFFICIENT

As presented in Chapter 2, the cross-spectrum of pressure inside an acoustic cavity excited by a random vibrating plate is given by

$$S_p(x,y,z,\omega) = \frac{(\rho_o c_o^2)^2}{V^2} \sum_n \sum_m \frac{\psi_n(x,y,z)\psi_m(x,y,z)}{\Lambda_n \Lambda_m} \frac{[X_n - iY_n][X_m + iY_m]}{[X_n^2 + Y_n^2][X_m^2 + Y_m^2]} \times$$
$$\times \int_S \int_S S_a(x_1,y_1,x_2,y_2,\omega)\psi_n(x_1,y_1,z_o)\psi_m(x_2,y_2,z_o)dx_1 dx_2 dy_1 dy_2 . \quad (2.10)$$

Assuming the plate natural modes of vibration are available, a similar expression can be written for the plate response to a random field of cross-spectrum $S_f(\varepsilon_1,\xi_1,\varepsilon_2,\xi_2,\omega)$,

$$S_a(x_1,y_1,x_2,y_2,\omega) = \omega^4 \sum_p \sum_q \frac{\phi_p(x_1,y_1)\phi_q(x_2,y_2)}{M_p M_q} \frac{[H_p - iW_p][H_q + iW_q]}{[H_p^2 + W_p^2][H_q^2 + W_q^2]} \times$$
$$\times \int_S \int_S S_f(\varepsilon_1,\xi_1,\varepsilon_2,\xi_2,\omega)\phi_p(\varepsilon_1,\xi_1)\phi_q(\varepsilon_2,\xi_2)d\varepsilon_1 d\varepsilon_2 d\xi_1 d\xi_2 , \quad (3.48)$$

where $\phi_p(x_1,y_1)$ represents the mode shape of the pth plate mode with natural frequency ω_p at point 1, η_p is the modal loss factor, M_p is the modal mass, $H_p = \omega_p^2 - \omega^2$ and $W_p = \eta_p \omega \omega_p$. When the modal overlap factor is very much smaller than unity the cross-terms do not contribute significantly to the response and can be neglected. Expression (3.48) is then written as

$$S_a(x_1,y_1,x_2,y_2,\omega) = \omega^4 \sum_p \frac{\phi_p(x_1,y_1)\phi_p(x_2,y_2)}{\Delta_p^2} \frac{1}{[H_p^2 + W_p^2]} \times$$
$$\times \int_S \int_S S_f(\varepsilon_1,\xi_1,\varepsilon_2,\xi_2,\omega)\phi_p(\varepsilon_1,\xi_1)\phi_p(\varepsilon_2,\xi_2)d\varepsilon_1 d\varepsilon_2 d\xi_1 d\xi_2 . \quad (3.49)$$

The implications of neglecting the cross terms in the evaluation of equations that have the form of equation (3.49) have been discussed by a number of authors as described by Elishakoff et al (pag. 153, ref. [74]).

3.6.1 Mechanical excitation applied at a single point

The cross-spectrum of a stationary random force applied at the point (x_o,y_o) is given by (eq. (190), ref. [75]),

$$S_f(\varepsilon_1,\xi_1,\varepsilon_2,\xi_2,\omega)=\delta(\varepsilon_1-x_o)\delta(\xi_1-y_o)\delta(\varepsilon_2-x_o)\delta(\xi_2-y_o)S_f(\omega), \quad (3.50)$$

where $S_f(\omega)$ is the force spectral density and δ is the Dirac delta function. Substituting (3.50) in (3.49) and evaluating the double integral we obtain that,

$$S_a(x_1,y_1,x_2,y_2,\omega)=\omega^4\sum_p \frac{\phi_p(x_1,y_1)\phi_p(x_2,y_2)}{\Delta_p^2}\frac{1}{\left[H_p^2+W_p^2\right]}\phi_p^2(x_o,y_o)S_f(\omega). \quad (3.51)$$

From (3.51) we can show that the correlation coefficient is given by

$$\gamma_{12}(\mathbf{x_1},\mathbf{x_2},\omega)=\frac{\sum_p \phi_p(\mathbf{x_1})\phi_p(\mathbf{x_2})\phi_p^2(\mathbf{x_o})\frac{1}{\Delta_p^2\left[H_p^2+W_p^2\right]}}{\left[\sum_p \phi_p^2(\mathbf{x_1})\phi_p^2(\mathbf{x_o})\frac{1}{\Delta_p^2\left[H_p^2+W_p^2\right]}\right]^{1/2}\left[\sum_p \phi_p^2(\mathbf{x_2})\phi_p^2(\mathbf{x_o})\frac{1}{\Delta_p^2\left[H_p^2+W_p^2\right]}\right]^{1/2}}, \quad (3.52)$$

where $\mathbf{x_1}=(x_1,y_1)$, $\mathbf{x_2}=(x_2,y_2)$, $\mathbf{x_o}=(x_o,y_o)$.

The above expression enables the correlation coefficient to be computed for any pair of points and for any frequency. The disadvantage is that we need to estimate the plate natural frequencies and associated mode shapes. In order to compute a frequency-averaged value for the correlation coefficient it is necessary to integrate the term $\Delta_p^2\left[H_p^2+W_p^2\right]$ over frequency. A closed form solution for this integral for integration limits f_1 and f_2 is given by equation (A.7). As explained in ref. [75], when the natural frequencies ω_p do not overlap the limits of integration can be extended to infinity. Assuming the modal masses and loss factors are relatively uniform the following standard result is obtained

$$\int_{-\infty}^{\infty}\frac{d\omega}{\Delta_p^2\left[\left(\omega_p^2-\omega^2\right)^2+\left(\eta_p\omega_p\omega\right)^2\right]}=\frac{\pi}{M^2\eta}, \quad (3.53)$$

where M is the total mass of the plate and η is the plate frequency-averaged loss factor. Substituting (3.53) in (3.52) we obtain the frequency-averaged correlation coefficient of acceleration due to a random point force applied at $\mathbf{x_o} = (x_o,y_o)$

$$\gamma_{12}(\mathbf{x}_1,\mathbf{x}_2,f_c)=\frac{\sum_p \phi_p(\mathbf{x}_1)\phi_p(\mathbf{x}_2)\phi_p^2(\mathbf{x}_o)}{\left[\sum_p \phi_p^2(\mathbf{x}_1)\phi_p^2(\mathbf{x}_o)\right]^{1/2}\left[\sum_p \phi_p^2(\mathbf{x}_2)\phi_p^2(\mathbf{x}_o)\right]^{1/2}}, \qquad (3.54)$$

where the summation indicated involves all the modes whose natural frequencies are situated inside the frequency band whose centre frequency is f_c. This expression was employed in section 3.7 to obtain theoretical results for the correlation coefficient using modal summation. In the spirit of the approximations employed in this chapter the modal summation can be substituted by an integration in wavenumber space. As a result the asymptotic form of equation (3.54) in terms of circular coordinates (k_B,θ) in wavenumber space is given by

$$\gamma_{12}(\mathbf{x}_1,\mathbf{x}_2,f_c)=\frac{\int_{\Delta k}\int_0^{\pi/2}\phi(k_B,\theta,\mathbf{x}_1)\phi(k_B,\theta,\mathbf{x}_2)\phi^2(k_B,\theta,\mathbf{x}_o)\,d\theta dk_B}{\left[\int_{\Delta k}\int_0^{\pi/2}\phi^2(k_B,\theta,\mathbf{x}_1)\phi^2(k_B,\theta,\mathbf{x}_o)\,d\theta dk_B\right]^{1/2}\left[\int_{\Delta k}\int_0^{\pi/2}\phi^2(k_B,\theta,\mathbf{x}_2)\phi^2(k_B,\theta,\mathbf{x}_o)\,d\theta dk_B\right]^{1/2}}, \qquad (3.55)$$

where for a simply-supported plate: $\phi(k_B,\theta,\mathbf{x}_1)=\sin(k_B x_1\cos\theta)\sin(k_B y_1\sin\theta)$. Results from equations (3.55) and (3.54) were compared for the case of a simply-supported plate. Some of the results obtained are presented in section 3.7. As shown in figs. 3.14 and 3.15 good agreement was obtained when the discrete modal summation of expression (3.54) was computed and compared to the asymptotic results from equation (3.55). This indicates that expression (3.55) is a good approximation of the correlation coefficient of point excited structures. This agrees with the analysis of ref. [75] (pag. 60) in which it is suggested that an asymptotic expression in the form of expression (3.55) provides an excellent approximation to the exact discrete sum of an equation similar to equation (3.54). In addition, it is observed that considerations similar to the ones employed in this sections will lead to the expression (196) of ref. [75].

From equations (3.10) and (3.54) we can show that the frequency-averaged normalised cross-power spectral density for a point excited plate is given by

$$\mathrm{Re}\left[\gamma_a(\mathbf{x}_1,\mathbf{x}_2,f_c)\right]=\frac{\int_{\Delta k}\int_0^{\pi/2}\phi(k_b,\theta,\mathbf{x}_1)\phi(k_b,\theta,\mathbf{x}_2)\phi^2(k_b,\theta,\mathbf{x}_o)\,d\theta dk_B}{\frac{1}{S}\int_S\left[\int_{\Delta k}\int_0^{\pi/2}\phi^2(k_b,\theta,\mathbf{x})\phi^2(k_b,\theta,\mathbf{x}_o)\,d\theta dk_B\right]dS}. \tag{3.56}$$

3.6.2 Acoustic excitation in the form of a diffuse sound field excitation

The cross-spectrum of the random force due to a excitation field in the form of a diffuse acoustic field is given by [76]

$$S_f(\varepsilon_1,\xi_1,\varepsilon_2,\xi_2,\omega)=\frac{\sin kr}{kr}\frac{S_P(\omega)}{2}, \tag{3.57}$$

where r is the distance between points (ε_1,ξ_1) and (ε_2,ξ_2), k is the acoustic wavenumber and $S_P(\omega)$ is the power spectral density of the pressure field. Substituting (3.57) in (3.49) we obtain an expression for the cross-spectral density of the generalised force due to diffuse field excitation,

$$I_p(\omega)=\int_S\int_S\frac{\sin kr}{kr}S_P(\omega)\phi_p(\varepsilon_1,\xi_1)\phi_p(\varepsilon_2,\xi_2)d\varepsilon_1 d\varepsilon_2 d\xi_1 d\xi_2. \tag{3.58}$$

From (3.58) and (3.49) we obtain an exact expression for the cross-spectral density of the acceleration response,

$$\begin{aligned}S_a(x_1,y_1,x_2,y_2,\omega)=\omega^4\sum_p\frac{\phi_p(x_1,y_1)\phi_p(x_2,y_2)}{\Delta_p^2}\frac{1}{\left[H_p^2+W_p^2\right]}\times\\ \times\int_S\int_S\frac{\sin kr}{kr}S_P(\omega)\phi_p(\varepsilon_1,\xi_1)\phi_p(\varepsilon_2,\xi_2)d\varepsilon_1 d\varepsilon_2 d\xi_1 d\xi_2.\end{aligned} \tag{3.59}$$

Assuming the power spectral density of the pressure field varies slowly with frequency and is equal to S_0 we can write that

$$S_0 I_p(\omega)=S_0\int_S\int_S\frac{\sin kr}{kr}\phi_p(\varepsilon_1,\xi_1)\phi_p(\varepsilon_2,\xi_2)d\varepsilon_1 d\varepsilon_2 d\xi_1 d\xi_2. \tag{3.60}$$

For cases in which the modal mass Δ_p is almost the same for all the modes we can express the correlation coefficient due to acoustic excitation in the form of a diffuse acoustic field as

$$\gamma_{12}(\mathbf{x}_1,\mathbf{x}_2,\omega)=\frac{\sum_p \phi_p(\mathbf{x}_1)\phi_p(\mathbf{x}_2)\dfrac{I_p(\omega)}{\left[H_p^2+W_p^2\right]}}{\left[\sum_p \phi_p^2(\mathbf{x}_1)\dfrac{I_p(\omega)}{\left[H_p^2+W_p^2\right]}\right]^{1/2}\left[\sum_p \phi_p^2(\mathbf{x}_2)\dfrac{I_p(\omega)}{\left[H_p^2+W_p^2\right]}\right]^{1/2}}. \qquad (3.61)$$

The evaluation of the discrete modal summations presented in the above expression involves computing the plate natural frequencies and associated mode shapes. A frequency-averaged result for expression (3.61) can be derived by following a similar procedure to the one employed for the case of a point excited plate. This expression is

$$\gamma_{12}(\mathbf{x}_1,\mathbf{x}_2,f_c)=\frac{\sum_p \phi_p(\mathbf{x}_1)\phi_p(\mathbf{x}_2)I_p(\omega)}{\left[\sum_p \phi_p^2(\mathbf{x}_1)I_p(\omega)\right]^{1/2}\left[\sum_p \phi_p^2(\mathbf{x}_2)I_p(\omega)\right]^{1/2}}, \qquad (3.62)$$

where the modes that are include in the summation have resonance frequencies inside the band of interest. The acoustic wavenumber k corresponds to the frequency f_c.

Substituting the modal summation by an integration in wavenumber space we have, in cylindrical coordinates,

$$\gamma_{12}(\mathbf{x}_1,\mathbf{x}_2,f_c)=\frac{\int_{\Delta k}\int_{\theta_1}^{\theta_2}\phi(k_B,\theta,\mathbf{x}_1)\phi(k_B,\theta,\mathbf{x}_2)I(k,k_B,\theta)\,d\theta\,dk_B}{\left[\int_{\Delta k}\int_{\theta_1}^{\theta_2}\phi^2(k_B,\theta,\mathbf{x}_1)I(k,k_B,\theta)\,d\theta\,dk_B\right]^{1/2}\left[\int_{\Delta k}\int_{\theta_1}^{\theta_2}\phi^2(k_B,\theta,\mathbf{x}_2)I(k,k_B,\theta)\,d\theta\,dk_B\right]^{1/2}} \qquad (3.63)$$

where k is calculated for the band centre frequency f_c and

$$I(k,k_B,\theta)=\int_S\int_S\frac{\sin kr}{kr}\phi(k_B,\varepsilon_1,\xi_1,\theta)\phi(k_B,\varepsilon_2,\xi_2,\theta)\,d\varepsilon_1\,d\varepsilon_2\,d\xi_1\,d\xi_2. \qquad (3.64)$$

Similar to the procedure presented in section 3.4.1, for cases in which the bandwidth is not too large, the integral in k_B can be approximated by the expression in the integrand with k_B substituted by the bending wavenumber k_b calculated at the band centre frequency f_c.

The limits of integration θ_1 and θ_2 for the case of acoustic excitation are defined by the relative values of the acoustic wavenumber k and the bending wavenumber k_b. As explained in ref. [19], plate modes which satisfy the condition

$$k_x^2+k_y^2<k^2 \qquad (3.65)$$

produce a component that radiates well. By reciprocity, we can suggest that only the plate modes that satisfy the above condition will be efficiently excited by an acoustic field. Therefore, it seems reasonable to evaluate the integral in wavenumber space presented in equation (3.63) for a region that satisfies the condition (3.65). From fig. 3.10 we observe that such region is situated at the top and bottom ends of the wavenumber quarter-circle. Then if we divide the region of integration in two we obtain the following pair of integration limits,

$$\begin{aligned} &1) \quad \theta_1' = 0 && \theta_2' = \frac{k}{k_b} \\ &2) \quad \theta_1'' = \frac{\pi}{2} - \frac{k}{k_b} && \theta_2'' = \frac{\pi}{2} \end{aligned} \tag{3.66}$$

where the first pair correspond to the bottom region and the second pair correspond to the top region. These integration limits were obtained from an approximate analysis of the geometry representation of acoustic and bending wavenumbers on a wavenumber space.

In order to obtain a first approximation for the correlation coefficient due to acoustic excitation, the integration limits presented in (3.66) were used as limits of integration for the standard correlation coefficient expression (equation (3.23)). It was found that this approximation gave results very similar to ones computed with equation (3.63). It was also observed that the integration limits employed in the integration of equation (3.63) do not affect the correlation coefficient results as the multiplication by the factor $I(k,k_b,\theta)$ will have a similar effect to using the integration limits presented in (3.66).

Unfortunately, as described in section 4.4 (fig. 4.5), when results from this approximation were compared to experimental results using acoustic excitation by a sound field in a cavity the agreement obtained was poor. The main reason for such poor agreement is that the acoustic field inside the small acoustic cavity is not diffuse as assumed in the present section. A better model for the type of acoustic excitation employed in the experimental work reported in section 4.4 could be one which explicitly included each individual acoustic mode in the computation of $I_p(\omega)$. Such procedure is equivalent to the hybrid model suggested in this work and will allow the computation of the response of the modally-dense plate due to an acoustic source

generating a modally-sparse acoustic field. This is left as a suggestion for future work. Another explanation for such disagreement is that all the points in the acoustic field are coherent due to the use of a single source. As a result, the assumed cross-spectrum in the form of equation (3.57) is no longer valid.

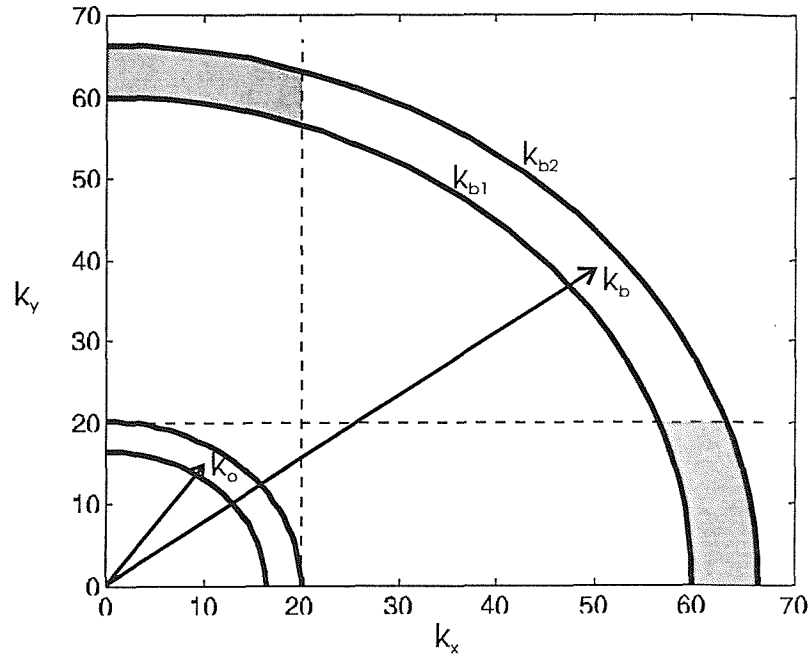

Fig. 3.10 - Illustration of wavenumber region with plate modes excited by an acoustic field of wavenumber k_o.

3.7 Simply-supported flat plates: a modal summation approach

A modal summation model that employs the mode shapes of a simply-supported flat plate was used to simulate the dynamic behaviour of two simply-supported flat plates. The modal summation results are compared with analytical results (equations (3.17) and (3.18)) presented in section 3.4.

The advantages of using a modal summation model are that the number of modal responses summed in each frequency band can be controlled, and the effects of point excitation can be assessed in relation to an assumed model of spatially-uncorrelated excitation (rain-on-the-roof). An asymptotic approximation for correlation coefficients on point excited plates is also used in the comparison.

3.7.1 Description of modal summation approach

For a flat plate with simply-supported boundary conditions a modal summation expression for the frequency-averaged correlation coefficient of acceleration ($\gamma_{12}(\mathbf{x}_1,\mathbf{x}_2,f_c)$) can be derived from equations (3.8), (3.12), (3.14) and (3.16). The result is

$$\gamma_{12}(\mathbf{x}_1,\mathbf{x}_2,f_c) = \frac{\sum_N \sin(k_x x_1)\sin(k_x x_2)\sin(k_y y_1)\sin(k_y y_2)}{\left[\sum_N \sin^2(k_x x_1)\sin^2(k_y y_1)\right]^{1/2}\left[\sum_N \sin^2(k_x x_2)\sin^2(k_y y_2)\right]^{1/2}}. \quad (3.67)$$

where $k_x = m\pi/a$, $k_y = n\pi/b$, m and n are the modal numbers, a and b are the dimensions of the plate in x and y directions, respectively, and N represents the number of modes summed in each frequency band.

Based on the above equation the frequency-averaged correlation coefficient in each frequency band was estimated in the following way :

- The plate natural frequencies were calculated and the modes grouped according to frequency band,
- The summations presented in equation (3.67) were then computed for modes whose resonance frequencies are in the respective band,

- The summations were repeated for each consecutive pair of points on the line analysed,
- The results at each line were then plotted as a function of non-dimensional separation distance $k_b r$, where k_b is the bending wavenumber calculated at the band centre frequency and r is the distance between each pair of points.

3.7.2 Discussion of results

The above procedure was employed to estimate the vibration field correlation of two simply-supported plates which are illustrated in fig. 3.11. They both had the same thickness, h = 0.001 m, and were assumed to be made of aluminium. One of the plates had dimensions a = b = 0.48 m (small plate) and the other a = b = 1.5 m (large plate). Consequently, both plates had the same bending wavenumber in each frequency band but the large plate had a much higher modal density. In addition, because of the square geometry of both plates, a large number of vibration modes having different shapes but the same natural frequencies were used in the summation.

The correlation coefficient evaluation was carried out for points equally spaced along lines whose positions are indicated in fig. 3.11. One of the points was assumed fixed and the other displaced from it along the line in nine equally spaced points. Correlation coefficient results were computed for lines B, C and D in one third octave bands from 63 Hz to 3150 Hz and also for 20 frequency bands of constant width of 100 Hz from 50 Hz to 1950 Hz. A large amount of data was obtained in this investigation but only a small selection of significant results are presented here.

The comparison between modal summation and analytical results (eq. (3.17)) for points along line C is shown in fig. 3.12 for some frequency bands. Equal spacing of 2 cm between the points was used on this line. Good agreement was observed between analytical and modal summation results for both plates for frequency bands above (and including) 200 Hz. Results for the small plate did not agree with the theoretical results below 200 Hz because of the small number of modes summed in each 1/3 octave band. For instance, in the 200 Hz one third octave band the number of modes used in the small plate modal summation was five.

As a means of further assessing the number of modes necessary for the analytical frequency-averaged results agree with modal summation ones, the modal summation simulation was performed in constant bandwidths of 100 Hz for the small plate. For all the lines the number of modes summed in each band varied from 4 to 8. Results for line C in four frequency bands are presented in fig. 3.13. For centre frequencies 250 Hz and 450 Hz, six modes were included in the summation, seven modes were summed for 550 Hz band, and only four modes for the 850 Hz frequency band. As shown in fig. 3.13, when only four modes were included in the summation a poor agreement was observed. A mix of good and reasonable agreement results was verified for cases when six or seven modes were present in a band. Good agreement was only obtained for cases in which eight modes were included in the summation.. Similar behaviour was observed for results along the other lines. Stearn [76] employed a similar modal summation procedure to observe that at least ten modes need to be excited at resonance in a frequency band for the correlation coefficient to approximate the diffuse bending wave field function far from the edges of a randomly excited structure. Thus, neglecting the effect of damping, it can be inferred that for bands in which more than eight modes are excited by spatially uncorrelated forces, the modal summation results agree with those of the theoretical model proposed in this chapter (equation (3.17)).

The theoretical analysis presented in this chapter presupposes that the excitation applied to the plate is random and spatially uncorrelated (rain-on-the-roof). Unfortunately, this type of excitation is rarely encountered in real situations as the force is normally applied over a small surface area. The influence of the excitation spatial distribution on the vibration field correlation was analysed using the modal summation model. In the previous section, it was shown that the frequency-averaged correlation coefficient due to point excitation at $\mathbf{x}_0 = (x_o, y_o)$ is given by

$$\gamma_{12}(\mathbf{x}_1, \mathbf{x}_2, f_c) = \frac{\sum_p \phi_p(\mathbf{x}_1)\phi_p(\mathbf{x}_2)\phi_p^2(\mathbf{x}_o)}{\left[\sum_p \phi_p^2(\mathbf{x}_1)\phi_p^2(\mathbf{x}_o)\right]^{1/2}\left[\sum_p \phi_p^2(\mathbf{x}_2)\phi_p^2(\mathbf{x}_o)\right]^{1/2}}, \qquad (3.54)$$

where $\phi_p(\mathbf{x})$ represents the mode shape of the structure: $\sin(k_x x)\sin(k_y y)$ for a simply-supported flat plate. The same procedure as that described in section 3.7.1 was used to

obtain the correlation coefficients using equation (3.54) along the lines sketched in fig. 3.11. For each line, different positions of the excitation point were used.

A typical result of this simulation is presented in fig. 3.14. Line D was chosen for this representation as it is reasonably far (in terms of wavelength) from all the boundaries in almost all frequency bands analysed. As expected, it was observed that, along this line, equation (3.17) (simply-supported flat plate) and equation (3.18) (two-dimensional diffuse wave field) gave the same results. Thus, only the theoretical results for a simply-supported flat plate (equation (3.17)) are plotted in fig. 3.14. The asymptotic expression for the correlation coefficient due to point excitation shown in eq. (3.55) is also employed in this comparison and is named 'point' in figs. 3.14 and 3.15.

As shown in figs. 3.14 and 3.15, results for the large plate and for the asymptotic expression of the point excited correlation coefficient (equation (3.55)) agreed quite well in the frequency range analysed. Furthermore, both results approached the expression for the spatially-uncorrelated correlation coefficient as the frequency increased. Based on modal summation numerical procedure results, Stearn [76] also observed that point-excited correlation functions approach that of diffuse bending wave fields for points far (in terms of wavelength) from the edges and excitation point. However, when comparing experimental observations on point-excited plates to the diffuse field result, this agreement was not observed. He explained this discrepancy by pointing out that the plates were relatively highly damped.

The relative strengths of the field directly radiated from the point of excitation and the plate reverberant field is strongly dependent on the system damping. An analysis of such relative strength was presented by Skudrzyk [77]. He demonstrated that the distance in which the strength of the field radiated by the point force equals that of the reverberant field is given by (pag. 259, ref. [77])

$$r = \frac{2\pi l l_o \eta}{\lambda_B} = l l_o \eta k_b, \tag{3.68}$$

where l is the average distance the wave front travels between successive reflections, l_o is the averaged distance to the boundary of the plate, η represents the plate loss factor and k_b is the bending wavenumber. An estimate of this distance for the small

plate is presented in fig. 3.16 as a function of typical loss factors. As shown, for the case of relatively highly damped systems ($\eta > 0.04$) the direct field will dominate the vibration field. However, for moderate to low values of loss factor ($\eta < 0.01$) the reverberant field will predominate over most of the vibration field, apart from a region very close to the excitation point.

For points close to the system boundaries, such as line B, for which the results are presented in fig. 3.15, the effect of the point excitation on the vibration field was less pronounced than for points situated far from the edges. This is because the interference field generated by the edges dominates the vibration field in this region. These are only preliminary observations on the influence of the excitation on the correlation coefficients of a vibration field and, as discussed in the section 3.6, further work is necessary to clarify this situation. At present, it can be stated that the theoretical approximations for the correlation coefficient derived in this chapter can be approximately applied for point-excited structures having moderate damping.

Unlike the situation observed for line D, the theoretical results from equations (3.17) and (3.18) differ considerably for points placed along line B. As presented in fig. 3.15, the zero-crossing points and peak values for results from equation (3.18) (diffuse bending wave field) are consistently different from that from equation (3.17) (simply-supported flat plate). It was found that, above 400 Hz, both small and large plate results agree with the theoretical results for a simply-supported flat plate, whereas results from equation (3.18) are very different from the other three results in all frequency bands analysed. This disagreement happened irrespective of the type of excitation (spatially-uncorrelated or point excitation) and it clearly illustrates the effect of the boundaries in correlating the wave field near the edges.

Furthermore, it was also observed that the relative position of both measurement points in relation to the edges is relevant. In the results presented in fig. 3.15, one of the points was assumed fixed and placed at the bottom of the line (closer to the edge) and the other moved along the line towards the plate centre. However, were the fixed point placed closer to the centre of the plate, the theoretical formulations (equations (3.17) and (3.18)) and modal summation results would be more similar. This indicates that both points need to be placed inside the "one-

wavelength-from-the-edges" region for the diffuse wave field and simply-supported results disagree. This observation supports the theoretical analysis of section 3.4.1.

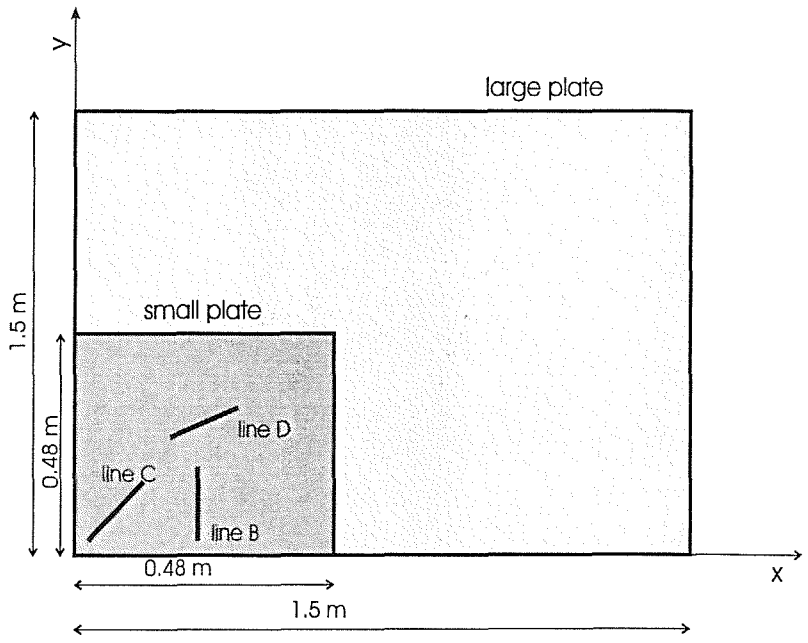

Fig. 3.11- Sketch of lines used in the verification of correlation coefficient results.

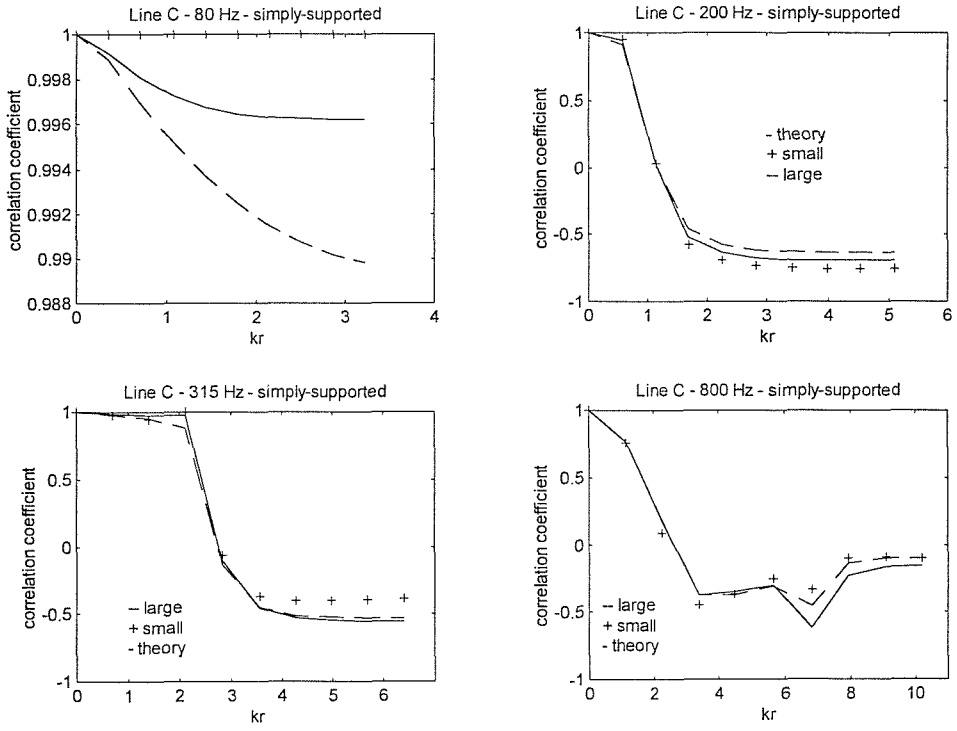

Fig. 3.12 - Comparison of results from equation (3.17) with modal summation results (eq. (3.67)) along line C. 1/3 octave bands. key: ——— theory (eq. (3.17)); — — — large plate; + + small plate.

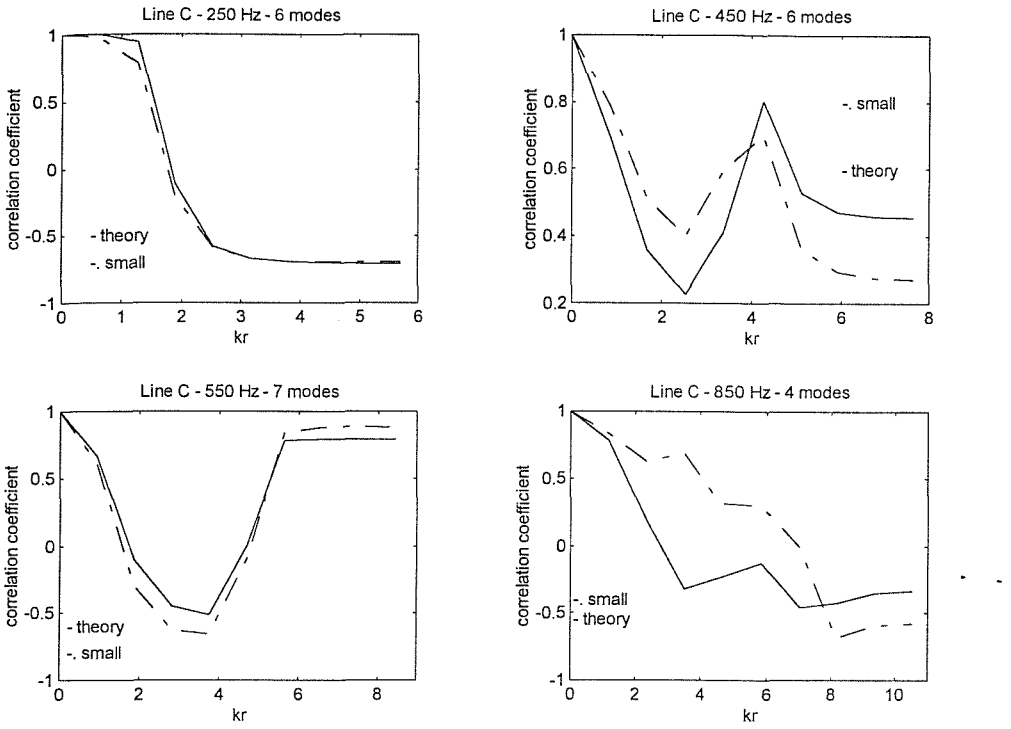

Fig. 3.13 - Comparison of results from equation (3.17) with modal summation results (eq. (3.67)) for the small plate along line C . 100 Hz constant bands. ——— theory (eq. (3.17)); – · – · – modal sum.

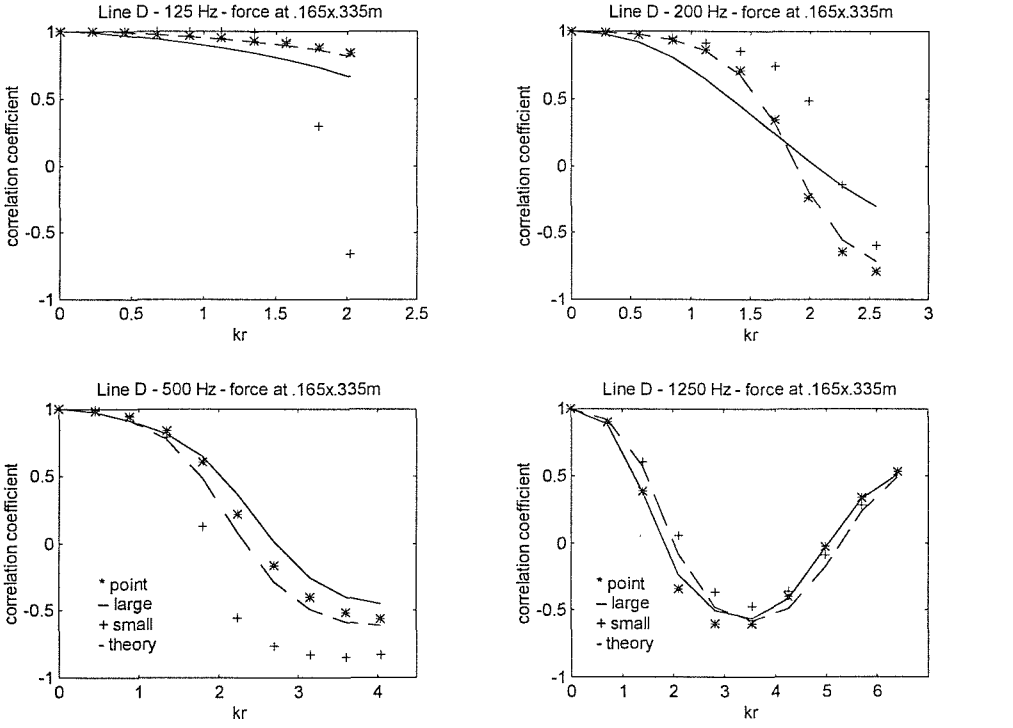

Fig. 3.14 - Comparison of results from equation (3.18) with modal summation results due to point excitation (eq. (3.54)). Line D, force at x = 0.165 m, y= 0.335 m. 1/3 octave bands. ——— theory (eq. (3.18)); — — — large plate; + small plate; * point excitation (eq. (3.55)).

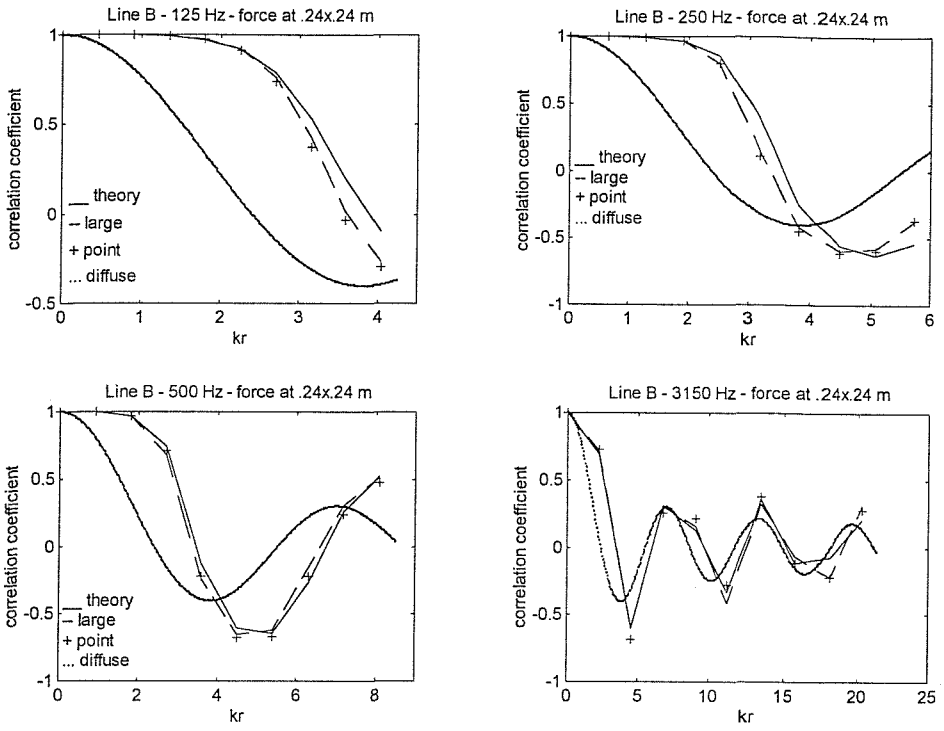

Fig. 3.15 - Comparison of results from eq. (3.17) and eq. (3.18) with modal summation results due to point excitation. Line B, force at x = 0.24 m, y = 0.24 m. 1/3 octave bands.
——— simply-supported (eq. (3.17)); — — — large plate, modal sum.;
+ point excitation (eq. (3.55)); - - - - - diffuse field (eq. (3.18)).

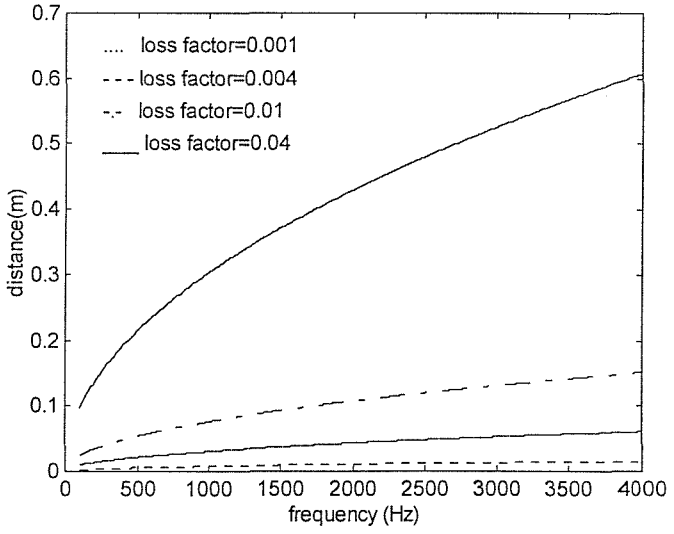

Fig. 3.16 - Distance from excitation point at which the strength of the field radiated by the driver equals that of the plate reverberant field as a function of damping. key: ——— $\eta = 0.04$;
– · – · – · – $\eta = 0.01$; — — — $\eta = 0.004$; - - - - - $\eta = 0.001$.

CHAPTER 4

EXPERIMENTAL INVESTIGATION OF VIBRATION FIELD CORRELATION ON FLAT PLATE STRUCTURES

4.1 Introduction

This chapter presents the results of an experimental investigation of vibration field correlation carried out on four different flat plate structures and on a car bodyshell. Measurements of vibration acceleration were used as a means of estimating the frequency-averaged correlation coefficient and the normalised cross-spectral density of these structures under random excitation. The main purpose of this investigation was to assess the validity of the theoretical correlation coefficient and normalised cross-spectral density approximations derived in the previous chapter.

The flat plate structures used in the experimental investigation were as follows: a 1 mm thick clamped square aluminium plate that bounds a rectangular box; a 3.5 mm thick rectangular steel plate with a steel bar attached and clamped along the four edges; a rectangular aluminium plate with free edges hung by two thin wires from a frame; two irregularly-shaped flat steel plates with free edges, connected by metal straps and hung from a frame.

The results are compared with estimates of vibration field correlation based on the theory presented in the previous chapter. In addition, results from a similar experimental investigation carried on a car body shell [54,78] are also compared with the theoretical estimates. Modal density and structural loss factors estimates were also obtained on some of the investigated structures as means of assessing their modal overlap factors and the number of modes resonating in each frequency band.

4.2 Experimental procedure

The experimental procedure applied was similar to all flat plates. Each plate was mechanically or acoustically excited. The input signals were broad-band random. These sources produced sufficient vibrational response to guarantee a good signal to noise ratio as the response levels were, in average, 30 dB higher than the background noise level. Two accelerometers (Bruel & Kjaer Type 4374) were placed along different lines on the plate surface. In each set of measurements one accelerometer was held at one extreme of the line (marked 1 in figs. 3.11, 4.2, 4.11) and the other displaced from it along the line at equally spaced points.

The acceleration signals were acquired using a ZONIC+AND 3524 Dual Channel FFT Analyzer and transferred to a PC-compatible microcomputer. The frequency-averaged correlation coefficient between the two acceleration signals was then estimated using equation (3.6) and the normalised cross-power spectral density estimated from equation (3.10). For this purpose cross- and auto-power spectrum of acceleration in each pair of points were acquired in the frequency range 0-5000 Hz. These estimates were integrated in 1/3 octave bands and in bands of constant width. The frequency separation of these spectra was 2.5 Hz (400 lines) for lines A, B and C (section 4.3) and 3.125 Hz (1600 lines) for all the other lines. Finally, the frequency-averaged estimates were plotted as a function of the non-dimensional distance kr, where k is the bending wavenumber calculated at the band centre frequency and r is the distance in metres between each pair of points.

A large accelerometer can considerably load thin plates as the ones here investigated. As a result lightweight accelerometers (B&K 4374, mass=0.6 grams) were chosen for this investigation and it was estimated that they only affect the present results for frequencies above 3000 Hz for the car roof (thickness = 0.8 mm). For the other plates the mass load of the accelerometer is negligible. In addition, it is important to mention that as the correlation coefficient is a normalised quantity this mass load effect will be cancelled when the experimental results are combined using equations (3.6) or (3.10).

One-third octave bands were chosen for the analysis because, in such bands, the bending wavenumber of each resonant mode does not vary more than 6 %

from the assumed mean value of the bending wavenumber (k_b) corresponding to the band centre frequency. This can be explained by the fact that the bending wavenumber is proportional to the square root of the associated frequency. So, if the square root of upper or lower frequency limits of 1/3 octave bands are divided by the square root of the band centre frequency the result is close to 6%.

The repeatability of the measurements were verified by estimating the correlation coefficient in the same pair of points ten times. In such exercise, before the acceleration signals were acquired, both accelerometers were removed and fixed again to the plate as a way of simulating a real laboratory situation. The largest normalised standard deviation (σ/m) of the estimated correlation coefficient was 0.1.

The real part of the normalised cross-spectral density of acceleration was estimated using the same data employed in the correlation coefficient experimental estimation. The space average of the acceleration was obtained from the average of the auto-spectrum at four different positions along the structure surface. This space average was then employed to normalise the real part of the cross-spectrum along each measurement line following equation (3.10).

4.3 Errors associated with the correlation coefficient estimation

The variance and the confidence limits of the present measurements are estimated following the procedure suggested by Bendat and Piersol [85] and Newland [67]. Random errors associated with statistical sampling considerations and bias errors associated with data acquisition errors are here considered. From Bendat and Piersol [85] we have that the normalised random error associated with the auto-spectrum estimation is

$$\varepsilon_r^G = \frac{\sigma_G}{m_G} = \frac{1}{\sqrt{B_e T_t}} \approx \frac{1}{\sqrt{n_d}}, \tag{4.1}$$

where σ is the standard deviation of the measurement of average m, n_d is the number of non-overlapping averages and T_t is the total duration of the record data. The normalised bias error is a function of the resolution bandwidth, B_e, and of the system half-power bandwidth, $B_r \approx 2\zeta f_d$, where ζ is the damping ratio and f_d is the damped

natural frequency. The normalised bias error for auto-spectrum measurements is given by [39]

$$\varepsilon_b^G = -\frac{1}{3}\left(\frac{B_e}{B_r}\right)^2, \tag{4.2}$$

and the normalised r.m.s. error is expressed as

$$\varepsilon = \sqrt{\varepsilon_r^2 + \varepsilon_b^2}. \tag{4.3}$$

As in the present measurements the bias errors associated with the auto-spectrum estimation were normally much smaller than the random errors we can say that the normalised r.m.s. error is approximately equal to the normalised random error.

Assuming the probability density function for the estimates G to be approximated by a chi-square distribution we can obtain confidence intervals for these measurements [67]. The number of degrees of freedom (κ) of the chi-square distribution is related to the standard deviation and measurement average by

$$\sqrt{\frac{2}{\kappa}} = \frac{\sigma}{m}. \tag{4.4}$$

By knowing the number of degrees of freedom we can obtain confidence limits from statistical tables of percentage points of a chi-square distribution [67,85].

The normalised random error associated with the real part of the cross-spectrum can be obtained from expression (9.25) of ref. [85]. After some mathematical manipulation we have that

$$\varepsilon_r = \frac{\sqrt{G_{xx}G_{yy} + \left(\mathrm{Re}\left[G_{xy}\right]\right)^2 - \left(\mathrm{Im}\left[G_{xy}\right]\right)^2}}{\sqrt{2n_d}\,\mathrm{Re}\left[G_{xy}\right]}. \tag{4.5}$$

Assuming the imaginary part of the cross-spectrum, G_{xy}, to be negligible compared to the real part we can show that equation (4.5) is equal to

$$\varepsilon_r = \frac{1}{\sqrt{2n_d}}\sqrt{\frac{1+\gamma_{xy}^2}{\gamma_{xy}^2}}, \tag{4.6}$$

where γ_{xy}^2 is the ordinary coherence function. For cases in which the coherence function is close or equal to one the normalised random error associated with the

cross-spectrum approaches the normalised random error associated with the auto-spectrum (equation (4.1)).

The random error associated with the correlation coefficient and with the normalised cross-spectral density can be derived following the procedure outlined in section 9.2.3 of ref. [85]. Assuming the imaginary part of the cross-spectral density is negligible in comparison to the real part we obtain that

$$\varepsilon_r^{\gamma} = \frac{\sigma_{\gamma}}{m_{\gamma}} \approx \sqrt{\frac{\left(1-\gamma_{xy}^2\right)}{\gamma_{xy}^2 n_d}}. \tag{4.7}$$

The above expression is valid for the correlation coefficient and for the normalised cross-spectral density. It shows that when the coherence function equals unity the random error associated with these two parameters is zero. Results for other values of the coherence function are shown in table 4.1. The number of non-overlapping averages used in the correlation coefficient estimation was 50.

γ_{xy}^2	0.9	0.7	0.5	0.3
ε_r^{γ}	0.065	0.1207	0.1732	0.2463
κ	473	137	66.7	33.0

Table 4.1 - Random error (eq. (4.7)) associated with correlation coefficient estimation as a function of the ordinary coherence function.

As shown, the number of degrees of freedom of the chi-square distribution were reasonably high for practical values of the coherence function. In most of the experiments performed the average value for the coherence function was in the band 1.0-0.9. In particular, when the coherence function equals 0.7 we have that the 95 % confidence limits for the correlation coefficient are given by

$$0.742\gamma_{12} < m < 1.296\gamma_{12}. \tag{4.8}$$

Similarly we have that the random errors associated with the estimation of the auto-spectrum of acceleration are defined by equation (4.1). In this case, we obtain that ninety per cent of all values of the autospectrum G_{xx} will lie in the band

$$0.779G_{xx} < m < 1.243G_{xx}. \tag{4.9}$$

The confidence limits presented in (4.8) and (4.9) show that the experimental results of correlation coefficient and normalised cross-spectral density presented in this chapter have low values of random error.

4.4 Square flat plate with four clamped edges

4.4.1 Description of apparatus

An aluminium plate of 0.001 m thickness, with equal sides of 0.48 m and clamped along the four edges was one of the flat structures used in the experimental verification of frequency-averaged correlation coefficient theoretical results. This plate bounded an acoustical enclosure in which the other five walls were of double plywood construction with the cavity between them filled with sand. This plate/box system was employed in the experimental analysis of vibroacoustic response reported in Chapter 5. Typical wavelengths for this plate were: 0.222 m at 200 Hz, 0.111 m at 800 Hz, 0.078 m at 1600 Hz and 0.057 m at 3000 Hz. The edges of the plate were sandwiched by two square metal frames used to simulate a clamped type of support (fig. 4.1). Point excitation from a non-contact shaker or acoustic excitation generated by a loudspeaker placed inside the enclosure were used to vibrate the plate.

The correlation coefficients were estimated using the procedure described in section 4.2 along three lines sketched in fig. 3.11 (lines B, C and D) and three lines that are sketched in fig. 4.2 (lines A, E and F). The spacing between the points varied: 2 cm was used for lines A, B and C and 1 cm for lines D, E and F. These estimates were integrated in 1/3 octave bands from 63 Hz to 800 Hz for lines A, B and C and from 80 Hz to 4000 Hz for lines D, E and F. In addition, some of the experimental results were also analysed in frequency bands of 100 Hz constant bandwidth.

4.4.2 Discussion of results

It is impractical to present all results obtained in this experimental investigation. As in section 3.7, a selection of some results is presented in order to highlight the most important findings of this investigation. The theoretical correlation coefficient results presented in this section were computed using results for a clamped plate based on Bolotin's dynamic edge effect method (equation (3.23)), with the coefficients for a clamped boundary as derived in Appendix B (expressions (B.4)).

It was confirmed by modal summation results (section 3.7) that at points removed from the edges (at least one wavelength from the edges), simply-supported plate correlation coefficient results converge to those of a diffuse bending wave field. The same verification was carried out for points situated along line D of the clamped plate as, for most frequency bands, these points were outside the one-wavelength-from-the-edges region. Fig. 4.3 shows the average of correlation coefficient results obtained from experiments in which the shaker was placed at four different points along the plate surface. The shaker coordinates are listed in table 5.7. For each shaker position, a separate estimate of the correlation coefficient in 1/3 octave bands was made, following the procedure outlined in section 4.2. The resultant correlation coefficients were then arithmetically averaged and plotted as a function of kr. The first clear conclusion from this set of results was that, above 200 Hz, the diffuse wave field (equation (3.18)) and clamped plate results (section 3.4.2) are coincident. This was expected because the estimated wavelength at 200 Hz was 0.22 m and thus, only the inner solution of Bolotin's edge effect method contributes to the analytical clamped plate result. Then, following an analysis presented by Bolotin [56], it was confirmed that, when a large number of modes is summed, or the asymptotic limit is taken in a limited band, the clamped plate result approaches the simply-supported one and they both approach the diffuse field result. Similar results were obtained for plates with free edges (sections 4.6 and 4.7).

It was also verified that clamped plate and diffuse field correlation coefficients agree reasonably well with the experimental results for one-third octave bands whose centre frequencies are equal or higher than 315 Hz. This situation is

illustrated in fig. 4.3 by showing results at 160 Hz and 315 Hz 1/3 octave bands. Theoretical estimates of natural frequencies on flat plates [79] suggests that at the 315 Hz 1/3 octave band at least 5 resonant modes have been excited. Similar trends were observed in the other lines. Nevertheless, it is important to note that for practical structures this agreement is also governed by the damping of the structure. A specific investigation of such dependence is presented in section 4.5.2.

One of the exceptions of the good agreement between theoretical and experimental results was in the 1/3 octave band centred on 500 Hz. In this 1/3 octave band, experimental results for the four mechanical excitation positions were consistently different from the theoretical results. On the contrary, correlation coefficient results obtained with broad-band random acoustic excitation from a loudspeaker agree with the theoretical estimates at this frequency band.

In addition, a slight disagreement between theoretical and experimental results was observed at the 1/3 octave band centred on 4000 Hz. In this high frequency range, the theoretical results begin to depart from the experimental ones. This happens because, as explained in section 3.4.2, the importance of the second order terms in the solution of integral (3.16') increase with the width of the integration strip. Therefore, the analytical approximation used for this integral is no longer strictly valid. Moreover, low values of the coherence function were observed in this frequency band indicating that random errors can be quite important in this band.

The influence of the edges on correlating the wave field inside the one-wavelength-from-the-edges region is illustrated by showing results obtained on line B (fig. 4.4). In this case, only experiments using a loudspeaker placed inside the acoustic box were performed. Two theoretical results are shown in this figure: one is the standard edge effect method result that includes the inner (sin k_x (x-ξ_x)) and outer (C_x exp(-μ_xx)) solutions; the other one only includes the inner solution. As one can observe, the results without the outer solution are completely wrong. The agreement between experimental and theoretical results is not remarkable but at least a similar trend in both graphs is shown with similar zero-crossing values. This example illustrate the importance of the outer solution in representing the interference in the wave field due to the edges.

A comparison between mechanical excitation from a non-contact shaker and acoustic excitation from a loudspeaker placed inside the box is shown at fig. 4.5. As illustrated in this figure, it was observed that the vibration field due to mechanical excitation appears to follow the theoretical results more closely. Above a certain frequency, both results tend to converge and approach the theoretical results. The better agreement between point excited experimental results in comparison to acoustically excited ones is contrary to the results reported by Stearn [76]. In that work he concluded exactly the opposite suggesting that a diffuse bending wave field could not be set up on a point excited plate. As mentioned in section 3.7.2, he justified the difference based on an analysis of the field radiated by the point force. No strong indication of disagreement between the present theory and point excited correlation coefficient results were observed on the different random excited structures analysed in this work. The loss factors of these structures ranged from 0.0005 to 0.08.

The difference between mechanically and acoustically excited structures in terms of correlation coefficients can be explained by the selective way that vibration modes are excited by an acoustic field. This filtering phenomenon would probably be of less concern in the case of an acoustic field like a very large room. As a matter of fact, a comparison between internal and external acoustic excitation was presented in refs. [54] and [78], and the general trend observed was that results from external acoustic excitation (from a loudspeaker in a laboratory room) approach the theoretical results above a frequency lower than that for internal acoustic excitation (source inside a passenger car compartment). This suggests that the filtering phenomenon is less important for diffuse acoustic fields.

The comparison between theoretical results of correlation coefficient due to acoustic excitation modelled by modifying the integration limits (as described in section 3.6.2) and experimental results due to acoustic excitation were inconclusive. This stems from the fact that theoretical results that simulate acoustic excitation (equation (3.23) with integration limits (3.66)) were very similar to spatially-uncorrelated ones (equation (3.23) with integration limits 0 and $\pi/2$) and were different from the experimental results due to acoustic excitation. As discussed in section 3.6.2, the main reason for this disagreement was the fact that the acoustic field used to excite the plate was not diffuse. Moreover, results from equation (3.63) and

(3.23) with integration limits (3.66) were very similar indicating that the acoustic excitation does not strongly affect the resonant response of the structure in a given frequency band. As presented in section 4.8, this explain the agreement between the experimental results obtained on a car bodyshell and the theory of Chapter 3.

As presented in fig. 4.5, in some cases, the theoretical results for acoustic excitation followed quite closely the experimental ones and, at the same time, they were both different from the experimental results due to mechanical excitation. An example of such agreement is presented in fig. 4.5 for line F at the one-third octave band centred on 2000 Hz. Unfortunately, we can not take such isolated cases as evidence that equation (3.23) with the integration limits given by expression (3.66) can be employed to represent the correlation coefficient due to acoustic excitation. This implies that further work is necessary to assess the application of section 3.6 results to acoustically excited structures.

In order to illustrate the equivalence between wave and modal models in terms of the correlation coefficient, theoretical results that employ these two approaches are shown in fig. 4.6. These results are also compared with numerical results from a modal summation procedure similar to the one described in section 3.7, but assuming that the edges were clamped, and carried out for a plate similar to the large plate described in section 3.7.2. As presented in fig. 4.6, the agreement between these three approaches is quite good, showing that the wave and modal representations are totally equivalent. This equivalence has been previously indicated by Langley [55]; however, this agreement contributes to increase the confidence that one can have in the theoretical analysis developed in this work. Further analyses of wave and modal representation is presented in Appendix E.

4.4.3 Results with a small stiffener attached to the plate

A small stiffener was attached to the clamped plate during the experimental response work (Chapter 5). The type of attachment used, position and dynamic characteristics of this stiffener are described in section 5.4. A thorough discussion of the effects of a stiffener on a plate vibration field are reported in section 4.5 and in this section we only present experimental results of correlation coefficient

and normalised cross-power spectral density of acceleration on a line close to this stiffener. The position of this line, named line G, is sketched in fig. 4.7. This line was placed in a region reasonably close to the position of the force excitation. The correlation coefficient on this line was computed following the procedure described in section 4.5.1, while the normalised cross-power spectral density was computed from equation (3.23') with the coefficients for a spring-supported edge given in appendices B and C.

A selection of correlation coefficient results along line G are presented in fig. 4.8. As shown, reasonably good agreement between experiments and theory is observed above the 250 Hz 1/3 octave band. This is slightly different from previous results without the stiffener in which experimental and theoretical results only agreed above the 315 Hz 1/3 octave band. The normalised cross-power spectral density results have also shown a similar agreement. As presented in fig. 4.9, for cases in which the correlation coefficient was similar to theoretical results the same happened with the normalised cross-power spectral density. In general, for the great part of the experimentally obtained normalised cross-power spectral density results, the agreement between experiments and theory followed the same pattern as the correlation coefficient. The main difference is that when theory and experiments disagree such disagreement was more pronounced in normalised cross-power spectral density results.

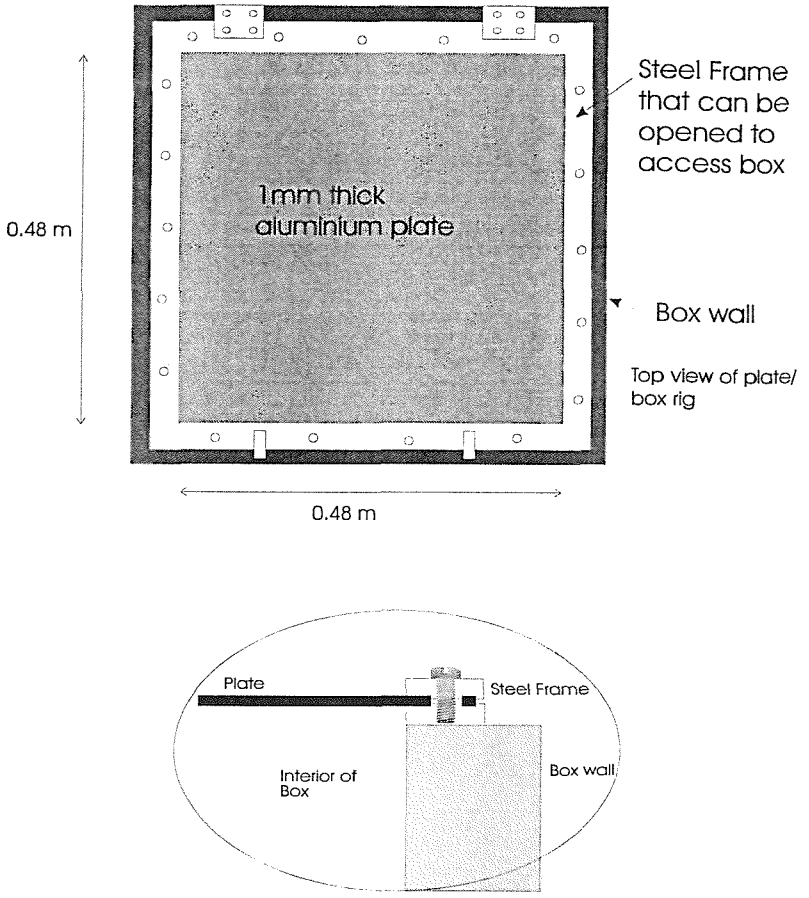

Fig. 4.1 - Top view of plate on top of wooden box and sketch of its fixation to the steel frame.

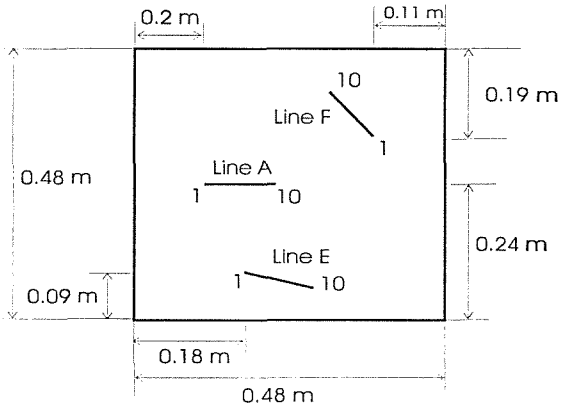

Fig. 4.2 - Sketch of some of the lines used in the experimental investigation. The numbers placed along the lines indicate the points location, 1 is the first point (fixed accelerometer) and 10 is the last point

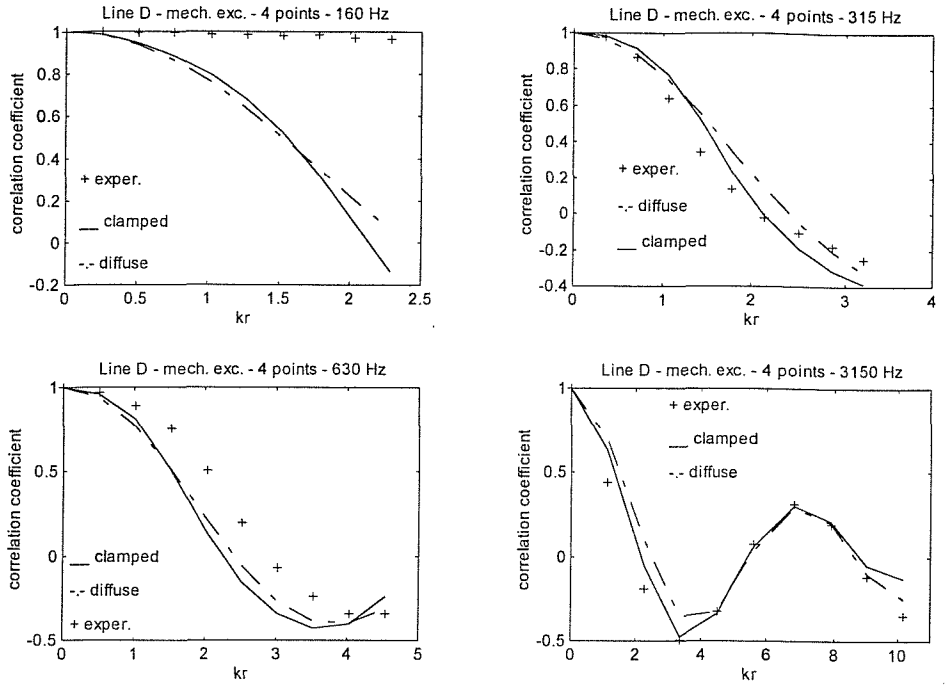

Fig. 4.3 - Comparison of results from equation (3.18) and equation (3.23) with experimental results from average of four excitation points along line D. 1/3 octave bands. + experimental results; ——— clamped plate (eq. (3.23)); – · – · – · – diffuse field (eq. (3.18)).

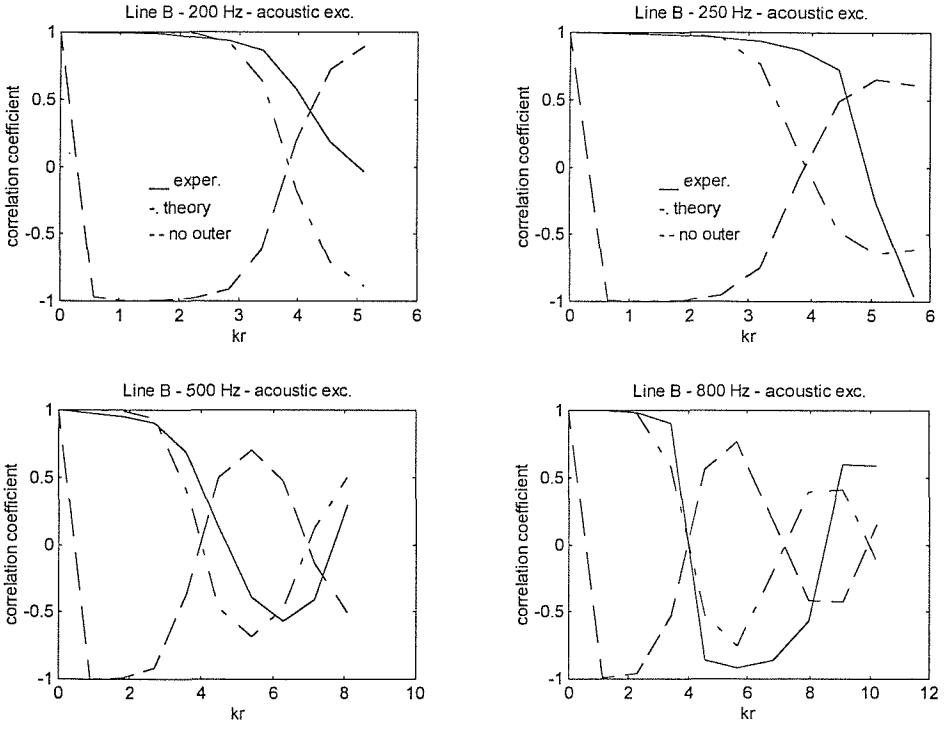

Fig. 4.4 - Comparison of results from eq. (3.30) and eq. (3.41) with experimental results due to internal acoustic excitation along line B. 1/3 octave bands. ——— experiments; — — — theory without evanescent waves (eq. (3.30)); – · – · – · – theory with evanescent waves (eq. (3.41)).

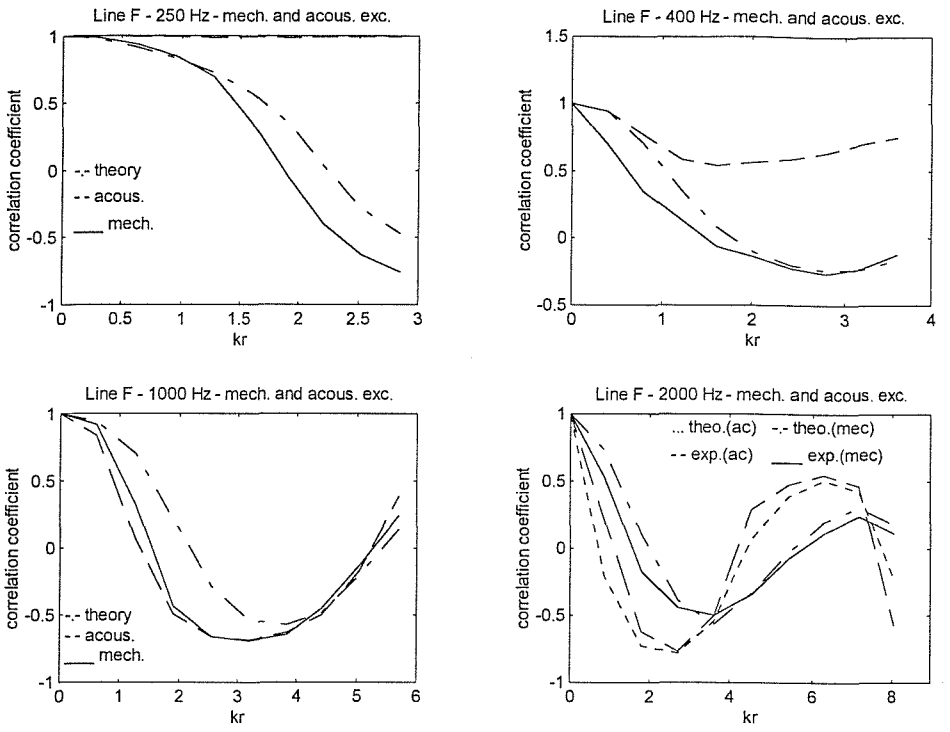

Fig. 4.5 - Comparison of theoretical results from equations (3.55) and (3.66) with experimental results due to mechanical and acoustic excitation. Line F. 1/3 octave bands. ——— experiments (mech. excit.); — — — experiments (acoustic exc.); – · – · – · – theory (point excitation) (eq. (3.55)); - - - - - theory (acoustic excitation) (eq. (3.66)).

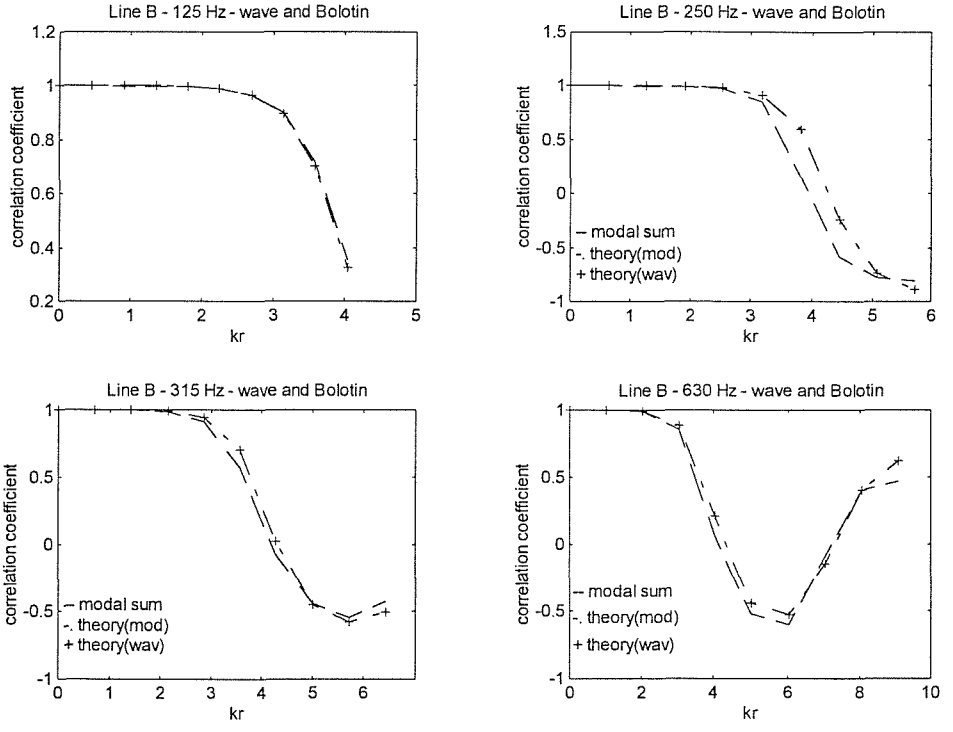

Fig. 4.6 - Comparison of theoretical results from modal and wave representation with modal summation results along line B. 1/3 octave bands. — — — modal summation for clamped plate (large plate); – · – · – · – modal representation (eq. (3.23)); + + wave representation (eq. (3.41)).

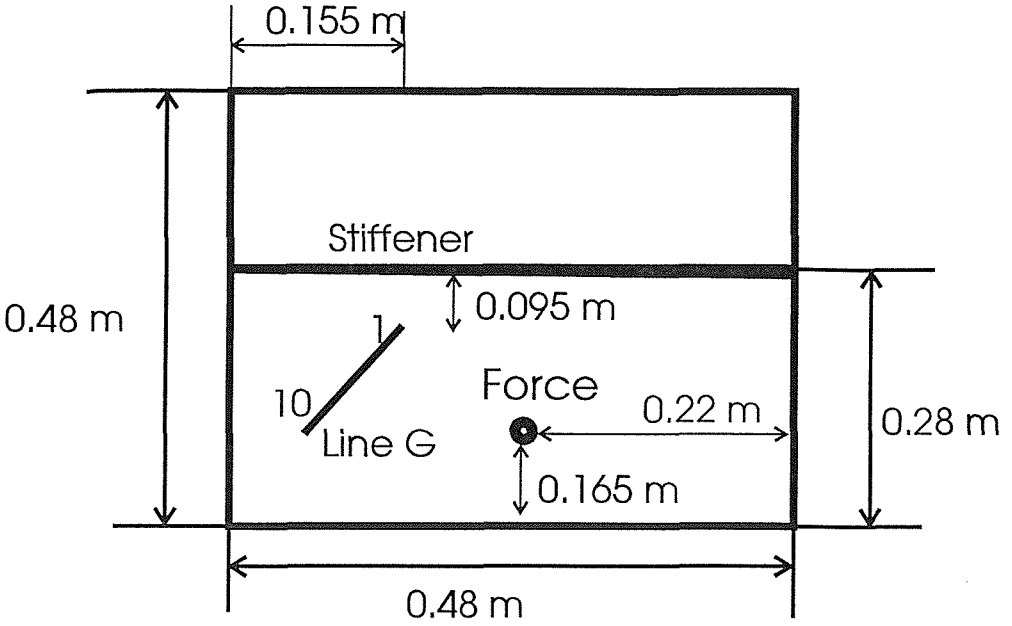

Fig. 4.7 - Sketch of small stiffener and line G position.

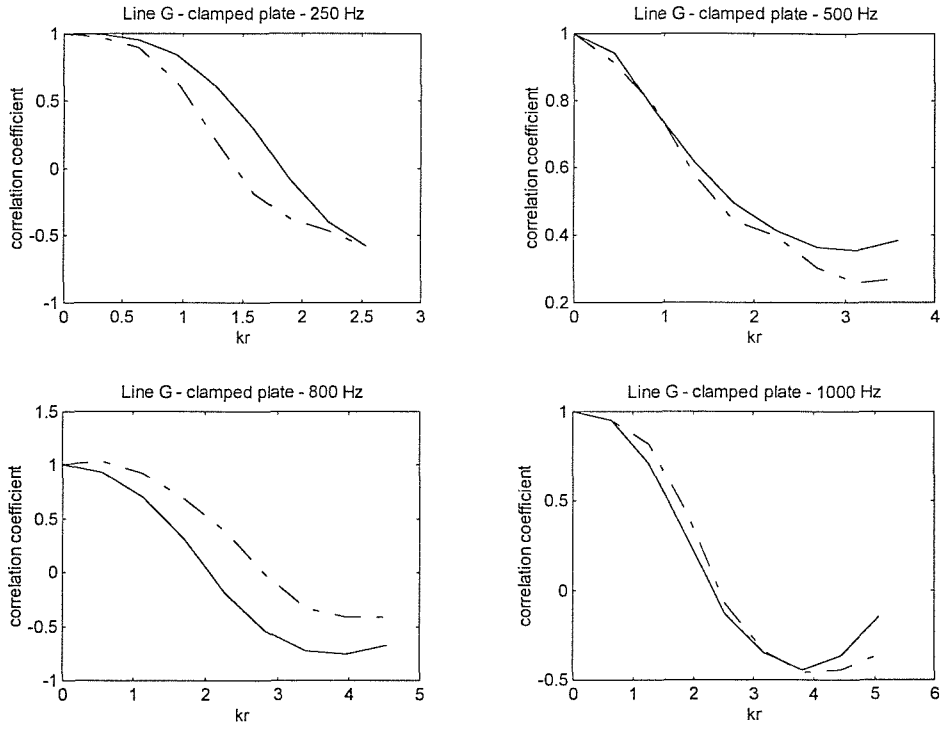

Fig. 4.8 - Comparison of theoretical correlation coefficient results with experimental results along line G. Mechanical excitation. 1/3 octave bands. ——— theory (eq. (3.23)); – · – · – · – experiments.

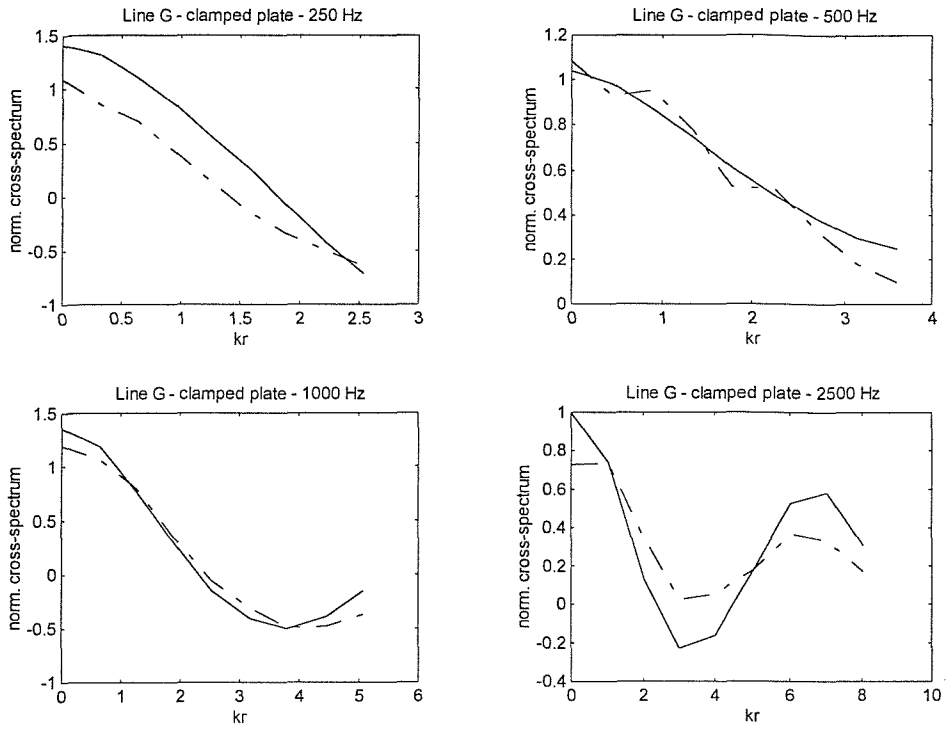

Fig. 4.9 - Comparison of normalised cross-power spectral density results from equation (3.23') with experimental results along line G. Mechanical excitation. 1/3 octave bands.
——— theory (eq. (3.23')); – · – · – · – experimental results.

4.5 Rectangular stiffened plate with four clamped edges

A second clamped plate of regular geometry was employed in this experimental work. A removable steel bar was attached to this plate permitting the analysis of the influence of the perturbation (stiffener) on the plate vibration field.

4.5.1 Description of the apparatus

The flat plate was of 3.53 mm thick aluminium. It was (weakly) clamped along the edges by a wooden frame which was placed on a rigid wooden table. The exposed dimensions of the plate were 0.876 m x 0.576 m and it was divided, along its larger dimension, in two identical sections by a hollow steel bar having a cross sectional area of (25 x 25) mm^2 and thickness of 3.16 mm (illustration in fig. 4.12). The steel bar was fixed to the plate by five light screws. This permitted the easily removal of the steel bar enabling a comparison of the vibration characteristics of the plate with and without the stiffener. The first three natural frequencies of transverse, longitudinal and torsional vibration of this bar are listed in table 4.2. Such natural frequencies were computed following the expressions presented by Blevins [79]. As shown in this table, the steel bar does not have many resonance frequencies in the frequency band of analysis.

order of natural frequency	transverse vibration (Hz)	longitudinal vibration (Hz)	torsional vibration (Hz)
1	500.6	4489.8	2387.2
2	1379.0	8979.6	4774.4
3	2705.6	13469.0	7161.6

Table 4.2 - Natural frequencies of vibration of the steel bar.

An illustration of the test rig used is presented in fig. 4.10. Typical wavelengths for the plate were: 0.415 m at 200 Hz, 0.24 m at 600 Hz, 0.186 m at 1000

Hz and 0.131 Hz at 2000 Hz. Point excitation by a electrodynamic shaker (Ling Dynamic V101) was used to vibrate the plate. The excitation signal employed was broadband random from 0 to 5000 Hz. The point marked 'Force' in fig. 4.11 indicates the position on which the force was applied. The vibrational response obtained was sufficiently high to guarantee a good signal-to-noise ratio.

The experimental procedure employed was that described in section 4.2 and the lines used are illustrated in fig. 4.11. Lines 3 and 5, and lines 1 and 7 were coincident, however results for lines 5 and 7 were carried out for the plate without the stiffener. The spacing between the ten equally spaced points used on each line was 1 cm.

The theoretical results used in the comparison with the experimental ones were based on Bolotin's dynamic edge effect method as derived in section 3.4.2, with the coefficients given by expressions (B.4) for a clamped edge and by expressions (B.10), (B.11) and (B.12) for a spring-supported edge (the steel bar dynamic characteristics defined the spring rotational, translational and coupling stiffnesses, as shown in Appendix B). As shown in Appendix E and section 4.4.2, exactly the same results can be obtained with the free wave model (section 3.5.2). For the free wave model, the reflection, transmission and evanescent coefficients are defined by expressions (C.4) for a clamped edge and by expressions (C.11) to (C.14) for a spring supported edge.

The loss factor and modal density of this plate were estimated via measurement of point mobility and power injection following the procedure suggested by Clarkson as described in refs. [39,80]. As only an approximate estimate of these parameters was required, the point mobility was obtained in just one point. Ideally, at least three measurements points should be used in order to obtain a spatially-averaged estimate. The shaker was fed with broad-band random signal from the FFT analyser and the accelerometer was placed on the opposite face of the plate in line with the shaker contact point. Modal density estimates obtained following this procedure were similar to theoretical predictions (fig. 4.14).

Typical estimated point mobilities for both stiffened and non-stiffened cases are presented in figs. 4.13a,b. In the loss factor estimation only one excitation point and ten vibration velocity measurement points were employed. Nevertheless, the

loss factor results obtained were reasonably similar to the ones reported by Mohammed [45] for the same plate and test apparatus. The loss factor, modal density and modal overlap factor results obtained for the plate with and without stiffeners are shown in figs. 4.14 and 4.15. The results presented in these figures are for constant bands of 200 Hz and the modal overlap factor was estimated from the relation $M = \eta(f_c)n(f_c)f_c$ [45], where f_c is the band centre frequency, $n(f_c)$ is the modal density and $\eta(f_c)$ is the loss factor.

The results presented in fig. 4.15 are for the plate with the stiffener excited at only one point. As expected, the loss factor for the plate with the stiffener (fig. 4.15) is slightly higher than that for the plate without the stiffener (fig. 4.14). The stiffened plate theoretical modal density employed in the comparison was calculated as the sum of the modal density of a flat plate in flexural vibration and of a uniform beam in flexural vibration (equation (6.24), ref. [39]).

4.5.2 Results for the plate without a stiffener

The results for the correlation coefficient for the plate without a stiffener are presented in this section. Results from lines 5, 6 and 7 were used in this part of the work.

A common characteristic of the results from lines 5, 6 and 7 was that, above the 1000 Hz one-third octave band, all experimental results approached the theoretical results (given by equation (3.23) combined with parameters (B.4)). Figures 4.16 and 4.17 were included in order to illustrate this observation. As a matter of fact, it is clearly shown in fig. 4.17 that in each one-third octave band above 1250 Hz, the theoretical results on line B approach the experimental results. Reasons for this are two-fold. First, the number of modes that have resonance frequencies inside the 1250 Hz 1/3 octave band was estimated to be 14, which is higher (even if one assumes that 25 % of the modes are not excited due to shaker position) than the figure of eight modes suggested in the section 3.7.2 and ten as suggested by Stearn [53]. Second, from fig. 4.14 it is observed that above 1000 Hz the modal overlap factor is greater than unity.

As a means of checking the combined role of number of modes in the band and modal overlap factor in the applicability of the present approach on a practical situation, the results obtained on lines 6 and 7 were averaged in bands of 10 Hz, 40 Hz, 100 Hz and 400 Hz in regions of low and high modal overlap. Some of such results obtained at line 6 are shown in fig. 4.18. On one hand, it is observed that for regions in which the modal overlap factor is higher than unity, the frequency-averaged correlation coefficients are similar to the theoretical ones, even in a narrow band of only 10 Hz: the correlation characteristics are rather insensitive to frequency bandwidth. On the other hand, for frequencies regions in which the modal overlap factor is lower than unity, the frequency-averaged correlation coefficients are extremely dependent on the width of the frequency band. Results from other frequency bands show similar behaviour.

For the case of acoustically excited structures, Stearn [76] reported that the degree of modal overlap does not influence correlation coefficient results. This is another result that is not corroborated by the present work. With the purpose of double-checking the present observations, the frequency average was performed in bands of 10 Hz and 600 Hz for eight frequency bands whose centre frequencies were equally spaced. One group of frequencies was situated in a region of modal overlap factor lower than unity and the other group of frequencies was placed in a region of modal overlap factor higher than unity. A separation of 20 Hz was chosen for the centre frequencies to assure that the points from the line spectra used in the averaging process for the 10 Hz band were different in each consecutive band.

Results for the frequency region with low modal overlap are presented in fig. 4.19 for points placed along line 7. The modal overlap factor in this frequency region was estimated to be around 0.6 as shown in fig. 4.14. It is verified in fig. 4.19 that the 600 Hz result is always close to the theoretical estimate but the 10 Hz result varies considerably between each adjacent band. The 10 Hz-frequency-averaged results clearly exhibit modal behaviour, indicating that the modes in this frequency region are not overlapping (see figs. 4.13a and 4.21). If one examines a typical frequency response function of this plate (fig. 4.21), three clear resonance frequencies are observed in this frequency region: the first at around 330 Hz, the second at 400 Hz and the third at 440 Hz. This explains why the 10 Hz-frequency-averaged results at

centre frequencies 320 Hz and 340 Hz are so similar and at the same time why they are so different from results at centre frequencies 400 Hz or 460 Hz.

The modal overlap factor is a measure of the ratio between average modal bandwidth ($\eta\omega$) and average separation between resonance frequencies ($\delta\omega = 1/n(\omega)$, where $n(\omega)$ is the modal density). Modal half-power bandwidth is defined as the difference between the frequencies at which the mean-square modal response is half its maximum value (3 dB down). A modal overlap factor equal or higher than unity indicates that at least three natural modes contribute significantly to the system response in a single frequency. A high modal overlap also implies a smooth frequency response function in which individual resonance frequency peaks can not be distinguished. Such smooth behaviour are exemplified by the point mobility results above 3000 Hz presented in figs. 4.13a and 4.21.

Results for a frequency region in which the modal overlap factor is higher than unity is presented in fig. 4.20 for points placed along line 6. The modal overlap factor in this frequency region was estimated to be around 2.5. It is observed that, for frequency averages carried out in 10 Hz bandwidths, the results did not vary strongly between each adjacent band. Moreover, these results generally lie close to those averaged over 600 Hz bands (with the clear exception of centre frequency 3020 Hz) and as consequence are not far from the theoretical estimates. The small difference between the theoretical and the experimental results observed in fig. 4.20 are assumed to be related to the boundary conditions which are not perfectly clamped. It is not expected that such agreement would be improved if more points were used in the digital discretization of the response signals for the 10 Hz frequency-averaged results.

Frequency-averaged results of the normalised cross-power spectral density of acceleration obtained along line 7 are presented in fig. 4.22. As shown, a strong disagreement between experimental and theoretical results is observed at 200 Hz 1/3 octave band. Similar to what was observed for the correlation coefficient, experimental results for the normalised cross-power spectral density only approached theoretical results for frequencies above 1000 Hz. The main difference is that a disagreement between experiments and theory is much clearer in a presentation of normalised cross-power spectral density graph than in that of correlation coefficients.

From the results presented in this section we can state that:

- for cases of low modal overlap (M < 1) the theoretical model of correlation coefficient presented in Chapter 3 is only valid as a frequency-average estimate for bands in which at least 8 to 10 modes are excited,
- when the modal overlap factor is high (M > 1) the theoretical representation of correlation coefficients suggested in Chapter 3 can be used as a narrow band estimate for mechanically excited structures. The validity of such approach as a broadband estimate is only limited to the increase of importance of second order terms as the bandwidth increases (as discussed in section 3.4.2).
- The normalised cross-power spectral density of acceleration has a similar behaviour to that of the correlation coefficient and same conclusions reached for the correlation coefficient also apply to this parameter.

Further investigation is necessary to assess the reasons why the results presented by Stearn [76] did not change with the increase in the modal overlap. This investigation could form part of a more thorough study of the influence of different types of excitation on correlation coefficients as suggested in section 4.4.2.

4.5.3 Results for the plate with a steel bar (stiffener) attached

This section presents the experimental results of correlation coefficient on the clamped plate with the steel bar attached. In this investigation, only one side of the panel was directly excited (as illustrated in fig. 4.11). The influence of the steel bar on the plate vibrational field is illustrated by comparing figs. 4.13a and 4.13b. The frequency response function has changed and is now much more complex than the one for the unstiffened plate. As a matter of convenience the stiffened plate was represented by two separate plate subsystems. In this model the steel bar acts as a coupling element between the two sides of the plate, reflecting and transmitting the incident energy.

Some of the results obtained for points placed along lines 3, 4 and 5 are presented in fig. 4.23. The points used on these lines had similar distances to the nearest two edges and thus the theoretical model gave the same result for the three lines. As already explained, lines 3 and 5 were coincident, though line 5 indicates

measurements made on the plate without the stiffener and line 3 on the plate with the stiffener. Results for line 4 were for the panel with the steel bar attached. Above 1000 Hz, results for all three lines were similar (e.g. 1250 Hz results presented in fig. 4.23) while below 1000 Hz those results were quite different (e.g. 630 Hz results presented in fig. 4.23). As observed on the plate without the stiffener (section 4.5.2), the frequency-averaged experimental results approached the theoretical ones in one-third octave bands above 1250 Hz. This is a clear indication that, as predicted by our theoretical model, the influence of both clamped edges is dominant on the region in which lines 3 and 4 are situated. Moreover, this also shows that a perturbation placed outside a region one wavelength far from the measurement points will not affect the frequency-averaged correlation coefficient associated with these points. However, for points situated in a region less than one wavelength far from the perturbation (steel bar) the situation is quite different.

As presented in fig. 4.24, experimental results of correlation coefficient obtained on the right (line 1) and left (line 2) hand sides of the steel bar were dissimilar. In order to represent this situation the theoretical correlation coefficients were estimated on the basis of the two subsystems model. On the side in which the panel was directly excited, the correlation coefficients were calculated using the reflection and evanescent (reflection side) field component coefficients (Appendix C). On the indirectly excited side the transmission and evanescent (transmission side) field component coefficients (Appendix C) were used for points approaching the steel bar. These wave coefficients were transformed into Bolotin's edge effect method parameters using the equivalence equations presented in Appendix E. Near the other boundaries, parameters for a clamped edge were used.

In the region in which line 1 was situated the reflected and evanescent reflected field components were dominant and the theoretical model employed was able to predict the correlation coefficient with reasonable success on 1/3 octave bands above 1000 Hz. On the other hand, transmitted and transmitted evanescent field components were more important in the region in which line 2 was placed. Again, the theoretical model was able to predict such results with reasonable success. Below 1000 Hz, no agreement between the theoretical and experimental results was achieved. Some of the results obtained on lines 1 and 2 are presented in fig. 4.24.

For cases in which the experimental results were averaged in bands of varying width, the observations of the previous section were confirmed. For instance, in fig. 4.25 results for line 1 averaged in bands of 10 Hz, 40 Hz, 100 Hz and 400 Hz are presented. As shown for frequency regions in which the modal overlap is low, experimental results only approached the theoretical ones for the 400 Hz bandwidth. However, when the overlap factor is higher than unity, as for the 3300 Hz centre frequency, results for the four bandwidths analysed are coincident and they are also reasonably close to the theoretical results. Similar results were obtained for experimental results obtained on points along lines 3, 4 and 5 for averages carried out in the same bandwidths.

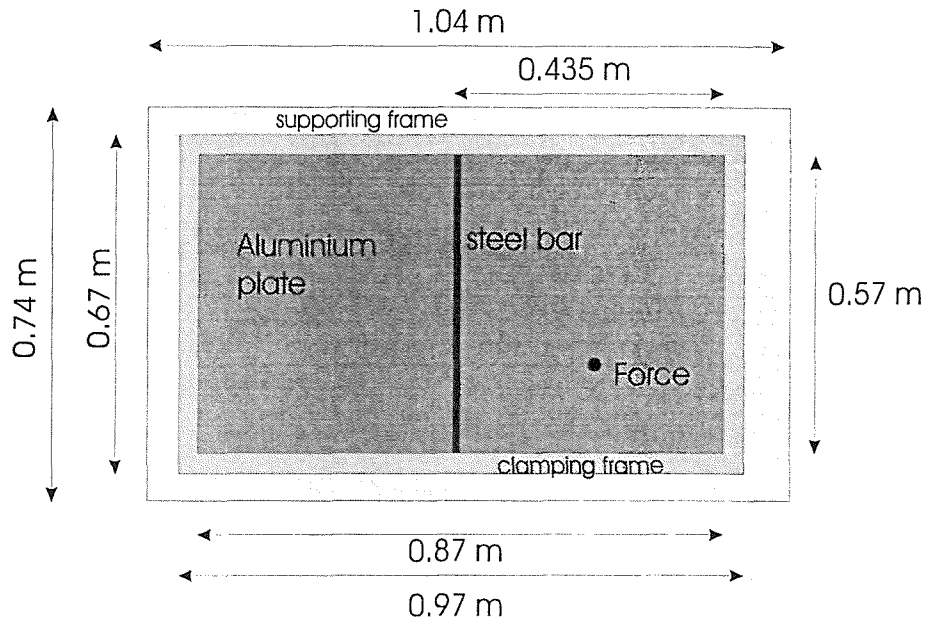

Fig. 4.10 - Sketch of rig with clamped plate and steel bar.

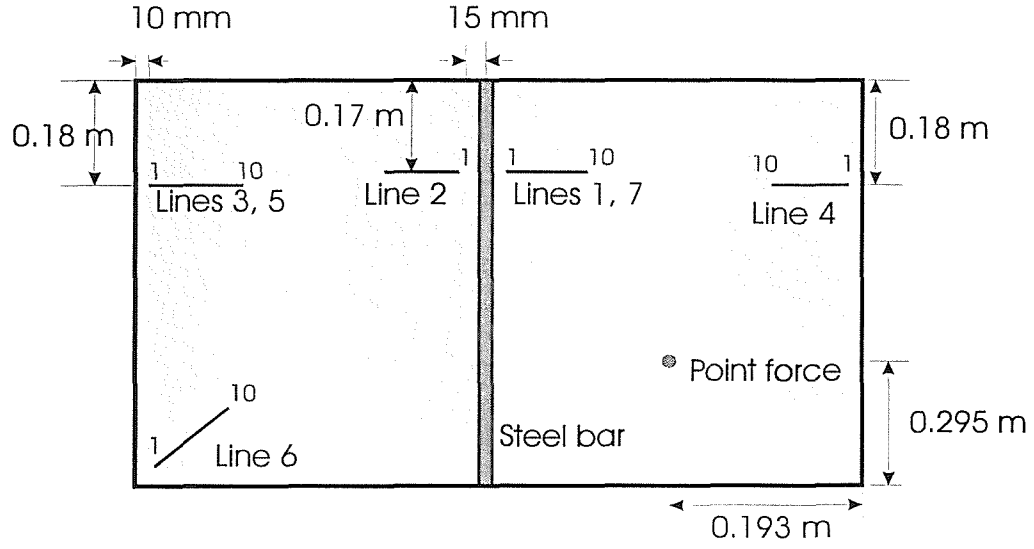

Fig. 4.11 - Position of measurement lines and excitation point on clamped plate with stiffener.

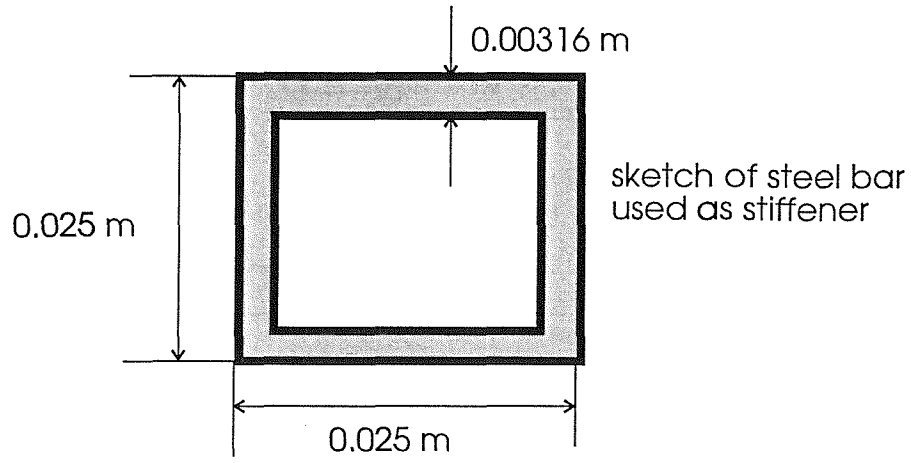

Fig.4.12 - Cross-section of steel bar used as stiffener

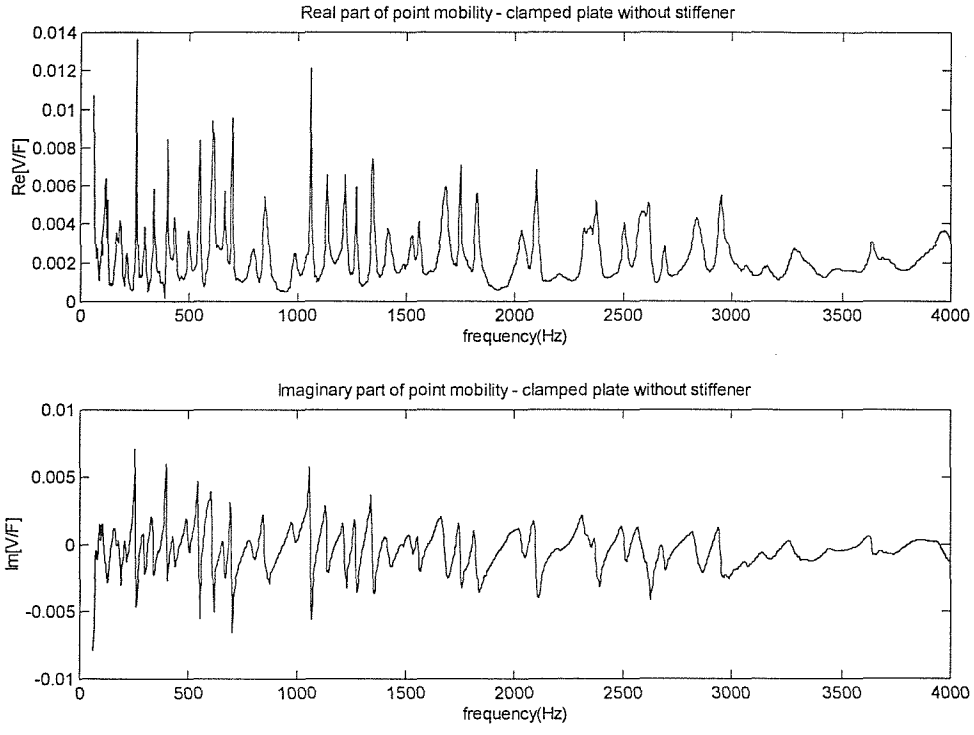

Fig. 4.13a - Real and imaginary parts of point mobility for clamped plate without stiffener.

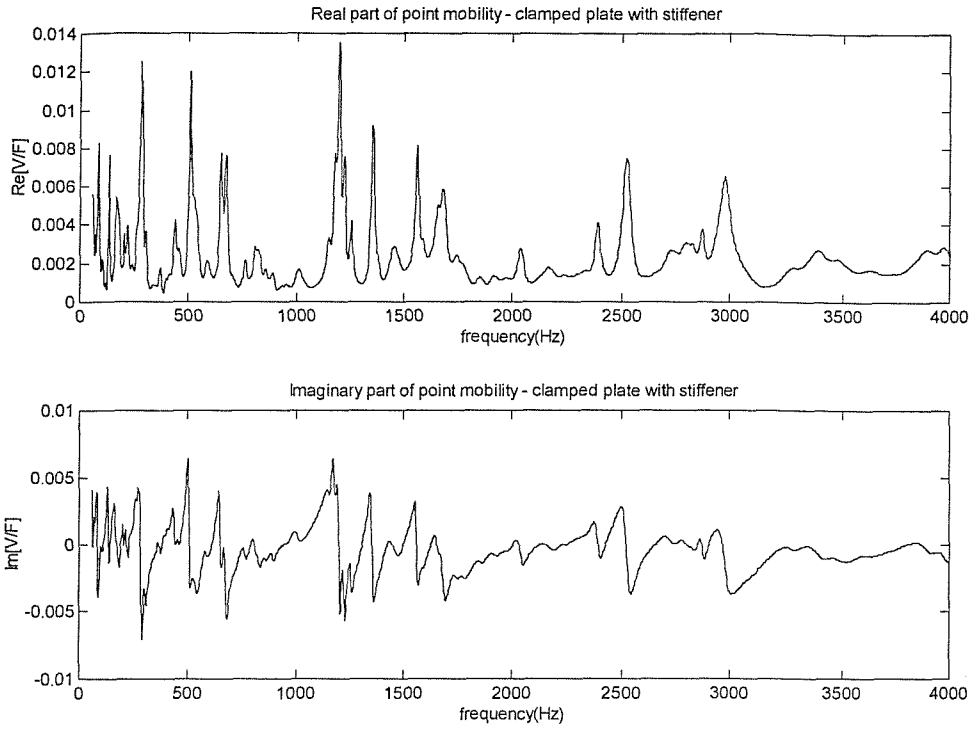

Fig. 4.13b - Real and imaginary parts of point mobility for clamped plate with stiffener.

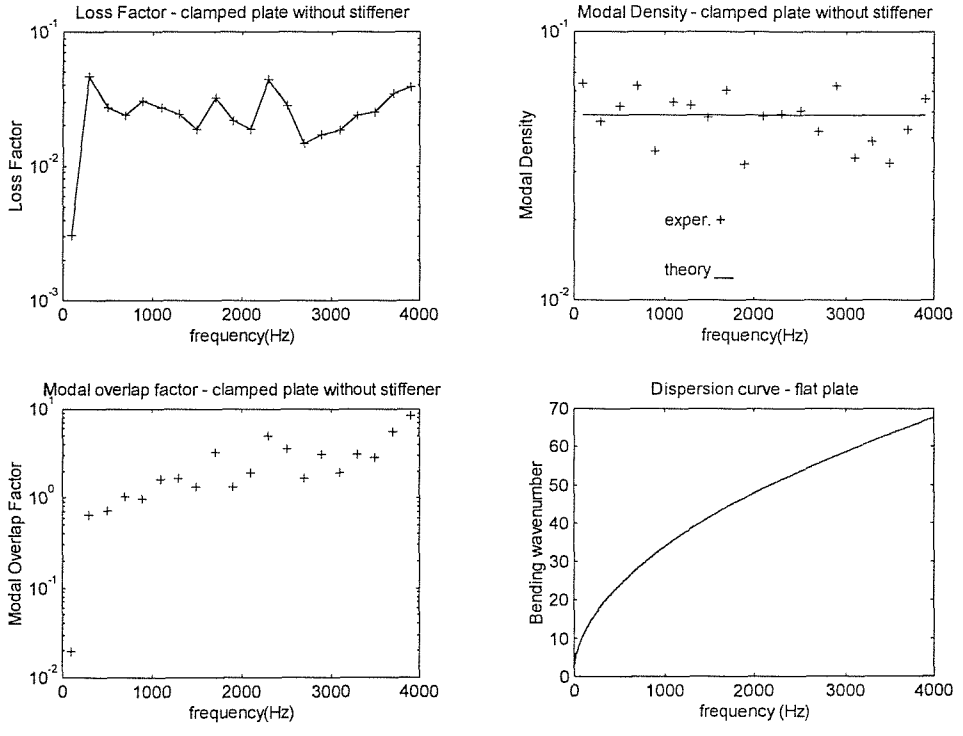

Fig. 4.14 - Loss factor, modal density and modal overlap factor experimental estimates on clamped plate (0.876 m x 0.576 m x 3.5 mm) without stiffener. Frequency bands of 200 Hz bandwidth.

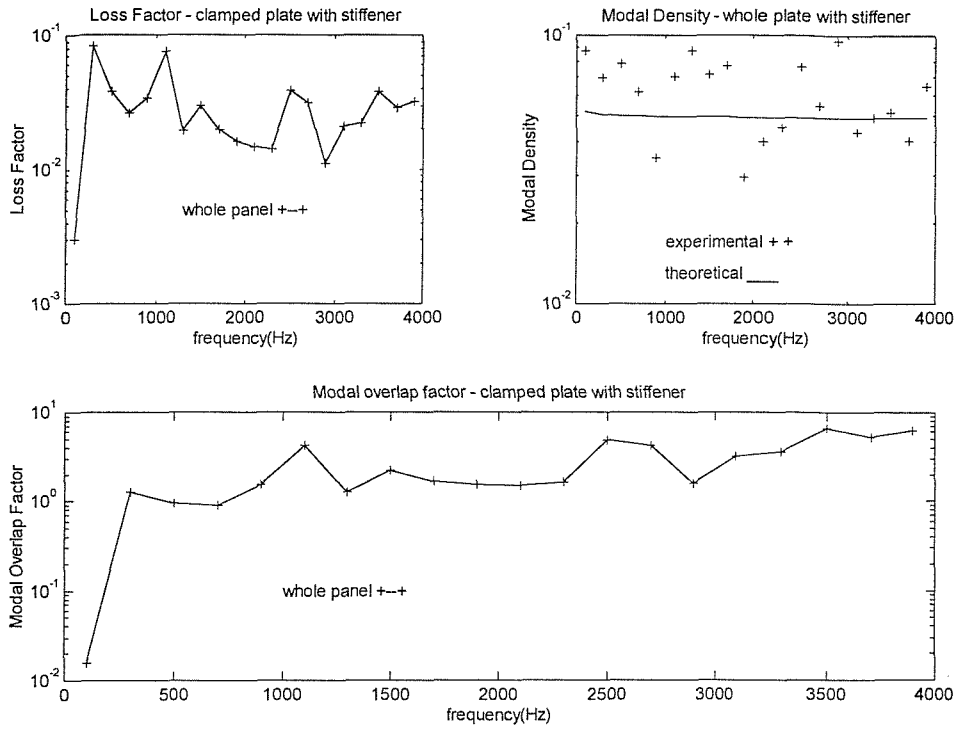

Fig. 4.15 - Experimental results of loss factor, modal density and modal overlap factor for clamped plate with stiffener. Constant bands of 200 Hz. +—+ results for whole panel (plate + steel bar).

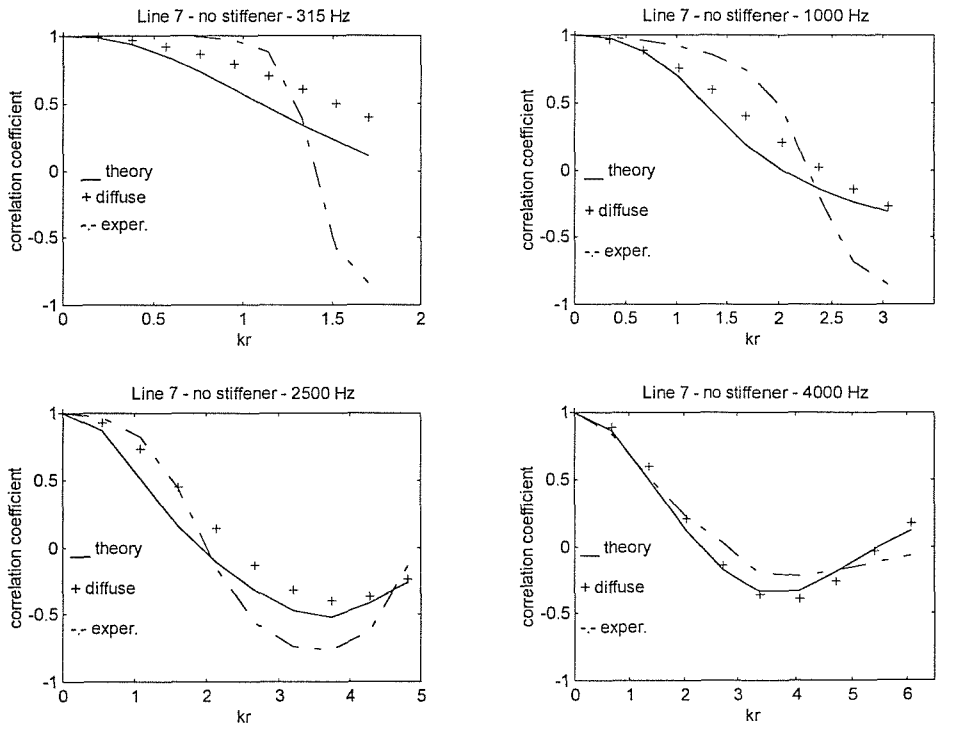

Fig. 4.16 - Comparison of theoretical results for a clamped plate (eq. (3.23)) with experimental results due to point mechanical excitation. Line 7. 1/3 Octave bands. ——— theory (clamped plate) (eq. (3.23)); – · – · – · – experimental results; + + diffuse bending wave field (eq. (3.18)).

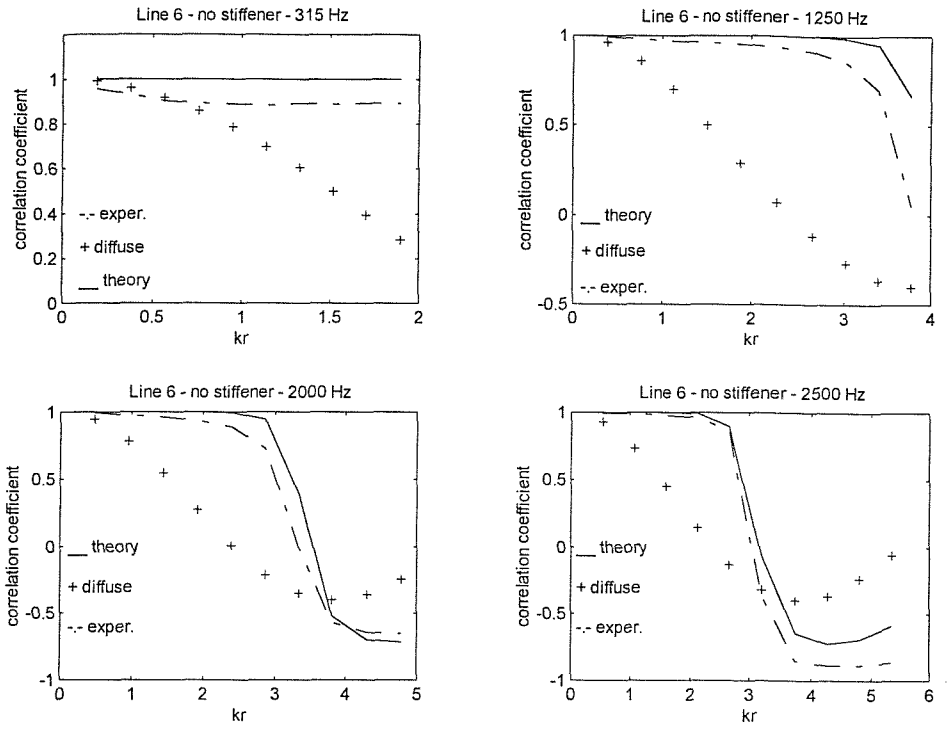

Fig. 4.17 - Comparison of theoretical results for a clamped plate (eq. (3.23)) with experimental results due to point mechanical excitation. Line 6. 1/3 Octave bands. ——— theory (clamped plate) (eq. (3.23)); – · – · – · – experimental results; + + diffuse bending wave field (eq. (3.18)).

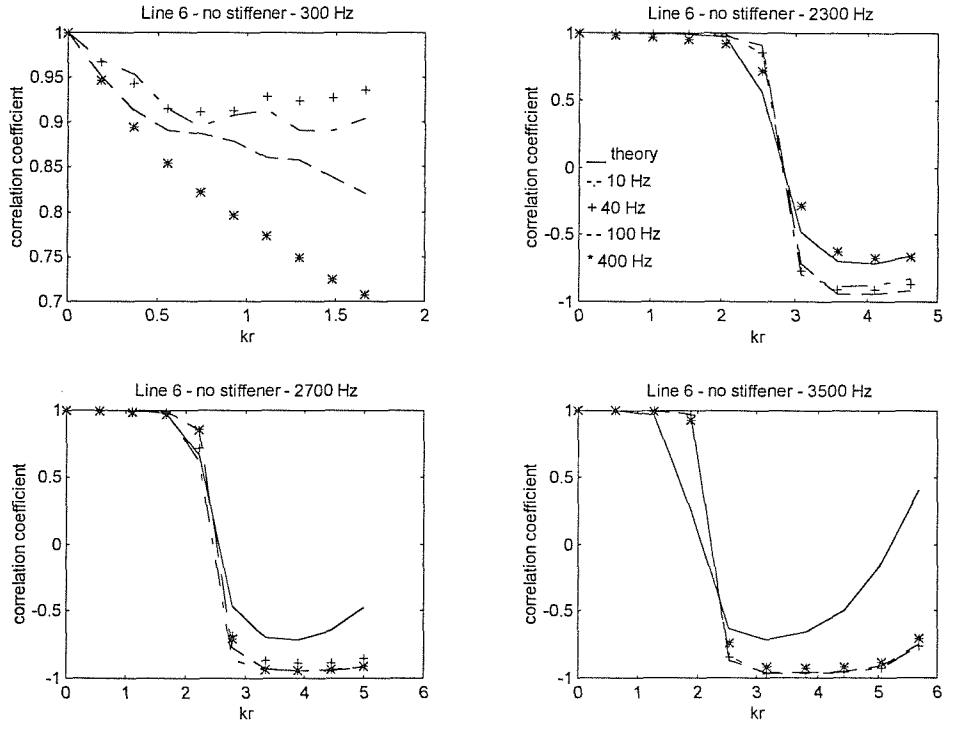

Fig. 4.18 - Frequency-averaged correlation coefficients along line 6. Experimental results due to point mechanical excitation averaged in bands of different widths: ——— theory (eq. (3.23)); – · – · – 10 Hz band; + + 40 Hz band; — — — 100 Hz band; * * 400 Hz band.

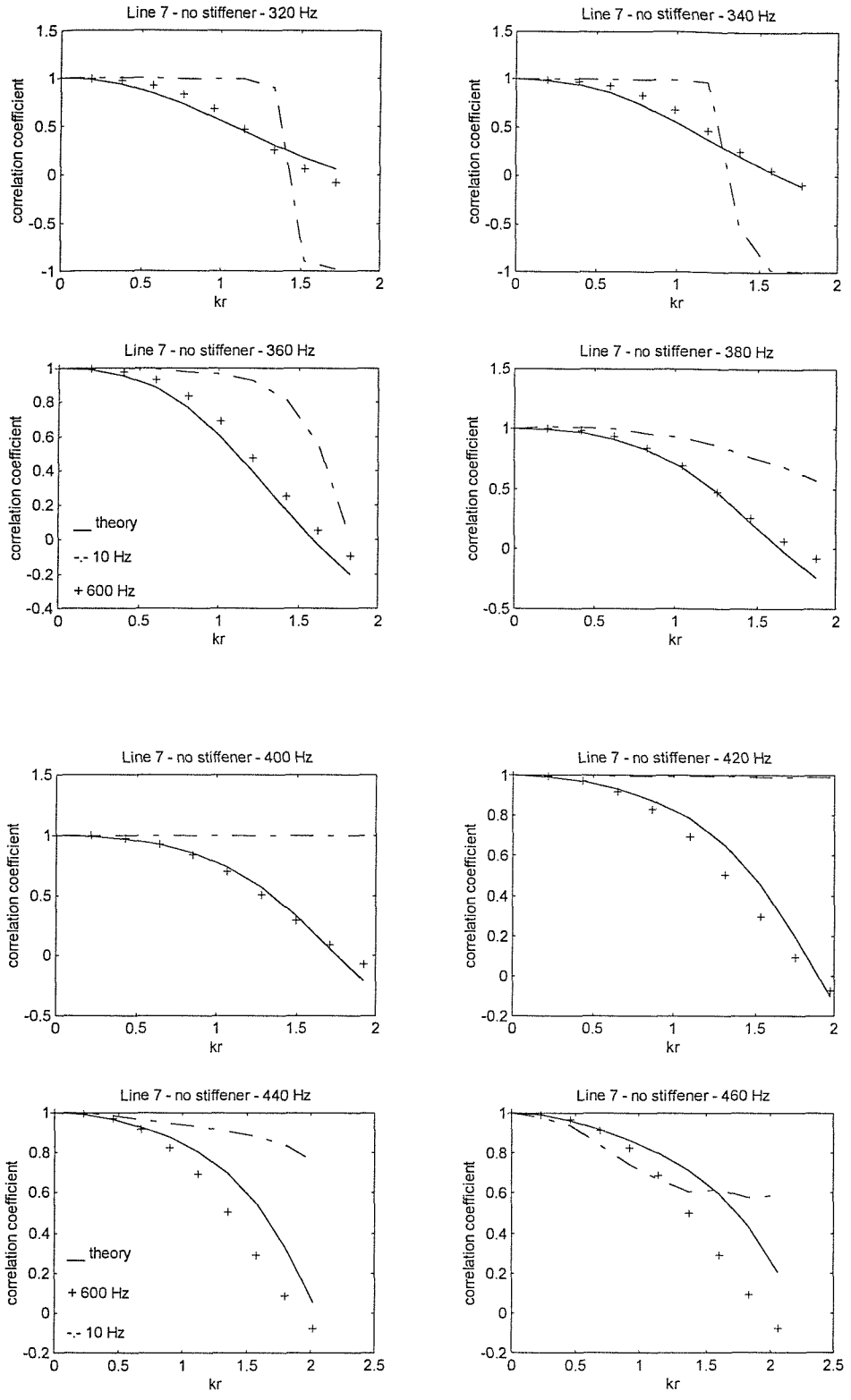

Fig. 4.19 - Frequency-averaged correlation coefficients along line 7. Experimental results due to point mechanical excitation averaged in bands of different widths. key: ——— theory (eq. (3.23)); – · – · – · – 10 Hz band; + + 600 Hz band. Modal overlap factor ≅ 0.6.

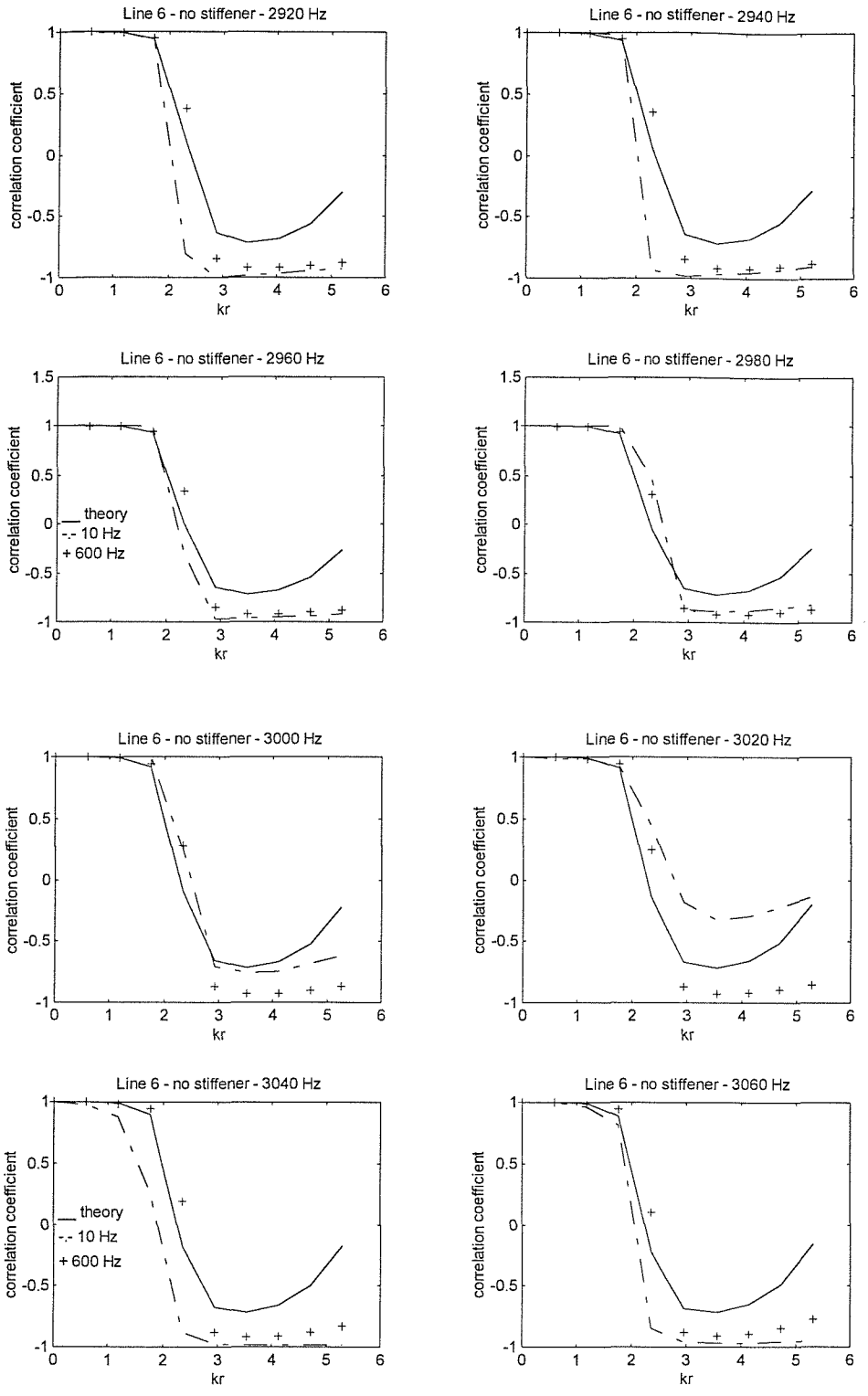

Fig. 4.20 - Frequency-averaged correlation coefficients along line 6. Experimental results due to point mechanical excitation averaged in bands of different widths. key: ——— theory (eq. (3.23)); – · – · – · – 10 Hz band; + + 600 Hz band. Modal overlap factor ≅ 2.5.

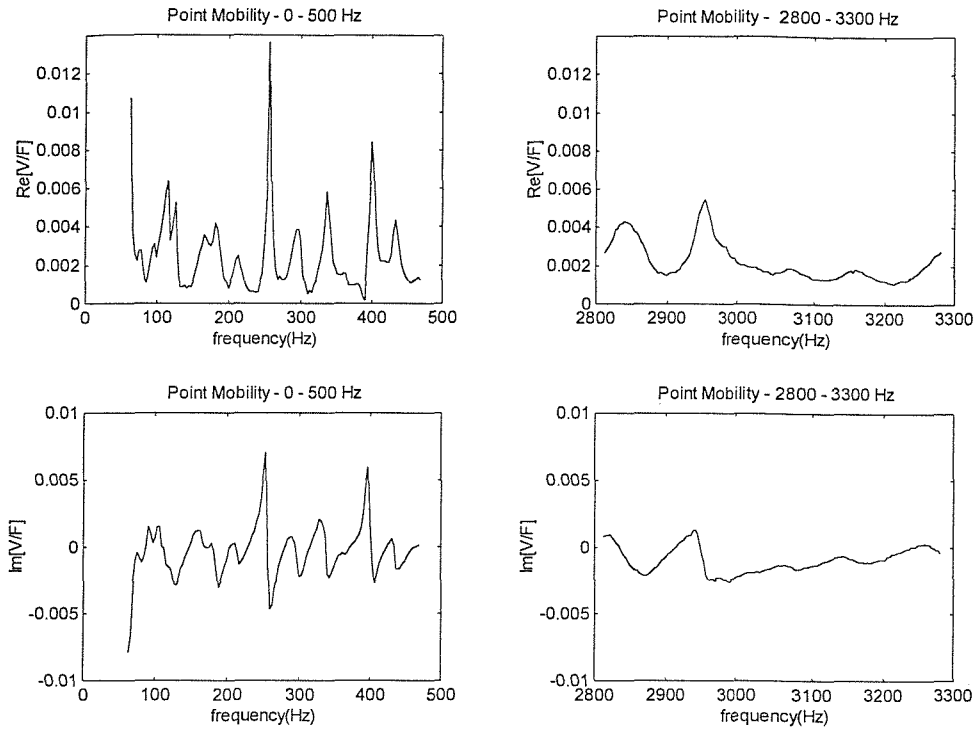

Fig. 4.21 - Frequency response functions (velocity/force) on clamped plate without stiffeners from 0 to 500 Hz and from 2800 to 3300 Hz. Plotted as real and imaginary parts.

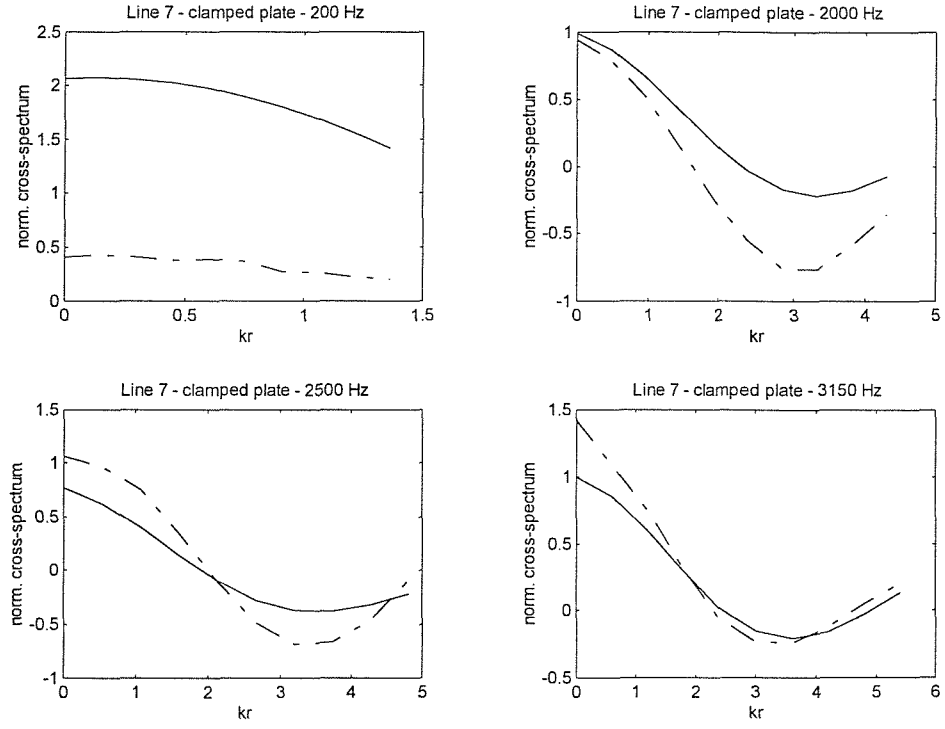

Fig. 4.22 - Frequency-averaged normalised cross-power spectral density of acceleration measured along line 7. Experimental results due to point mechanical excitation averaged in 1/3 octave bands. key: ——— theory (eq. (3.23')); – · – · – · – experimental results.

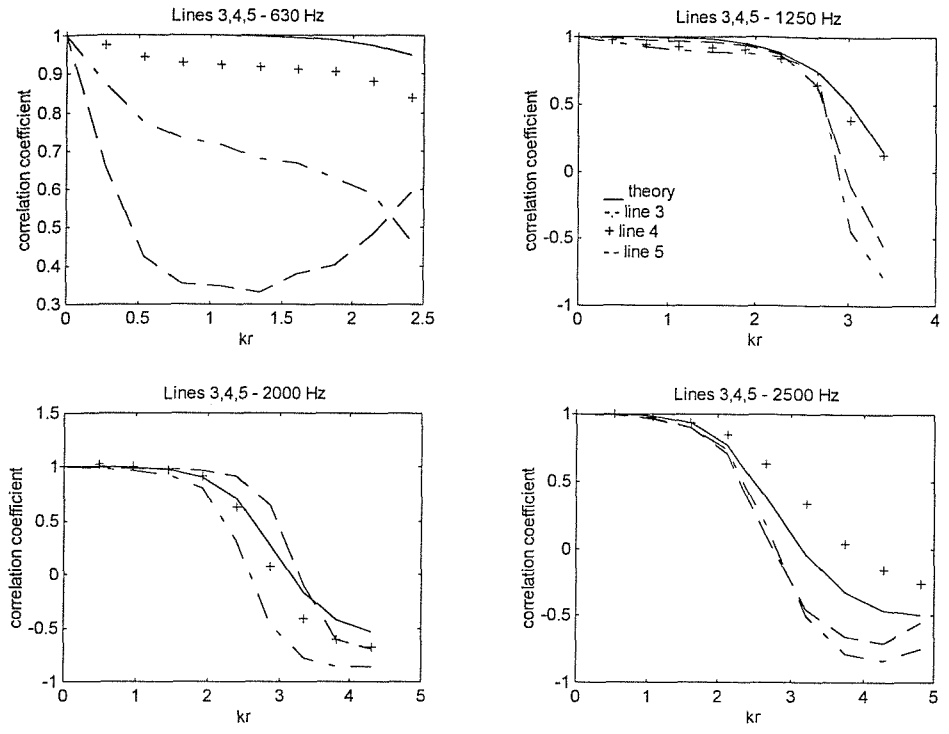

Fig. 4.23 - Frequency-averaged correlation coefficients on lines 3, 4 and 5. 1/3 Octave bands. Experimental results due to point mechanical excitation. ——— theory (eq. (3.23)); – · – · – · – line 3; + + line 4; — — — line 5;.

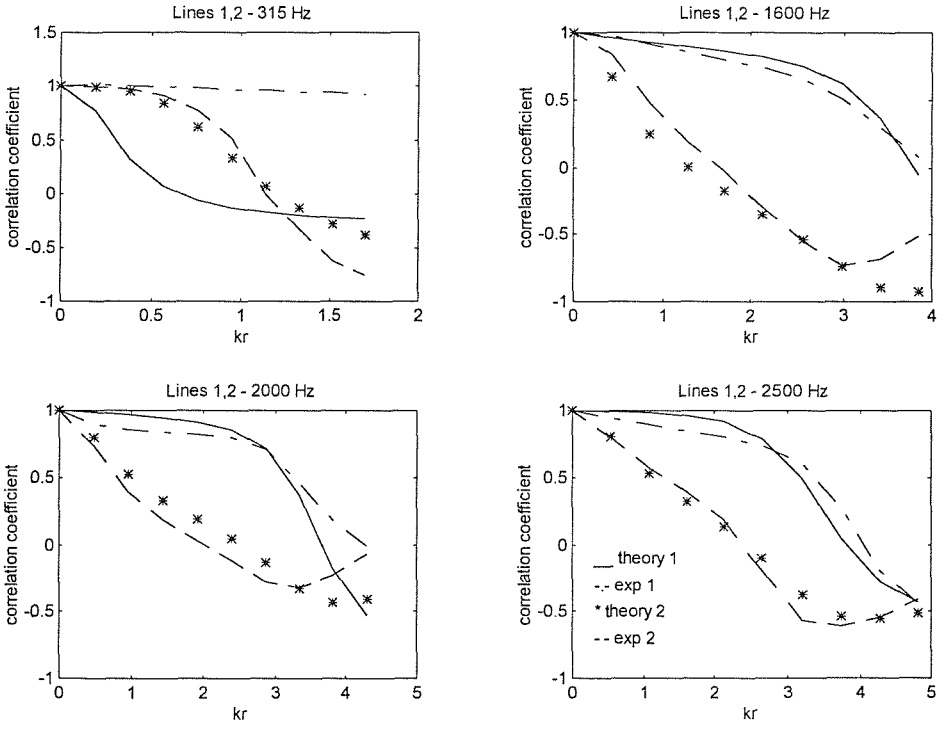

Fig. 4.24 - Frequency-averaged correlation coefficients on lines 1 and 2. 1/3 Octave bands. Point mechanical excitation on side in which line 1 is placed. line 1: ——— theory (eq. (3.23)); – · – · – · – experiments. line 2: * * theory (eq. (3.23)); — — — experiments.

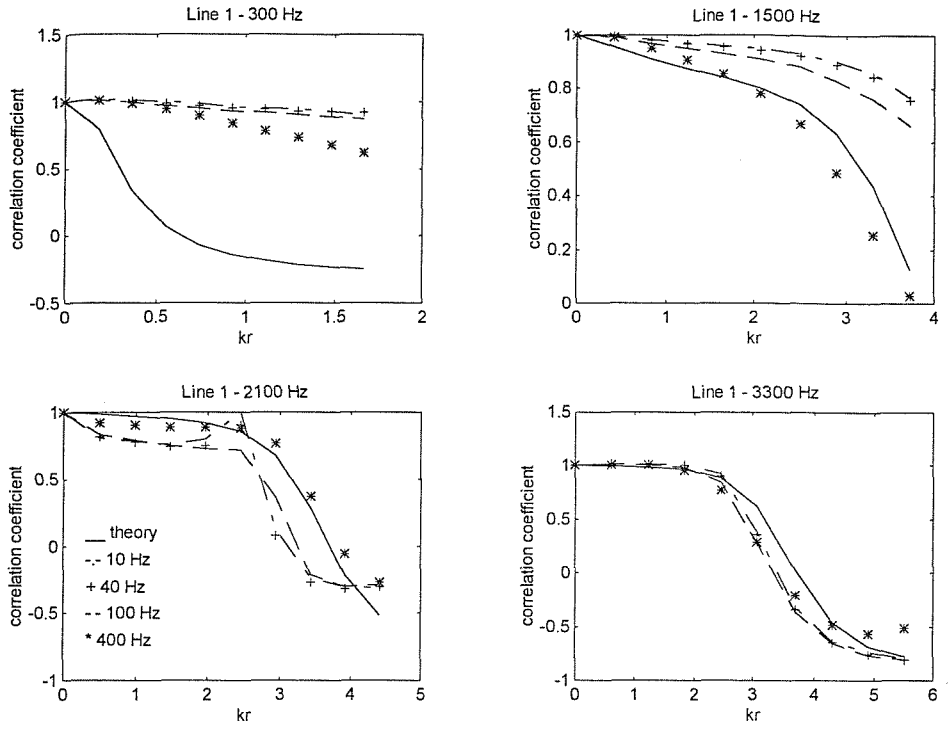

Fig. 4.25 - Frequency-averaged correlation coefficients on line 1. Experimental results due to point mechanical excitation averaged in bands of different widths: ——— theory (eq. (3.23)); – · – · – · – 10 Hz band; + + 40 Hz band; — — — 100 Hz band; * * 400 Hz band.

4.6 Rectangular flat plate with four free edges

4.6.1 Description of the apparatus

A flat aluminium plate of 2 mm thickness suspended by two thin wires from a steel frame was another structure used in the experimental investigation of frequency-averaged correlation coefficients. The plate was of rectangular geometry with sides of 0.50 m and 0.70 m length and it had free boundary conditions all along the edges. No damping material was placed on the plate. An sketch of the plate and rig used are shown in fig. 4.26. Typical bending wavelengths for this plate were: 0.442 m at 100 Hz, 0.167 m at 700 Hz, 0.14 m at 1000 Hz and 0.081 m at 3000 Hz. The plate was excited with broadband random excitation from 0 to 5000 Hz by a electrodynamic shaker (Ling Dynamic V101) at only one position (marked F on fig. 4.26).

The experimental procedure employed in this investigation is described in section 4.2. Acceleration signals were acquired in pair of points situated along lines 1, 2 and 3 as illustrated in fig. 4.26. The measurement points were placed along these lines in 1 cm steps. The first point of line 1 was placed just 5 mm from the edge while the first point of line 2 was situated 10 mm from the plate corner.

Bolotin's dynamic edge effect method results were used as theoretical estimates of the correlation coefficients. As usual the procedure suggested in section 3.4.2 was combined with parameters presented in Appendix B (equations (B.5) to (B.7)) and the coefficients calculated from the numerical integration of equation (3.23). Needless to say, similar results were obtained when free wave theoretical results were used instead (equation (3.41) combined with reflection and evanescent wave coefficients from Appendix C). In Appendix E, a small difference in the results from direct (Appendix B) and indirect (Appendix C combined with expressions presented in Appendix E) derivations of the parameters C_x and C_y was reported. Both expressions, B.7 and E.25, were then used in the theoretical values calculated for line 1. As shown in fig. 4.28, both values of correlation coefficients are very similar indicating that the small difference in the C_x and C_y expressions is negligible.

In view of the low damping of this plate the modal overlap was low within the frequency range analysed. The estimated modal density for this plate was 0.056 modes/Hz and the average dissipation loss factor was assumed to be around 0.001 [80]. Thus, typical values of modal overlap factor were: 0.005 at 100 Hz, 0.03 at 600 Hz, 0.05 at 1000 Hz and 0.22 at 4000 Hz. An illustration of a typical frequency response function (point inertance at the excitation point) is presented in fig. 4.27 and it is observed that most of the resonance peaks do not overlap within the 0 to 4000 Hz range. Therefore, the experimental results were only expected to agree with theoretical ones for frequency bands with width greater than 200 Hz, as more than ten modes are estimated to be excited in this bandwidth.

4.6.2 Discussion of results

The aim of this part of the investigation was to check the theoretical results for boundary conditions other than simply-supported, clamped or spring supported. With the addition of the free boundary condition we could cover all boundary conditions encountered in practice. A free edge boundary condition is not directly relevant to practical studies of internal radiation; however it can give a lower limit of sound pressure levels inside the enclosure that can be achieved by modifying the structure boundary conditions. This type of control has been discussed by Cheng and Nicolas [33] and it is further analysed in Chapter 5.

Experimental results obtained on lines 1, 2 and 3 and that were averaged in 1/3 octave bands agreed with theoretical results above the 800 Hz 1/3 octave band. This is in accordance with the observation made at the end of section 4.5.2 as the bandwidth of the 800 Hz 1/3 octave band is 183 Hz and ten modes were predicted to be excited at this frequency band. In addition, good agreement was also observed for lines 1 and 2 on some frequency bands below 800 Hz.

In particular, results for line 2 agreed with the theory on all frequency bands analysed and the agreement was exceptionally good above, and including, 250 Hz. Such good agreement near the corner was rather surprising as the Bolotin's dynamic edge effect method parameters presented in Appendix B and the reflection and transmission coefficients presented in Appendix C were derived assuming that

only one edge is important to the edge solution and the other three edges do not affect this solution. This is a standard assumption of Bolotin's dynamic edge effect method [56] and it is the type of consideration normally associated with the derivation of reflection coefficients on flexural wave motion [82]. Nevertheless, the agreement observed on line 2 together with the results obtained for line C on the simply-supported plate (section 3.7) demonstrates that the frequency-averaged correlation model here presented is a valid approximation even near the corner of a structure.

A selection of one-third octave band results obtained on lines 1, 2 and 3 is presented in figs. 4.28, 4.29 and 4.30. As mentioned, reasonable agreement with the theory has been observed on some frequency bands below 800 Hz. This agreement was more pronounced for points approaching the edges (line 1) and the corners (line 2) even when less than 4 modes are estimated to be excited in one frequency band (e.g. 250 Hz, 1/3 octave band). This is probably due to the interference of the waves near the edges. Hence, as the vibration field near the edges dominates the acoustic radiation (as discussed in Chapter 5) reasonable results are expected to be obtained with the hybrid model even when a small number of structural modes are excited in a frequency band. On the other hand, for points far from the edges (in terms of wavelength) the suggestion (sections 3.7, 4.5 and ref. [53]) that eight to ten modes need to be excited in a frequency band for the validity of the present model is also applicable to the case of free edges.

Correlation coefficients frequency averaged in narrow bands were not expected to agree with theoretical results due to the vibration field low modal overlap. This was confirmed by the computation of frequency-averaged results in bands of varying width. The only exception were results on line 2 as most of the narrow band results (10 Hz and 40 Hz) were also similar to results in wider bands (100 Hz and 400 Hz). An example of this agreement on line 1 is presented in fig. 4.31 for bands with centre frequency 300 Hz. The strong interference near the corner appears to be the explanation for this agreement. On the other lines, only results that were frequency averaged in 400 Hz bandwidths approached the theoretical results.

Experimental results of the real part of the normalised cross-power spectral density obtained along line 2 also agreed with the theoretical results for most of the 1/3 octave bands above 160 Hz. As shown in fig. 4.32, the agreement was good

till the last frequency band analysed, 4000 Hz, and it confirms our previous conclusion that all observations that are valid for the correlation coefficient are also valid for the normalised cross-power spectral density. A slightly disagreement was only observed when kr is equal to zero indicating that the present theory will overpredict the results when either the wavenumber or the separation distance between the two points is very small. However, this disagreement could also have been caused by experimental circumstances. This is related to the fact that the distance between the accelerometers in the first measurement position is not zero but equals the diameter of the accelerometer as both were placed one beside the other in this measurement position.

All the 18 one-third octave bands analysed (80 Hz - 4000 Hz) are included in fig. 4.32 in order to illustrate how experimental and theoretical results compare. As shown, there is a spread between good and bad agreement in different frequency bands. In general, in this chapter, when we suggest there is a good agreement between experimental and theoretical results it is because more than fifty percent of all bands in a frequency region present good matching between experimental and theoretical results. Due to space limitations, it was difficult to include all frequency bands analysed for each of the lines studied in the different plates used in the experimental investigation. As a result, only four bands are chosen for each line in order to illustrate the main points discussed.

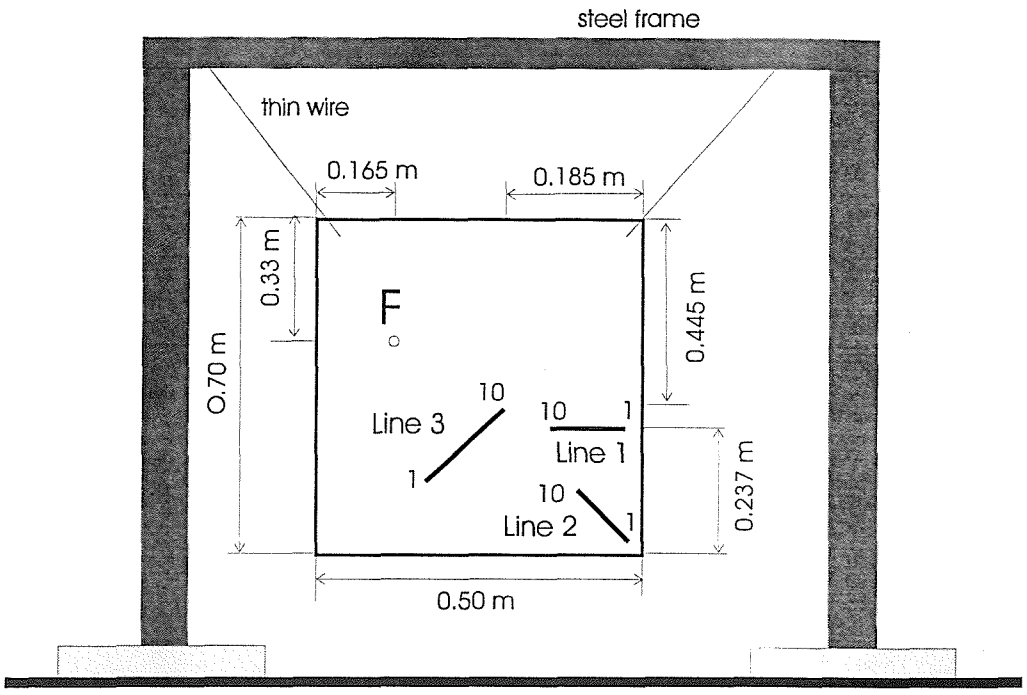

Fig. 4.26 - Sketch of experimental rig and lines used on free rectangular plate

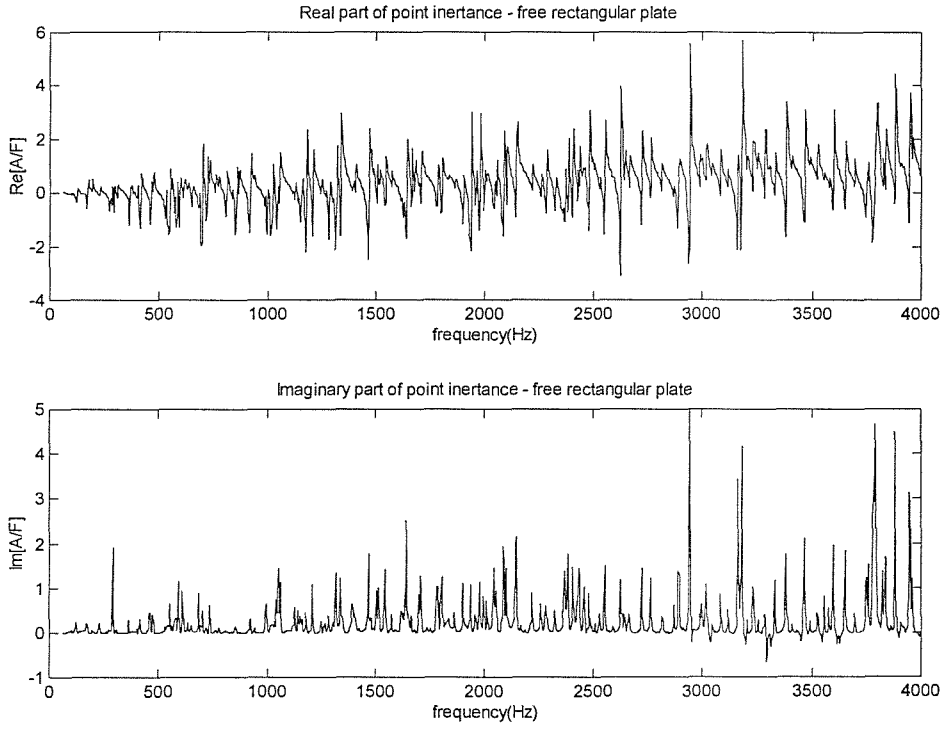

Fig. 4.27 - Frequency response function of aluminium plate with free edges. Point Inertance.

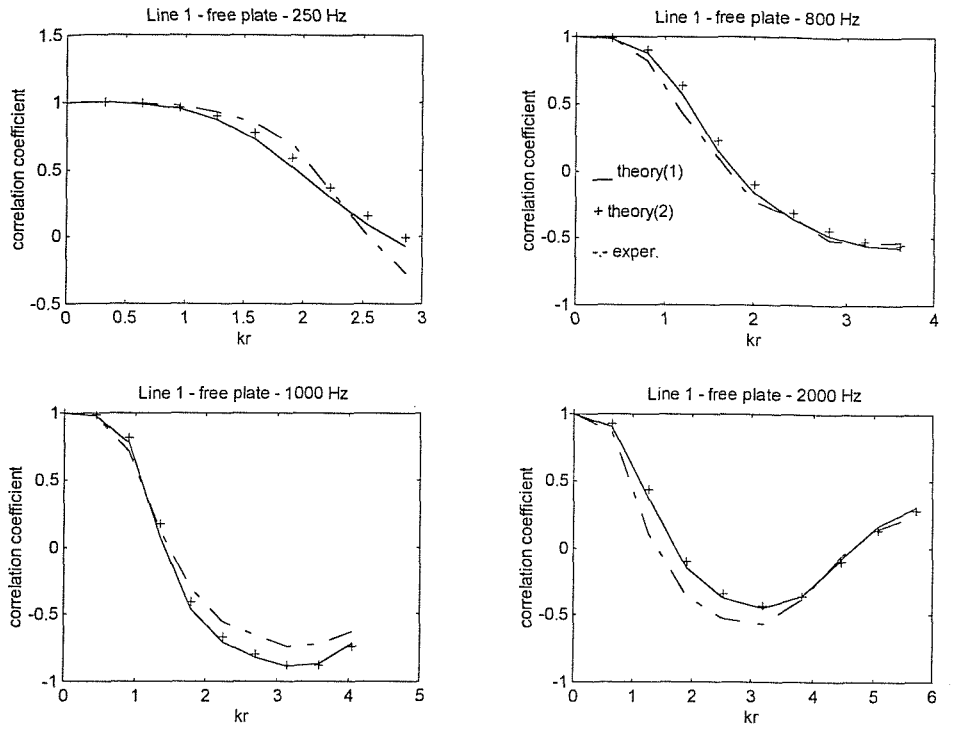

Fig. 4.28 - Frequency-averaged correlation coefficient results along line 1 on free rectangular plate. 1/3 octave bands. Experimental results due to point mechanical excitation. ——— theoretical results using free edge parameters from direct derivation (Appendix B,(B.7)); + + theoretical results using free edge parameters from indirect derivation (Appendix E (E.25)); – · – · – · – experimental results.

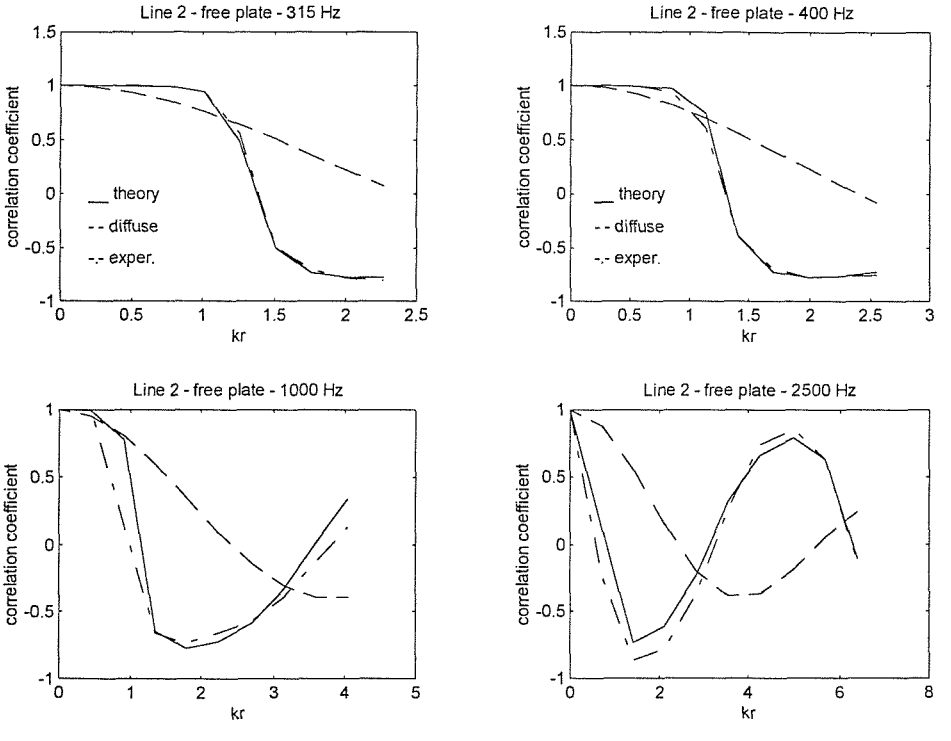

Fig. 4.29 - Frequency-averaged correlation coefficient results along line 2 on free rectangular plate. 1/3 octave bands. Experimental results due to point mechanical excitation. ——— theoretical results (eq. (3.23)); — — — diffuse bending wave field (eq. (3.18)); – · – · – · – experimental results.

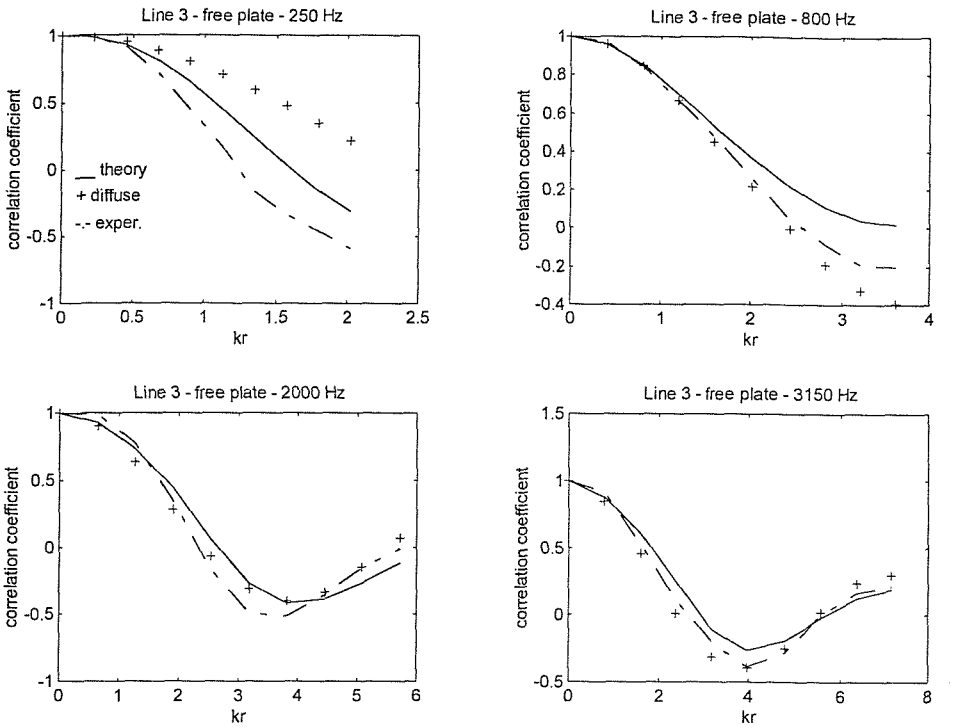

Fig. 4.30 - Frequency-averaged correlation coefficient results along line 3 on free rectangular plate. 1/3 octave bands. Experimental results due to point mechanical excitation. ——— theoretical results (eq. (3.23)); – · – · – · – experimental results; + + + diffuse bending wave field result (eq. (3.18)).

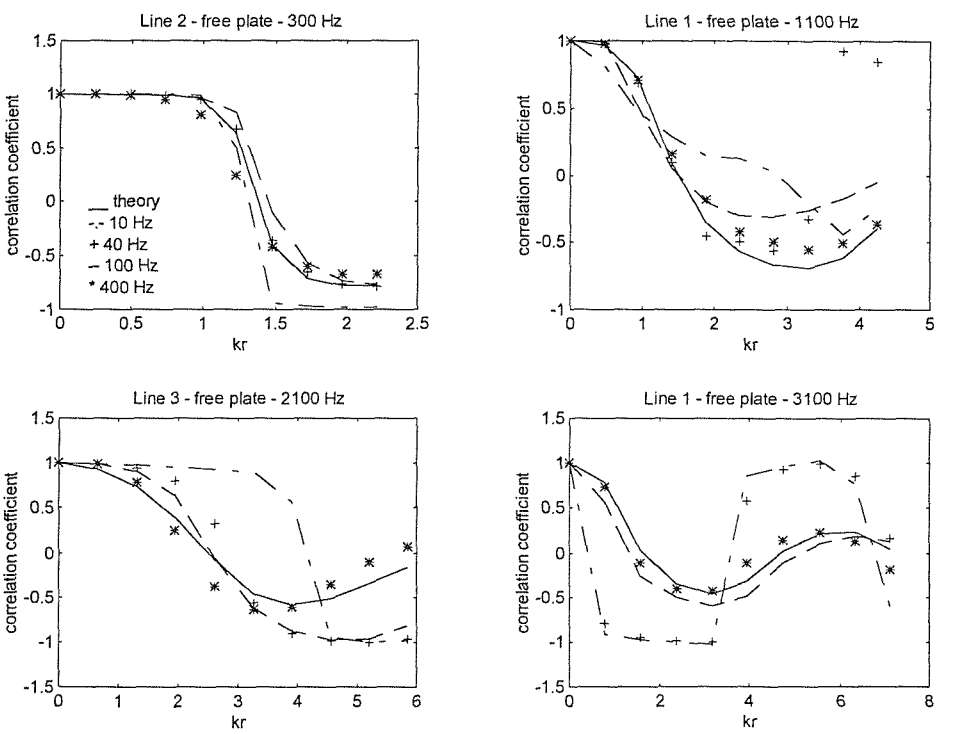

Fig. 4.31 - Frequency-averaged correlation coefficient results along lines 1, 2, 3 on free rectangular plate. Experimental results due to point mechanical excitation on bands of varying width. key: ——— theory (eq. (3.23));; – · – · – · – 10 Hz; + + + 40 Hz; — — — 100 Hz; * * 400 Hz.

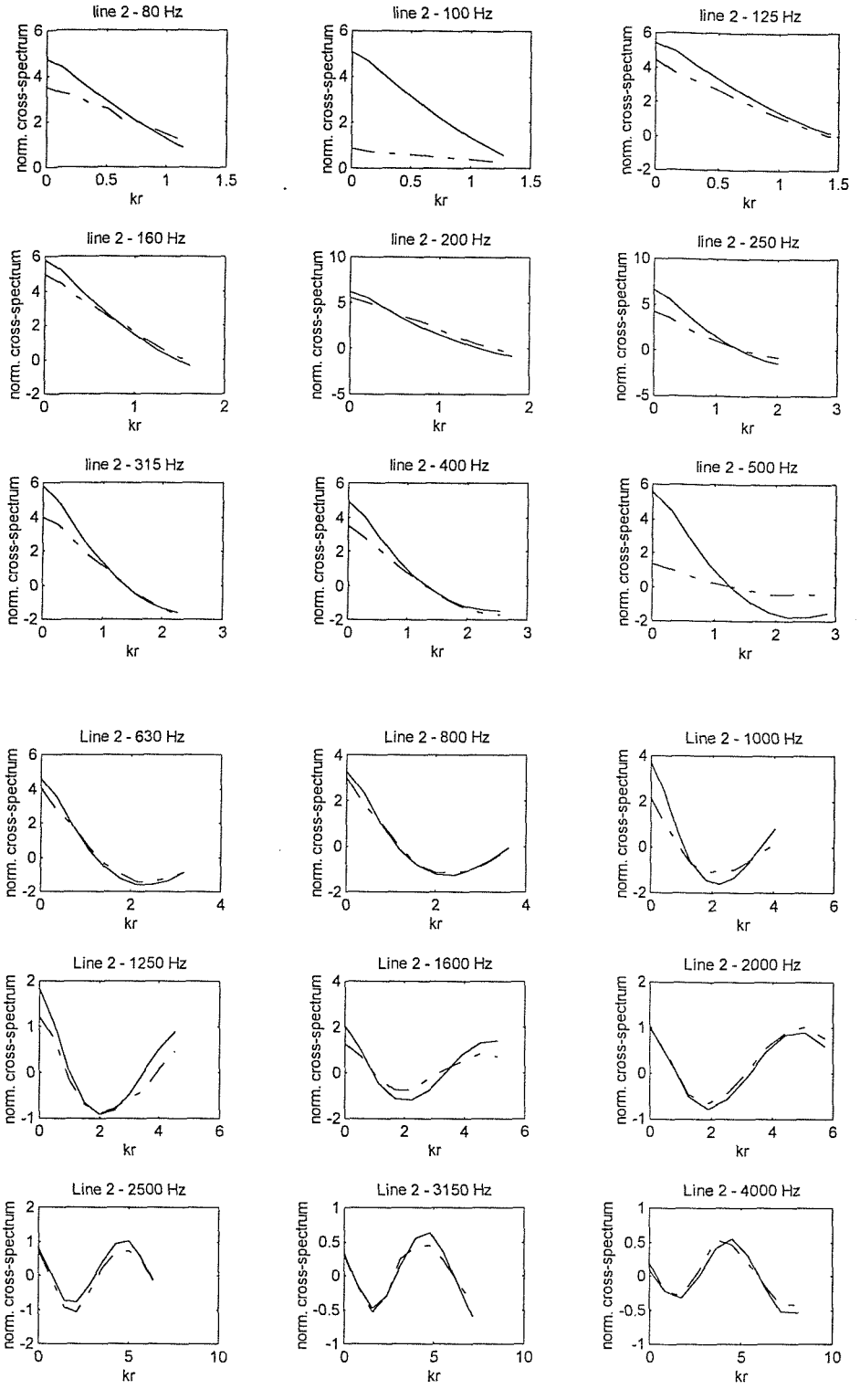

Fig. 4.32 - Frequency-averaged real part of the normalised cross-power spectral density along line 2 on free rectangular plate. 1/3 octave bands. Experimental results due to point mechanical excitation. ——— theoretical results (eq. (3.23)); – · – · – · – experimental results.

4.7 Two irregularly shaped coupled plates

4.7.1 Description of the apparatus

This part of the experimental investigation was carried out on two coupled steel plates of same thickness (3 mm), irregular shapes, identical material properties and with free edges. These plates were coupled by means of ten thick steel straps that were attached to the plates by heavy bolts. Some damping material was added to the plates. The plate system was suspended from a steel frame by a hook. The dimensions and particulars of this rig are described in ref. [83] and only a sketch of this rig is here presented (fig. 4.33). Typical wavelengths for both plates were: 0.544 m at 100 Hz, 0.181 m at 900 Hz, 0.14 m at 1500 Hz and 0.086 m at 4000 Hz.

Experimentally obtained estimates of loss factor and modal overlap factor for both plates are presented in fig. 4.34. These loss factors were estimated using a power injection technique in which coupling loss factors were also obtained (ref. [84]). Hence these individual loss factors do not include energy transferred to the other plate. The theoretical modal density for the upper plate was estimated to be 0.0656 modes/Hz and for the bottom plate was 0.0926 modes/Hz (results obtained from ref. [84]).

The experimental procedure employed in this investigation is described in section 4.2. Broad-band random was the forcing function used to excite the upper plate through a non-contact magnet and coil shaker. Only one excitation point was used, marked 'Force' on fig. 4.33. Acceleration signals were acquired at points situated along line 1 on the upper plate and along lines 2, 3 and 4 on the lower plate.

The experimental results were compared to theoretical estimates obtained with the Bolotin's dynamic edge effect method. The procedure suggested in section 3.4.2 was combined with parameters presented in Appendix B (equations (B.5) to (B.7)) and the coefficients calculated using numerical integration. These theoretical expressions are only applicable to rectangular regions. They are here compared to experimental results from odd-shaped plates in order to assess how much odd-shaped results depart from the ideal rectangular plate results.

4.7.2 Discussion of results

From the experimental results obtained on the upper and lower plates and averaged in 1/3 octave bands it was observed that they only approached the theoretical results in 1/3 octave bands above 500 Hz. The exception for this were results for line 4 that were close to theoretical ones for all 1/3 octave bands above 250 Hz. Though, as shown in figs. 4.35 and 4.36, the agreement between theoretical and experimental results is only reasonable for lines 1, 2 but relatively good for line 4. In particular, the disagreement was more pronounced for points situated along line 3 (fig. 4.36) as this line was placed very close to a non-rectangular corner. The main reason for this difference is the irregular geometry of both plates as the derivation of frequency-averaged correlation coefficients presented in Chapter 3 presupposes that the plates have perpendicular edges. Hence, the theoretical results here employed are only an approximation of the real correlation coefficients of plates of irregular geometry. The inclusion of non-perpendicular corners on the theoretical derivation presented in Chapter 3 can be achieved by including the angle between the corners in the geometrical analysis. This is left as a suggestion for future work.

The good agreement with the theory observed for experimental results obtained at line 4 when only six modes were predicted to be excited (315 Hz 1/3 octave band) is probably due to the type of excitation applied to the lower plate (fig. 4.36). In this plate the excitation was applied almost uniformly through the straps along one of its edges. Such type of excitation can excite all the modes of the plate in comparison with the point excitation that will not excite modes that have nodal lines that pass through the excitation point.

Some of the experimental results obtained on lines 1 and 2 are shown in fig. 4.35. The measurement points used on these lines were situated at same distances from the nearest edge. In both lines the fixed accelerometer was placed 5 mm from one of the edges (that had free boundary conditions) and 30 cm from the other edge. For line 1 the correct boundary condition of the non-free edge would be given by the reflection properties of the straps coupling. These properties would be based on equivalent translational and rotational stiffness as employed in the theoretical results for lines 1 and 2 presented in section 4.5.3.

Based on the observations made in section 4.5.3, we can suggest that in view of the relative value between a typical bending wavelength above 800 Hz (less than 0.2 m) and the distance to the straps coupling (0.305 m) only the inner solution of Bolotin's edge effect method obtained for this edge will contribute to line 1 theoretical results. As for different boundary conditions this inner solution gets similar the farther the points depart from the edges (in terms of wavelength), the use of free boundary condition for this other edge is a reasonable approximation. In addition, if fewer straps were used to couple both plates, the boundary conditions would approach free edges due to a decrease in the edge translational and rotational stiffness.

Consequently, free edges were assumed in the estimation of theoretical values of correlation coefficients for lines 1 and 2 and these values were coincident. Even considering that both plates had different geometries and the type of excitation applied was not the same it was observed that the experimental results on lines 1 and 2 were reasonably similar and not much different from the theoretical ones (fig. 4.35).

Results obtained on bands of varying width confirmed the conclusions presented at the end of section 4.5.2. Because of the low modal overlap of both plates along the frequency analysed (as presented in fig. 4.34) only results for the wider bands approached the theoretical results. The small difference observed between results for bands of 400 Hz widths and the theoretical ones were due to the plate irregular geometry. Nevertheless, as shown in fig. 4.37, results on line 4 agreed with the theoretical ones as this line was situated reasonably far from all edges.

It was also verified that theoretical results for points situated far from the edges approached the diffuse bending wave field ones as the frequency increased. Another observation was that the agreement between the 400 Hz bandwidth and the theoretical results on line 2 improved with frequency. Similar observation applies to results in narrower bands that approached the 400 Hz bandwidth results as the frequency increased. The reason for the former is the decrease in the bending wavelength that makes the non-perpendicular corner influence less important along line 2 while the reason for the latter is the increase in the plates' modal overlap factor.

The relative values between the real and imaginary parts of the normalised cross-power spectral density and between the correlation coefficient and the quadrature density coefficient (as defined in section 3.3) were also investigated in

this work. In figure 4.38, experimental results for the correlation coefficient and for the quadrature density coefficient (estimated from the imaginary part of the cross-spectrum) at lines 1 and 2 that were averaged in 1/3 octave bands are presented. It was observed that for these two lines the quadrature coefficient was close to zero for all 1/3 octave bands below 2500 Hz. Similar situation was verified for results obtained at lines 3 and 4. If one carefully examines the equations that define the cross-spectrum of acceleration of randomly excited structures expanded into its normal modes one verifies that the imaginary part of this function is controlled by the cross-coupling between the normal modes. For undamped systems this imaginary part is zero, however when damping is taken into account this imaginary part will be controlled by the modes average bandwidth ($\eta\omega$) and by the average separation between them (δf). As already discussed in this chapter, these two parameters define the modal overlap factor of a structure. Therefore, one can conclude that as the modes start to overlap the value of the quadrature density coefficient will approach the value of the correlation coefficient (estimated from the real part of the cross-spectrum). This is exactly what was observed in this investigation. When the modal overlap factor was close to one, the values of the quadrature density coefficient were of same order as the correlation coefficient values (3150 Hz 1/3 octave band, fig. 4.38). Similar observations apply to the normalised cross-power spectral density.

The imaginary part of the normalised cross-power spectral density was neglected in the equations presented in Chapter 2 as it only affects the cross-coupling coefficient (equation (2.14)), which for cases of lightly damped and well separated acoustic modes was assumed to be negligible. However, for cases of external acoustic radiation and for plates that radiate into modally-dense damped acoustic spaces, the cross coupling coefficient may play an important part in the estimation of the nearfield radiated pressure. As a result, the extension of this work to the analysis of external radiation as proposed by Fahy [81], who assumed that the imaginary part can be neglected, will lead to reliable results for cases of structural systems with low modal overlap. For systems with high modal overlap further studies must be carried out in other to assess the extent of the error caused by the neglection of the cross-coupling coefficient.

Notes:

1) Dimensions in mm;

2) Plate thickness = 3 mm;

3) Drawing not to scale.

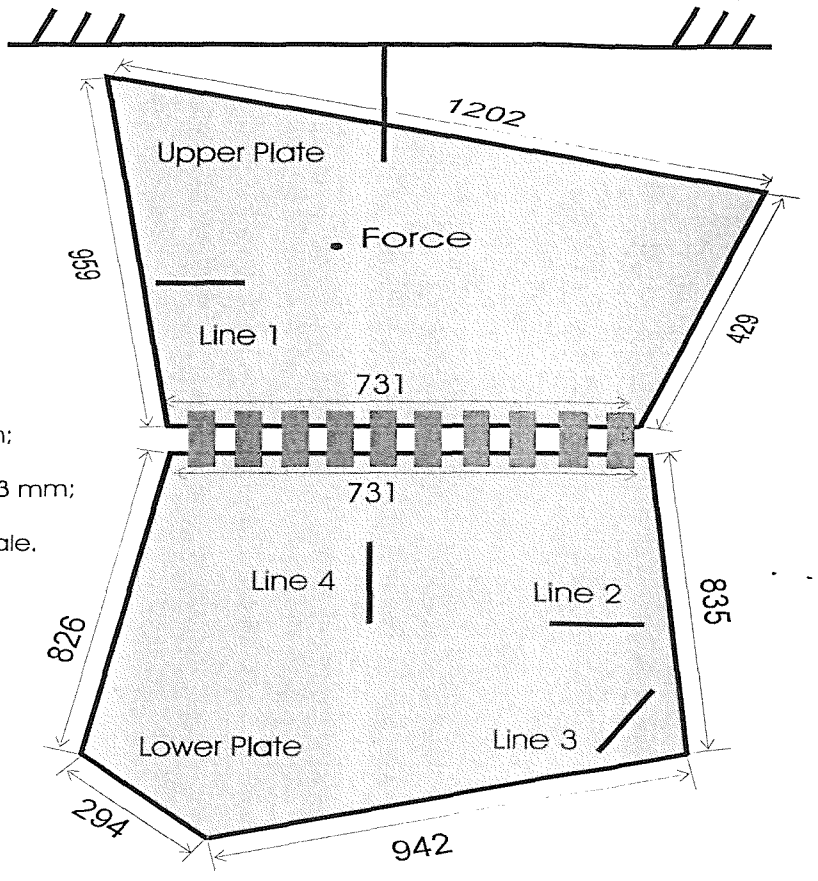

Fig. 4.33 - Sketch of measurement lines used and dimensions of coupled plates.

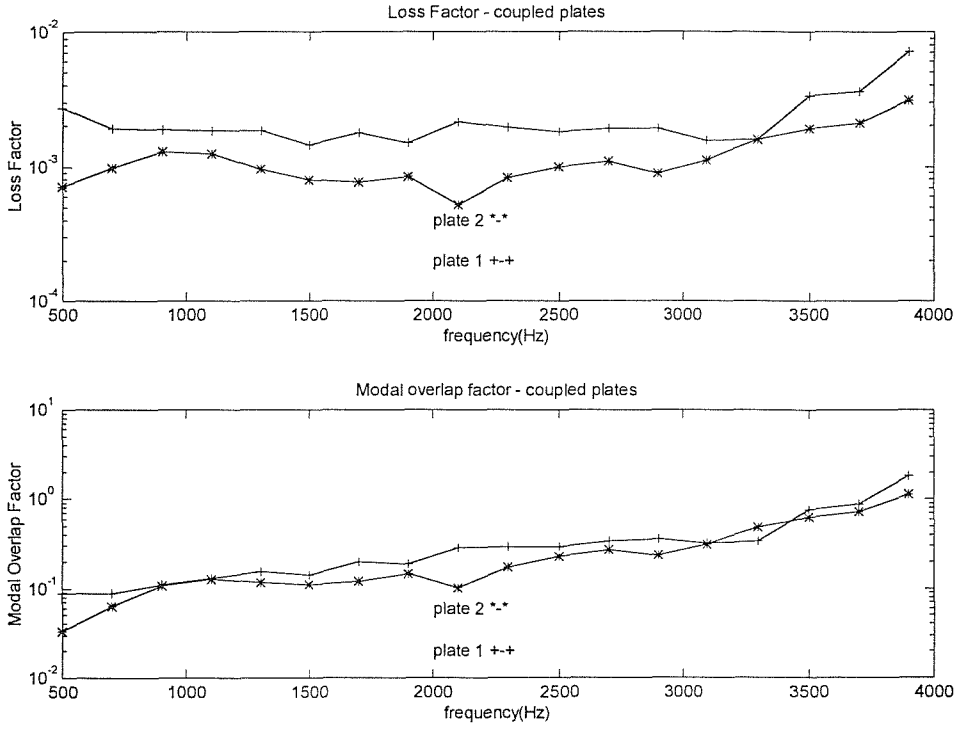

Fig. 4.34 - Loss and modal overlap factors for coupled irregular shaped plates. Constant bands of 200 Hz. +—+ upper plate (plate 1), *—* lower plate (plate 2). [84]

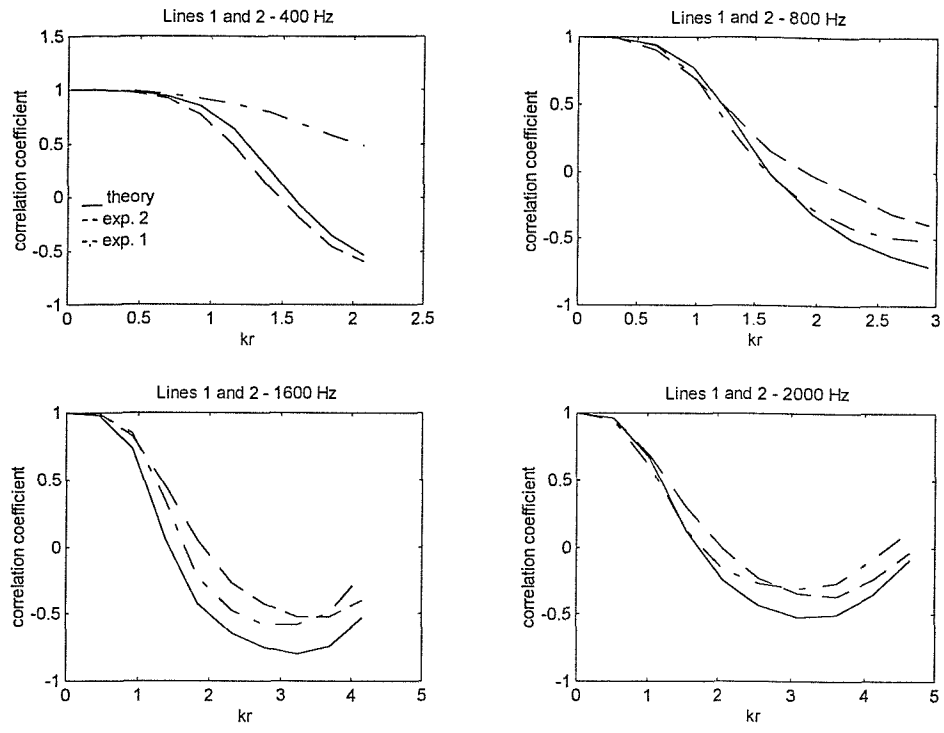

Fig. 4.35 - Experimental results of correlation coefficient averaged in 1/3 octave bands. Point excitation applied in plate in which line 1 is placed. ——— theoretical results (eq. (3.23)); – · – · – · – experimental results along line 1; — — — experimental results along line 2.

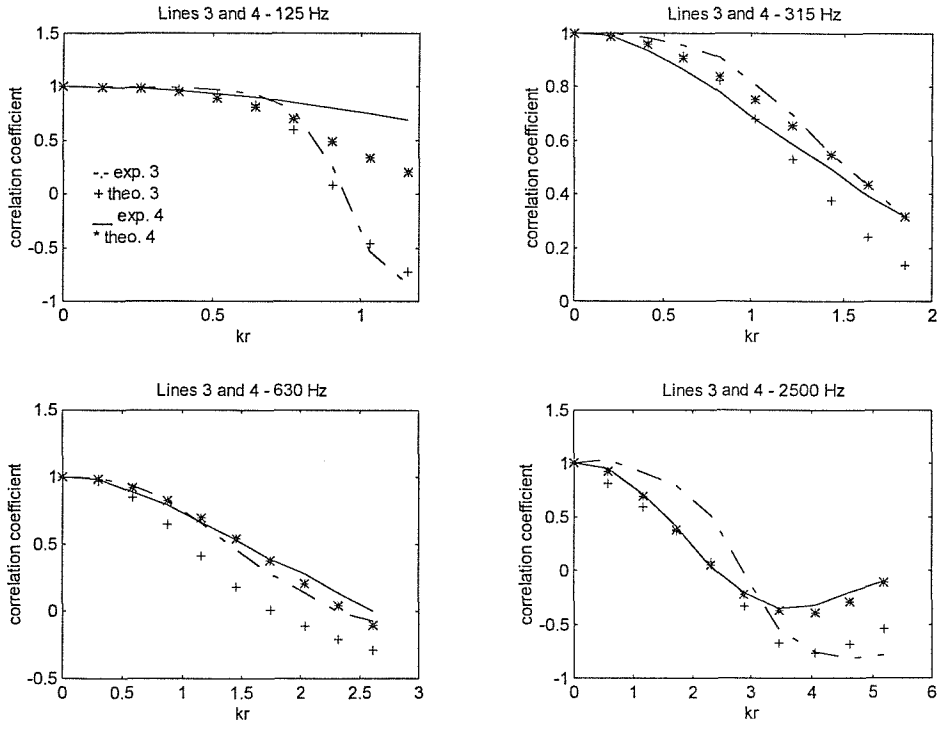

Fig. 4.36 - Experimental results of correlation coefficient averaged in 1/3 octave bands. Lines placed on lower plate and mechanical excitation applied to upper plate. Line 3: – · – · – · – experimental results, + + theory (eq. (3.23)). Line 4: ——— experimental results, * * theory (eq. (3.23)).

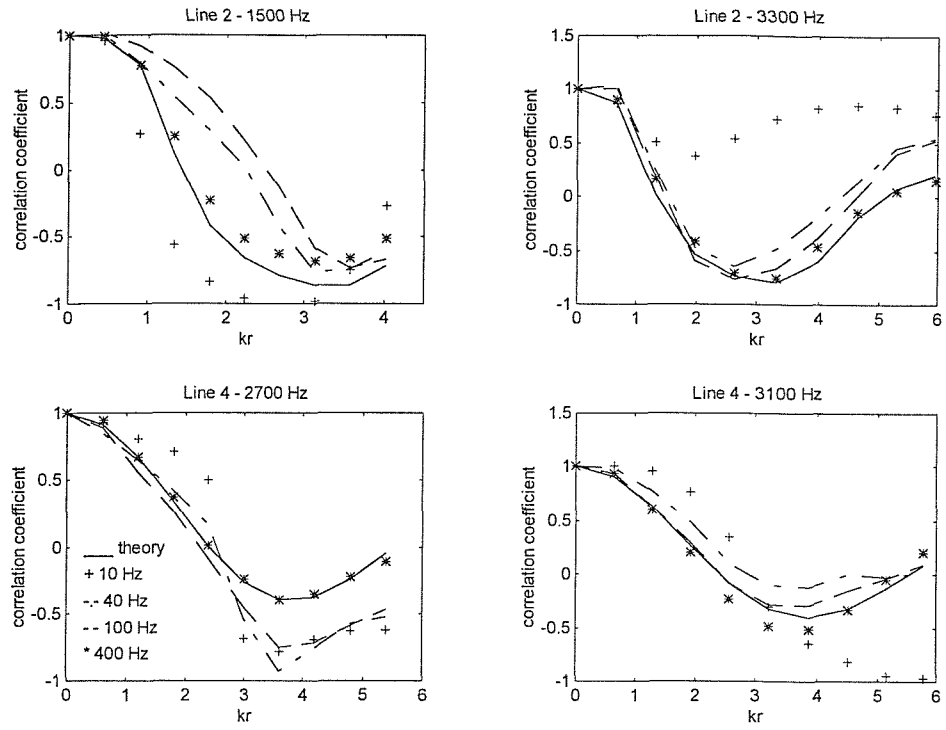

Fig. 4.37 - Experimental results of correlation coefficient averaged on bands of varying width. Point excitation applied on upper plate and lines 2 and 4 situated on lower plate. ——— theoretical results (eq. (3.23)), bandwidths: + + 10 Hz, – · – · – · – 40 Hz, — — — 100 Hz, * * 400 Hz.

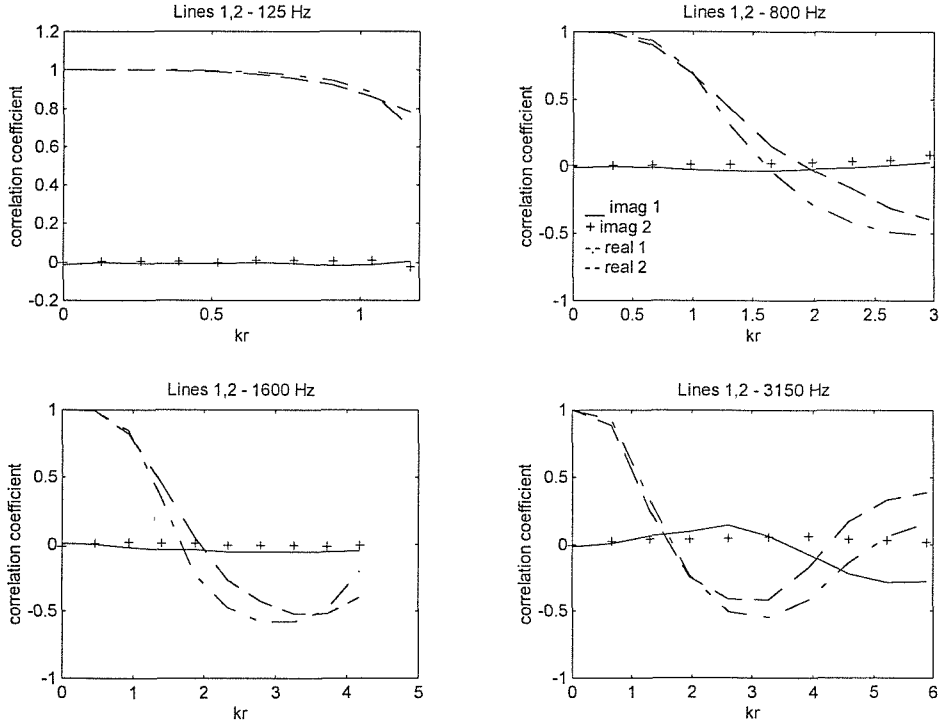

Fig. 4.38 - Correlation coefficient and quadrature density coefficient of acceleration averaged in 1/3 octave bands. Point excitation applied to plate in which line 1 is placed. Line 1: – · – · – · – correlation, ——— quadrature. Line 2: — — — correlation, + + quadrature.

4.8 Roof and windscreen of a passenger car

In refs. [54,78] results of measurements of vibration field correlation carried out at different parts of a car body shell are reported. Such results indicate that even when a large number of modes are excited in a frequency band a diffuse field is not necessarily set up in a two-dimensional plane structure. In part, the results of that investigation motivated the development of the approach presented in Chapter 3, as a means of representing vibration field correlation for different boundary conditions. Thus, in what follows, a comparison between some of those experimental results and the model suggested in Chapter 3 is presented.

4.8.1 Experimental procedure and description of the apparatus

Vibration field correlation measurements, identical to the ones reported in the previous sections, were made on the body of a Nissan Bluebird passenger car which was parked inside a laboratory room measuring 8 m x 5 m x 3 m. Three sources of random excitation were used: (i) that of a reverberant sound field set up by acoustically exciting the laboratory room with white noise; (ii) that of a sound field set up by acoustically exciting the car interior with white noise; and (iii) that set up by mechanically exciting the car offside lateral pillar.

Two lightweight accelerometers (Bruel & Kjaer 4374) were placed along different lines on certain parts of the car body. Results for four lines on the roof (shown in fig. 4.39) and two on the windscreen (shown in fig. 4.39) are here included. Results at other lines along the car body were also obtained and presented in ref. [54]. In each set of measurements one accelerometer was held at the beginning of the line (marked 1 in fig. 4.39) and the other displaced from it along the line at eight equally spaced points. The spacing varied with the frequency range of the measurements and for the 0-400 Hz range the spacing was 3 cm. The acceleration signals were acquired using an HP 5420A Signal Analyzer and transferred to a PC-compatible microcomputer, via an IEEE interface. The 1/3-octave-band-averaged correlation coefficients were then estimated using equation (3.6).

4.8.2 Discussion of results - roof vibration field

In the analysis presented in refs. [54] and [78] it was suggested that the roof vibrational field approached that of a doubly-curved shell. This suggestion was based on the geometrical characteristics of the roof and on experimental results of correlation coefficients, that were clearly different for two perpendicular directions in a certain frequency region. The estimation of the ring frequencies of the equivalent doubly curved shell model employed was not straightforward because the roof curvature varied along the two principal directions. Inspection of the roof dynamic characteristics was employed in this estimation. The lower ring frequency was estimated to be around 100 Hz as no resonant modes were present in the measured roof frequency response functions [54,78] below this frequency. The upper ring frequency was assumed to be around 300 Hz.

From frequency response functions measured near line D (presented in ref. [54]) it was observed that no mode was excited below 150 Hz and hence, the lower ring frequency in the region where line D was placed was assumed to be 150 Hz. This was the result of a different roof curvature near line D. The experimentally estimated roof modal density was almost flat above 500 Hz and approached that of an equivalent flat plate of 0.8 mm thickness. The estimated modal density for the equivalent plate is 0.56 modes/Hz [78].

In the frequency range between the lower ring frequency, and $\sqrt{2}$ times the upper ring frequency, the bending wavenumber in a doubly curved shell depends upon the wave direction. This was the reason used in ref. [78] to explain the change of the correlation coefficient zero crossing and shape with the lines orientation. An expression for the dispersion relation of a doubly curved shell is presented in Appendix F. This dispersion relation is here employed in the estimation of the centre frequency wavenumber for different wave directions. These wavenumbers were combined with expression (3.23) and the parameters for clamped edges (equations (B.4)) and the correlation coefficients computed from numerical integration of equation (3.8). These correlation coefficients were evaluated for different lines and plotted against the experimental results at these lines.

In figs. 4.40 and 4.41 results at lines A, B, C and D for 250 Hz and 315 Hz 1/3 octave bands are presented. As shown, the variation of the experimental correlation coefficients with the lines orientation is quite clear and the theoretical results were able to represent this variation. Bearing in mind that the roof curvature varied along the two principal directions and that the edges were not clearly defined, the agreement between the experimental and theoretical results was considered reasonable. Above the 315 Hz 1/3 octave band both theoretical and experimental results tended to approach the results for a diffuse bending wave field. As discussed in ref. [78], only at 1000 Hz 1/3 octave band was the roof vibrational field considered nearly diffuse.

4.8.3 Discussion of results - windscreen vibration field

The other part of the car that could be idealised as a simple homogeneous structure was the windscreen. Such model is a clamped flat plate of equal windscreen area and thickness. The experimentally estimated modal density confirmed this model as a reasonable approximation for the windscreen [78]. Theoretical values of correlation coefficient were computed for points along lines E and H (illustrated at fig. 4.39) following this clamped plate model. Typical wavelengths for the windscreen were: 0.649 m at 100 Hz, 0.458 m at 200 Hz, 0.41 m at 250 Hz and 0.365 m at 315 Hz.

Experimental results obtained at these lines are presented in fig. 4.42. Excitation was that set up by acoustically exciting the car interior with white noise. The fixed accelerometer for line E measurements was placed at the top of this line, close to the connection with the roof, while the fixed accelerometer for line F was placed at the junction of both lines. As shown in fig. 4.42, the results at both lines are quite different and in view of the relative value of the wavelength and the distance from the edges it appears that the evanescent waves generated at the top edge dominates the vibration field in the region where lines E and H were placed. The theoretical results were able to represent this influence as illustrated in fig. 4.42. The agreement between theoretical and experimental results were only reasonable due to

non-regular geometry and low modal density (n(f) = 0.074 modes/Hz) of the windscreen.

The theoretical representation suggested in Chapter 3 appears to be a valid approximation even for practical structures like a car body shell. Some of the points raised in refs. [54] and [78] as reasons for the departure of the roof vibrational field from a diffuse field state, even when a large number of natural modes are assumed to be excited, have been proved to be valid. Wavenumber variation with wave propagation direction and edge boundary conditions were the points incorporated in the present theoretical model. The influence of the excitation on the present approach remains to be better addressed, however for point-excited and indirectly-excited system good results have been obtained.

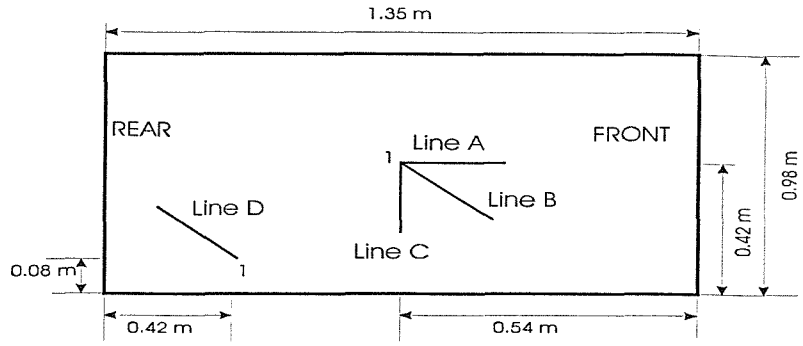

SKETCH OF ROOF

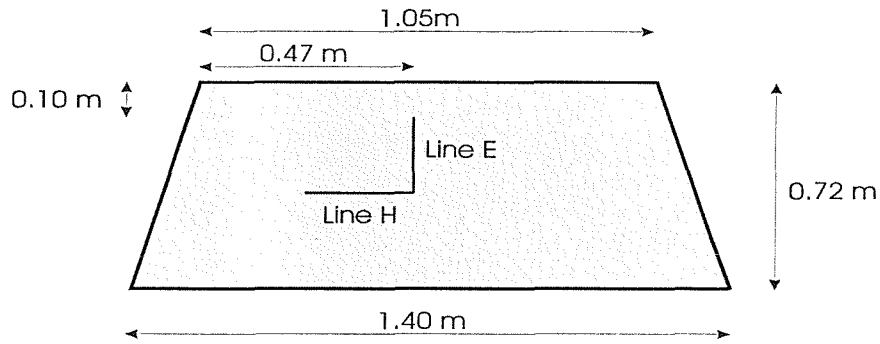

Sketch of windscreen

Fig. 4.39 - Position of measurement lines on roof and windscreen with dimensions in metres.

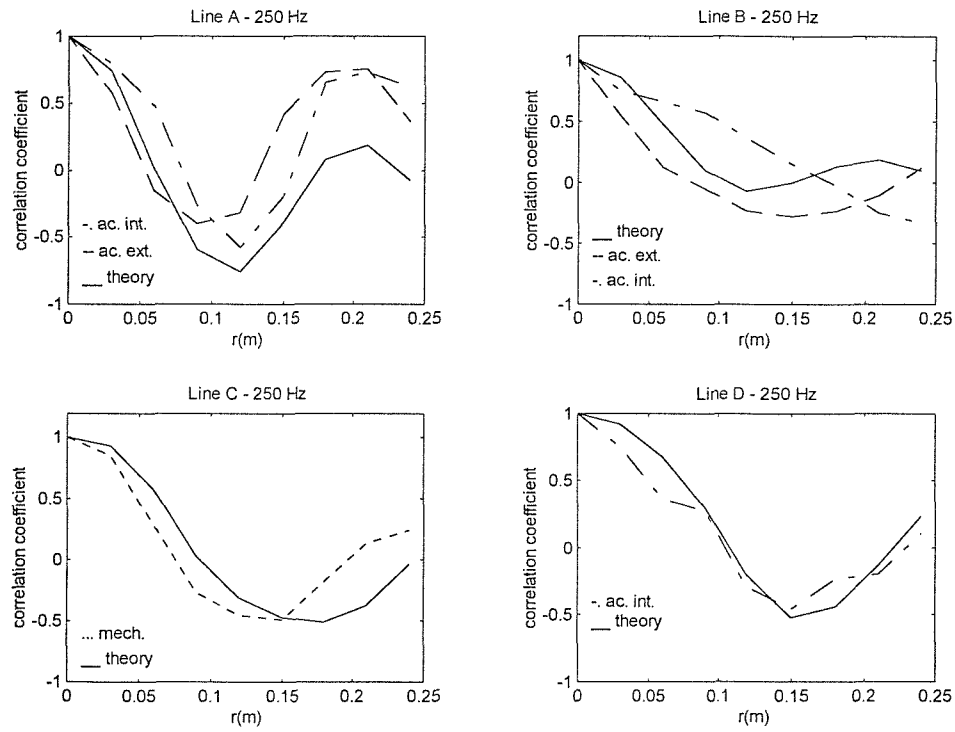

Fig. 4.40 - Roof correlation coefficients, 250 Hz (1/3 octave band). ——— theoretical results (eq. (3.23)); – · – · – · – internal acoustic excitation; — — — external acoustic excitation; - - - - - mechanical excitation.

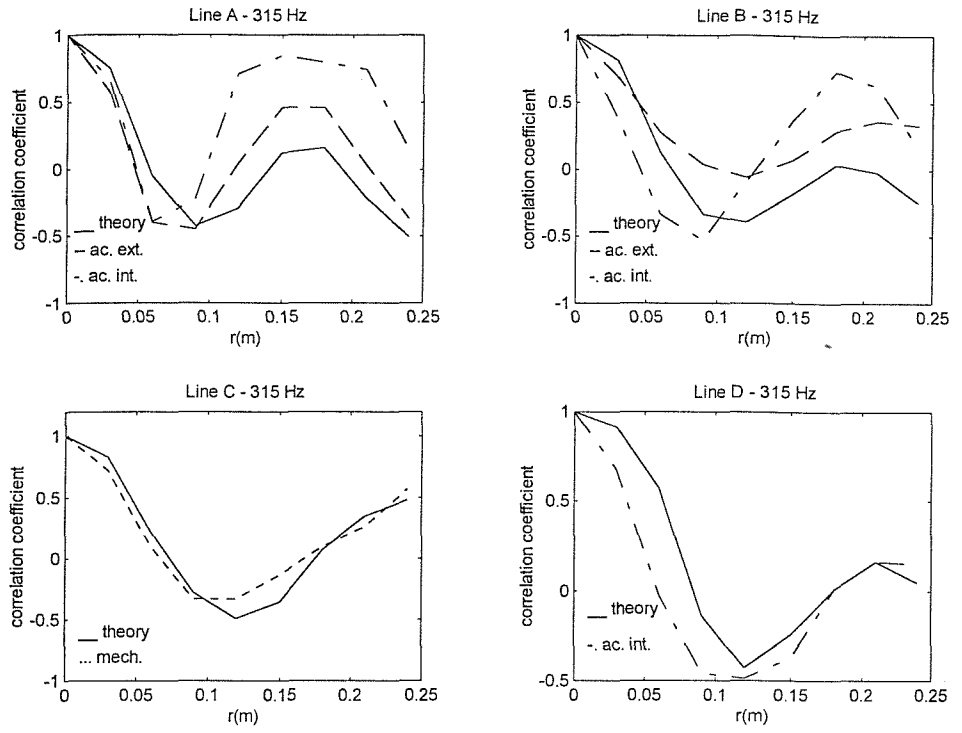

Fig. 4.41 - Roof correlation coefficients, 315 Hz (1/3 octave band). ——— theoretical results (eq. (3.23)), – · – · – · – internal acoustic excitation; — — — external acoustic excitation; - - - - - mechanical excitation.

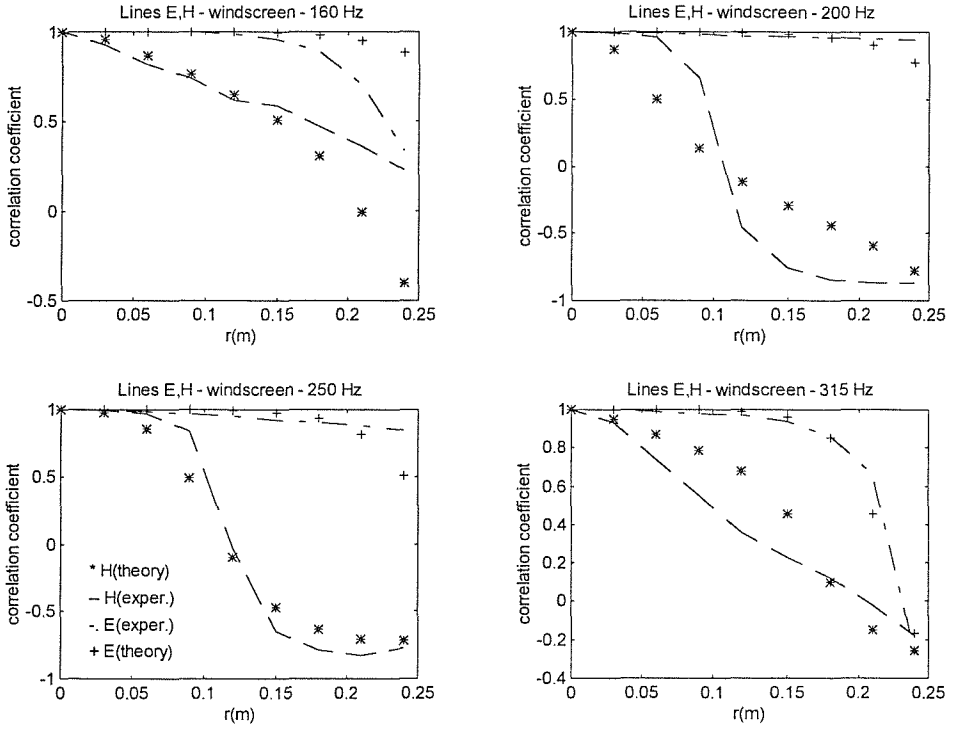

Fig. 4.42 - Experimental results of correlation coefficients on a passenger car windscreen. Internal acoustic excitation. 1/3 octave bands. Line E: + + + theoretical results (eq. (3.23)); – · – · – · – experimental results. Line H: * * theoretical results (eq. (3.23)); — — — experimental results.

4.9 Conclusions

From the results presented in this chapter the following conclusions can be drawn about the theoretical model of randomly excited two-dimensional vibration fields represented in terms of correlation coefficients, as presented in Chapter 3 :

(i) For cases of low modal overlap ($M < 1$) this model is valid as a frequency-average estimate in bands in which at least eight to ten modes are excited at resonance. This conclusion agrees with similar one reached by Stearn [53,76] in the analysis of diffuse bending wave fields.

(ii) When the modal overlap is high ($M > 1$) this model can be used as a narrow band estimate.

(iii) The validity of the present model as a broadband estimate is only limited to the increase of importance of second order terms as the bandwidth increases (as discussed in section 3.4.1).

(iv) For points in a region one wavelength from the edges it was found that the experimental and modal summation results depart considerably from correlation coefficients as given by the diffuse bending wave field assumption. The model presented herein was able to reproduce with reasonable precision the distortion field created by the edges and corners.

(v) Away from the edges (distance greater than at least one wavelength) the theoretical and experimental correlation coefficient results approached that given by the diffuse bending wave field assumption irrespective of the boundary condition.

(vi) When the Bolotin's dynamic edge effect parameters (Appendix B) and/or reflection and transmission wave coefficients (Appendix C) are employed, the experimental results obtained on simply-supported, clamped and free plates are predicted with reasonable precision using the present model.

(vii) For the case of spring supported boundaries (like stiffeners), the correlation characteristics of the vibration fields on the reflection and transmission sides are satisfactorily predicted.

(viii) Despite the fact that the theoretical results were derived using the assumption of spatially-uncorrelated random excitation, it was experimentally verified that they can be used as an approximation for cases of mechanically excited plates and plates excited by diffuse acoustic fields. It was also verified that they apply to directly and indirectly-excited plates.

(ix) Free wave and modal representation of correlation coefficients were shown to be equivalent, irrespective of the plate boundary conditions. This conclusion supports previous analysis of equivalence between wave and modal representation of two- and three-dimensional wave fields as presented by Waterhouse and Cook [73], Chu [60] and Langley [55].

(x) The conclusions here presented for correlation coefficients are also valid for the frequency-average normalised cross-power spectral density of acceleration.

(xi) When the theoretical results are modified in order to account for changes in the wavenumber due to curvature effects (Appendix F), the experimental results obtained on a car roof are reasonably well predicted with the model proposed.

CHAPTER 5

ANALYTICAL AND EXPERIMENTAL VERIFICATION OF HYBRID MODEL APPLICATION TO RESPONSE PREDICTION

This chapter presents the application of the equations introduced in Chapter 2 to the prediction of the sound pressure response inside an acoustic cavity due to one vibrating wall. The bending wave field generated by the random vibration of the thin wall is modelled using the approximate modal and free wave representations of Chapter 3. Comparison are presented for the results of two different rigs in one-third octave and in narrow frequency bands.

5.1 Description of the computation routine

The computational routine used to estimate the pressure response inside an acoustic cavity due to a bounding random vibrating plate is described in this section. This routine computes the terms of equation (2.16)

$$S_p(x,y,z,\omega) \approx \frac{(\rho_o c_o^2)^2 S^2}{V^2} S_a(\omega) \sum_n \frac{\psi_n^2(x,y,z)}{\Lambda_n^2} \frac{1}{[X_n^2 + Y_n^2]} C_{nn}^2(\omega), \qquad (2.16)$$

using closed form expressions for the acoustic cavity natural frequencies and mode shapes (eqs. (5.3),(5.4)), experimental estimates of acoustic loss factors, and numerical integration to compute the coupling coefficient. The numerical integration routine employed in the computation of the coupling coefficient is described in sections 5.1.1, 5.1.2 and 5.1.3.

The final result is expressed as a ratio between the autospectrum of the space-averaged sound pressure inside the cavity ($S_p(\omega)$) normalised by the autospectrum of the space-averaged plate vibration acceleration ($S_a(\omega)$). The space average of the pressure inside the cavity can be obtained either from the response in a

large number of cavity points or by obtaining the space average of each acoustic mode shape. In this second case we have that

$$\left\langle \psi_n^2(x,y,z) \right\rangle = \frac{1}{V} \int_V \psi_n^2(x,y,z) dV, \tag{5.1}$$

where < > denotes spatial average. Substituting equation (5.1) in equation (2.16) we have that the frequency averaged ratio $<p^2>/<a^2>$ is given by

$$\frac{\left\langle p^2 \right\rangle}{\left\langle a^2 \right\rangle} = \frac{\left\langle S_p(x,y,z,\omega) \right\rangle}{\left\langle S_a(\omega) \right\rangle} \approx \frac{(\rho_o c_o^2)^2 S^2}{V^2} \sum_n \frac{1}{\Lambda_n [X_n^2 + Y_n^2]} C_{nn}^2(\omega). \tag{5.2}$$

Alternatively, the autospectrum of the sound pressure in a point inside the cavity ($S_p(x,y,z,\omega)$) can also be directly computed from equation (2.16). The results can be estimated for any frequency and so, they can be compared to narrow band or frequency-averaged experimental results. The program was written in Fortran and runs in a SunSparc workstation or in a PC-compatible computer. The output was downloaded to a MATLAB routine in order to obtain a graphical output of the results.

The natural frequencies and mode shapes of the acoustic modes of a rectangular hard-walled acoustic cavity are expressed as [26]

$$f_n = \frac{c_o}{2} \sqrt{\left(\frac{r_x}{L_x}\right)^2 + \left(\frac{r_y}{L_y}\right)^2 + \left(\frac{r_z}{L_z}\right)^2} \tag{5.3}$$

$$\psi_n(x,y,z) = \cos\left(\frac{r_x \pi x}{L_x}\right) \cos\left(\frac{r_y \pi y}{L_y}\right) \cos\left(\frac{r_z \pi z}{L_z}\right) \tag{5.4}$$

where L_x, L_y, L_z are the internal dimensions of the acoustic cavity and r_x, r_y, r_z are positive integers. In the low frequency range (from 0 to the frequency of the 10th acoustic mode) all modes are included in the summation. However, above the frequency of the 10th acoustic mode or when more than 5 acoustic modes are excited in a frequency band, only the acoustic modes that have natural frequencies within the frequency band of interest are included in the summation. This procedure enables the computation of the response in bands in which no acoustic mode is excited and saves computer time by avoiding including modes that contribute little to the response in a specific frequency band. The modal loss factors are estimated from experimental measurements of the acoustic cavity frequency-averaged loss factors.

The numerical integration procedure used to compute the coupling coefficient between each acoustic mode and the vibration field at specific frequencies is discussed in the next three sections. The numerical integration results were checked against the closed form result for the integral of the product of two functions similar to the ones computed for the case of hard-walled acoustic cavities. The coupling coefficient was assumed constant in each frequency band and computed for each acoustic mode that was included in the modal summation. This is based on the fact that the coupling coefficient is a smooth function of frequency and therefore, the error associated with assuming it does not depart considerably from the value computed at the centre frequency of the band is small. This procedures enables the saving of considerable amount of computer time.

5.1.1 Coupling coefficient between an acoustic mode and a vibration field

It was shown in Chapter 2 that for coupling between acoustic modes of an enclosed fluid space and a bounding vibration field a direct coupling coefficient ($C^2_{nn}(\omega)$) can be defined as

$$C^2_{nn}(\omega) = \frac{1}{S^2} \int_S \int_S \mathrm{Re}[\gamma_a(x_1, y_1, x_2, y_2, \omega)] \psi_n(x_1, y_1, z_o) \psi_n(x_2, y_2, z_o) dx_1 dx_2 dy_1 dy_2, \quad (5.5)$$

where $\psi_n(x_1,y_1,z_o)$ represents the acoustic mode shape at a point $X_1=(x_1,y_1)$, Re $[\gamma_a(x_1,y_1,x_2,y_2,\omega)]$ is the real part of the normalised cross-power spectral density of the vibration field acceleration between points (x_1,y_1) and (x_2,y_2) and S is the interface area (usually the plate area).

The acoustic modes of enclosures of any type or shape can be obtained either numerically via a FEM code or analytically in some specific cases (e.g., equations (5.3) and (5.4)). The normalised cross-power spectral density of the vibration field acceleration can be obtained from the approximate representation of a vibration field as presented in Chapters 3 and 4. For instance, for the case of a simply-supported flat plate the real part of the normalised cross-power spectral density of acceleration ($\mathrm{Re}[\gamma_a(x_1,y_1,x_2,y_2,\omega)]$) is given by equation (3.17'). For other boundary conditions results for the above parameter are computed using equation (3.23') and

the edge parameters presented in Appendices B, C and E. Results for excitations other than the spatially-uncorrelated type are obtained from the equations presented in section 3.6.

The numerical integration in wavenumber space used in equations (3.23) and (3.23') is computed from 0 to $\pi/2$ using the mid-point rule [72] with 15 integration points. This number of integration points was found to be sufficient in order to compute reliable values for equations (3.23) and (3.23'). Such verification was performed by comparing results from equation (3.23) (or (3.23')) for the case of simply-supported edges to the closed form solution for a plate with simply-supported edges (equations (3.17) or (3.17')). This numerical integration routine was the same employed to obtain theoretical results for correlation coefficient and normalised cross-power spectral density of plates with clamped, free and stiffened edges and validated against experimental results in Chapter 4.

The numerical integration of equation (5.4) was further optimised by truncating the computation in order to avoid the inclusion of terms which have a large $k_b r$ value because it was found that such terms do not contribute much to the summation.

5.1.2 One-dimensional numerical integration exercise

The numerical integration of a given function on a limited interval follows a similar procedure irrespective of the rule being used. In such procedure, the integration interval is divided into a number of segments (not necessarily of the same size) and the value of the function is calculated at the dividing points. The function's value at each point is weighted and all weighted values summed together. The final sum is then multiplied by the spacing between the integration points and the integral obtained. In view of the fact that the value of the function is obtained in a finite number of points the precision of the obtained value is related to the number of points used to discretize the function. As there is no recommendation for the definition of the optimum number of integration points to be applied in a specific situation, this number should be determined empirically (or known by past experience).

In the case of a slowly varying function a small number of points is sufficient to correctly represent it, but if the function varies abruptly the number of necessary points is much higher. Many numerical integration rules are available from the literature and some of them were chosen to be employed in a prediction exercise to decide which one is best suited to the evaluation of equation (5.5). The following numerical integration rules were chosen from ref. [72]: an extended trapezoidal rule, an extended Simpson's rule, an 8-point closed Newton-Cotes formula and a mid-point rule.

The first step in this exercise was to employ the above numerical integration rules in the numerical integration of the zero-order Bessel function ($J_0(z)$) because it represents the correlation coefficient and the normalised cross-power spectral density of a diffuse bending wave field. This function was integrated from 0 to 50 for various numbers of integration points and some of the results are presented in table 5.1. It was observed that the result obtained with the 8-point Newton-Cotes formula is very different from results given by the other three methods. Therefore, a larger number of points is necessary to improve precision. Unfortunately, in the case of the Newton-Cotes rule, every time we change the number of integration points a different set of weighting factors needs to be used and so, this rule is not convenient when the magnitude of the integration limits vary.

The result obtained with Simpson, mid-point and trapezoidal rules using 1000 integration points was the same and so this value could be used as the exact integral of $J_0(z)$ in the interval 0 to 50. In order to facilitate the interpretation of the results presented in table 5.1 a chart was prepared in which the results of table 5.1 are compared with the exact value and the difference between them presented as percentage of the exact result. This percentage difference is presented in fig. 5.1 in relation to the number of integration points and integration rule used. It is observed in this chart that when the number of integration points is 25, trapezoidal and mid-point rules give results less than 5 % different from the exact one. In contrast, for a similar number of points, the Simpson rule give results more than 20 % different from the exact value. However, the percentage difference between the results obtained with 10 integration points and the exact one is generally much higher than that obtained with

25 integration points. On the other hand, as the number of integration points increase above 25 points the difference between numerical and exact value does not drop considerably.

Routine	10 points	20 points	25 points	35 points	50 points	100 points	1000 points
Trapezoidal	1.317	0.9599	0.9363	0.9218	0.9134	0.9056	0.9023
Simpson	0.5227	0.8408	1.1024	1.0004	0.9058	0.9029	0.9023
Mid-point	0.6027	0.8703	0.8906	0.8926	0.8977	0.9011	0.9023
Newton	7.248						

Table 5.1 - Results for the integral of $J_0(z)$ from 0 to 50

From these results it is confirmed that a relation exists between the number of integration points and the precision obtained and that this relation depends on the integration limits. As the number of integration points is also related to the CPU time used in the numerical integration, there is a relation between the number of integration points and the value of the integration limits that gives the most 'economical' relation between CPU time employed and precision obtained. In the present case, a number of integration points (intpoint) equals to half the value of the higher integration limit (maxlim) gives a good estimate of the ratio 'maxlim/intpoint' for a reasonably fast and accurate numerical integration routine. Numerical integration results obtained for other integration limits also confirmed these observations. Finally, it is also observed in fig. 5.1 that the mid-point rule generally gives more precise results than the other methods for a similar number of integration points.

The second step in this exercise was to numerically obtain the integral of the product of two functions similar to those used in the coupling coefficient. The following standard integral can be obtained from ref. [72],

$$\int_0^z e^{it} t^v J_v(t) = \frac{e^{iz} z^{v+1}}{2v+1}\left[J_v(z) - iJ_{v+1}(z)\right] \quad v > -\frac{1}{2}, \tag{5.6}$$

and for v=0 we have from the above equation that

$$\int_0^z J_0(t)\cos t\,dt = z\left[J_0(z)\cos z + J_1(z)\sin z\right] \qquad (5.7)$$

where $J_1(z)$ is the first-order Bessel function. The trapezoidal, Simpson and mid-point rules were employed to numerically estimate the integral on the left-hand side of equation (5.7). The results obtained were then compared to the exact values given by the expression on the right-hand side of equation (5.7). Some of the results obtained with this procedure are presented in table 5.2.

Routine	0 to 10	0 to 50	0 to 100
Exact	1.8271	3.9721	5.6298
Mid-point	1.826 (0.06 %)	3.9321 (1.0 %)	4.5322 (19.5 %)
Simpson	1.7411 (4.7 %)	3.4442 (13.3 %)	6.4887 (15.2 %)
Trapezoidal	1.8251 (0.1 %)	4.0242 (1.3 %)	6.801 (20.8 %)

Table 5.2 - Numerical integration of $J_0(z)\cos z$ using 25 integration points and varying the integration limits. Exact result given by equation (5.7). Figures in parentheses show the percentage difference from corresponding exact values.

As shown in the above table for an upper integration limit of 50, 25 integration points give good results when either mid-point or trapezoidal rules are used. This number of integration points correspond to the previously suggested ratio maxlim/intpoint $\cong$ 2.0. As the mid-point rule is the simplest of those two, it was adopted in the coupling coefficient numerical integration routine. Furthermore, it is observed that the suggested relation maxlim/intpoint $\cong$ 2.0 is equivalent to adopt 3 integration points per wavelength. However, in the numerical integration of cosine or sine functions it is advisable to use 8 integration points per wavelength. Therefore, the following criterion was adopted for the definition of the number of integration points to be employed in the mid-point rule:

- for cases in which computer cost is at a premium and the precision can be slightly sacrificed the 'economic' ratio maxlim/intpoint $\cong$ 2.0 or 3 integration points per wavelength was used;

- on the other hand, when we can afford to spend more computer time 8 integration points or the 'ideal' ratio maxlim/intpoint $\cong 4/\pi$ was employed in the numerical integration routines. This is the alternative employed in the response results presented in this chapter.

5.1.3 Four-dimensional numerical integration routine

The acoustic mode shapes of a rectangular hard-walled enclosure are given by equation (5.4). Substituting these acoustic mode shapes and the normalised cross-power spectral density for a diffuse bending wave field (equation (3.18)) in equation (5.5) we obtain the following expression for the coupling coefficient,

$$C_{nn}^2(\omega) = \frac{1}{S^2}\int_S\int_S J_0(k_b r)\cos\left(\frac{r_x \pi x_1}{L_x}\right)\cos\left(\frac{r_y \pi y_1}{L_y}\right)\cos\left(\frac{r_x \pi x_2}{L_x}\right)\cos\left(\frac{r_y \pi y_2}{L_y}\right)dx_1 dx_2 dy_1 dy_2 . \quad (5.8)$$

As no closed form solution is available to the above integral a similar integral which can be solved exactly is employed in the verification of the numerical integration routine. One of the possible integrals is,

$$C_{nn}^2(\omega) = \frac{1}{L_x^2 L_y^2}\int_0^{L_x}\int_0^{L_x}\int_0^{L_y}\int_0^{L_y} J_0(k_b x_1)J_0(k_b y_1)J_0(k_b x_2)J_0(k_b y_2)\times \\ \times\cos(k_b x_1)\cos(k_b y_1)\cos(k_b x_2)\cos(k_b y_2)dx_1 dx_2 dy_1 dy_2 , \quad (5.9)$$

which can be solved with the help of equation (5.5),

$$C_{nn}^2(\omega) = \left[\cos(k_b L_x)J_o(k_b L_x)+\sin(k_b L_x)J_1(k_b L_x)\right]^2 \times \\ \times\left[\cos(k_b L_y)J_o(k_b L_y)+\sin(k_b L_y)J_1(k_b L_y)\right]^2 , \quad (5.10)$$

where L_x and L_y are the plate dimensions (assumed equal to the internal acoustic cavity dimensions in the directions x and y).

A Fortran routine was written to numerically integrate equation (5.9) using the mid-point rule. A polynomial approximation (ref.[72], pgs. 269,270) was employed in the estimation of the zero and first order Bessel functions. The error incurred in using this approximate representation of the Bessel functions is smaller than 10^{-8} [72].

As an example, this Fortran routine is employed to compute the coupling coefficient between the wood-walled enclosure (main dimensions: 0.7 m x 0.48 m x 0.48 m) and a square aluminium plate (0.48 m x 0.48 m, thickness= 1.0 mm). The geometric and material properties for these two subsystems are described in section 5.3. The coupling coefficient was estimated in the frequency interval 0 to 1000 Hz and the largest integration limit was given by $k_b L_x$. The results obtained are presented in fig. 5.2. From the suggested 'economic' ratio maxlim/intpoint $\cong 2.0$ the number of integration points necessary to obtain a reasonable precision is 15. The 40 points result correspond to the 'ideal' ratio maxlim/intpoint $\cong 4/\pi$. As shown in fig. 5.2, the results for 10 integration points depart considerably from the exact ones (given by equation (5.10)) above 600 Hz. On the other hand, both the 40 points and the 15 points results compare well with the exact ones. As a matter of fact the deviation, in the frequency range 0-1000 Hz, between the numerical (15 points) and the exact results is not higher than 1 dB, and the 40 points result does not show any apparent difference from the exact ones.

As observed in fig. 5.2, when the number of integration points is smaller than twice the higher integration limit the precision is poor but improves quickly as this number approaches the suggested value. If the number of integration points is higher than half the maximum integration limit the precision is good and so it does not improve considerably when the number of integration points increases. Similar results were obtained when this Fortran numerical integration routine was employed for the case of the concrete-walled enclosure (described in section 5.2). These results indicate that the criterion adopted for the one-dimensional integration (section 5.1.2) can also be employed for the case of a n-dimensional integration.

The speed of the numerical computation of the coupling coefficient (eq. (5.5)) was further improved by taking advantage of the plate symmetry. During the numerical integration one of the points is varied along only one quarter of the plate while the other point is varied along the entire plate area. The final result is multiplied by 4. The results of this computation were checked against results from a numerical integration in which both points varied along the entire plate area. The results from both computations were coincident.

In order to illustrate the characteristics of the coupling coefficient curves, the Fortran routine described in the preceding paragraphs was extended to compute equation (5.8) for various acoustic modes. For instance, the coupling coefficient between some of the acoustic modes of the wood-walled enclosure and the bounding square plate is presented in fig. 5.3. It is observed that for a value of frequency equals to 30 Hz, the response inside the cavity will be mainly due to the $(0,0,r_z)$ and $(0,1,r_z)$ acoustic modes, while for a frequency equals to 750 Hz all the acoustic modes represented in fig. 5.3 are similarly excited. Another noticeable characteristic is the shape of the curve. There is a initial peak which is controlled by the modal numbers (r_y and r_x in the present case) and the curve decays with a similar slope for all modes with the difference that when r_y equals to r_x the curve has a higher dynamic range than for cases in which r_y is not equal to r_x. In the case of an axial acoustic mode the coupling coefficient is maximum and equal to unity when the frequency (or $k_b r$) equals zero. On the other hand, the coupling coefficient has a minimum when the frequency (or $k_b r$) equals to zero for oblique modes.

The explanation for such behaviour is rather simple and can be found in ref. [68]. A diffuse bending wave field will only be completely correlated when $k_b r$ equals zero and in this situation only acoustic modes that involve a variation of volume in the interface area will be efficiently excited. That it is the reason for the unity value of the coupling coefficient when r_x and r_y are equal to zero and the very low value for most of the other modes. As the frequency increases the relative correlation of the velocity (or acceleration) at adjacent acoustic modes antinodes decreases and so, the excitation of the mode $(0,0,r_z)$. Though, all the modes are excited. On the other hand, when r_x and r_y are non-zero the separation between each antinode gets smaller and the occurrence of extremes in coupling coefficient values decreases, explaining the smoother aspect of the coupling coefficient for the $(1,2,r_z)$ acoustic mode. With the increase in frequency the possibility of occurrence of small values of correlation for point-to-point separations smaller than an antinodal region also increases and there will be a partial cancellation of the excitation within each antinode. All the modes are excited, but at a reduced level. This reduction in the level of excitation is offset by the increase in the number of acoustic modes summed in each frequency band when the overall sound pressure level is computed.

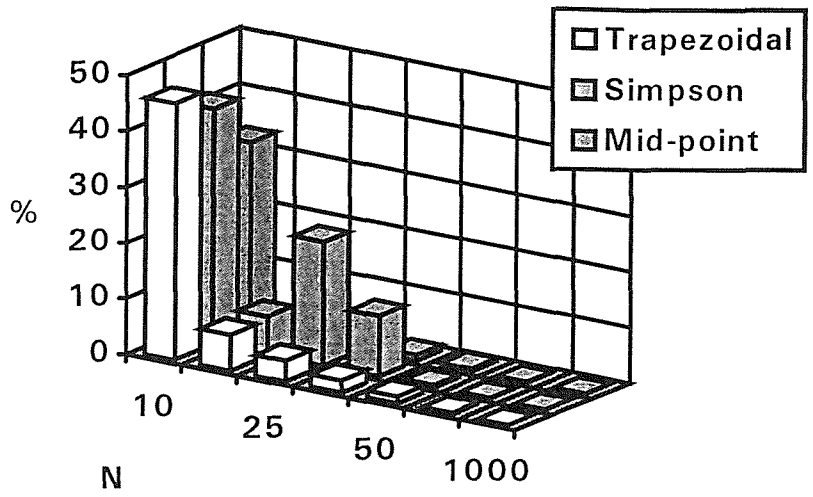

Fig. 5.1 - Comparison of Trapezoidal, Simpson and mid-point numerical integration rules. Results from table 5.1 plotted as percentage difference of exact value (%) and as a function of the number of integration points (N).

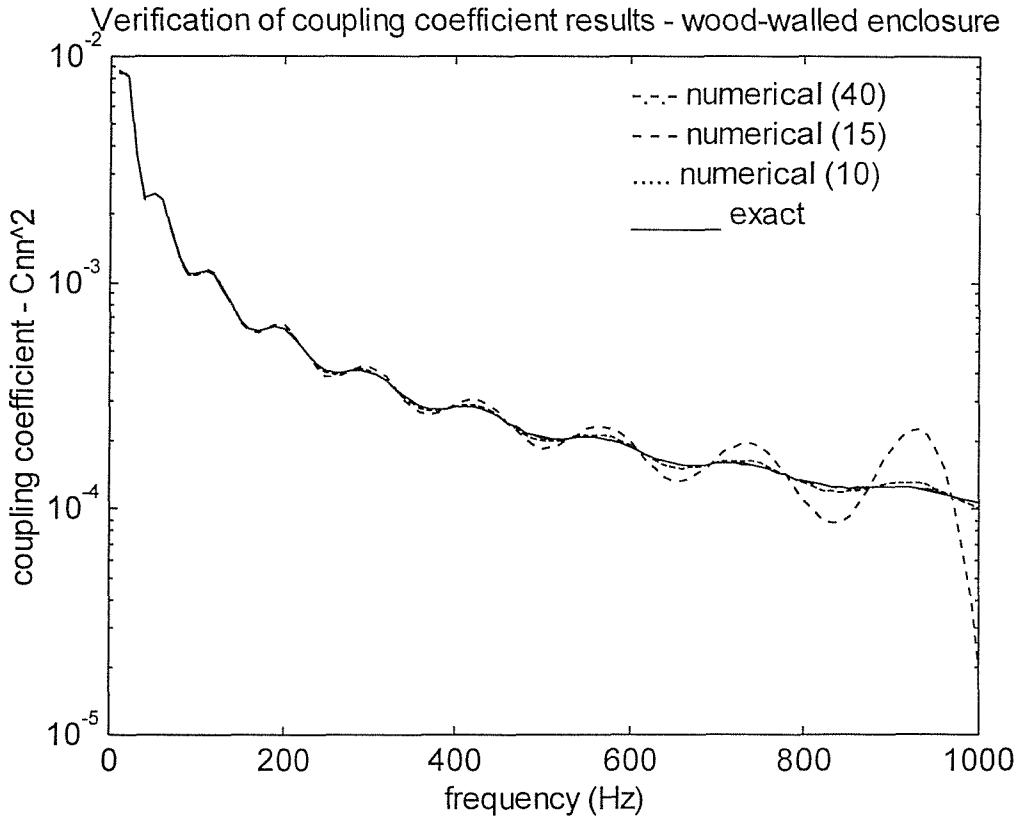

Fig. 5.2 - Computation of equation (5.9) for the wood-walled enclosure using various number of integration points. ——— exact solution (eq. (5.10)); — — — 15 points; – · – · – · – 40 points; - - - - - 10 points.

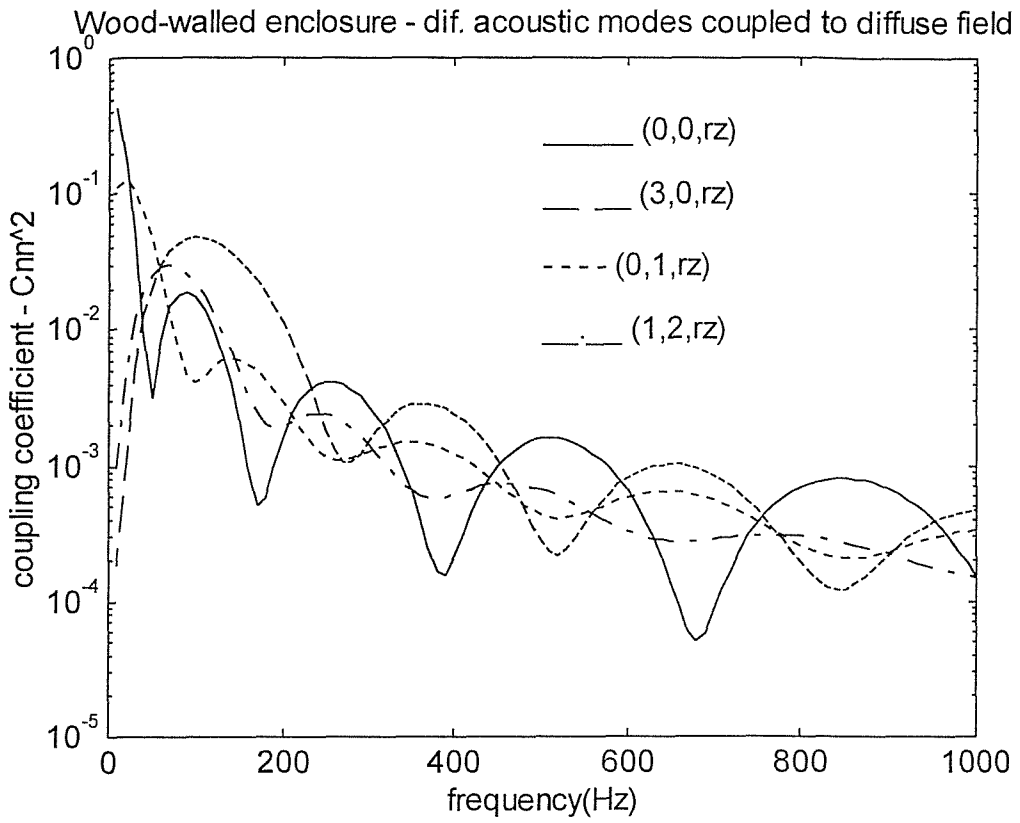

Fig. 5.3 - Coupling coefficient between different acoustic modes and a diffuse bending wave field (eq. (5.8)). 20 integration points. key for acoustic modes: ——— $(0,0,r_z)$; — — — $(3,0,r_z)$; – · – · – · – $(1,2,r_z)$; - - - - - $(0,1,r_z)$.

5.2 Concrete box bounded by a flat plate

5.2.1 Description of system

The system on which the experimental work reported in this section is based is sketched in fig. 5.4. The enclosure was built with three concrete walls and the top closed by a thick concrete panel. A layer of concrete was placed over the pavement surface to form the floor of the enclosure. The open side was closed by a 1.2 mm thick mild-steel plate which was sandwiched along its edges by two steel frames joined by bolts. The plate itself was kept separated from the two steel frames by a layer of draught excluder. This configuration was an attempt to simulate simply-supported boundary conditions but the resulting natural frequencies were higher than the ones for a simply-supported plate. The internal cavity dimensions are 0.6 x 0.75 x 1.05 m in the x, y, z directions, respectively. The flexible wall is situated in the plane x-y and its dimensions, for the purpose of SEA, FEM and hybrid model estimation, are 0.6 x 0.75 m (x and y directions, respectively).

The acoustic cavity and plate frequency-averaged loss factors were estimated using a decay technique. The burst of a balloon was used to excite the acoustic cavity while the plate was excited by a hammer blow. The signal decay after the impact excitation was acquired using a Bruel&Kjaer 2133 Dual Channel Real-Time Frequency Analyser and from the time the signal took to decay 60 dB the loss factor was estimated. The results were obtained in 1/3 octave bands. The results of such estimation are presented in table 5.3.

The response results for this acoustic cavity/plate were estimated using the hybrid model computation routine described in section 5.1. The acoustic cavity loss factors presented in table 5.3 were used in this calculation and the results were presented as the ratio between the space-averaged mean square pressure inside the acoustic cavity divided by the space average of the plate vibration velocity. One third octave band and narrow band results were computed assuming the coupling coefficient is constant in each 1/3 octave frequency band.

frequency (Hz)	Acoustic cavity frequency-averaged loss factor (η_a)	Plate frequency-averaged loss factor (η_p)
50	0.1	-
63	0.1	-
80	0.09	-
100	0.1	0.04
125	0.08	0.04
160	0.07	0.06
200	0.04	0.1
250	0.03	0.05
315	0.02	0.08
400	0.02	0.07
500	0.02	0.05
630	0.01	0.05
800	0.01	0.04
1000	0.006	0.03
1250	0.006	0.04

Table 5.3 - Frequency-averaged plate and acoustic cavity loss factors.

5.2.2 Comparison with FEM results

Several general purpose finite element (FEM) programs have been developed and are available in a wide range of mainframe, RISC workstations and personal computers. ANSYS [86] is one of such programs and its educational version was used in this work. Unfortunately, this version has a maximum wave-front limit of 400 (on SunSparc workstations) which restricts the model size and consequently the analysis frequency range. The version used in this computation is the 4.4a one.

The plate is modelled using a elastic quadrilateral shell element which has both bending and membrane capabilities. This element is represented by four

nodes, with six degrees of freedom at each node and both in-plane and normal loads permitted. The acoustic space inside the cavity is modelled using a 3-D isoparametric acoustic fluid which is also used to model the fluid/structure interface. In ANSYS this element is represented by eight nodes with four degrees of freedom per node. As the FEM matrices generated in a fluid/structure coupled analysis are unsymmetric, the Lanczos method is used to solve the associated eigenproblem. The main weakness of such analysis is that the damping is assumed constant in all frequency range and equal for all the elements. A damping ratio of 0.05 is assumed in this analysis.

Due to aforementioned limitations with the wave-front size the studied system is represented by only 120 acoustic elements and 20 plate elements. These number of elements restrict the maximum useful frequency of FEM analysis to 300 Hz. The procedure used to obtain space averaged mean square values of pressure and velocity is based on the determination of frequency response functions (FRF). In order to obtain these FRF's a full harmonic response analysis is applied. This type of analysis determines the steady-state response of a linear structure to a set of harmonic loads of known amplitude and frequency. The load used is a unit force applied over one of the plate nodes. A frequency step of 2.0 Hz is used to estimate the response.

The mean square space averaged values are calculated during the post-processing phase with the commands available in POST26 ANSYS module. The results of twelve plate nodes and forty cavity nodes are used to obtain the average values. The ratio $\langle p^2 \rangle / \langle v^2 \rangle$ is obtained at each frequency step as it is a measure of the relative energy of the two subsystems.

The FEM results for clamped and simply-supported plate boundary conditions are presented in figs. 5.5 and 5.6, respectively. These results are compared to hybrid model results for the same boundary conditions. The hybrid model results were computed using equation (5.2) with the acoustic loss factors listed in table 5.3. The computational procedure is described in section 5.1. The edge parameters for simply-supported and clamped boundary conditions are presented in Appendix B.

The first noticeable difference between both approaches is near the acoustic cavity resonance frequencies. This discrepancy originates from the use of an analytical formulation (eq. (5.3)) in the calculation of the acoustic modal frequencies in the hybrid model. Frequency response measurements carried out in the actual

concrete walled box indicate that the analytical acoustic natural frequencies as computed by equation (5.1) are much closer to actual ones than the FEM estimates. Another reason for this discrepancy is the apparent difference in the damping used in both approaches and the jumps observed in the hybrid model results. Such jumps are related to the assumption of a constant value of the normalised cross-power spectral density in each 1/3 octave frequency band. In addition, the large discrepancy obtained in the FEM model results are also related to the use of only one excitation point whereas the hybrid model assumes an spatially uncorrelated type of excitation. It is here suggested that the FEM model results can be improved by using a finer mesh, frequency dependant damping values and by averaging the response results due a larger number of excitation positions.

Regarding the overprediction of the response near the resonance frequencies by the FEM model, it is important to point out that a similar overprediction was observed by Franchek and Bernhard [13]. In their work, FEM response results on a slightly bigger acoustic cavity due to a thicker plate were compared to experimental response results. A difference of more than 30 dB in the acoustic pressure near the first acoustic resonance between experimental and FEM results was obtained and they observed that slight changes in the model could change the FEM results. This indicates that even with a very fine mesh care must be taken when employing a FEM model to predict the vibroacoustic response in frequency regions in which there is a sparsity of plate and acoustic modes.

5.2.3 Comparison with SEA results

The basic concepts and shortcomings of Statistical Energy Analysis (SEA) were discussed in Chapter 1. Following such concepts the concrete walled box system can be represented by two subsystems, the air space confined inside the box is one subsystem and the flat plate is the other. Based on this representation the SEA expression for the power flow between these two subsystems, when the plate is excited, leads to

$$\frac{\langle p^2 \rangle}{\langle v^2 \rangle} = \frac{\rho_o c_o^2 M_p N_a}{V_a N_p \left(1 + \frac{\eta_a}{\eta_{ap}} \right)}, \tag{5.11}$$

where N_a, N_p are the number of acoustic and plate modes resonating in the band, M_p is the total plate mass, η_a is the acoustic loss factor (table 5.3) and η_{ap} is the coupling loss factor between plate and acoustic cavity.

The coupling loss factor, η_{ap} and the parameters N_a and N_p can be obtained from experimental [39] or theoretical [14] estimation of the coupling loss factor and modal density. Modal density formulations for plates and acoustic cavities are widely available in the SEA literature (for instance [14,38,39]). A theoretical expression for the coupling loss factor, η_{ap}, can be obtained from ref. [38],

$$\eta_{ap} = \frac{N_p \rho_o c_o S_p \sigma_{rad}}{N_a M_p \omega}, \tag{5.12}$$

where σ_{rad} is the plate radiation efficiency and S_p is the plate surface area. This relation implies a weak coupling between plate and air space and that the sound wavelength is less than 1/3 of a typical cavity dimensions. In ref. [37] Maidanik presents a formulation for the radiation efficiency of simply supported flat plates and a correction for clamped boundary conditions has been proposed by Timmel [87]. When the plate is radiating inside a closed space it is suggested by Craik [96] that such radiation efficiency results need to be multiplied by a factor of 2.

SEA equations (5.11) and (5.12) were used to compute the ratio $\langle p^2 \rangle / \langle v^2 \rangle$ in 1/3 octave bands assuming two different boundary conditions for the plate: clamped and simply-supported. These results are presented in figs. 5.7 and 5.8. Timmel [87] and Maidanik [37] radiation efficiency formulations with a correction for radiation into a closed space were employed in the computation of the coupling loss factor (eq. (5.12)) and the acoustic loss factors used were those presented in table 5.3. The number of acoustic modes resonating in 1/3 octave bands only exceeds five above 500 Hz and the modal overlap factor for the acoustic cavity is only greater than one above 630 Hz. The number of plate modes excited in 1/3 octave bands exceed five above 200 Hz and the plate modal overlap factor is close to unity in this frequency. These figures indicate that the assumptions in which SEA is based are only strictly valid above the 630 Hz 1/3 octave band.

The SEA results presented in fig. 5.7 are compared to hybrid model results. These hybrid model results are exactly the same ones presented in figs. 5.5 and 5.6 with the difference that in this case they are averaged in 1/3 octave bands. It is observed that both simply-supported plate results converge for frequencies above 500 Hz. This convergence between hybrid model and SEA results can be demonstrated by the use of asymptotic approximations of acoustic modal quantities in a way similar as in Kubota et al. [50]. This good agreement between SEA and hybrid model indicates that above 630 Hz there is no clear advantage in using the hybrid model if only frequency-averaged and space-averaged results are sought. Though, the main shortcoming of SEA is that it is not able to provide narrow band results or any estimate of the local response.

5.2.4 Experimental results

In order to obtain actual values of acoustic pressure due to the plate vibration, the pressure response inside the cavity formed by the concrete box was measured. A set of frequency response functions (FRF's) were measured in order to obtain both plate and acoustic cavity natural-frequencies and space-averaged vibration velocity and acoustic pressure. Steady-state and transient point excitation were used to obtain the FRF's. In the case of hammer excitation the accelerances (A/F) were measured at ten different points due to three different excitation positions over the plate. Ten measurement points and one excitation point were used when the plate was excited with band-limited white noise by a non-contact electrodynamic shaker. A lightweight Bruel&Kjaer 4393 accelerometer was used to measure the acceleration and a Bruel&Kjaer 8200 force transducer coupled to the hammer tip (or shaker) used to measure the associated force. After being amplified by charge amplifiers Bruel&Kjaer 2635 both signals were acquired with a HP 5420A Digital Signal Analyser. The imaginary and real parts of these FRF's were then squared and summed in a HP9816 computer and the 1/3 octave band results computed. The results obtained with impact and random excitation are similar, and so, only the impact excitation results were used in the estimation of $\langle p^2 \rangle / \langle v^2 \rangle$.

The same procedure was applied to obtain the pressure inside the cavity using a Bruel&Kjaer 4133 condenser microphone in the acoustic pressure measurement. The microphone signal was amplified by a Bruel&Kjaer 2209 sound level meter and was acquired with a HP 5420A Signal Analyser. In this case, three excitation points and six microphone positions were used. The microphone positions are listed in table 5.4. The FRF's were measured in the range 0-1600 Hz and the 1/3 octave band values were automatically calculated from 50 to 1250 Hz. Unfortunately, the narrow band results for this enclosure were not stored in PC-compatible files at the time of the measurements and the analyser tapes have deteriorated making difficult to recover the narrow band results. Therefore, as presented in figs. 5.8 and 5.9, only the 1/3 octave band results were compared with hybrid model results.

measurement point	x (m)	y (m)	z (m)
1	0.13	0.20	0.25
2	0.44	0.52	0.07
3	0.55	0.39	0.90
4	0.33	0.49	0.50
5	0.20	0.05	0.79
6	0.34	0.65	1.0

Table 5.4 - Positions of microphone used in acoustic pressure measurements

The normalised random error associated with frequency response function estimation is given by [85]

$$\varepsilon_r^H = \frac{\sqrt{1-\gamma_{xy}^2}}{|\gamma_{xy}|\sqrt{2n_d}}, \tag{5.13}$$

where n_d is the number of nonoverlapping averages and γ_{xy}^2 is the ordinary coherence function. In the FRF's estimation the number of averages used was 10 and the ordinary coherence function was reasonably close to one. Assuming the average value of the coherence function in the entire frequency range was 0.8 we have that the 95 % confidence limits for the response estimation are

$$0.6971\frac{\langle p^2\rangle}{\langle v^2\rangle} < m < 1.3571\frac{\langle p^2\rangle}{\langle v^2\rangle}. \qquad (5.14)$$

If instead of using (5.13) to estimate the variance of the response we employ expression (4.1), the 95 % confidence limits for the present measurements are given by

$$0.479\frac{\langle p^2\rangle}{\langle v^2\rangle} < m < 1.710\frac{\langle p^2\rangle}{\langle v^2\rangle}. \qquad (5.15)$$

The confidence limits given by (5.15) are much wider than those given by expression (5.14). As only the FRF's were measured we decided to use the confidence limits given by (5.14) in the comparison with hybrid model results. Though it is important to note that real limits can be much wider than the ones we are predicting.

The hybrid model results presented in fig. 5.8 were computed using the computer program described in section 5.1. However, in this case, local pressure response values (eq. (2.16)) were calculated at the six different positions listed in table 5.4 and the results mathematically averaged in order to obtain the space average in positions similar to the ones employed in the experimental work. Considering the uncertainties related to the modelling of the plate boundary conditions good agreement between experiments and hybrid model results is observed above the 315 Hz 1/3 octave band. However, a difference of near 3 dB between the upper limit of the experiments 95 % confidence limits and the hybrid model results are observed at the 160 Hz and 250 Hz 1/3 octave bands. The discrepancy observed at the 160 Hz 1/3 octave band could be explained by the reasonably low number of plate modes excited in this band and by the fact that the modal overlap factor of the plate in this band is lower than unity. As shown in Chapter 4, for cases in which the modal overlap factor was lower than unity good agreement between experimentally and theoretically estimated correlation coefficients was only achieved when more than 7 modes were excited in a frequency band. This could explain the discrepancy at 160 Hz but the situation in the 250 Hz 1/3 octave band is quite different. In this band the plate modal overlap factor equals 2 and seven plate modes are estimated to be excited. Such situation is considered good for the application of the hybrid model and one could

expect these results to approach the experimental ones. Unfortunately, the narrow band results for this system are not available and thus, a deeper analysis of this situation can not be carried out. Similar discrepancies obtained in the wooden box analysis indicate that this difference is relate to a shift in some of the acoustic modes in relation to analytical estimates employed in the computation.

5.2.5 General discussion

A general comparison of all results of this section is presented in fig. 5.9. In this case, 1/3 octave band results of the FEM, SEA and hybrid models with clamped boundary conditions are plotted together with experimental results of the space-averaged acoustic pressure divided by the space-averaged vibration velocity. As shown FEM, hybrid model and experimental results have a similar shape below the first acoustic resonance frequency. At the first resonance frequency, both hybrid and FEM overpredict the experimental result by more than 4 dB. The same situation is repeated at 250 Hz when FEM and hybrid model overpredict the response by 6 and 4 dB, respectively.

As the frequency increases, the number of acoustic and plate modes excited in 1/3 octave bands also increase and the hybrid model results approach that obtained with a SEA model. They are both reasonably close to the 95 % confidence limits for the experimental results above the 500 Hz 1/3 octave band.

In summary it appears that the hybrid model is able to reproduce the results that would have been obtained with either a FEM or a SEA model in their ideal frequency range of applicability. Unfortunately, for the situation in which the hybrid model should give ideal results, differences of 3 dB with experimental results are observed. In order to assess the reasons for such difference a more careful experimental investigation was carried out in a different box. This investigation is described in the next section.

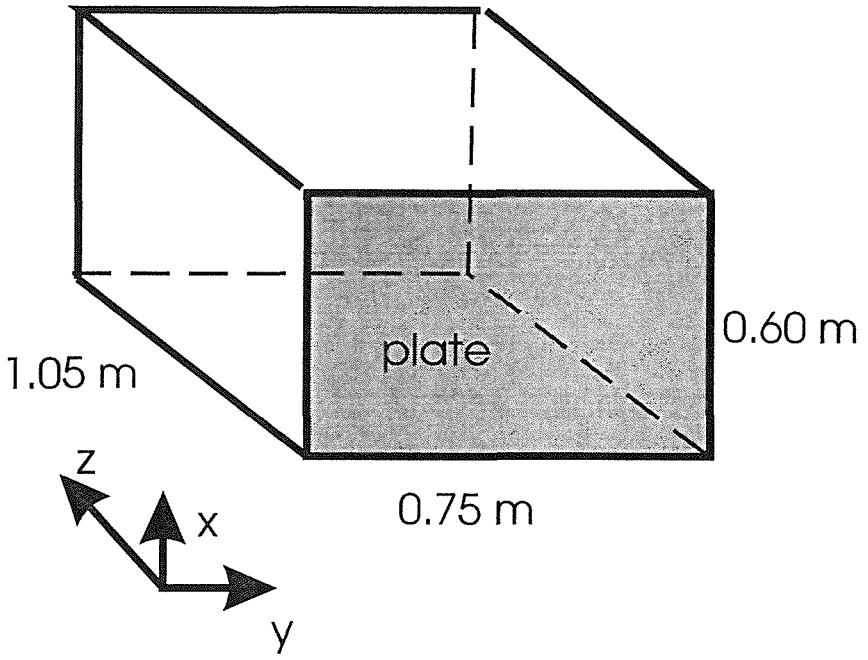

Fig. 5.4 - Sketch of the concrete walled acoustic enclosure and enclosing plate

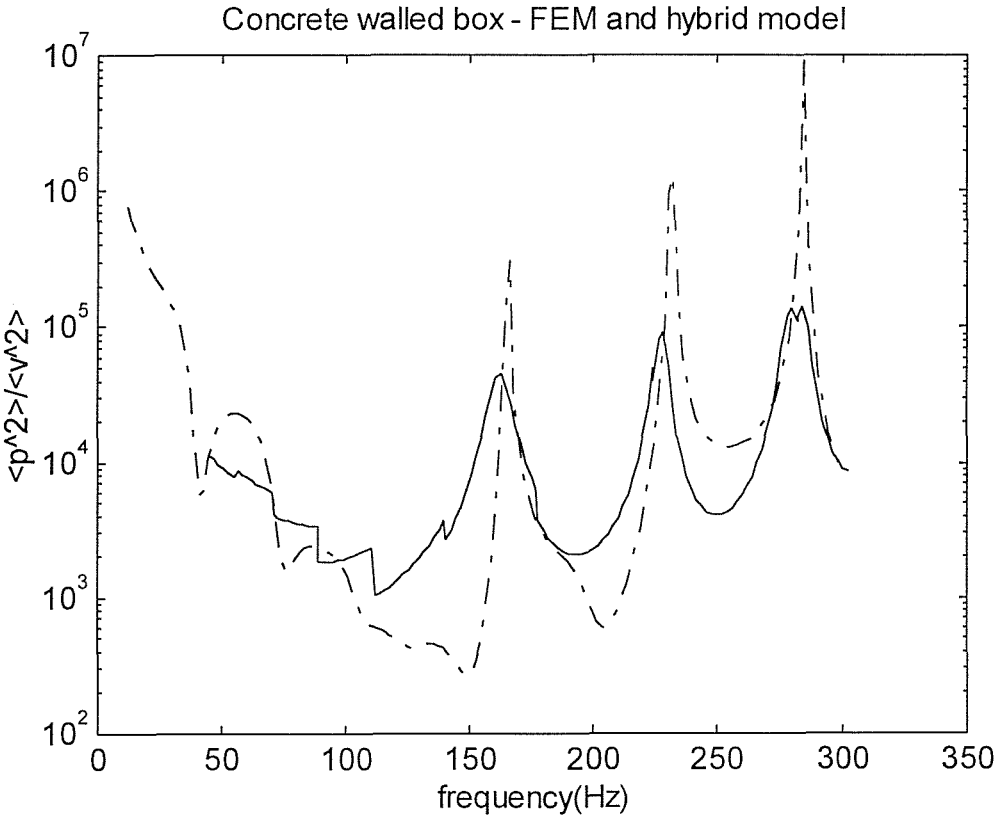

Fig. 5.5 - Space averaged acoustic pressure divided by space averaged vibration velocity on a concrete walled box. Narrow frequency bands. Clamped boundary conditions assumed for plate.
key: ——— hybrid model; – · – · – · – FEM.

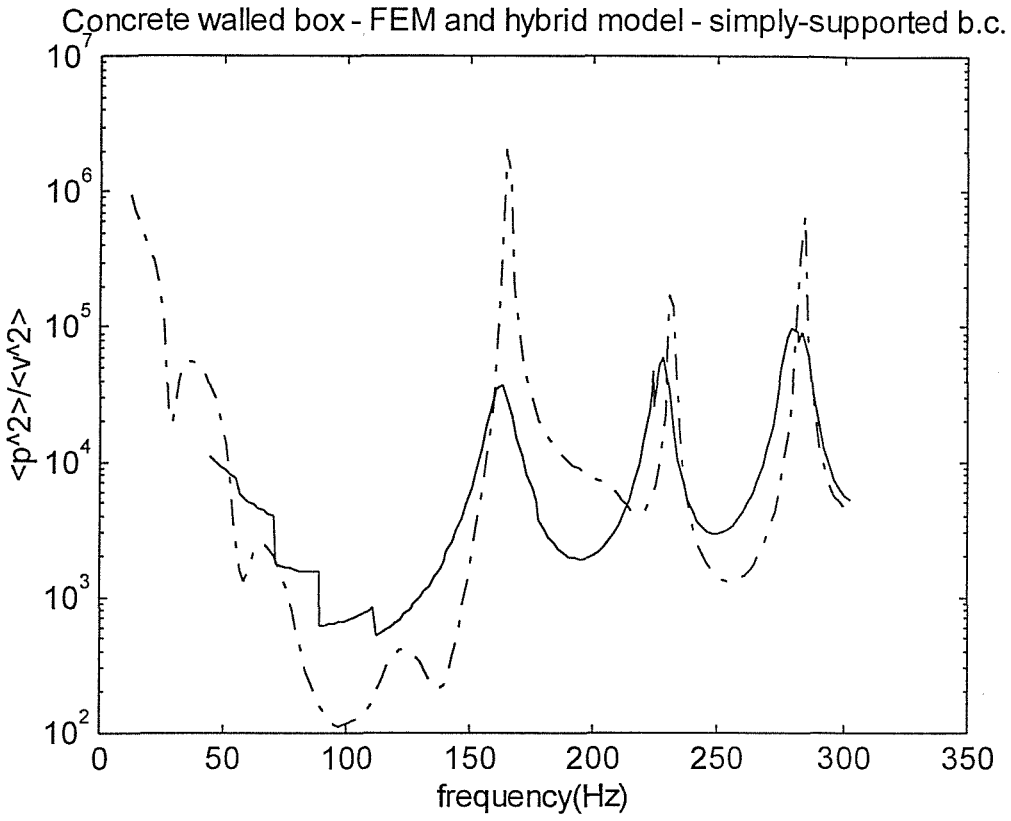

Fig. 5.6 - Space averaged acoustic pressure divided by space averaged vibration velocity for concrete walled box. Narrow frequency bands. Simply-supported boundary conditions assumed for plate. key: ——— hybrid model; – · – · – · – FEM.

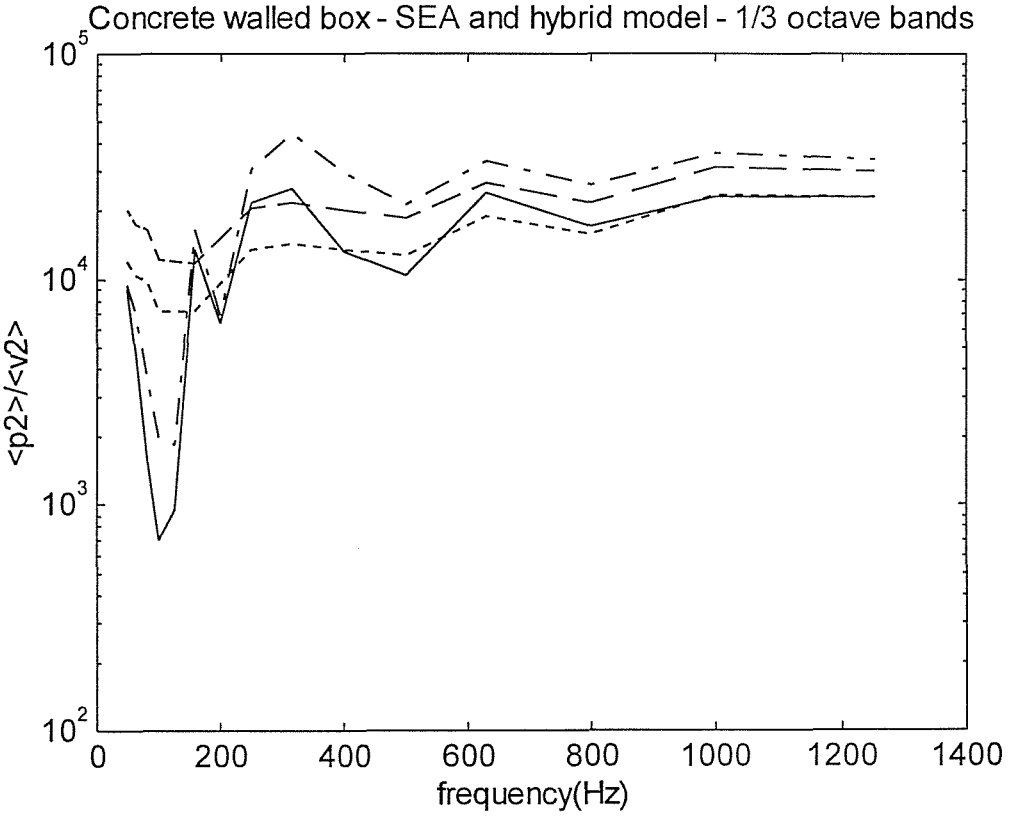

Fig. 5.7 - Space averaged acoustic pressure divided by space averaged vibration velocity for concrete walled box. 1/3 octave bands. key: ——— hybrid model, simply-supported b.c.; — — — SEA, clamped b.c.; – · – · – · – hybrid model, clamped b. c.; - - - - - SEA simply-supported b.c.

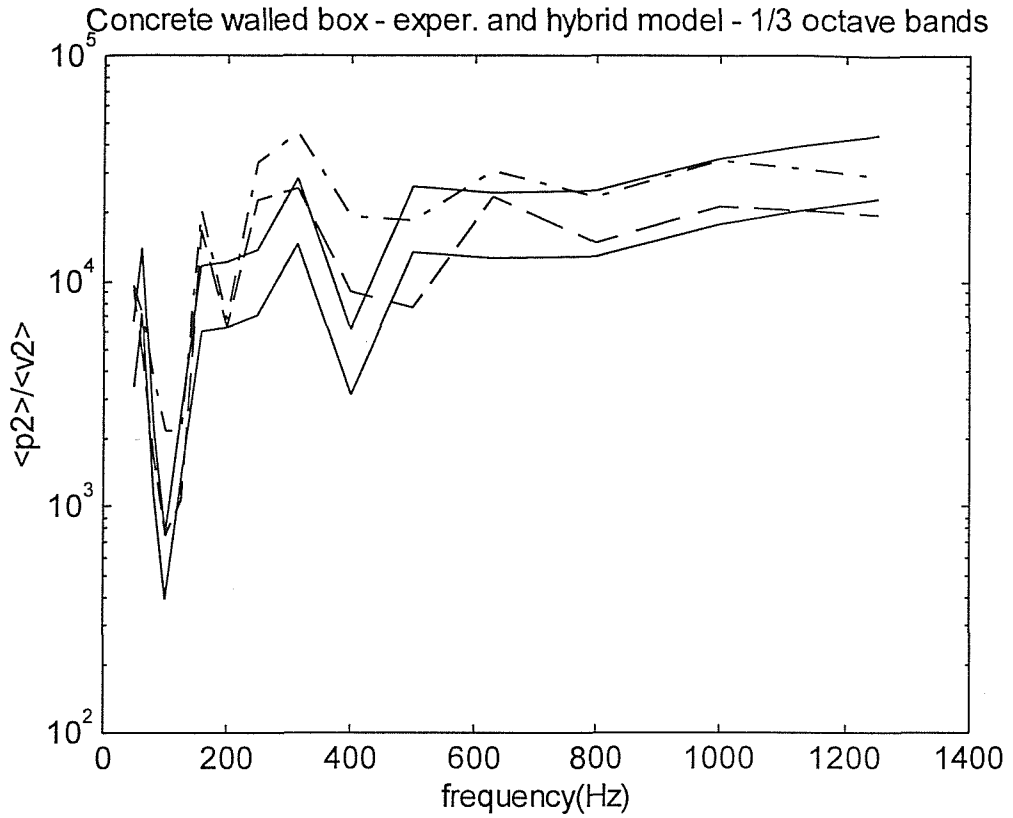

Fig. 5.8 - Space averaged acoustic pressure divided by space averaged vibration velocity for concrete walled box. 1/3 octave bands. key: ——— experimental results, 95 % confidence limits; — — — hybrid model, simply-supported b. c.; – · – · – · – hybrid model, clamped b. c..

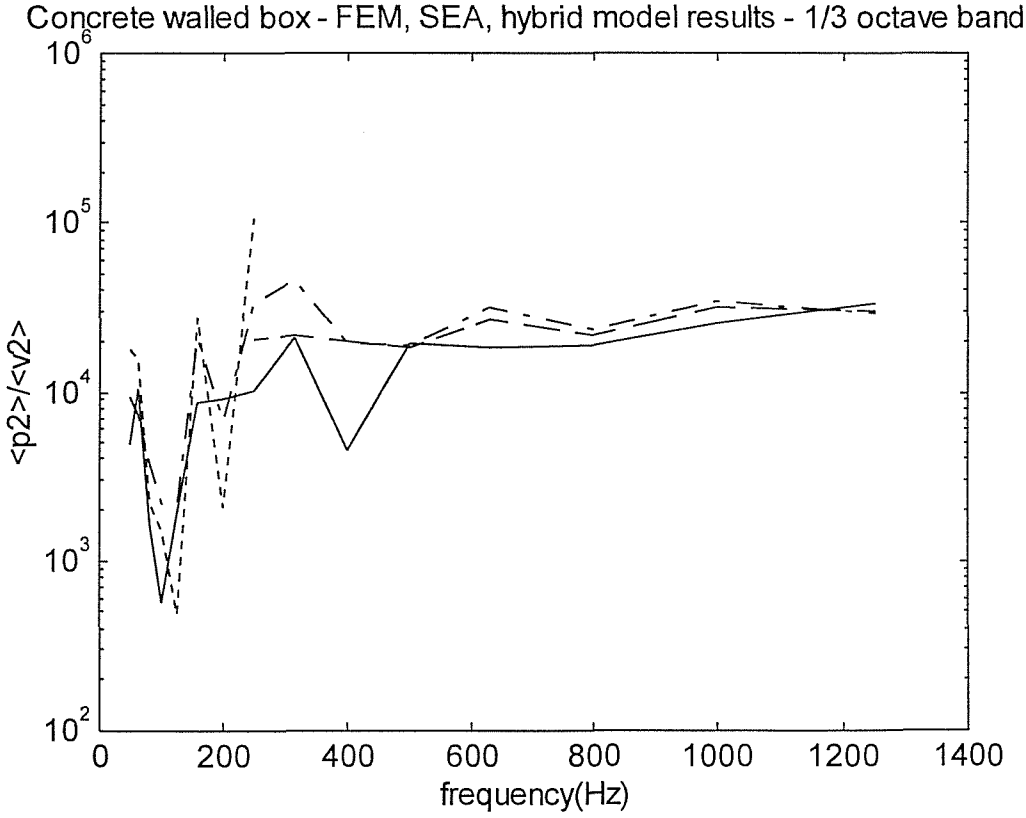

Fig. 5.9 - Space averaged acoustic pressure divided by space averaged vibration velocity for concrete walled box. 1/3 octave bands. key: ——— experimental results; — — — SEA, clamped b.c.; – · – · – · – hybrid model, clamped b.c.; - - - - - FEM results, clamped b.c.

5.3 Wooden box bounded by a flat plate

5.3.1 Description of system

The second box used in this experimental investigation is an enclosure built with five double-sided wood walls filled with sand and one 1.0 mm thick aluminium plate (flexible wall). The internal cavity dimensions are 0.48 x 0.48 x 0.70 m in the x, y, z directions as sketched in fig. 5.10. The plate has dimensions 0.48 x 0.48 m and it is placed in the x-y plane. The edges of the plate are sandwiched by two square metal frames used to simulate a clamped type of support as shown in fig. 4.1. This plate was employed in the experimental investigation of correlation coefficients as reported in section 4.4. Typical frequency response functions for the plate and acoustic cavity are presented in fig. 1.1. As shown in this figure, the acoustic modes are overlapping in the frequency range above 1500 Hz while the plate modes have a high modal overlap factor above 700-800 Hz.

The acoustic loss factors of this acoustic cavity were measured using the half-bandwidth method. For this purpose the flexible wall was removed and another sand-filled wood wall was placed in its position. The acoustic field was excited by a loudspeaker located inside the cavity and the acoustic pressure measured with electret microphones located at four different positions. Each one of the acoustic modal loss factors was estimated using the half-bandwidth function of the ZONIC+AND 3524 Dual Channel FFT Analyser. A frequency separation of 0.625 Hz was employed in the analysis of the pressure signals. These individual loss factors were then averaged in 1/3 octave bands and the results are shown in table 5.5.

5.3.2 Experimental procedure

The experimental results presented in this section are due to mechanical excitation of the flexible wall using a non-contact shaker. Random noise from 0-2000 Hz was used and the results acquired using 4096 FFT points. The resultant spectra have 1600 points with a frequency separation of 1.25 Hz, enough to

guarantee small bias error. Acceleration results were space averaged in 10 points randomly placed over the plate area and the pressure results were averaged in 4 points inside the enclosure. The position of the shaker was varied four times and in each time the acceleration and the acoustic pressure measurements were repeated. As shown in table 5.6, one of the pressure measurement positions was placed near one of the enclosure corners (microphone 2). The positions of the non-contact shaker are listed in table 5.7. These are the same positions employed in the correlation coefficient measurements carried out on this plate for the case of mechanical excitation (section 4.4). Unfortunately, the positions of the excitation were all situated along the same line in the x coordinate because the device that holds the magnet only allows movement in the y direction.

1/3 octave band	acoustic loss factor - η_a
250	0.01
315	0.009
400	0.01
500	0.009
630	0.008
800	0.004
1000	0.004

Table 5.5 - Acoustic loss factor results for the wood walled box

A Bruel&Kjaer 4374 lightweight accelerometer was used to measure the acceleration and electret microphones used to measure the acoustic pressure. Due to the low weight of the accelerometer (0.6 grams) it was estimated that they caused an error of less than 1% in the true plate vibration acceleration for frequencies below 2000 Hz. The electret microphones have flat spectrum from around 80 Hz to 5000 Hz and so, the measured acoustic pressure is only strictly correct above 100 Hz. As no suitable device to calibrate the electret microphones was available a portable

Bruel&Kjaer 4230 calibrator was employed. The calibration factor obtained for the four microphones was very similar indicating that the calibration procedure is reliable.

microphone	x (m)	y (m)	z (m)
1	0.09	0.16	0.25
2	0.005	0.475	0.685
3	0.365	0.26	0.28
4	0.19	0.08	0.48

Table 5.6 - Position of acoustic pressure measurement inside the acoustic cavity

excitation position n.	x (m)	y (m)
1	0.165	0.335
2	0.165	0.10
3	0.165	0.19
4	0.165	0.257

Table 5.7 - Coordinates of the shaker position on flat plate

The acoustic pressure and acceleration signals were acquired using a ZONIC+AND 3524 Dual Channel FFT Analyser and the spectra transferred to a PC-compatible computer where MATLAB was used to analyse the data. Acceleration results were converted to velocity and the spectra calibrated. Data from three and four microphones were used to obtain the space average of the acoustic pressure. The corner microphone (microphone 2) was not included in the first average. The mean-square space averaged acoustic pressure ($<p^2>$) was then divided by the mean-square space averaged vibration velocity ($<v^2>$) and the results plotted in narrow, 1/3 octave bands and bands with constant width of 100 Hz. Alternatively, results from each microphone were divided by the space averaged vibration velocity and the results averaged in terms of excitation position.

The sound pressure level measured by each microphone due to 4 excitation points is presented in fig. 5.11, in order to illustrate the variation of the response with the position of the microphone. As can be seen in this figure, results obtained with the corner microphone (microphone 2) are 6-9 dB higher than the results from the other three microphones for frequencies above 1000 Hz. This agrees with Waterhouse [64] observation that the mean-square sound pressure level in the corners are 9 dB higher than the real space averaged acoustic pressure in a reverberant sound field. The force signal introduced in excitation point 1 was obtained by placing a Bruel&Kjaer 8200 transducer between the coil and the point of connection to the plate. The force auto-spectrum was then used to normalise the space averaged sound pressure level and the space average vibration velocity. These results are presented in fig. 5.19.

The normalised random errors associated with these measurements can be estimated from the expression for the auto-spectrum random error (equation (4.1)). As 100 non-overlapping averages were used to estimate the auto-spectrum of the acoustic pressure we have that the 95 % confidence limits for these measurements are given by

$$0.763\frac{p^2}{\langle v^2\rangle} < m < 1.268\frac{p^2}{\langle v^2\rangle}. \qquad (5.16)$$

These confidence limits for the experimental results are presented in figs. 5.13 and 5.18.

5.3.3 Discussion of results

The computational routine described in section 5.1 was used in the estimation of hybrid model results. Overall sound pressure levels were computed using equation (5.2) while sound pressure levels at individual positions were computed using equation (2.16).

The effect of the plate boundary conditions on the acoustic field inside the acoustic cavity is illustrated by the results presented in fig. 5.12. The plate was assumed to be excited with a spatially-uncorrelated random force and to have all around clamped, simply-supported or free edges or to be represented by a diffuse

bending vibration field. The equations of Chapter 3 and edge parameters of Appendices B and C were employed to simulate these boundary conditions. The overall sound pressure level divided by the space-averaged vibration velocity was computed in 1/3 octave bands from 50 to 800 Hz. The 'ideal' number of integration points and an upper limit of 40 for $k_b r$ were assumed in the computation. As shown, results for clamped edges are slightly higher than those for simply-supported edges and they are both 5-6 dB higher than those of a diffuse field above 315 Hz. As expected, the less efficient in terms of sound generation is the plate with free edges. Results for a plate with this type of boundary condition are 10-20 dB lower than those for a clamped plate. Considering that, as shown in Chapter 4, the vibration field in the centre of these plates approach that of a diffuse bending wave field, the differences in terms of overall sound pressure levels clearly show that the radiation of the plate into the cavity interior is controlled by the vibration field near the edges.

Cheng and Nicolas [33] reported similar results for the case of a circular plate radiating into a cylinder when a variational approach was used to model the vibroacoustic interaction. In this work, it is shown that the plate with free edges can induce sound pressure levels 10-20 dB lower than the clamped one, which is in agreement with the results presented in fig. 5.12. They also observed that the overall level of the plate vibration is not strongly affected by the boundary conditions. This observation supports the results of this work as we are assuming that the boundary conditions only affect the vibroacoustic interaction between the plate and the acoustic cavity without much change to the plate vibration levels.

Some difficulty was encountered with the computation of results for a plate with free edges. Negative values of $\langle p^2 \rangle / \langle v^2 \rangle$ were obtained for the first two 1/3 octave bands (50 and 63 Hz) irrespective of the number of integration points employed in the numerical computation. Therefore, results for the free plate are only reliable above 80 Hz.

The comparison between the sound pressure level averaged from four microphone positions and the hybrid model results for the same positions are presented in figs. 5.13 and 5.14. The microphone positions used in the computation are those listed in table 5.6. The experimental results are due to the four excitation positions listed in table 5.7. The 95 % confidence limits (equation (5.16)) estimated

for the experimental results are presented in fig. 5.13. The theoretical results are averaged in 1/3 octave bands and the coupling coefficient used in the narrow band theoretical results are assumed constant in each 1/3 octave band. As already observed in section 5.2, the use of such assumption leads to the appearance of jumps in the narrow band results (fig. 5.14).

Good agreement between experimental and theoretical results are observed above the 315 Hz 1/3 octave band (fig. 5.13). This agreement was expected because, as reported in section 4.4, the experimental results of correlation coefficient on this plate due to mechanical excitation only approach the theoretical correlation model at frequencies above the 315 Hz 1/3 octave band. Such agreement in terms of correlation coefficients is illustrated in fig. 4.3. However, as shown in the same figure, for frequencies below 315 Hz (like the 160 Hz 1/3 octave band results), both models are quite different. This disagreement reflects in the response results as exemplified by the result at 250 Hz 1/3 octave band, the frequency in which the first acoustic resonance frequency is situated. In this frequency band, differences of over 8 dB in 1/3 octave band results and 4 dB in the narrow band results are observed.

The plate modal overlap factor is estimated to be lower than unity and only 4 plate modes are assumed to be excited in the 250 Hz 1/3 octave band. As discussed in Chapter 4, when the modal overlap factor is lower than unity at least 8 to 10 plate modes need to be excited in a frequency band for the correlation model described in Chapter 3 be valid. This explains the difference observed in figs. 5.13 and 5.14. In addition, we also observe that, in contrast to the concrete walled box, the first acoustic resonance frequency was underpredicted in this case.

As presented in Chapter 1, based on a modal coupling study between a plate and an acoustic cavity Pan and Bies [28] concluded that the overall nature of the coupling in the region of a cavity mode resonance frequency is governed by the average number of plate resonance frequencies available in this region. As a result, when the acoustic cavity and plate modal densities are low the energy transfer between acoustic and plate systems will usually be dominated by one single plate mode. Therefore, small changes in the plate resonance frequencies will lead to substantial changes in the coupling between both systems. This observation agrees with that from Franchek and Bernhard [13] and with the experimental results here

reported for the frequency band in which the first acoustic resonance frequency appears. The increase in the plate modal density leads to a decrease in the importance of individual coupling between each pair of modes and to a decrease in the variation of the frequency averaged modal coupling coefficient. This situation is exemplified by the results of the Monte Carlo study performed by Mohammed [45] in coupled plate and acoustic cavity systems. As mentioned in Chapter 1, he observed that the fluctuation of the radiation resistance (vibroacoustic coupling) with the mean diminishes as the modal density and modal overlap factors of both systems increase. Therefore, a reliable prediction of the response of the first acoustic mode to plate vibration is only possible if the plate modal density is high and/or its modal overlap factor is close or higher than unity. This applies irrespective of the procedure used to model the vibroacoustic coupling between an acoustic mode and a few plate modes.

The narrow band results, fig. 5.14, show that most of the acoustic cavity modes observed in the experiments are predicted by the hybrid model. There are some differences, mainly near 800 Hz, when some of the real acoustic modes shift from the theoretically predicted values and the theoretical model is not able to predict this shifting. Experimental modal analysis could be an alternative to overcome such difficulty in predicting the exact value of the first acoustic modes. However, if one is only concerned with frequency averages, the results above 315 Hz show that the present method provides a efficient way of predicting the response. Moreover, the results in narrow bands are reasonably good for most of the practical situations.

One of the advantages of the approach proposed in this research in relation to SEA is the capability of predicting local sound pressure levels. This capability is exemplified by the results presented in figs. 5.15, 5.16 and 5.17. Experimental results averaged in three and four microphone positions are presented in fig. 5.15. As mentioned, the three microphone result is lower than the four microphone result as the microphone n. 2 (corner microphone) sound pressure levels are included in the latter. Both theoretical results computed with the hybrid model assuming clamped boundary conditions for the plate are reasonably similar to the experimental results for frequencies above 315 Hz 1/3 octave band. The narrow band results presented in this figure are for the 3 microphones average and they show a similar behaviour to the one presented for 4 microphones.

Results for the sound pressure level near one of the acoustic cavity corners are presented in fig. 5.16. The 1/3 octave band averages show a similar behaviour to the results presented in figs. 5.15 and 5.13, but in this case only 6 dB separates experimental and theoretical results at 250 Hz. The theoretical model uses clamped and simply-supported boundary conditions for the plate, but the agreement is better between clamped and experimental results. The results presented in this section indicate that clamping is the most suitable boundary condition for the plate used in the wood walled box. This conclusion is also corroborated by the correlation coefficient results (section 4.4).

A slightly better agreement between experimental and theoretical results near the first acoustic resonance frequency can be achieved if the experimental results are averaged in constant bands. Figure 5.17 shows hybrid model results computed at the coordinates (0.365,0.26,0.28) in constant bands of 100 Hz centred at 50 to 1350 Hz. In this model the acoustic damping was estimated based on the 1/3 octave band loss factors listed in table 5.5 and the 'ideal' number of integration points was employed in the numerical integration. The numerical integration results were truncated for $k_b r$ equals to 50. This truncation only affects higher frequencies and enough care was taken to avoid underestimating the response in the higher end of the spectrum. The theoretical results are not more than 3 dB different from experimental results for all frequency bands down to 150 Hz. The only unexpected variation was at 750 and 850 Hz where the shape of the experimental and theoretical results are different. As shown by the narrow band results this difference is due to an acoustic resonance frequency near 800 Hz which is not predicted by the hybrid model. In this case, it is the variation of the acoustic resonance frequencies in relation to the analytical model employed in the hybrid model that is responsible for the difference. The good agreement in terms of level and shape between most of the acoustic resonances indicates that the vibroacoustic coupling is well represented by the hybrid model. This is expected as nearly 8 plate modes are excited in frequency bands of 100 Hz width and the modal overlap factor of this plate exceeds unity above 800 Hz.

In section 3.3, the effect of the type of excitation in the correlation model adopted for the plate was discussed. It was shown that when the structure is modally-dense the resonant response of the structure in terms of correlation

coefficients (or normalised cross-power spectral density) is not greatly affected by the excitation. This conclusion was further checked by computing hybrid model response results assuming spatially uncorrelated excitation ('rain-on-the-roof') or point excitation. The results obtained in both cases were very similar and it appears that the assumption of point excitation does not affect the response results. One of these results is presented in fig. 5.18.

The hybrid model results shown in fig. 5.18 were calculated for only one excitation point, point n. 4 (table 5.7), and the sound pressure level at coordinates (0.005,0.475,0.685) computed in 1/3 octave bands. The parameters of this computation were the same as the one employed for the results presented in fig. 5.16. The hybrid model results fall close or inside the experimental results 95 % confidence limits for all 1/3 octave bands above 200 Hz. The agreement between experimental and theoretical results in frequency bands in which few plate modes are excited is not expected, although, as shown by this result, it is not unlikely to happen.

The use of equation (2.21) in the computation of the ratios $\langle p^2 \rangle / \langle F^2 \rangle$ and $\langle v^2 \rangle / \langle F^2 \rangle$ is exemplified by the results presented in fig. 5.19. In this case, the plate loss factor was assumed to be 0.005 and a spatially uncorrelated random force to be applied on the plate. The theoretical results were computed for four microphone positions (table 5.6) using equation (2.21) while the space average vibration velocity was computed using equation (2.20). Both were assumed to be normalised by the space averaged random force. The use of these equations imply that the power input is computed on a number of points over the plate area. This involves experimentally estimating the force power spectrum and the real part of the point mobility in various points over the plate area to obtain the space average of the power input. Unfortunately, we only had the spectrum of the force for one excitation point. In view of this, we did not expect to obtain a good agreement between experiments and theoretical results. To our surprise, the results were not too different above 400 Hz and it is clearly shown in fig. 5.19 that some of the difference is related to the computation of $\langle v^2 \rangle / \langle F^2 \rangle$ which is theoretically equal to

$$\frac{n(f)}{4\omega_c M^2 \eta_p}. \tag{5.17}$$

This result uses a power flow balance similar to SEA in order to compute the space average vibration velocity from the power input in the structure. Therefore, the recommendations related to SEA described in Chapter 1 and in the SEA literature ([10,14,38,39]) applies to the computation of equation (2.21). In this case we need a high modal overlap factor and at least 8-10 modes to guarantee the validity of the equations used in the derivation of equation (2.21). These are similar recommendations as the one described at the end of Chapter 4 and therefore, we expect equation (2.21) to be valid in the same frequency range that equations (2.16) or (5.2) are valid.

In general, a reasonably good agreement between experimental and theoretical results was observed for the wood walled box analysed in this section. The plate vibration field is modelled using the modally-dense representation suggested in Chapter 3 and as a result, such agreement was verified in frequency bands in which the number of excited plate modes was estimated to exceed 6-10 modes. The boundary condition of the clamped type was the one that gave best results for the present acoustic cavity/plate system. Poor agreement was observed when a few plate modes excite a single acoustic mode. The results for the same acoustic cavity/plate system in which an aluminium bar are attached to the plate are reported in the next section. Such stiffened plate aims to represent typical panels encountered in aircraft and car structures.

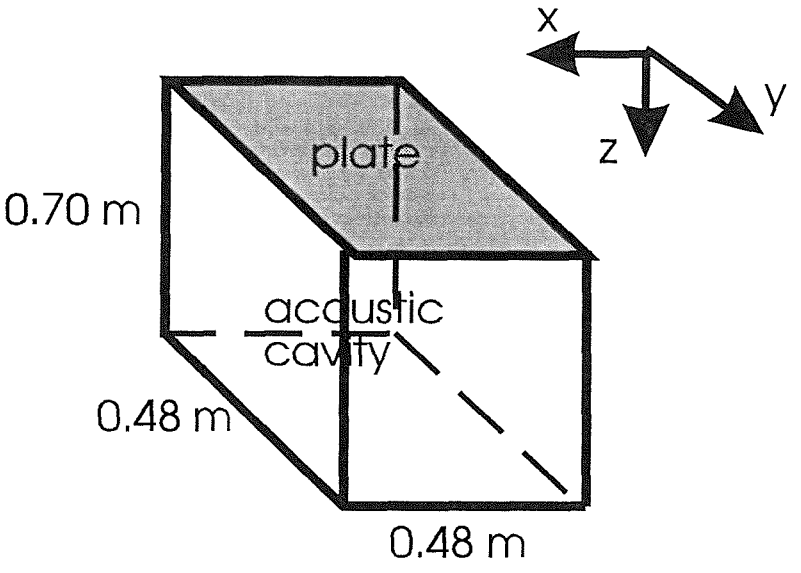

Fig. 5.10 Sketch of wood walled box and enclosing plate

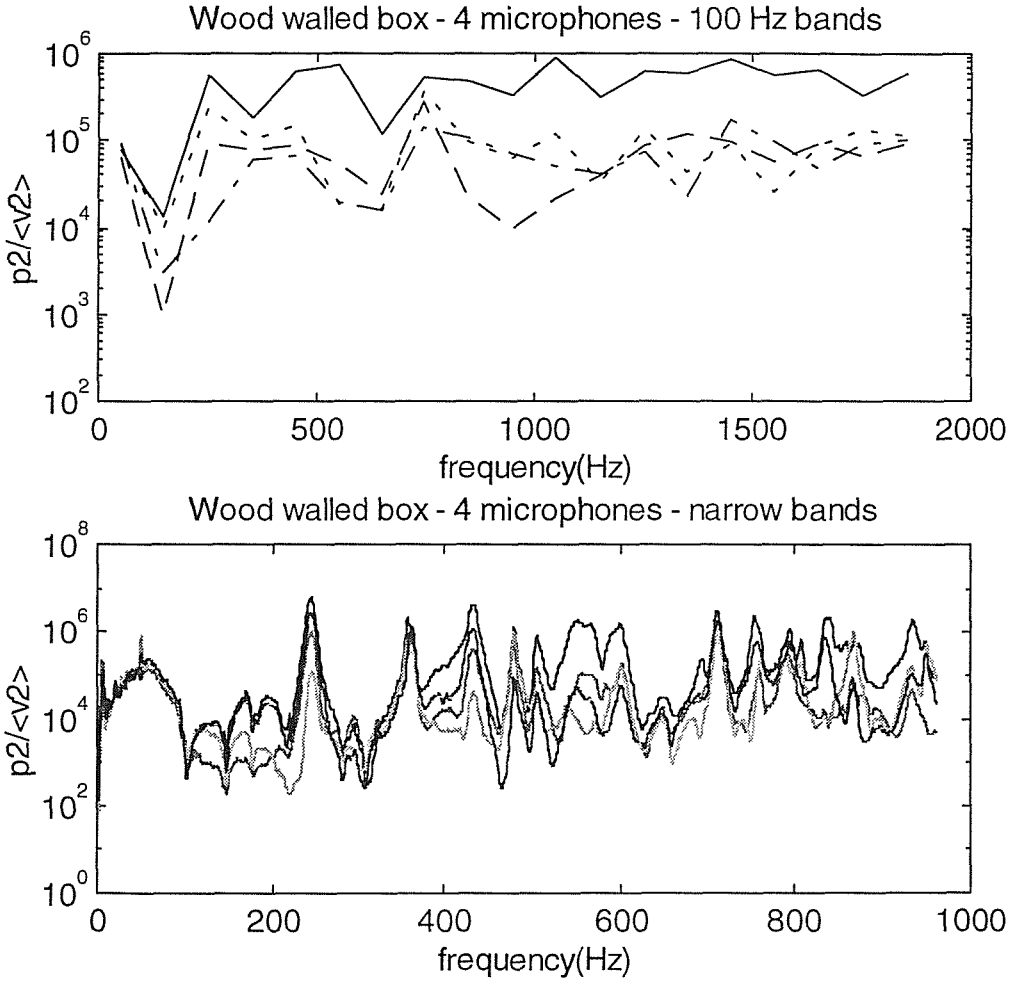

Fig. 5.11 - Experimental results of sound pressure level divided by space averaged vibration velocity in wood walled box. 100 Hz bands. key: ——— microphone 2; — — — microphone 1; – · – · – · – microphone 3; - - - - - microphone 4.

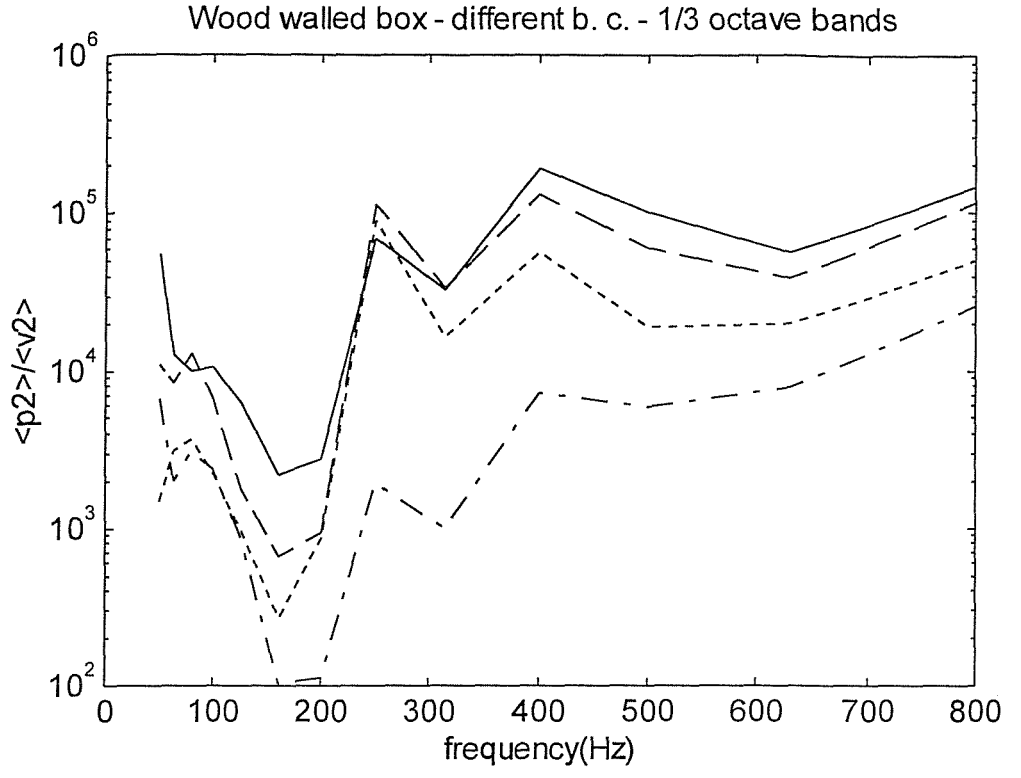

Fig. 5.12 - Hybrid model results for overall sound pressure level divided by space averaged vibration velocity in wood walled box. 1/3 octave bands. key for boundary conditions: ——— clamped; — — — simply-supported; – · – · – · – free edges; - - - - - diffuse bending wave field.

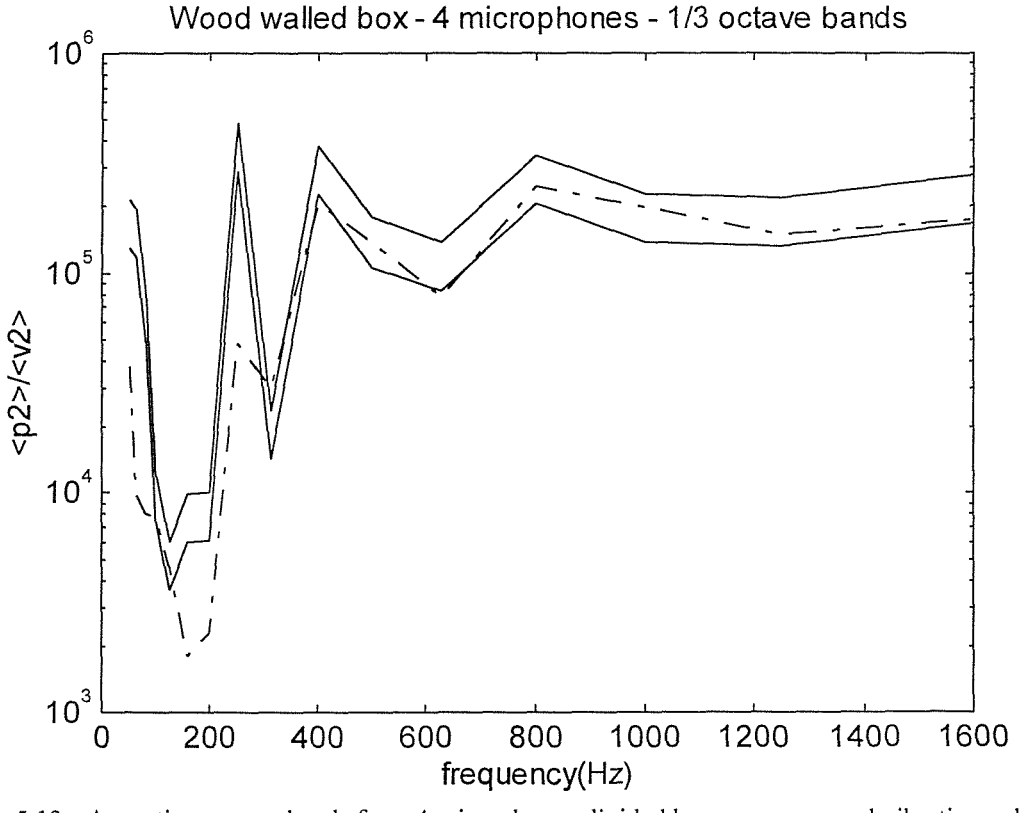

Fig. 5.13 - Acoustic pressure levels from 4 microphones divided by space averaged vibration velocity for wood walled box. 1/3 octave bands. key: ——— experimental results, 95 % confidence limits; – · – · – · – hybrid model, clamped b.c..

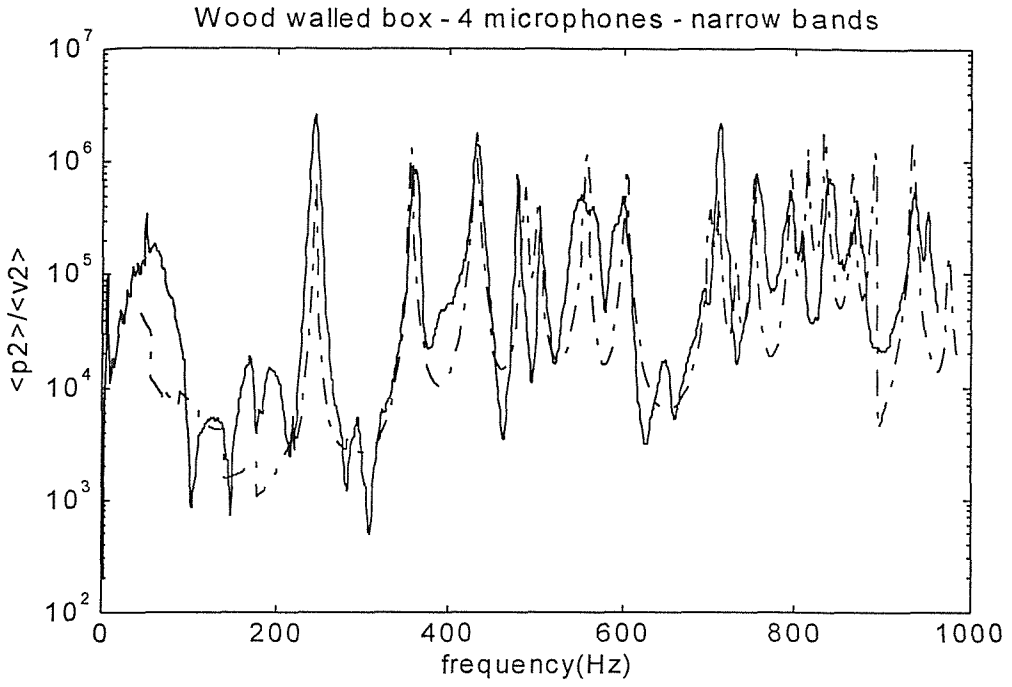

Fig. 5.14 - Acoustic pressure levels from 4 microphones divided by space averaged vibration velocity for wood walled box. narrow bands. key: ——— experimental results from 4 microphones average; – · – · – · – theory, clamped plate.

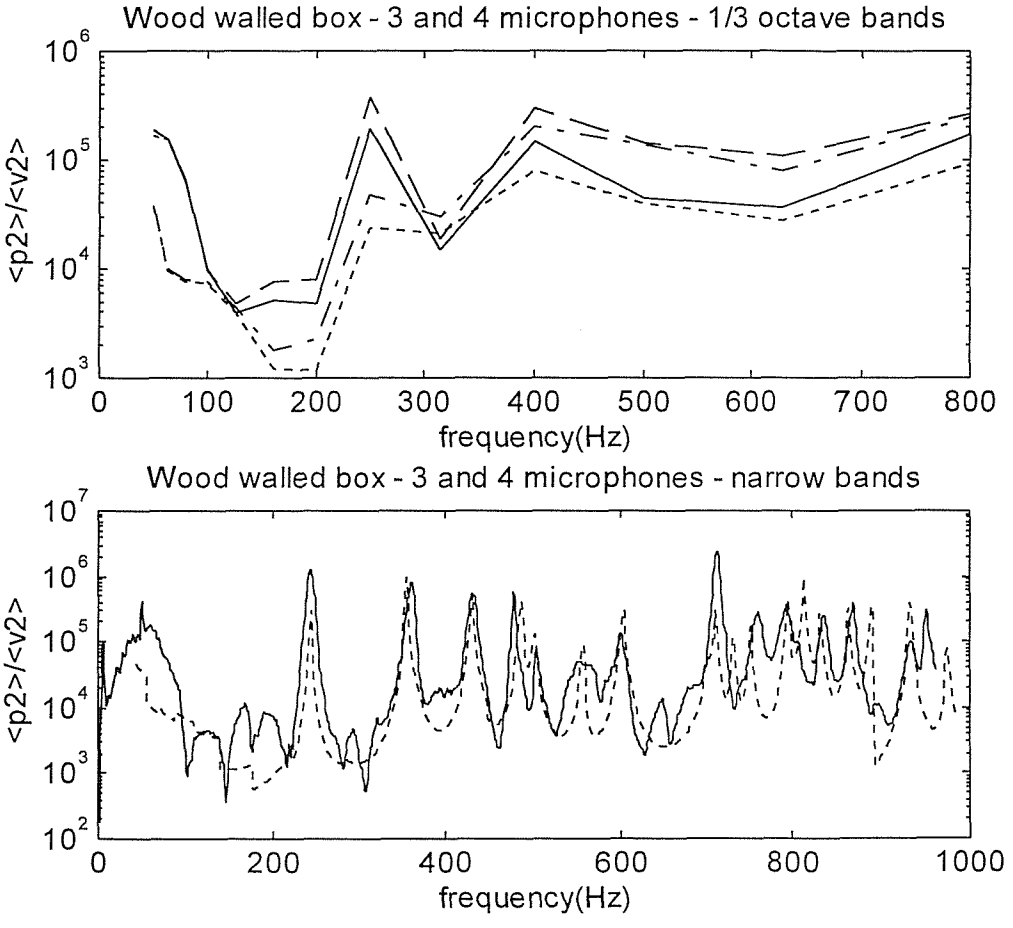

Fig. 5.15 - Sound pressure levels from 3 and 4 microphones divided by space averaged vibration velocity for wood walled box. key: ——— experiments, 3 mics; — — — experiments, 4 mics; – · – · – · – theory, 4 mics; - - - - - theory, 3 mics.

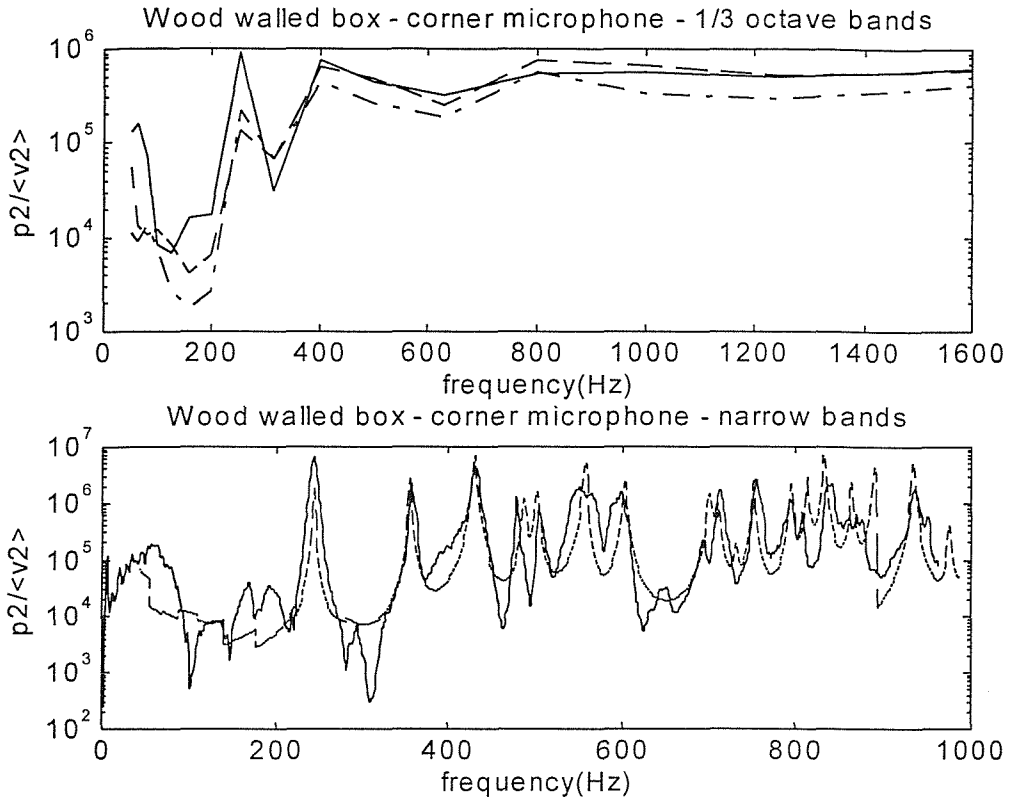

Fig. 5.16 - Acoustic pressure from corner microphone (microphone 2) divided by space averaged vibration velocity for wood walled box. key: ——— experimental results, microphone at (0.005,0.485,0.695); — — — theory, clamped plate; – · – · – · – theory simply-supported plate.

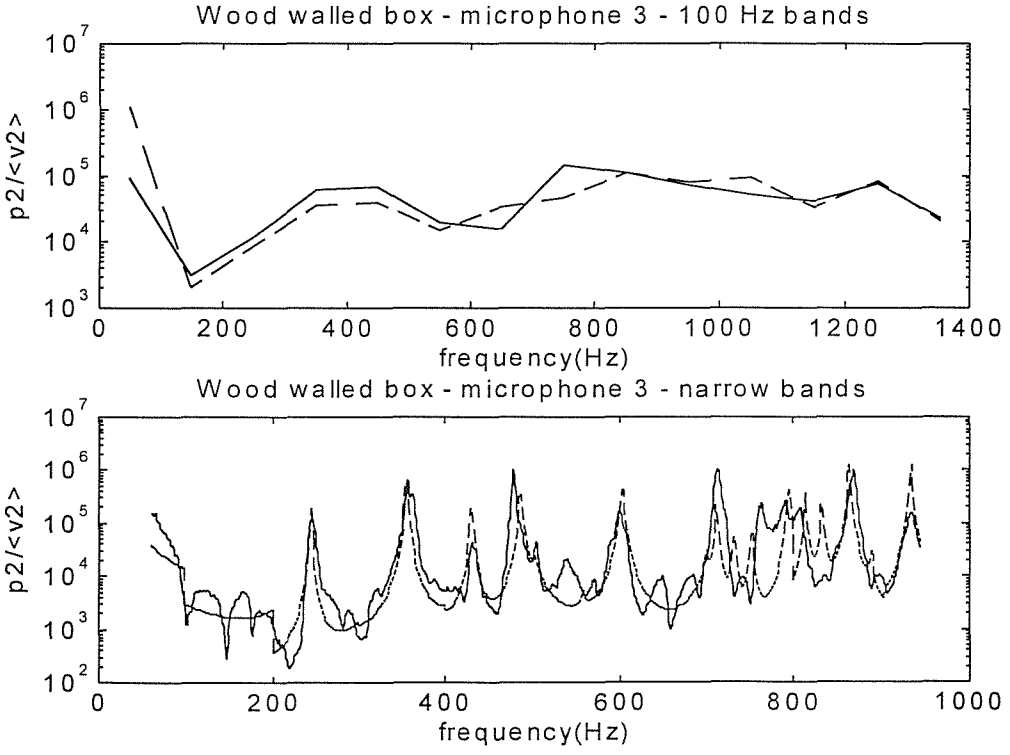

Fig. 5.17 - Acoustic pressure from microphone 3 divided by space averaged vibration velocity. Average of 4 excitation positions. 100 Hz constant bands. key: ——— experimental results, microphone 3, coordinates (0.365,0.26,0.28); — — — theory, clamped plate.

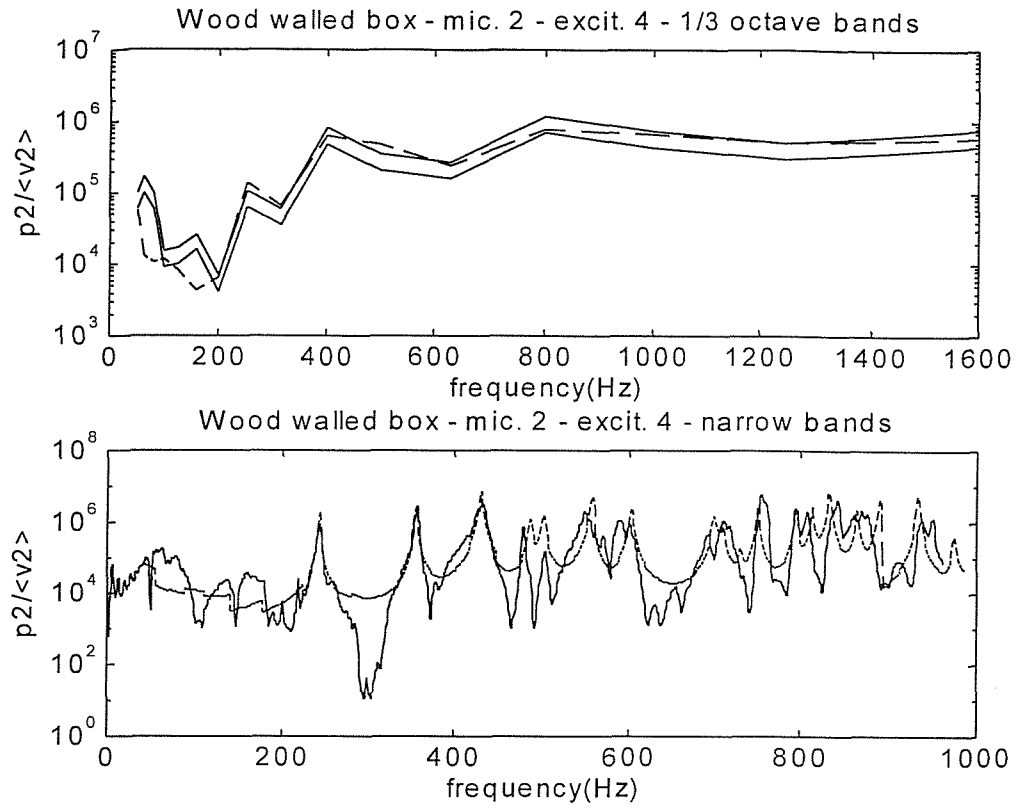

Fig. 5.18 - Acoustic pressure from corner microphone (microphone 2) divided by space averaged vibration velocity from excitation at position 4. key: ——— experimental results, microphone at (0.005,0.485,0.695), 95% confidence limits; — — — theory, clamped plate.

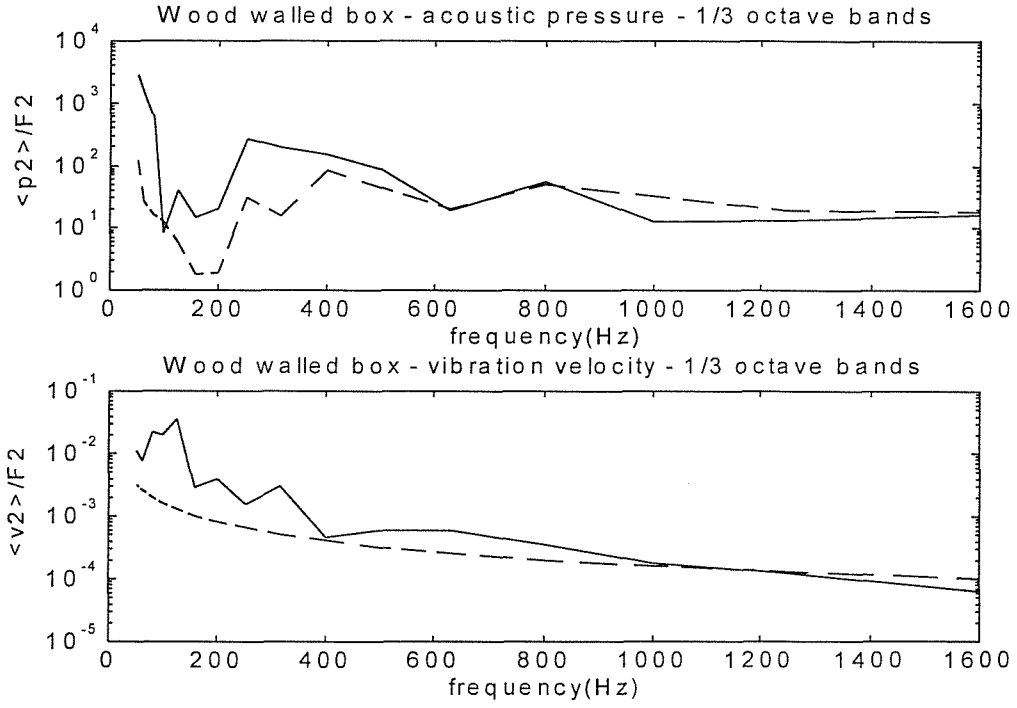

Fig. 5.19 - Four microphone average acoustic pressure and space average vibration velocity divided by mean square force at excitation point 1. key: ——— experimental results; — — — theory (eq. (2.21)), clamped plate.

5.4 Wooden box bounded by a stiffened plate

5.4.1 Description of system

In order to represent a typical stiffened panel, a small aluminium bar was attached to the flat plate that bounds the wood walled box described in section 5.3. As a result the plate was divided in two sections of 0.28 m and 0.20 m length along the x axis. The bar was fixed to the plate using a thick double-sided tape. A sketch of the position in which the bar was placed is represented in fig. 4.7 while a typical section of this bar is shown in fig. 5.20. The natural frequencies of longitudinal, torsional and transverse vibration of this bar are listed in table 5.8. Such natural frequencies were computed following the expressions presented by Blevins [79].

order of natural frequency	transverse vibration (Hz)	longitudinal vibration (Hz)	torsional vibration (Hz)
1	282.0	5341.7	913.5
2	776.9	10683.0	1827.0
3	1522.7	16025.0	2740.5

Table 5.8 - Natural frequencies of vibration of the stiffener sketched in fig. 5.20.

The correlation coefficient and normalised cross-power spectral density for the flat plate with the stiffener are compared to corresponding theoretical results in section 4.4. As shown in figs. 4.8 and 4.9, the results at 250 Hz 1/3 octave bands are reasonably similar indicating that some agreement between experimental and theoretical response results can be expected in this frequency band. This is confirmed by the results presented in this section.

5.4.2 Experimental procedure

The experimental procedure and apparatus used in this experimental investigation are identical to those described in section 5.3.2. The only difference concerns the mechanical excitation applied to the plate as different coils were used with the same magnet employed in the previous experiment. As a result, slightly different excitation positions had to be employed and they were reduced to 3 instead of 4. The excitation positions are listed in table 5.9. It can be noted from this table that the shaker was placed in the 0.28 m length section in which the plate was divided due to the restriction imposed by the device that holds the magnet.

excitation position n.	x (m)	y (m)
1	0.165	0.26
2	0.165	0.10
3	0.165	0.345

Table 5.9 - Coordinates of the non-contact shaker position on stiffened plate

Ten measurement positions were employed to estimate the plate vibration levels, 4 positions were situated on the indirectly excited side and 6 on the directly excited side. As shown in fig. 5.21, the vibration levels in both sides were quite different with levels in the directly excited side 2-4 dB higher than in the indirectly excited one. This departs greatly from the spatially uncorrelated type of excitation assumed in the hybrid model. In this model, the space-averaged vibration levels are assumed to be relatively constant along the plate, which is clearly not the case here. Because of restrictions with the test rig, the shaker could not be moved to the small side of the stiffened plate which could be a way of averaging the results in terms of excitation and overcoming this problem. Another way of overcoming this problem is by correcting the experimental results in order to simulate that the vibration levels are the same in both sides. In this alternative, the space average is

multiplied by a correction factor calculated from the ratio of the spectra presented in fig. 5.21. Far from ideal, this was the alternative adopted in the present work.

5.4.3 Discussion of results

The normalised cross-power spectral density for the stiffened plate was computed using the model described in Chapter 3 (equation (3.23')). The plate was divided in two sides defined by the position of the stiffener. In one side, the edge parameters for a clamped boundary and that for the reflecting side of a spring coupling are employed in the computation. In the other side, clamped and transmitting side of a spring coupling edge parameters are adopted. Expressions employed in the computation of the edge parameters are presented in Appendices B, C and E. The stiffness coefficients for the spring coupling are computed with the expressions presented in section B.6 based on the aluminium bar dynamic characteristics. The vibration levels are assumed to be similar in both sides of the plate.

The computational model here employed uses the 'ideal' number of integration points and an upper limit of 60 for $k_b r$. Results are averaged in 1/3 octave bands from 50 to 1600 Hz and 100 Hz constant bands from 50 to 1350 Hz. The sound pressure levels in the four points listed in table 5.6 are computed and arithmetically averaged. These theoretical results are compared to the 95 % confidence limits of the experimental results in figs. 5.24 and 5.27.

The increase in the sound pressure levels induced by the stiffened plate are illustrated in fig. 5.22. Experimental results for the plate with and without the stiffener are presented in this figure. These sound pressure levels have been obtained from the average of four microphones measurements. An increase of nearly 2 dB above the first acoustic resonance frequency in the sound pressure level due to the stiffener addition is observed. A similar increase is predicted by the theoretical results computed at the same microphone positions. This increase in the plate radiation due to the addition of a stiffener also agrees with the factor suggested by Maidanik [37]. In ref. [37], Maidanik suggests that stiffeners added to a flat plate will increase its radiation efficiency below the critical frequency by a factor of

$$(2L_{st} + P)/P, \qquad (5.18)$$

where L_{st} is the stiffener length and P is the plate perimeter. This suggestion is based on the idea that the stiffener will make the stiffened plate radiate as two plates with similar vibration levels and that the radiation resistance below the coincidence frequency is proportional to the plate perimeter. When applied to the present case this factor estimates that the radiation efficiency of the stiffened plate will be increased by 1.5 which is equivalent to 1.7 dB in a logarithmic scale. This agrees with the results presented in fig. 5.22. Moreover, this increase is another evidence that the acoustic radiation of a flat plate is controlled by the edges vibration field. In the present situation the perturbation created by the stiffener looks like a boundary for the vibration field and the increase in the acoustic radiation is caused by the interference created by the stiffener.

The point mobility for plates with and without a stiffener are illustrated in figs. 4.13a and 4.13b. In these figures we observe that the frequency response is clearly altered with the addition of the stiffener and it is now more complex with an apparent increase in its loss factor. As shown in fig. 5.23, this is reflected in the spectrum induced by the stiffened plate which is more erratic and less clean than the one induced by the plate without the stiffener. As these results are normalised by the space-averaged vibration velocity, such difference appears to be related to the stiffener addition. However, similar acoustic natural frequencies appear in both spectra. Another difference observed in this figure is the increase in the height of the valley between two adjacent natural frequency peaks for the stiffened plate case. Such increase is also observed in the narrow band theoretical results and is responsible for the higher frequency averaged levels induced by the stiffened plate.

The agreement between the predicted and measured sound pressure levels when the stiffened plate is modelled using the hybrid model is reasonably good in the case of 1/3 octave bands. The only major difference is in the 1000 Hz 1/3 octave band when the hybrid model underpredicts the sound pressure level. This underprediction is also observed when the experimental results are averaged in constant bands of 100 Hz. This difference is illustrated in fig. 5.24 where theoretical results computed for these frequency bands are compared to the 95 % confidence limits of the experimental results. Experimental results are underpredicted in the 950

Hz band by nearly 3 dB. On the other hand, the same experimental results are overpredict by 3 dB in the 750 Hz band. These differences are mostly related to a shift in some of the acoustic modes in relation to the ones predicted by the analytical expressions (equations 5.3 and 5.4) and by the increase in the level of the valleys between two acoustic resonances. The level of this increase appears to not be well predicted by the coupling coefficient employed in the hybrid model. Narrow band results presented in fig. 5.25 clearly show this difference for the case of acoustic modes in the 700-800 Hz interval. Finally, as shown in fig. 5.24, the theoretical results are reasonably similar to the experimental ones in the other bands.

The spatial variation of the sound pressure level is again reasonably well predicted as presented in figs. 5.26 and 5.27. The theoretical results shown in figure 5.26 are from a computation in which 1/3 octave bands, an upper limit equals to 60 for $k_b r$ and the ideal number of integration points were adopted. The vibration level was assumed to be the same for both sides of the plate. The 3 and 4 microphones results are clearly distinct and the theoretical model manages to reproduce this distinction. For the four microphones case there is a clear difference in the 1/3 octave band centered in 800 Hz. The reasons for the difference in this band are the same quoted for the difference in the 950 Hz band shown in fig. 5.24. The situation for the three microphones case is slightly different. In this case, there is a clear distinction of around 2 dB for the 800, 1000 and 1250 Hz 1/3 octave bands. This is similar to the predictions in the non-stiffened plate case in which a better agreement was observed in the four microphones average than in the three microphones one. Moreover, as shown in figs. 5.15 and 5.26, the theoretical results underpredict the three microphones average results.

It is here suggested that such discrepancy is associated with the error in the analytical prediction of some of the acoustic cavity resonance frequencies. For the wooden box such error is probably related to the existence of a device to hold the magnet for the non-contact shaker inside the cavity. This device is formed by a network of beams and because it is quite bulky it can perturbe the mode shape of some of the acoustic modes, altering their vibroacoustic coupling characteristics and resonance frequencies. This suggestion is based on the fact that the acoustic pressure results that apppears to be less affected by the presence of this bulky device are the

ones obtained with the corner microphone (microphone 2) which is the microphone most distant from this device.

The sound pressure levels in the band in which the first acoustic mode appears are better predicted for this system than for the non-stiffened plate case. As discussed in section 4.5, one of the effects of a stiffener on the plate vibration field is to increase its apparent loss factor and therefore increasing its modal overlap factor. These changes are reflected in the fact that experimental correlation coefficients (and normalised cross-power spectral density) results for the stiffened plate approach the theoretical predictions in the 250 Hz 1/3 octave band. Such agreement is illustrated by the results presented in figs. 4.8 and 4.9 for line G which is placed near the stiffener. Furthermore, this is also reflected in the better agreement between experimental and theoretical sound pressure levels in the 250 Hz 1/3 octave band. In this frequency band, the difference between both results is only 2 dB in comparison with a 8 dB difference for the non-stiffened plate.

The capability of the present approach in predicting local response values is further illustrated by the results presented in fig. 5.27. The sound pressure level measured by the corner microphone (microphone 2) and divided by the space average vibration velocity is compared to hybrid model results at the same acoustic cavity position. As shown, most of the frequency averaged results are very close to the experimental results 95 % confidence limits. The parameters used in this computation are those described for the results presented in fig. 5.26 with 139 acoustic modes included in the modal summation. The inclusion of such large number of acoustic modes caused the running time on a Sun-Sparc Unix system (University of Southampton Solaris system) to average between 30 to 100 minutes depending on the boundary conditions adopted. The good agreement observed for the results in the higher 1/3 octave bands indicates that the neglect of the cross-terms in the derivation of equation (2.16) is valid even for cases in which the acoustic modal overlap factor is higher than unity.

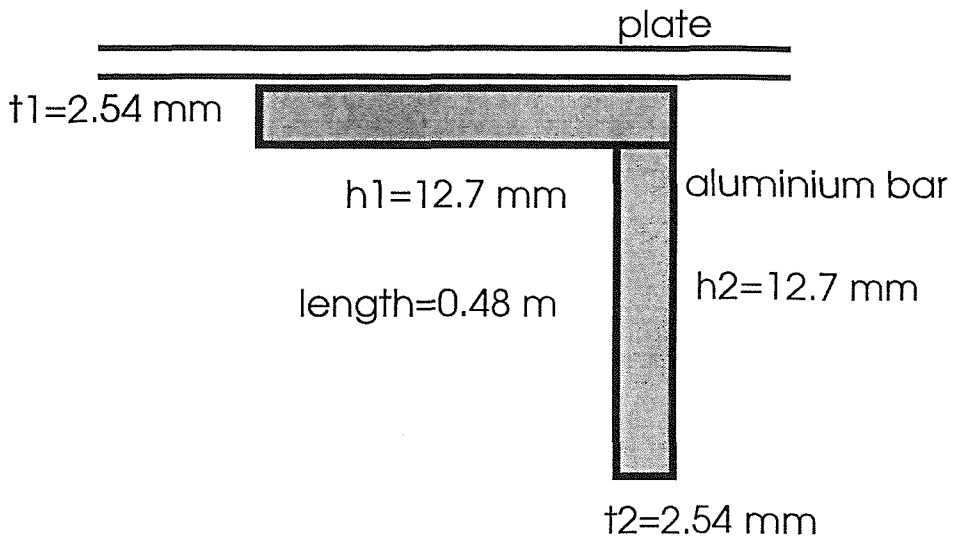

Fig. 5.20 - Sketch of aluminium bar attached to plate

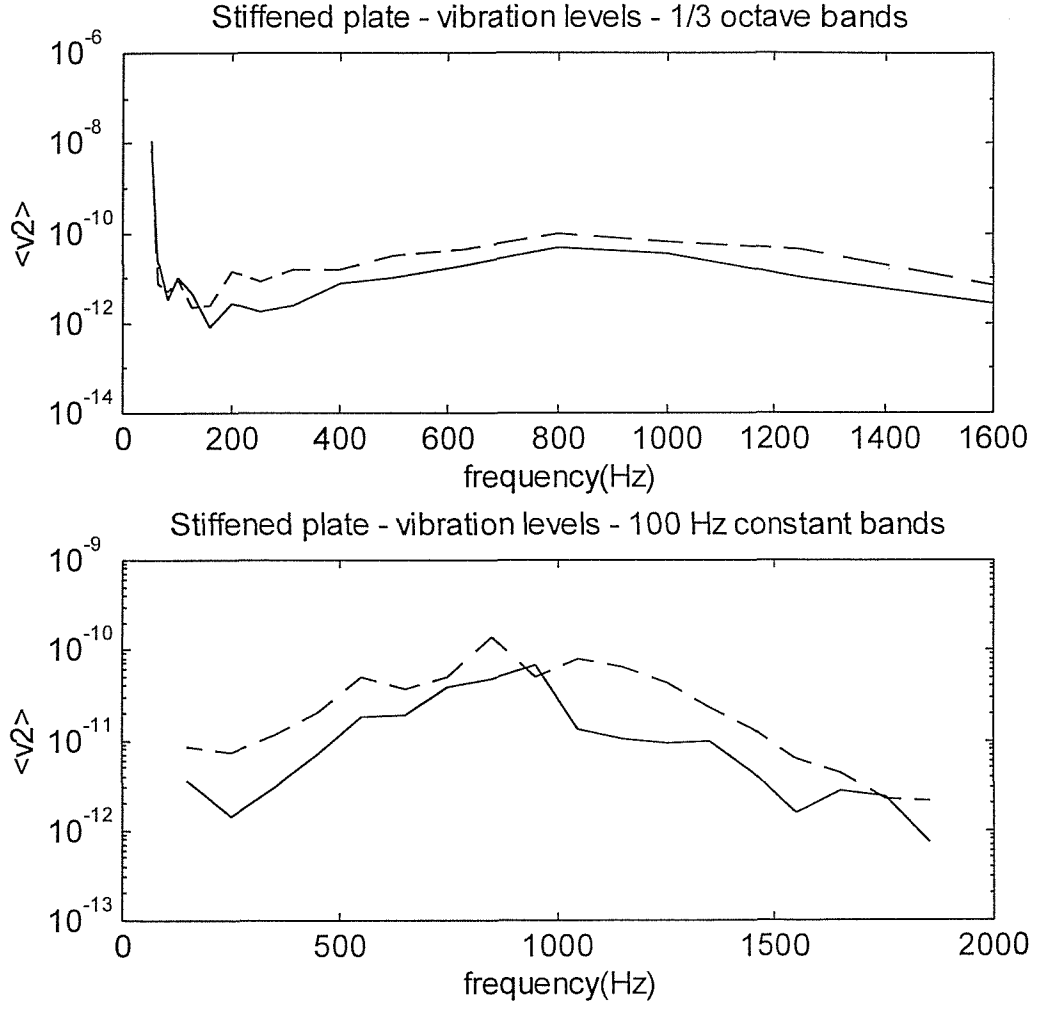

Fig. 5.21 - Vibration velocity level on both sides of stiffened plate. 1/3 octave and 100 Hz constant bands. Excitation position 2. Experimental results for stiffened plate; — — — directly excited side; ——— indirectly excited side.

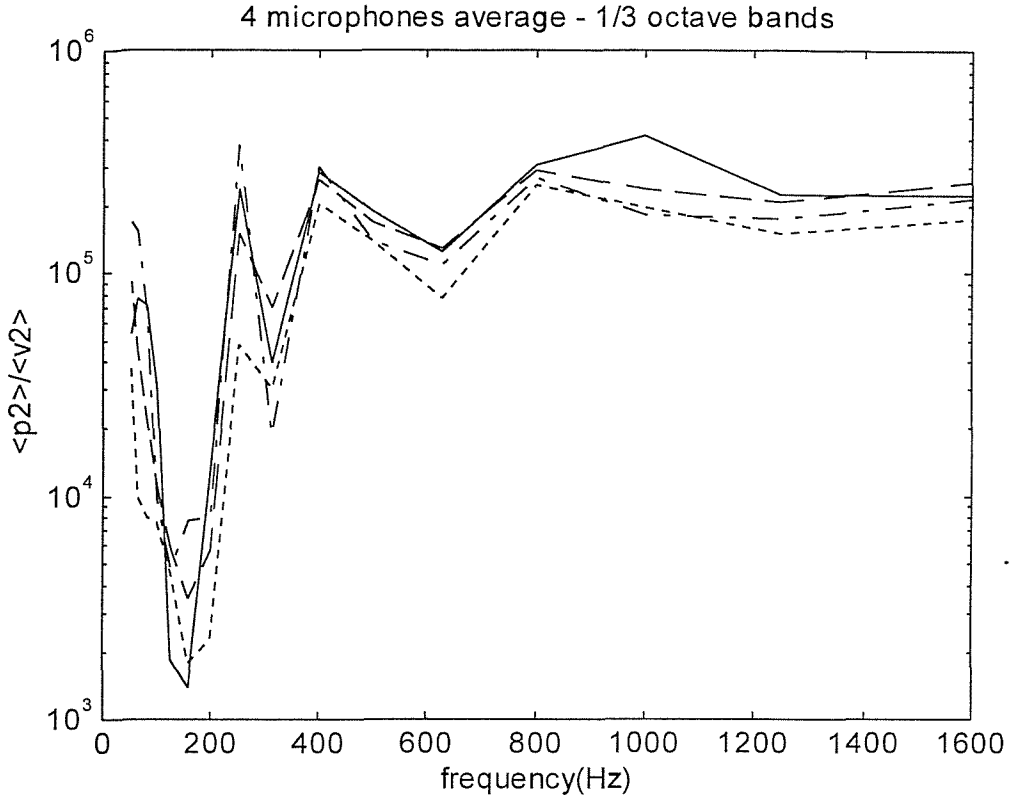

Fig. 5.22 - Comparison of sound pressure level excited by plate with and without stiffener. 4 microphones average. 1/3 octave bands. key: ——— experiments, stiffened plate; — — — theory, stiffened plate; – · – · – · – experiments, non-stiffened plate; - - - - - theory, non-stiffened plate.

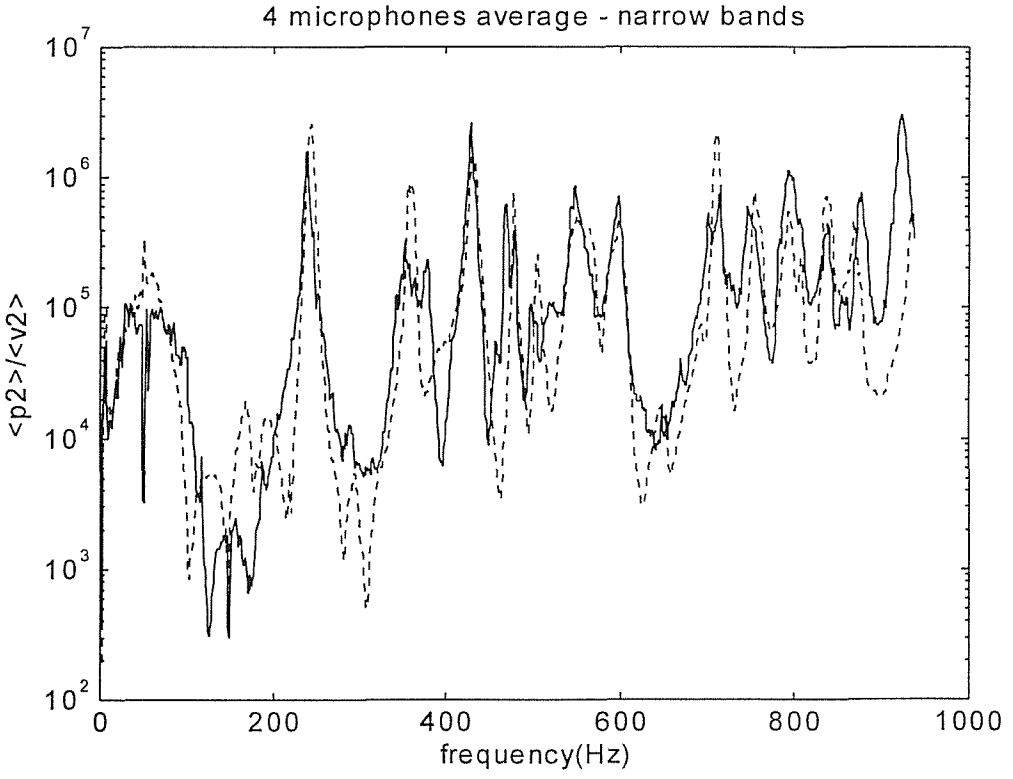

Fig. 5.23 - Comparison of sound pressure level excited by plate with and without stiffener. 4 microphones average. Narrow bands. Experimental results: ——— stiffened plate; - - - - - non-stiffened plate.

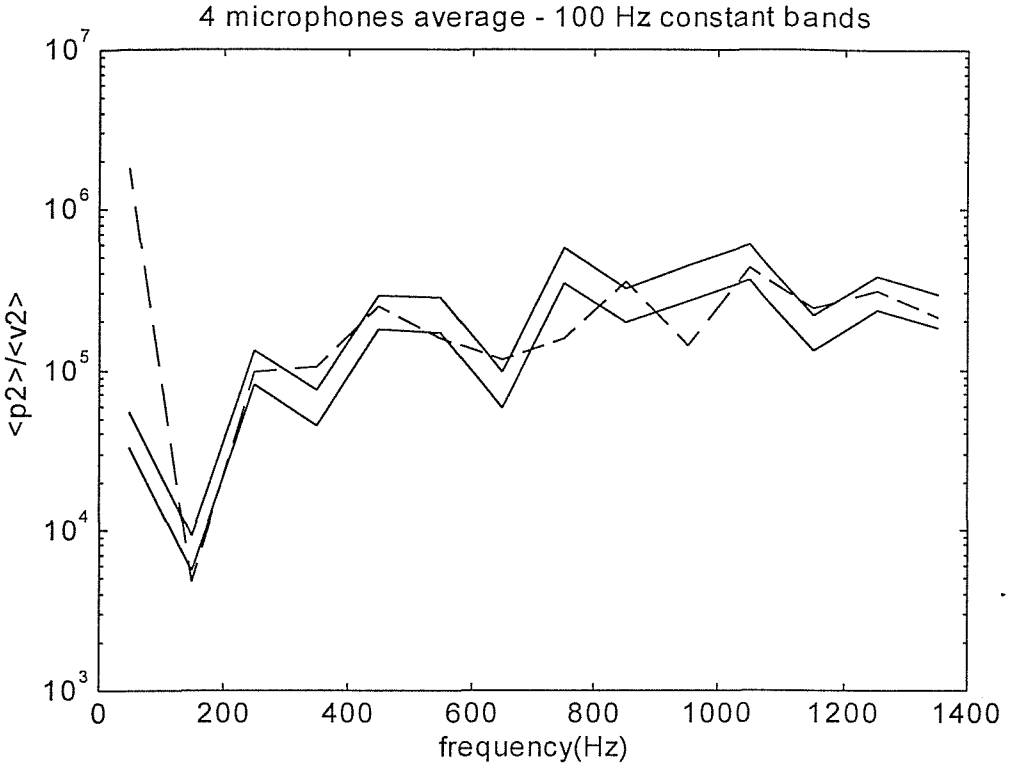

Fig. 5.24 - Sound pressure level averaged from 4 microphones and divided by space averaged vibration velocity. 100 Hz constant bands. key: ——— experiments, 95 % conf. limits; — — — theory.

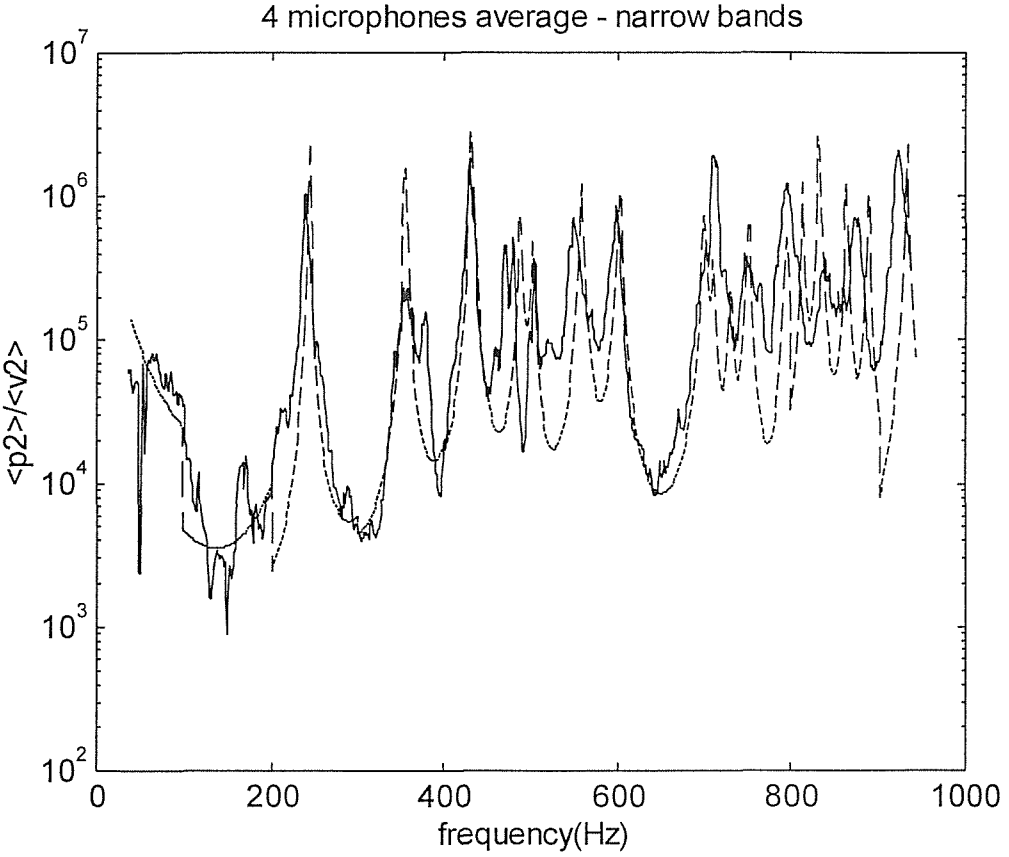

Fig. 5.25 - Sound pressure level averaged from 4 microphones and divided by space averaged vibration velocity. Narrow bands. key: ——— experimental results; — — — theory.

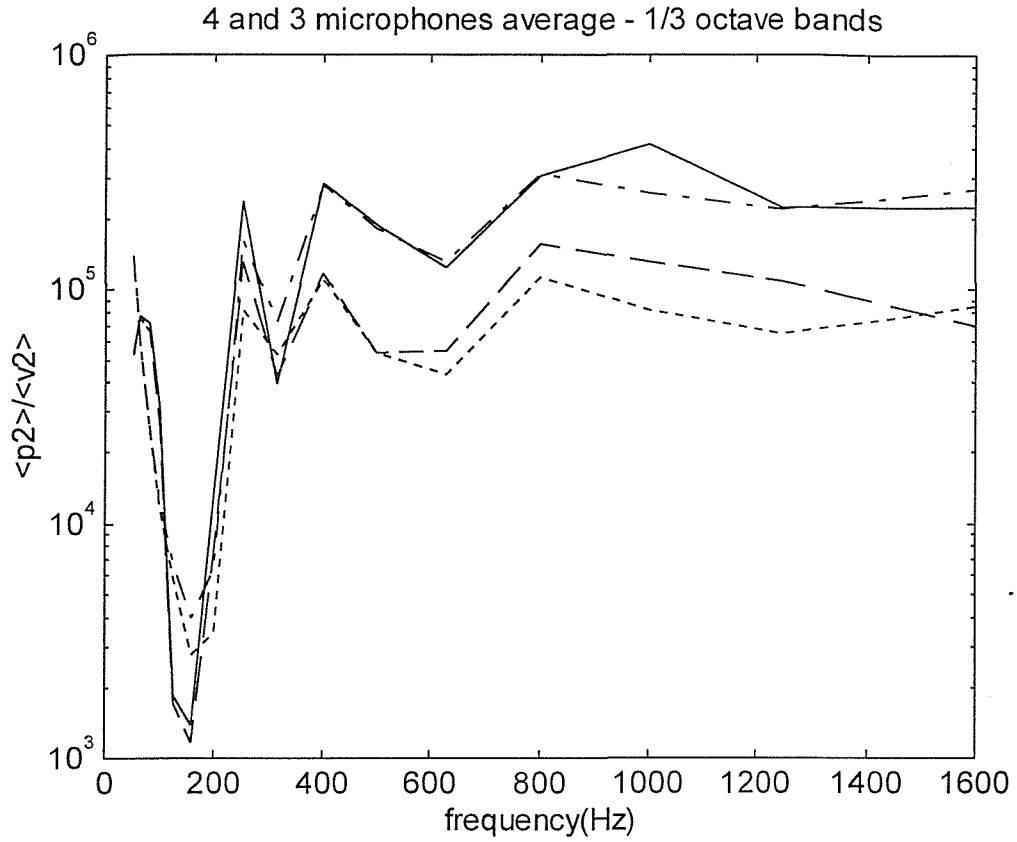

Fig. 5.26 - Sound pressure levels averaged from four and three microphones divided by space averaged vibration velocity. 1/3 octave bands. Wood walled box with stiffened plate. key: ——— experiments, 4 mics; — — — experiments, 3 mics; – · – · – · – theory, 4 mics; - - - - - theory, 3 mics.

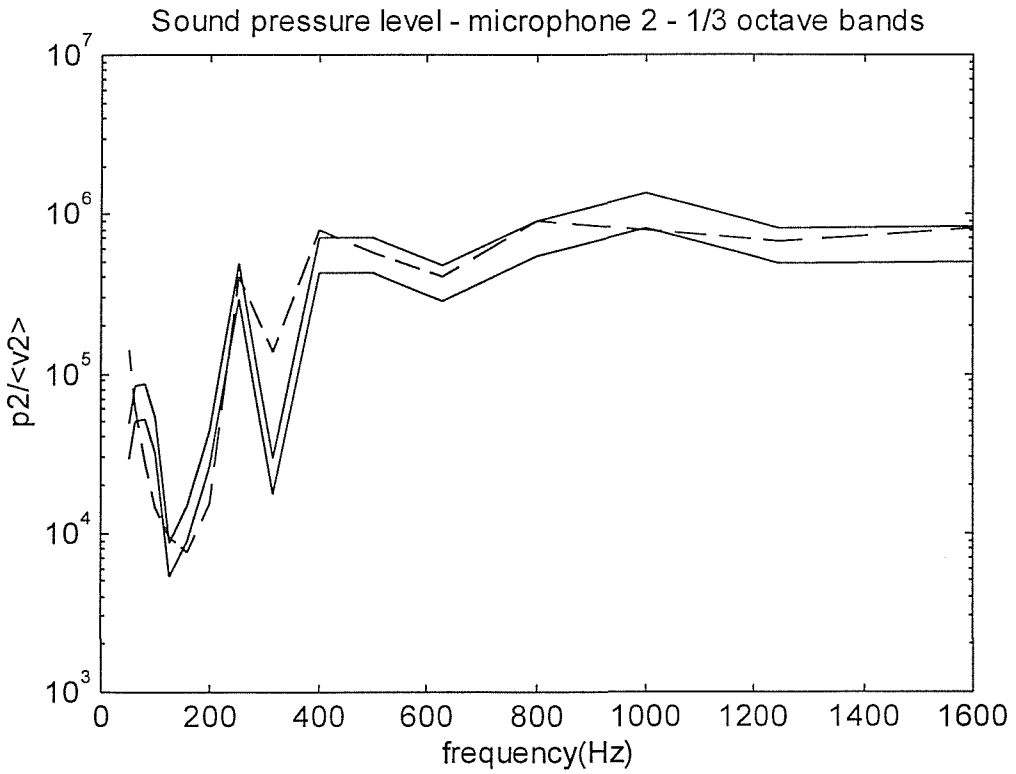

Fig. 5.27 - Sound pressure level from microphone 2 divided by space averaged vibration velocity. 1/3 octave bands. Wood walled box with stiffened plate. key: ——— experimental results, microphone 2, 95 % confidence limits; — — — theory, coordinates (0.005,0.475,0.685).

5.5 Conclusions

It was shown in this chapter that the hybrid deterministic-probabilistic model proposed in this work is adequate for the modelling of the vibroacoustic interaction between a flat plate and an acoustic cavity. Good agreement between theoretical and experimental results were observed when the results are averaged in frequency bands containing at least 6-8 plate modes. This is a restriction common to SEA, however, it was shown that, in contrast to SEA, the hybrid model is able to predict frequency-averaged local sound pressure levels with reasonable precision. The increase in the sound pressure levels induced by a stiffened plate in relation to a non-stiffened one has also shown to be reasonably well predicted by the present approach.

When the acoustic modes are reasonably sparse the hybrid model is also capable of predicting narrow band estimates which were shown to agree with experimental results. For cases in which the acoustic modes are dense, the same agreement was not observed for narrow band results due to the shifting of these modes in relation to the analytical predictions (equation (5.3)). On the other hand, the frequency averaged results are greatly improved due to the increase in the number of acoustic modes and they were shown to converge to SEA results for an enclosed acoustic field induced by clamped plates. Simply-supported plate results were not coincident but were very similar.

Strong disagreement was observed when the frequency band in which the first acoustic mode appears does not contain more than 4 plate modes and the plate modal overlap is low ($M<1$). This disagreement is related to the physical nature of the coupling between an isolated acoustic mode and sparse plate modes. As shown by Kompella and Bernhard [13], small shifts in the plate natural frequencies can cause large variations in the sound pressure level. The increase in the modal overlap improves this situation and, as presented in section 5.4, good agreement between experimental and theoretical estimates of the first acoustic resonance was observed for the stiffened plate case in narrow bands. When one is only concerned with frequency averaged results this situation can be tackled by widening the frequency band in which the results are averaged.

Another disagreement between experimental and theoretical results was observed in the frequency region around 800-1000 Hz for the wooden box and 315-500 Hz in the concrete box. It is here suggested that such discrepancy is associated with the perturbation caused by a bulky device used to hold the shaker magnet inside the wooden box. This device causes some of the medium-order acoustic modes to change their shape and frequencies in relation to the analytical expressions adopted for such modes (fig. 5.3 and 5.4).

CHAPTER 6

CONCLUSIONS AND SUGGESTIONS FOR FUTURE WORK

6.1 A review of the main results

The principal objective of this research was to develop a model for the vibroacoustic analysis of a modally-sparse enclosed sound field excited by the random vibration of a modally-dense enclosing structure. We sought an approach that would provide estimates of local and space-averaged sound pressure levels in the enclosed sound field in the form of either frequency-averaged or narrow band spectra. A basic assumption was that only the gross properties of the structure would be available, with full information available for the enclosed fluid and its boundaries.

The equations for the proposed approach are derived in Chapter 2. The modal equations for the response of the enclosed sound field to a uniform plane structure vibrating in flexure are presented and the structural vibration is represented by the normalised cross-power spectral density of normal acceleration (or velocity). The representation adopted for the acoustic system is therefore deterministic, while that for the structure is essentially probabilistic. A coupling coefficient evaluated over the vibroacoustic interface provides the connection between the two representations. Based on this idealisation the sound pressure levels are then estimated from the space-averaged vibration velocity.

Further equations are provided for the relation between the sound pressure levels and a space-averaged excitation force. Equations derived from a modal-interaction model are also developed using a power flow approach and the Green's function model.

In Appendix A, the equations for the coupling between the enclosed sound field and a single structure are extended for the case of n-structural systems exciting the enclosed sound field. The power flow approach relations presented in

Chapter 2 are employed in this derivation and the final model is a hybrid between a Statistical Energy Analysis model of the coupled structural systems and the enclosed sound field modal representation. The interaction between each structural system and the enclosed sound field is represented by a coupling loss factor obtained from the coupling coefficient.

The application of the present model to the analysis of acoustic radiation due to bending vibration presupposes that a model is available to represent the normalised cross-power spectral density of acceleration for typical plate structures. In order to permit the results derived in this work to be compared with results available in the literature it was decided to concentrate the present study on the analysis of the correlation coefficient of the vibration field. However, this analysis also provided results for the normalised cross-power spectral density.

The probabilistic representation adopted for the structural system based on a correlation model is thoroughly discussed in Chapter 3. This probabilistic representation presupposes that a large number of plate modes, or bending wave directions, are available. Based on such description, expressions for the correlation coefficient of acceleration are derived for simply-supported, clamped, free or guided boundary conditions. Additional results are provided for a generic spring coupling, thereby allowing the modelling of stiffeners. The large variations of these correlation coefficients near the edges of a structure are illustrated by presenting 3-dimensional graphs of the field in the vicinity of the edges. It is clear from these graphs that the influence of the boundary on the vibration field is restricted to a distance of about one wavelength from the edges. In regions more remote from the edges it was observed that the form of the correlation is essentially independent of the boundary conditions and approach that of a diffuse bending wave field [53]. It is shown that in the case of a diffuse bending wave field the expressions for the normalised cross-power spectral density of normal acceleration and the correlation coefficient of acceleration are the same.

The correlation coefficient results were derived on the basis of a free travelling wave model [55] and also on an approximate modal representation known as Bolotin's dynamic edge effect method [56]. Correlation coefficient expressions obtained with both approaches are shown to be coincident. The equivalence between

the free wave model and the Bolotin's dynamic edge effect method was previously discussed by Langley [55] and additional results concerning their equivalence are discussed in Appendix E. The effects of curvature, shear deformation and rotary inertia on vibrational wavenumber are expressed in terms of a dispersion relation that is included in the correlation coefficient computation. These dispersion relations are presented in Appendix F.

The effect of the excitation type on the correlation model is addressed in Chapter 3. Expressions for structures subject to point-excitation and a diffuse sound field reveal that, due to the normalisation adopted, these expressions are not much different from those for spatially uncorrelated type of excitation. These expressions are restricted to resonant structural response.

The last section of Chapter 3 is dedicated to comparing closed form correlation coefficient expressions for the case of simply-supported plates to a modal summation in which the exact plate modes are calculated and summed in each frequency band to give a deterministic result. The results presented in this section lead to the conclusion that at least eight resonant modes need to be included in a frequency band for the correlation model adopted for the vibration field be valid. In addition, in contradiction to the conclusions of Stearn [76], it was also concluded that a close approximation to a diffuse bending wave field can be set up in a moderately-damped, point-excited bounded structure. Experimental results presented in Chapter 4 support this conclusion.

The theoretical expressions derived for the correlation coefficient and normalised cross-power spectral density were verified by experiments on plate structures: the findings are reported in Chapter 4. It is concluded that the condition that eight to ten modes need to be available in a frequency band for the present results be valid was a little severe and the theoretical results were valid even for cases in which only five to six plate modes were included. In disagreement with Stearn [76], it was found that the structure's modal overlap plays an important part in the validity of the correlation model adopted. Good agreement between experimental and theoretical results were observed in frequency bands as narrow as 10 Hz when the plate modal overlap factor was higher than unity. Therefore, the following criterion was proposed

for the validity of the theoretical correlation coefficient and normalised cross-power spectral density expressions:

- when the modal overlap factor is lower than unity they can be used as frequency-average estimates as long as eight to ten resonant modes are available in the band;
- when the modal overlap factor is higher than unity they can also be used as narrow band estimates.

Irrespective of the boundary conditions, the forms of the correlation coefficient converged to that for a diffuse bending wave field in regions distant from the edges, confirming previous theoretical findings. Near the edges it was shown that the evanescent field components are of extreme importance for the correct representation of the correlation coefficient and strong disagreement with experimental results were observed when they were neglected in the theoretical model. Experimental results for free, clamped and stiffened plates were reasonably well predicted with the correlation model. Mechanical excitation in the form of point applied force proved to give similar results as those predicted by the spatially uncorrelated type of excitation. However, they only agreed with acoustically excited experimental results when a large number of modes was available in the frequency band. It was concluded that this discrepancy is connected to the acoustic field used as excitation which is not diffuse in good part of the frequency range analysed.

The correction adopted to account for curvature effects proved to be useful when the present model was compared to experimental results obtained on a car roof. This roof had double curvature and the variation of the wavenumber with measurement (or wave) direction was reasonably well predicted with the suggested correction. Finally, experimental evidence was obtained that this model is also approximately valid for the case of plates with irregular geometry. Evidence was provided to show that the same results and conclusions that apply to the correlation coefficient are also applicable to the normalised cross-power spectral density.

In Chapter 5, the normalised cross-power spectral density expressions were incorporated to the hybrid model and applied to the prediction of acoustic response inside two different boxes with one flexible wall. It was found that the present results approach those predicted by Statistical Energy Analysis when plate and acoustic cavity are modally-dense. When few modes are available, hybrid model and

Finite Element Analysis results compared well for the prediction of narrow band estimates of the overall sound pressure level. However, they both departed considerably from frequency-averaged experimental results in the band in which the first acoustic mode appears. This difference was attributed to the modal sparsity in both systems and, as observed by previous researchers, a small change in one of the plate natural frequencies can cause a large change in the level of the first acoustic resonance. The widening of the frequency band in which the experimental results are averaged improved the agreement between experimental and theoretical frequency-averaged response results.

An increase in the number of plate modes due to a higher plate modal density improved the agreement with experimental results, as predicted from the correlation model adopted for the plate. This agreement was observed in narrow band and frequency-averaged estimates. Furthermore, it was also found that good results can be obtained when the present approach is applied to the prediction of local sound pressure levels inside the acoustic cavity.

Stiffening of a flat plate is associated with increasing the level of the induced enclosed sound field and it was found that the present approach is able to represent such increase in sound pressure levels. It was also found that the predicted increase when frequency averaged approaches that suggested by Maidanik [37].

The existence of a bulky device to hold the magnet for the non-contact shaker caused some of the wooden box acoustic resonance frequencies to be shifted. This shifting lead to a noticeable departure between predicted and experimental results for the wooden box in the frequency region around 800 Hz.

It was found that frequency averaged radiation efficiency expressions for modally-dense structural systems can be written using the correlation model adopted for the plate. Results obtained with these expressions were compared to standard radiation efficiency results and, as shown in Appendix G, good agreement with exact results was observed for frequency ranges above $0.06\ f_{crit}$.

In summary, the present model provides an useful tool for the estimation of acoustic response of modally-sparse fluid volumes to vibration of a modally-dense bounding structure.

6.2 Suggestions for future work

Two avenues are seen as most important for further development of the present model. One is chiefly concerned with practical applications and the other concentrates on providing further theoretical results for other types of systems following similar procedure as the one introduced by this research.

The present approach could be used as a basis for a computer code in which the acoustic mode shapes and resonance frequencies are computed using a FEM code and the coupling coefficient evaluated from a numerical integration of the FEM-computed mode shapes and the normalised cross-power spectral density here presented. For cases in which the form of the structure turns to be too complex, normalised cross-power spectral density estimates in frequency bands could be obtained from a FEM computation in which a coarse mesh is adopted to obtain the plate correlation characteristics.

Theoretical extensions of the present approach to other types of coupling and systems is the second avenue suggested to be explored. The first step would be to write hybrid model equations for the case in which the modally-sparse acoustic system excites the modally-dense structural system. This situation is of lesser practical importance than the one here tackled but it will provide complimentary results to the ones here presented. The analysis of the coupling between a modally-sparse one- or two-dimensional system with another modally-dense one- or two-dimensional system is another situation worth of development. As a matter of fact, general equations need to be written that will be valid for any type or dimension of dynamic systems.

Finally, as extensively discussed during this work, further studies need to be carried out to assess the implication of different types of acoustic excitation (reverberant or not) on vibration field correlation characteristics.

LIST OF REFERENCES

[1] Saab-Scania Fights to Stay Airborne. *The European* 30 September - 6 October 1994, 32.

[2] J. P. SHEDLOWSKY 1992 *Proceedings of Inter-Noise 92, Toronto, Canada, July 20-22*, 1073-1078. Interior Noise Control in an Automobile - a Complex and Significant Challenge.

[3] E. H. DOWELL 1980 *American Institute of Aeronautics and Astronautics Journal*, **18**(4), 353-366. Master Plan for Prediction of Vehicle Interior Noise.

[4] S. K. JHA 1976 *Journal of Sound and Vibration* **47**(4), 543-558. Characteristics and Sources of Noise and Vibration and their Control in Motor Cars.

[5] S. E. MARSHALL and L. M. BUTZEL 1994 *Proceedings of Noise-Con 94, Ft. Lauderdale, Florida, May 01-04*, 493-494. Comments on the Use of Structureborne Noise Analysis for Large Commercial Airplanes.

[6] S. SUZUKI 1991 Chapter 7: Applications in the Automotive Industry in *Boundary Element Methods in Acoustics*, edited by R. D. Ciskowski and C. A. Brebbia. Elsevier Applied Science. London.

[7] R. S. LANGLEY 1993 *Journal of Sound and Vibration* **163**(2), 207-230. A Dynamic Stiffness/Boundary Element Method for the Prediction of Interior Noise Levels.

[8] S. H. SUNG and D. J. NEFSKE 1984 *Journal of Vibration, Acoustics, Stress, and Reliability in Design, Transactions of ASME*, **106**, 314-318. A Coupled Structural-Acoustic Finite Element Model for Vehicle Interior Analysis.

[9] J. F. UNRUH and S. A. DOBOSZ 1988 *Journal of Vibration, Acoustics, Stress, and Reliability in Design, Transactions of ASME*, **110**, 226-233. Fuselage Structural-Acoustic Modelling for Structure-Borne Interior Noise Transmission.

[10] F. J. FAHY 1994 *Philosophical Transactions of The Royal Society of London, series A*, **346**, 431-447. Statistical Energy Analysis: a Critical Overview.

[11] M. S. KOMPELLA and B. J. BERNHARD 1993. *Proceedings of SAE 1993 Noise and Vibration Conference, Warrendale, U.S.A.*. Measurement of the Statistical Variation of Structural-Acoustic Characteristics of Automotive Vehicles.

[12] N. LALOR and G. STIMPSON 1992 *Proceedings of Vehicle Comfort, ATA, Bologna, October 1992.* FEM+SEA+Optimisation = Low Noise.

[13] N. M. FRANCHEK and R. J. BERNHARD 1994 *Proceedings of Noise-Con 94, Ft.Lauderdale, Florida, May 01-04*, 495-500. Analytical, Numerical, and Experimental Comparisons of Structure-Borne Noise in a Rectangular Acoustic Enclosure.

[14] R. H. LYON 1975 *Statistical Energy Analysis of Dynamical Systems: Theory and Applications.* The MIT Press. Cambridge, Massachusetts.

[15] R. G. DeJONG 1985 *Society of Automotive Engineers paper n. 850960.* A Study of Vehicle Interior Noise using Statistical Energy Analysis.

[16] G. P. MATHUR and J. E. MANNING 1988 *Presented at the 44th. Forum of the American Helicopter Society, Washington, D.C., June 16-18*, 719-729. Analytical Prediction and Flight Test Evaluation of Bell Acap Helicopter Cabin Noise.

[17] J. L. GUYADER 1993 *Proceedings of the Institute of Acoustics,* **15** (3), 131-142. Methodes de Prevision Vibroacoustique aux moyennes frequences.

[18] L. D. POPE and J. F. WILBY 1977 *Journal of the Acoustical Society of America,* **62** (4), 906-911. Band-Limited Power Flow into Enclosures.

[19] F. J. FAHY 1985 *Sound and Structural Vibration: Radiation, Transmission and Response.* London: Academic Press Limited.

[20] E. H. DOWELL and H. M. VOSS 1963 *American Institute of Aeronautics and Astronautics Journal*, **1**, 476-477. The Effect of a Cavity on Panel Vibration.

[21] A. J. PRETLOVE 1965 *Journal of Sound and Vibration*, **2** (3), 197-209. Free Vibrations of a Rectangular Panel Backed by a Closed Rectangular Cavity.

[22] A. J. PRETLOVE 1966 *Journal of Sound and Vibration*, **3** (3), 252-261. Forced Vibrations of a Rectangular Panel Backed by a Closed Rectangular Cavity.

[23] E. H. DOWELL, G. F. GORMAN, III and D. A. SMITH 1977 *Journal of Sound and Vibration,* **52** (4), 519-542. Acoustoelasticity: General Theory, Acoustic Natural Modes and Forced Response to Sinusoidal Excitation, Including Comparisons with Experiments.

[24] L. MEIROVITCH 1974 *American Institute of Aeronautics and Astronautics Journal,* **12** (10), 1337-1342. A New Method of Solution of the Eigenvalue Problem for Gyroscopic Systems.

[25] P. M. MORSE and K. U. INGARD 1968 *Theoretical Acoustics.* The MIT Press. Cambridge, Massachusetts.

[26] A. D. PIERCE 1989 *Acoustics: An Introduction to Its Physical Principles and Applications.* Acoustical Society of America. New York.

[27] R. D. CISKOWSKI and C. A. BREBBIA (edits.) 1991 *Boundary Element Methods in Acoustics.* Elsevier Applied Science. London.

[28] J. PAN and D. A. BIES 1990 *Journal of the Acoustical Society of America,* **87** (2), 691-707. The Effect of Fluid-Structural Coupling on Sound Waves in an Enclosure - Theoretical Part.

[29] J. PAN and D. A. BIES 1990 *Journal of the Acoustical Society of America,* **87** (2), 708-717. The Effect of Fluid-Structural Coupling on Sound Waves in an Enclosure - Experimental Part.

[30] J. PAN 1992 *Journal of the Acoustical Society of America,* **91** (2), 949-956. The Forced Response of an Acoustic-Structural Coupled System.

[31] M. PETYT, J. LEA and G. H. KOOPMANN 1976 *Journal of Sound and Vibration*, **45** (4), 495-502. A Finite Element Method for Determining the Acoustic Modes of Irregular Shaped Cavities.

[32] P. K. BANERJEE, S. AHMAD and H. C. WANG 1988 *International Journal for Numerical Methods in Engineering*, **26**, 1299-1309. A New BEM Formulation for the Acoustic Eigenfrequency Analysis.

[33] L. CHENG and J. NICOLAS 1992 *Journal of the Acoustical Society of America,* **91** (3), 1504-1513. Radiation of Sound into a Cylindrical Enclosure from a Point-Driven End Plate with General Boundary Conditions.

[34] T. D. SCHARTON and R. H. LYON 1968 *Journal of the Acoustical Society of America,* **43** (6), 1332-1343. Power Flow and Energy Sharing in Random Vibration.

[35] F. J. FAHY 1969 *Journal of Sound and Vibration,* **10**, 490-512. Vibration of Containing Structures by Sound in Contained Fluid.

[36] R. H. LYON 1963 *Journal of the Acoustical Society of America,* **35** (11), 1791-1797. Noise Reduction of Rectangular Enclosures with One Flexible Wall.

[37] G. MAIDANIK 1962 *Journal of the Acoustical Society of America,* **34**(6), 809-826. Response of Ribbed Panels to Reverberant Acoustic Fields.

[38] L. CREMER, M. HECKL and E. E. UNGAR 1987 *Structure Borne Sound: Structural Vibration and Sound Radiation at Audio Frequencies.* Springer Verlag. Berlin. 2nd. edition.

[39] M. P. NORTON 1989 *Fundamentals of Noise and Vibration Analysis for Engineers.* Cambridge University Press. Cambridge.

[40] C. GULIZIA and A. J. PRICE 1977 *Journal of the Acoustical Society of America*, **61** (6), 1511-1515. Power Flow between Strongly Coupled Oscilattors.

[41] J. E. HOWLETT 1972 *Ph.D. Thesis, University of Southampton.* The Vibrations of Enclosure Panels Strongly Coupled to Acoustic Fields in the Enclosed Fluid.

[42] R. H. LYON 1969 *Journal of the Acoustical Society of America*, **45** (3), 545-565. Statistical Analysis of Power Injection and Response in Structures and Rooms.

[43] F. J. FAHY 1971 *Proceedings of 7th. ICA, Budapest*, 561-564. Statistics of Acoustically Induced Vibration of Structures.

[44] C. H. HODGES and J. WOODHOUSE 1986 *Reports of Progress in Physics*, **49**, 107-170. Theories of Noise and Vibration Transmission in Complex Structures.

[45] A. D. MOHAMMED 1990 *Ph.D. Thesis, University of Southampton.* A Study of Uncertainty in Applications of Statistical Energy Analysis.

[46] L. D. POPE 1971 *Journal of the Acoustical Society of America*, **50** (3), 1004-1018. On the Transmission of Sound through Finite Closed Shells: Statistical Energy Analysis, Modal Coupling, and Nonresonant Transmission.

[47] L. D. POPE and J. F. WILBY 1980 *Journal of the Acoustical Society of America,* **67** (3), 823-826. Band-Limited Power Flow into Enclosures.II.

[48] L. D. POPE, D. C. RENNISON, C. M. WILLIS and W. H. MAYES 1982 *Journal of Sound and Vibration,* **82**(4), 541-575. Development and Validation of Preliminary Analytical Models for Aircraft Interior Noise Prediction.

[49] L. D. POPE, E. G. WILBY, C. M. WILLIS and W. H. MAYES 1983 *Journal of Sound and Vibration,* **89**(3), 371-417. Aircraft Interior Noise Models: Sidewall Trim, Stiffened Structures, and Cabin Acoustics with Floor Partition.

[50] Y. KUBOTA, H. D. DIONNE, E. H. DOWELL 1988 *Journal of Vibration, Acoustics, Stress, and Reliability in Design, Transactions of ASME,* **110**, 371-376. Asymptotic Modal Analysis and Statistical Energy Analysis of an Acoustic Cavity.

[51] L. F. PERETTI and E. H. DOWELL 1992 *American Institute of Aeronautics and Astronautics Journal*, **30** (5), 1191-1198. Asymptotic Modal Analysis of a Rectangular Acoustic Cavity Excited by Wall Vibration.

[52] L. F. PERETTI and E. H. DOWELL 1992 *Journal of Vibration and Acoustics, Transactions of ASME*, **114**, 546-554. Experimental Verification of the Asymptotic Modal Analysis Method as Applied to a Rectangular Acoustic Cavity Excited by Wall Vibration.

[53] S. M. STEARN 1969 *Journal of Sound and Vibration,* **9** (1), 21-27. Measurements of Correlation Coefficients of Acceleration on a Randomly Excited Structure.

[54] M. W. BONILHA and F. J. FAHY 1993 *ISVR Technical Report n. 220.* Measurements of Correlation Coefficients of Vibration on a Car Body Shell.

[55] R. S. LANGLEY 1991 *Journal of Sound and Vibration*, **145** (2), 261-277. An Elastic Wave Technique for the Free Vibration Analysis of Plate Assemblies.

[56] V. V. BOLOTIN 1984 *Random Vibration of Elastic Systems.* Martinus Nijhoff Publishers. The Hague.

[57] A. POWELL 1958 *Journal of the Acoustical Society of America*, **30** (12), 1136-1139. On the Approximation to the 'Infinite' Solution by the Method of Normal Modes for Random Vibrations.

[58] A. POWELL 1958 *Journal of the Acoustical Society of America*, **30** (12), 1130-1135. On the Fatigue Failure of Structures due to Vibrations Excited by Random Pressure Fields.

[59] D. J. MEAD 1968 Chapter 14 in *Noise and Acoustic Fatigue in Aeronautics*, editors E. J. Richards and D. J. Mead. John Wiley & Sons. London.

[60] W. T. CHU 1980 *Journal of the Acoustical Society of America*, **68** (1), 184-190. Eigenmode Analysis of Interference Patterns in Reverberant Sound Fields.

[61] E. H. DOWELL and Y. KUBOTA 1985 *Journal of Applied Mechanics*, **52**, 949-957. Asymptotic Modal Analysis and Statistical Energy Analysis of Dynamical Systems.

[62] R. D. BLEVINS 1989 *Journal of Sound and Vibration*, **129** (1), 51-71. An Approximate Method for Sonic Fatigue Analysis of Plates and Shells.

[63] F. JACOBSEN 1979 *Report n. 27. Technical University of Denmark. Lingby, Denmark.* The Diffuse Sound Field. Statistical Considerations Concerning the Reverberant Field in the Steady-State.

[64] R. V. WATERHOUSE 1955 *Journal of the Acoustical Society of America*, **27** (2), 247-258. Interference Patterns in Reverberant Sound Fields.

[65] R. V. WATERHOUSE and R. K. COOK 1965 *Journal of the Acoustical Society of America*, **37** (3), 424-428. Interference Patterns in Reverberant Sound Fields II.

[66] W.T. CHU 1981 *Journal of the Acoustical Society of America,* **69** (6), 1710-1715. Comments On the Coherent and Incoherent Nature of a Reverberant Sound Field.

[67] D. E. NEWLAND 1993 *An Introduction to Random Vibrations, Spectral & Wavelet Analysis, 3rd. Edition.* Longman. London.

[68] C. T. MORROW 1971 *Journal of Sound and Vibration,* **16** (1), 29-42. Point-to-point Correlation of Sound Pressures in Reverberation Chambers.

[69] R. K. COOK, R. V. WATERHOUSE, R. D. BERENDT, S. EDELMAN, M. C. THOMPSON 1955 *Journal of the Acoustical Society of America*, **27** (6), 1072-1077. Measurement of Correlation Coefficients in Reverberant Sound Fields.

[70] I. S. GRADSHTEYN and I. M. RYZHIK 1980 *Table of Integrals, Series and Products.* Academic Press. London.

[71] G. N. WATSON 1958 *A Treatise on The Theory of Bessel Functions* (2nd edn). Cambridge University Press. Cambridge.

[72] M. ABRAMOVITZ and I. A. STEGUN 1972 *Handbook of Mathematical Functions.* Dover. New York.

[73] R. V. WATERHOUSE and R. K. COOK 1976 *Journal of the Acoustical Society of America*, **59** (3), 576-581. Diffuse Sound Fields: Eigenmode and Free-Wave Models.

[74] I. ELISHAKOFF, Y. K. LIN, L. P. ZHU 1994 *Probabilistic and Convex Modelling of Acoustically Excited Structures.* Elsevier Science. Amsterdam.

[75] S. H. CRANDALL 1979 Chapter 1 in *Developments in Statistics, volume 2,* edited by P. R. Krishnaiah. Academic Press. London.

[76] S. M. STEARN 1970 *Ph.D. Thesis, University of Southampton.* Stress Distributions in Randomly Excited Structures.

[77] E. SKUDRZYK 1968 *Simple and Complex Vibratory Systems.* The Pennsylvania State University Press. University Park.

[78] M. W. BONILHA and F. J. FAHY 1994 *Applied Acoustics*, **43**, 1-18. Measurements of Vibration Field Correlation on a Car Body Shell.

[79] R. D. BLEVINS 1979 *Formulas for Natural Frequency and Mode Shape.* Van Nostrand Reinhold.

[80] M. F. RANKY and B. L. CLARKSON 1983 *Journal of Sound and Vibration* **89** (3), 309-323. Frequency Average Loss Factors of Plates and Shells.

[81] F. J. FAHY 1995 *Euro-Noise 95, Lyon, France, 21-23 March.* Spatial Correlation in Vibroacoustics. (not included in the Proceedings)

[82] K. F. GRAFF 1975 *Wave Motion in Elastic Solids.* Dover. New York.

[83] P. P. JAMES and F. J. FAHY 1995 *ISVR Technical Report n. 242.* A Technique for the Evaluation of Strength of Coupling between SEA Subsystems: Experiments with Two Coupled Plates and Two Coupled Rooms.

[84] H. RUIVO 1995 *M.Sc. Thesis, University of Southampton.* In-Situ Evaluation of SEA Loss and Coupling Loss Factors between Two Connected Subsystems using Power Modulation Techniques.

[85] J. S. BENDAT and A.G.PIERSOL 1986 *Random Data: Analysis and Measurements Procedures.* 2nd. Edition. John Wiley & Sons, New York.

[86] G. DeSALVO et al. 1990 *ANSYS Version 4.4a - Users Manual* Swanson Analysis System Inc.

[87] R. TIMMEL 1991 *Acustica* **73**, 12-20. Investigations on the effect of edge boundary conditions for flexurally vibrating rectangular panels on the radiation efficiency as exemplified by clamped and simply-supported panels (original in German).

[88] J. J. GARCIA-BONITO 1996 *Ph.D. Thesis, University of Southampton.* Local Active Control in Pure Tone Diffracted Sound Fields.

[89] V.V.BOLOTIN 1960 *Appl. Math. Mech. (PMM)* **24**(5), 831-843. The Edge Effect in the Oscillations of Elastic Shells.

[90] A.L.GOL'DENVEIZER 1970 *Appl. Math. Mech. (PMM)* **34**(5), 952-956. On the Frequency Distribution Density of Oscillations of a Thin Shell.

[91] R. S. LANGLEY 1994 *Journal of Sound and Vibration* **169**(1), 43-53.The Modal Density and Mode Count of Thin Cylinders and Curved Panels.

[92] I. ELISHAKOFF 1994 *Proceedings of Noise-Con 94, Florida, USA, May 01-04*, 911-916. Generalization of the Bolotin's Dynamic Edge Effect Method for Vibration Analysis of Mindlin Plates

[93] F G LEPPINGTON, E G BROADBENT, K H HERON 1982 *Proceedings of the Royal Society of London* **A 382**, 245-271. The acoustic radiation efficiency of rectangular panels.

[94] J.-C. PASCAL, J-F. LI 1995 *Proceedings of Internoise 95, Newport Beach, CA, USA, July 10-12*, 261-264. New Approach to the approximation of the radiation efficiency of plates of arbitrary shape.

[95] A. BERRY, J.-L. GUYADER, J. NICOLAS 1990 *Journal of the Acoustical Society of America* **88** (6), 2792-2802. A general formulation for the sound radiation from rectangular, baffled plates with arbitrary boundary conditions.

[96] R. J. CRAIK 1996 *Sound Transmission through Buildings using Statistical Energy Analysis.* Gower, Aldershot UK.

APPENDIX A

HYBRID MODEL EQUATIONS FOR N-PLATES COUPLED TO AN ACOUSTIC CAVITY

The expression for the pressure response of an acoustic cavity, at frequencies where the modal density is low, generated by the vibration of a single bounding plate with high modal density, was derived in Chapter 2 using a modal-interaction model, the Green's function approach and the power balance model. Unfortunately, that formulation is inadequate when more than one plate is coupled to the enclosure. In this situation, the dynamic interaction between each connected plate must be taken into account in the model. In view of the fact that a high modal density is assumed for the plates, the power input and the power flow between each plate can be analysed using Statistical Energy Analysis (SEA). In what follows, a combined SEA/modal approach which takes advantage of the fact that the acoustic cavity can be represented by its normal acoustic modes is proposed. As discussed, the suggested procedure is approximate and it is expected that it will give good results in frequencies in which the acoustic modes do not overlap.

The system in study is represented in figure A.1. It is formed of N-1 plates which are coupled to an acoustic cavity (subsystem N). The plates are assumed to have high modal density and to be excited by spatially-uncorrelated time-stationary random forces. The steady-state power balance equations for this system are

$$\Pi_{in}^{1} = \Pi_{diss}^{1} + \Pi_{12} + \ldots + \Pi_{1N} \quad \text{(plate 1)}, \tag{A.1}$$

$$\Pi_{in}^{2} = \Pi_{diss}^{2} + \Pi_{12} + \ldots + \Pi_{2N} \quad \text{(plate 2)}, \tag{A.2}$$

.....

$$\Pi_{in}^{N-1} = \Pi_{diss}^{N-1} + \Pi_{1(N-1)} + \ldots + \Pi_{(N-1)N} \quad \text{(plate N-1)}, \tag{A.3}$$

$$0 = \Pi_{diss}^{N} + \Pi_{1N} + \Pi_{2N} \ldots + \Pi_{(N-1)N} \quad \text{(acoustic cavity)}, \tag{A.4}$$

where $\Pi_{in}^{\ i}$ is total real power input to plate i from an external source, $\Pi_{diss}^{\ i}$ is the power dissipated by subsystem i due to its internal damping and Π_{ij} is the power transferred between subsystems i and j. It is assumed that the acoustic cavity is only excited by the vibration of the surrounding plates.

Following standard SEA procedure the steady-state energy balance equations can be written in matrix form. The power flow between each pair of subsystems is written as an extension of the exact result for two oscillators (equation (1.5)). As a result, the loss factor matrix [L] is symmetric because of the reciprocity relationship between the coupling loss factors, $\eta_{ij}\, n_i = \eta_{ji}\, n_j$. The SEA matrix equation for the system presented in figure A.1 is,

$$\omega_c[L]\begin{bmatrix} E_1/n_1 \\ E_2/n_2 \\ \vdots \\ E_{N-1}/n_{N-1} \\ E_N/n_N \end{bmatrix} = \begin{bmatrix} \Pi_{in}^1 \\ \Pi_{in}^2 \\ \vdots \\ \Pi_{in}^{N-1} \\ 0 \end{bmatrix} \tag{A.5}$$

where,

$$[L] = \begin{bmatrix} (\eta_1 + \sum_{i\neq 1}^{N} \eta_{1i})n_1 & -\eta_{12}n_1 & \cdots & -\eta_{1N}n_1 \\ -\eta_{21}n_2 & (\eta_2 + \sum_{i\neq 2}^{N} \eta_{2i})n_2 & \cdots & -\eta_{2N}n_2 \\ \vdots & \vdots & \ddots & \vdots \\ -\eta_{N1}n_N & \cdots & \cdots & (\eta_N + \sum_{i}^{N-1} \eta_{Ni})n_N \end{bmatrix}$$

E_i is the total vibration energy of subsystem i, η_i is the loss factor of subsystem i, n_i is the modal density of subsystem i and η_{ij} is the coupling loss factor between subsystems i and j. All the above quantities are assumed to be frequency averaged and the equation solved for frequency bands $\Delta\omega$ whose centre frequency is ω_c.

Instead of solving the SEA model for a complete set of N subsystems, it is proposed that the above problem is reduced to a problem of size N-1. This reduction is done by eliminating line and column N of the loss factor matrix. As a result the term that gives the acoustic energy for the cavity disappears from the problem. This reduced problem complies with the power balance condition in each plate (equations (A.1) to (A.3)) because the energy radiated by the plates into the

acoustic cavity is taken into account. In SEA terminology this radiated power is equal to $\omega_c \eta_{iN} E_i$.

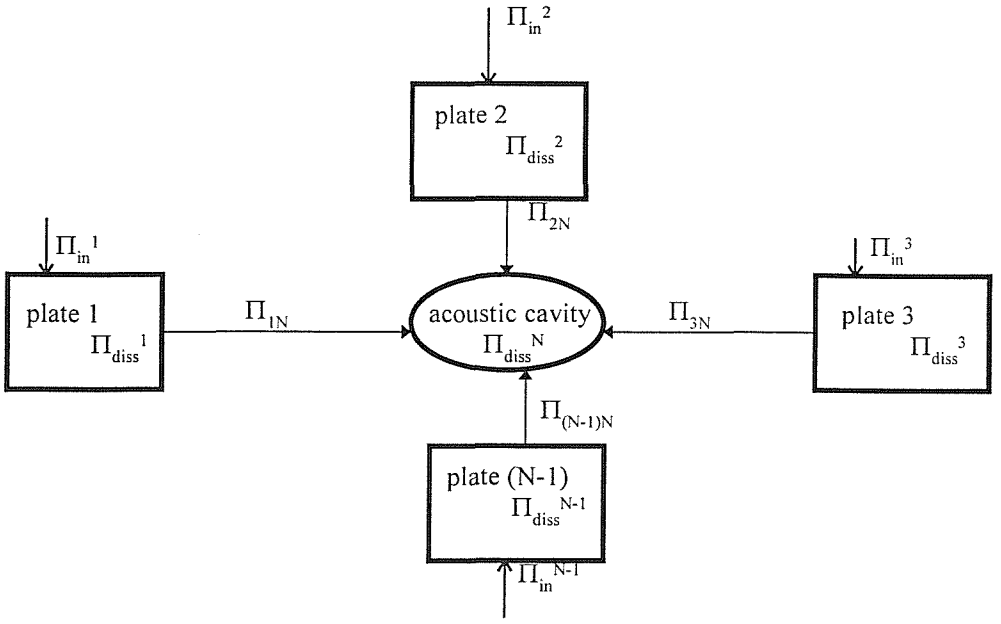

Fig. A.1 - Diagram representation of N-1 plates coupled to an acoustic cavity. The power transferred between the plates is not represented.

Apart from the coupling loss factor between each plate and the acoustic cavity all the other parameters of the reduced problem can be estimated, either analytically or empirically, in the usual SEA manner [10,14-16,39]. Therefore, if an estimate for the remaining coupling loss factors is obtained, the above SEA problem of dimension N-1 can be solved for the band-limited plate energies.

The band-limited power radiated by the plates into the acoustic cavity is presented in Chapter 2, equation (2.32). This expression was derived following a procedure suggested by Pope and Wilby [18,47]. As presented, in a SEA model this radiated power is equal to $\omega \eta_{iN} E_i$. If this term is equated to the one presented in equation (2.32), we have that the coupling loss factor between plate i and the acoustic cavity (subsystem N) is given by

$$\eta_{iN} = \frac{\rho_o c_o^2 S_i^2}{M_i V_N} \frac{1}{\omega_c \Delta\omega} \sum_n \frac{C_{nn}^2(\omega_c)\eta_n \omega_n}{\Lambda_n} \int_{\Delta\omega} \frac{1}{(X_n^2 + Y_n^2)} d\omega. \qquad (A.6)$$

In the above expression the coupling coefficient between the plate and each acoustic mode has been substituted by its frequency-averaged value. This is a valid approximation as the coupling coefficient varies slowly with frequency. This observation is further discussed in Chapter 5. The integral presented in equation (A.6) can be solved exactly as presented by Blevins [62]. The solution is

$$\int_{\Delta\omega} \frac{1}{(\omega_n^2 - \omega^2)^2 + (\eta_n \omega_n \omega)^2} d\omega = \int_{\alpha_1}^{\alpha_2} \frac{d\alpha}{(1-\alpha^2)^2 + (\eta\alpha)^2}$$

$$= \frac{1}{8\chi_n} \ln\left[\frac{(\alpha_2^2 + 2\alpha_2\chi_n + 1)}{(\alpha_2^2 - 2\alpha_2\chi_n + 1)} \frac{(\alpha_1^2 - 2\alpha_1\chi_n + 1)}{(\alpha_1^2 + 2\alpha_1\chi_n + 1)}\right] + \frac{1}{2\eta_n}\left[\arctan\frac{\eta_n\alpha_2}{1-\alpha_2^2} - \arctan\frac{\eta_n\alpha_1}{1-\alpha_1^2}\right], \qquad (A.7)$$

where $\alpha = \omega / \omega_n = f / f_n$, $\alpha_1 = f_1 / f_n = \omega_1 / \omega_n$, $\alpha_2 = f_2 / f_n = \omega_2 / \omega_n$, f_1 is the lower frequency limit of the band, f_2 is the upper frequency limit of the band and $\chi_n = (1 - (\eta_n^2 / 4))^{1/2}$.

Using equation (A.6), the coupling loss factors η_{iN} can be estimated from the modal characteristics of the enclosure. However, a question remains concerning the acoustic modes that should be considered in the modal summation. Ideally this summation should be infinite, but a truncation is necessary in order to make the estimation of these parameters attainable. The modes that are included in the truncated summation are dictated by the special characteristics of the term in the integral of equation (A.6). For instance, the acoustic modes that have their natural frequency in a band $\Delta\omega$ will dominate the summation in this band due to the behaviour of the $(\omega_n^2 - \omega^2)$ term near the acoustic resonance. However, for bands in which no acoustic modes are resonant, contributions from all the modes whose natural frequencies fall below the lower frequency of this band must be considered. This allows the estimation of the non-resonant response of the acoustic cavity, an estimation that can not be handled by conventional SEA modelling.

The estimation of the coupling loss factors between each plate and the acoustic cavity provides the solution of the proposed SEA problem in which only the structural subsystems are considered. Once the plate energies are computed, the pressure response can be predicted from equation (2.16) with an additional summation

to consider the effects of all the plates in the total acoustic pressure. As shown in Chapter 2, equation (2.16) fulfils the power balance condition for the acoustic cavity providing a solution to equation (A.4). Therefore, the steady-state power balance problem for the analysed system (equations (A.1) to (A.4)) is solved by a combination of a probabilistic treatment (the SEA model of the plate network) and a modal analysis of the acoustic cavity. The latter deterministic problem can be solved using either an analytical solution or, for more complicated geometries, a Finite Element Method (FEM) or a Boundary Element Method (BEM) model. The link between the probabilistic and the deterministic models is provided by equation (2.16).

APPENDIX B

DERIVATION OF PARAMETERS OF BOLOTIN'S DYNAMIC EDGE EFFECT METHOD OF MODAL REPRESENTATION FOR VARIOUS BOUNDARY CONDITIONS

In Chapter 3, expressions for the normalised cross-power spectral density and for the correlation coefficient of modally-dense flat plates have been derived using an approximate modal representation based on Bolotin's dynamic edge effect method [56]. This representation presupposes that the plate mode shapes remote from the boundaries approaches a sinusoidal function and close to the edges the sinusoidal functions are multiplied by an exponentially decaying function. A typical displacement function is then given by [56]

$$z(x,y,t) = X(x)Y(y)\cos\omega t, \qquad \text{(B.1)}$$

where the functions X(x) and Y(y) changes according to the position on the plate and are expressed as

$X(x) = \sin k_x(x-\xi_x) + C_x \exp(-\mu_x x)$, for points close to x=0,

$X(x) = \sin k_x(x-\xi_x)$, for points remote from x=0,

$Y(y) = \sin k_y(y-\xi_y) + C_y \exp(-\mu_y y)$, for points close to y=0,

$Y(y) = \sin k_y(y-\xi_y)$ for points remote from y=0.

As discussed in Chapter 3, the boundary conditions at the edges determine the coefficients $\sin k_x\xi_x$, $\cos k_x\xi_x$,C_x ,$\sin k_y\xi_y$, $\cos k_y\xi_y$ and C_y. In this appendix only coefficients in x are derived, however, the expressions for the coefficients in y are similar, the only modification necessary is to change the indices in x for y. Moreover, the wavenumbers k_x and k_y in the expressions shown below are substituted by $k\cos\theta$ and $k\sin\theta$ in the numerical computation.

B.1 Simply-supported edge

For a left simply-supported edge (x=0) we have the following boundary conditions [82]

$$X(0) = 0, \quad \text{and} \quad X''(0) = 0,$$

applying these boundary conditions in the equation for X(x) we have,

$$-\sin k_x \xi_x + C_x = 0,$$
$$k_x^2 \sin k_x \xi_x + \mu_x^2 C_x = 0.$$

The solution of the above system of equations is given by,

$$\sin k_x \xi_x = C_x = 0, \tag{B.2}$$

and as a result,

$$\cos k_x \xi_x = 1. \tag{B.3}$$

B.2 Clamped edge

The boundary conditions on a left clamped edge (x=0) are given by,

$$X(0) = X'(0) = 0.$$

Applying these boundary conditions in equation (B.1) we obtain the following system of equations,

$$\sin k_x \xi_x = C_x,$$
$$\cos k_x \xi_x = \frac{\mu_x}{k_x} C_x.$$

Solving this system of equations we obtain that,

$$C_x = \sin k_x \xi_x = \frac{k_x}{\sqrt{2\left(k_x^2 + k_y^2\right)}},$$
$$\cos k_x \xi_x = \frac{\mu_x}{\sqrt{2\left(k_x^2 + k_y^2\right)}} = \frac{\sqrt{k_x^2 + 2k_y^2}}{\sqrt{2\left(k_x^2 + k_y^2\right)}}. \tag{B.4}$$

B.3 Free edge

For a left free edge (x=0) we have that [82]

$$\frac{\partial^2 z}{\partial x^2} + \nu \frac{\partial^2 z}{\partial y^2} = \frac{\partial^3 z}{\partial x^3} + (2-\nu)\frac{\partial^3 z}{\partial x \partial y^2} = 0,$$

Applying these boundary conditions in equation (B.1), including evanescent terms for X(x) but neglecting evanescent terms for Y(y), we obtain the following system of equations,

$$\left(k_x^2 + \nu k_y^2\right)\sin k_x \xi_x + \left(\mu_x^2 - \nu k_y^2\right)C_x = 0,$$
$$\left(k_x^3 + (2-\nu)k_x k_y^2\right)\cos k_x \xi_x + \left(\mu_x^3 - (2-\nu)\mu_x k_y^2\right)C_x = 0.$$

The solution of this system of equations is given by,

$$\sin k_x \xi_x = \frac{|W_1|}{\sqrt{W_1^2 + W_2^2}}, \tag{B.5}$$

$$\cos k_x \xi_x = \frac{|W_2|}{\sqrt{W_1^2 + W_2^2}}, \tag{B.6}$$

$$C_x = \frac{1}{\sqrt{W_1^2 + W_2^2}}, \tag{B.7}$$

where,

$$W_1 = -\frac{\left(\mu_x^2 - \nu k_y^2\right)}{\left(k_x^2 + \nu k_y^2\right)}, \qquad W_2 = -\frac{\left(\mu_x^3 - (2-\nu)\mu_x k_y^2\right)}{\left(k_x^3 + (2-\nu)k_x k_y^2\right)}.$$

B.4 Guided edge

The following boundary conditions apply for a left guided edge (x=0),

$$X'(0) = X'''(0) = 0.$$

Similar to the previous cases, we can apply these boundary conditions to equation (B.1) and obtain,

$$k_x \cos k_x \xi_x - \mu_x C_x = 0,$$
$$k_x^3 \cos k_x \xi_x + \mu_x^3 C_x = 0.$$

The solution of the above system of equations is given by,

$$\cos k_x \xi_x = C_x = 0, \tag{B.8}$$

and as a result,

$$\sin k_x \xi_x = 1. \tag{B.9}$$

B.5 General spring attachment

As a means of deriving the coefficients for a general type of edge attachment we assume that the plate is uniformly supported along the edge by a translational and a rotational spring. This support provides translational, rotational and coupling resistance and the respective stiffness are k_{zz}, $k_{\theta\theta}$ and $k_{z\theta}$. A sketch of this support is presented in fig. B.1. For a left edge (x = 0) the equations associated with this type of support are given by,

$$D\left[\frac{\partial^3 z}{\partial x^3} + (2-\nu)\frac{\partial^3 z}{\partial y^2 \partial x}\right] = k_{zz} z + k_{z\theta}\left(\frac{\partial z}{\partial x}\right),$$

$$-D\left[\frac{\partial^2 z}{\partial x^2} + \nu\frac{\partial^2 z}{\partial y^2}\right] = k_{\theta\theta}\left(\frac{\partial z}{\partial x}\right) + k_{z\theta} z.$$

Applying these boundary conditions in equation (B.1), including evanescent terms for X(x) but neglecting evanescent terms for Y(y), we obtain the following system of equations,

$$\begin{aligned}
&\left(-Dk_x^3 - Dk_x k_y^2(2-\nu) - k_{z\theta}k_x\right)\cos k_x\xi_x + k_{zz}\sin k_x\xi_x \\
&+\left(-D\mu_x^3 + D(2-\nu)\mu_x k_y^2 - k_{zz} + k_{z\theta}\mu_x\right)C_x = 0, \\
&\left(Dk_x^2 + Dk_y^2\nu - k_{z\theta}\right)\sin k_x\xi_x + k_{\theta\theta}k_x\cos k_x\xi_x \\
&+\left(D\mu_x^2 - Dk_y^2\nu - k_{\theta\theta}\mu_x + k_{z\theta}\right)C_x = 0.
\end{aligned}$$

The solution of the above system of equations yields,

$$\sin k_x \xi_x = \frac{W_2 W_4 - W_3 W_5}{\sqrt{(W_1 W_5 - W_6 W_2)^2 + (W_2 W_4 - W_3 W_5)^2}}, \tag{B.10}$$

$$\cos k_x \xi_x = \frac{W_1 W_5 - W_6 W_2}{\sqrt{(W_1 W_5 - W_6 W_2)^2 + (W_2 W_4 - W_3 W_5)^2}}, \tag{B.11}$$

$$C_x = \frac{W_3 W_6 - W_1 W_4}{\sqrt{(W_1 W_5 - W_6 W_2)^2 + (W_2 W_4 - W_3 W_5)^2}}, \tag{B.12}$$

where,

$$W_1 = Dk_x^2 + Dk_y^2\nu - k_{z\theta},$$

$$W_2 = D\mu_x^2 - Dk_y^2\nu - k_{\theta\theta}\mu_x + k_{z\theta},$$

$$W_3 = k_{\theta\theta}k_x,$$

$$W_4 = -Dk_x^3 - Dk_xk_y^2(2-\nu) - k_{z\theta}k_x,$$

$$W_5 = -D\mu_x^3 + D(2-\nu)\mu_xk_y^2 - k_{zz} + k_{z\theta}\mu_x,$$

$$W_6 = k_{zz}.$$

B.6 Stiffness coefficients for a beam/stiffener coupling [55]

The parameters of the Bolotin's dynamic edge effect method can be applied to beam/stiffener coupling. It is only necessary to express the stiffness coefficients k_{zz}, $k_{\theta\theta}$ and $k_{z\theta}$ as a function of the stiffener dynamic properties. The stiffness coefficients of a general stiffener (illustrated in fig. B.2) have been considered in ref. [55] and were derived in the form

$$\begin{aligned} k_{zz} &= EI_1k_2^4 - \rho A\omega^2, \qquad k_{z\theta} = -EI_{12}c_0k_2^4 - \rho Ac_2\omega^2, \\ k_{\theta\theta} &= \left(E\Gamma + EI_2c_0^2\right)k_2^4 + GJk_2^2 - \left(I + \rho Ac_1^2 + \rho Ac_2^2\right)\omega^2, \end{aligned} \tag{B.13}$$

where EI_1, EI_2 and EI_{12} are the flexural rigidities of the stiffener, $E\Gamma$ and GJ are the torsional rigidities, ρA are the mass and polar moment of inertia per unit length. The points S, C and P in fig. B.2 represent the shear centre, the centroid and the plate attachment point, respectively. The stiffness coefficients presented in (B.13) were derived assuming the plate is effectively rigid in-plane (k_L and k_s = 0).

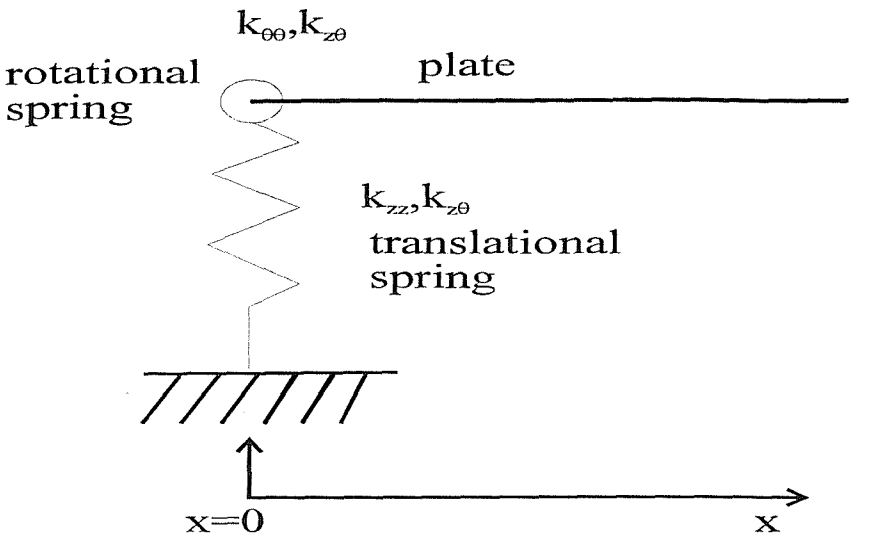

Fig. B.1 - General spring attachment along the left edge of a plate.

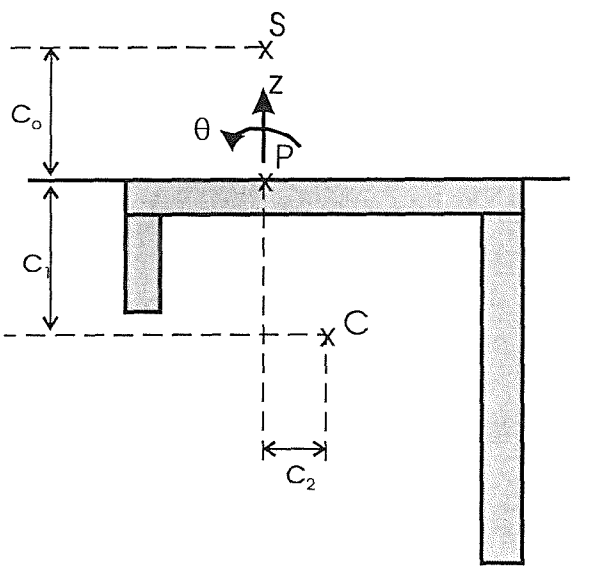

Fig. B.2 - Geometry of stiffener [55].

APPENDIX C

DERIVATION OF REFLECTION AND TRANSMISSION COEFFICIENTS FOR VARIOUS BOUNDARY CONDITIONS

As a means of deriving the reflection coefficients of edges with classical boundary conditions we assume that a travelling bending wave is incident upon a plate edge. This wave has a frequency ω and a wavenumber $k=\omega^{1/2}(m/D)^{1/4}$, where D is the flexural rigidity and m is the plate mass per unit area. As no wave is transmitted through the edge, a reflected and an evanescent field component are generated by the interaction between the incident wave and the edge (fig. 3.9). The motion of this semi-infinite flat plate is represented in wave terms as [38,55]

$$z(x,y,t) = \left\{A_{ref}e^{-ik_y y} + A_{in}e^{ik_y y} + A_e e^{-\mu_y y}\right\}e^{ik_x x}e^{i\omega t} \qquad (C.1)$$

where A_{ref} is the modulus of the reflected wave, A_{in} represents the incident wave, A_e represents the evanescent field component, $k_y = k\sin\theta$, $k_x = k\cos\theta$ and $\mu_y = \sqrt{k^2 + k_x^2}$.

C.1 Simply-supported edge

The static boundary conditions on a simply-supported edge situated at $y = 0$ are

$$z(x,0,t) = 0,$$
$$M(x,0,t) = -D\left\{\frac{\partial^2 z}{\partial y^2} + \nu\frac{\partial^2 z}{\partial x^2}\right\} = 0,$$

where M represents the bending moment, D is the flexural rigidity and ν is Poisson's ratio. Applying the boundary conditions at y=0 we have the following equations

$$A_{ref} + A_{in} + A_e = 0,$$
$$-k_y^2 A_{ref} - k_y^2 A_{in} + \mu_y^2 A_e - k_x^2\nu\left(A_{ref} + A_e + A_{in}\right) = 0.$$

The solution of the above equations is given by

$$R = \frac{A_{ref}}{A_{in}} = -1 \qquad \text{and} \qquad E = \frac{A_e}{A_{in}} = 0, \tag{C.2}$$

where R is the reflection coefficient and E is termed the coefficient of the evanescent field component.

C.2 Guided edge

The static boundary conditions on a guided edge situated at y = 0 are given by

$$\frac{\partial}{\partial y} z(x,0,t) = 0,$$

$$F(x,0,t) = D\frac{\partial}{\partial y}\left(\frac{\partial^2 z}{\partial y^2} + (2-\nu)\frac{\partial^2 z}{\partial x^2}\right) = 0,$$

where F is the shear force. Applying these boundary conditions on equation (C.1) and solving for the amplitudes we obtain,

$$R = \frac{A_{ref}}{A_{in}} = 1 \qquad \text{and} \qquad E = \frac{A_e}{A_{in}} = 0. \tag{C.3}$$

C.3 Clamped edge

The static boundary conditions of clamped edges are

$$z(x,0,t) = 0 \qquad \text{and} \qquad \frac{\partial z(x,0,t)}{\partial y} = 0.$$

Following similar procedure as before we can show that

$$R = \frac{A_{ref}}{A_{in}} = -\frac{\mu_y + ik_y}{\mu_y - ik_y} \qquad \text{and} \qquad E = \frac{A_e}{A_{in}} = \frac{i2k_y}{\mu_y - ik_y}. \tag{C.4}$$

It is observed that the above reflection and evanescent field component coefficients differ from the ones derived by Graff [82] for the same type of boundary conditions. The difference is on the signs of both imaginary parts and it is due to the use of an opposite orientation for the incident wave by Graff [82]. When the same orientation is employed in the derivation of the correlation coefficient (Chapter 3) and

the reflection coefficients, the final correlation coefficient results using Graff's convention or the convention here employed are coincident.

C.4 Free edge

The static boundary conditions of free edges situated at y = 0 are

$$F(x,0,t) = D\frac{\partial}{\partial y}\left(\frac{\partial^2 z}{\partial y^2} + (2-\nu)\frac{\partial^2 z}{\partial x^2}\right) = 0 \qquad \text{and}$$

$$M(x,0,t) = -D\left(\frac{\partial^2 z}{\partial y^2} + \nu\frac{\partial^2 z}{\partial x^2}\right) = 0.$$

The mathematical manipulation is cumbersome but the final result is given by

$$R = \frac{A_{ref}}{A_{in}} = -\frac{(W_1 + iW_2)}{(W_1 - iW_2)} \quad \text{and} \quad E = \frac{A_e}{A_{in}} = -\frac{i2W_2W_3}{(W_1 - iW_2)}. \qquad (C.5)$$

where

$$W_2 = k_y^3 + k_y k_x^2(2-\nu)\,, \qquad W_3 = \frac{k_y^2 + \nu k_x^2}{\mu_y^2 - \nu k_x^2} \qquad \text{and}$$

$$W_1 = \left(\mu_y^3 - \mu_y k_x^2(2-\nu)\right)\frac{\left(k_y^2 + \nu k_x^2\right)}{\left(\mu_y^2 - \nu k_x^2\right)}.$$

C.5 General spring attachment

A travelling wave of frequency ω is incident on a bottom boundary (y=0) that has a general spring element attached to it. This element provides translational, rotational and coupling resistance. The respective stiffness are k_{zz}, $k_{\theta\theta}$ and $k_{z\theta}$ (illustration in fig. C.1). A general solution to equation (C.1) on the left and right sides of the edge are

$$z_1(t) = \left\{A_{ref}e^{-ik_y y} + A_{in}e^{ik_y y} + A_{e1}e^{-\mu_y y}\right\}e^{ik_x x}e^{i\omega t} \qquad (C.6)$$

$$z_2(t) = \left\{A_t e^{ik_y y} + A_{e2}e^{\mu_y y}\right\}e^{ik_x x}e^{i\omega t} \qquad (C.7)$$

where A_t is the amplitude of the transmitted wave, A_{e1} and A_{e2} are the amplitudes of the evanescent field components on the left and right sides of the edge, respectively. The boundary conditions at y = 0 are

$$z_1(t) = z_2(t)$$

$$\frac{\partial z_1}{\partial y} = \frac{\partial z_2}{\partial y}$$

$$D\left[\frac{\partial^3 z_1}{\partial y^3} + (2-\nu)\frac{\partial^3 z_1}{\partial y \partial x^2}\right] - D\left[\frac{\partial^3 z_2}{\partial y^3} + (2-\nu)\frac{\partial^3 z_2}{\partial y \partial x^2}\right] = k_{zz} z_1 + k_{z\theta}\left(\frac{\partial z_1}{\partial y}\right) \quad \text{(C.8)}$$

$$-D\left[\frac{\partial^2 z_1}{\partial y^2} + \nu\frac{\partial^2 z_1}{\partial x^2}\right] + D\left[\frac{\partial^2 z_2}{\partial y^2} + \nu\frac{\partial^2 z_2}{\partial x^2}\right] = k_{\theta\theta}\left(\frac{\partial z_1}{\partial y}\right) + k_{z\theta} z_1 .$$

Assuming that the spring element is placed along the outer edge of the plate we have that the displacement of the region that is on the left side of the spring element is null. Applying this condition, z_2=0, the system of equations (C.8) is reduced to

$$\begin{aligned} D\left[\frac{\partial^3 z_1}{\partial y^3} + (2-\nu)\frac{\partial^3 z_1}{\partial y \partial x^2}\right] &= k_{zz} z_1 + k_{z\theta}\left(\frac{\partial z_1}{\partial y}\right) \\ -D\left[\frac{\partial^2 z_1}{\partial y^2} + \nu\frac{\partial^2 z_1}{\partial x^2}\right] &= k_{\theta\theta}\left(\frac{\partial z_1}{\partial y}\right) + k_{z\theta} z_1 . \end{aligned} \quad \text{(C.9)}$$

Substituting (C.6) in the above equations and rearranging the terms we obtain the following system of equations

$$\begin{aligned} L_1 A_{ref} - L_2 A_{in} + L_3 A_{e1} &= 0 \\ L_4 A_{ref} + L_5 A_{in} + L_6 A_{e1} &= 0, \end{aligned} \quad \text{(C.10)}$$

where

$$\begin{aligned} L_1 &= iDk_y^3 + iDk_y k_x^2 (2-\nu) + ik_{z\theta} k_y - k_{zz} \\ L_2 &= iDk_y^3 + iDk_y k_x^2 (2-\nu) + ik_{z\theta} k_y + k_{zz} \\ L_3 &= -D\mu_y^3 + D\mu_y k_x^2 (2-\nu) + k_{z\theta}\mu_y - k_{zz} \\ L_4 &= Dk_y^2 + Dk_x^2 \nu + ik_{\theta\theta} k_y - k_{z\theta} \\ L_5 &= Dk_y^2 + Dk_x^2 \nu - ik_{\theta\theta} k_y - k_{z\theta} \\ L_6 &= -D\mu_y^2 + Dk_x^2 \nu + k_{\theta\theta}\mu_y - k_{z\theta} . \end{aligned}$$

The relative amplitudes of the reflected and evanescent waves as a function of incident wave's amplitude are obtained from the solution of the system of

equations (C.10). These relative amplitudes (reflection and evanescent field components coefficients) are

$$\begin{aligned} R &= \frac{A_{ref}}{A_{in}} = \frac{L_6L_2 + L_5L_3}{L_1L_6 - L_4L_3} \\ E &= \frac{A_e}{A_{in}} = \frac{L_2L_4 + L_1L_5}{L_4L_3 - L_1L_6}. \end{aligned} \tag{C.11}$$

After some algebraic manipulation both reflection and evanescent field components coefficients can be expressed in real and imaginary parts as

$$\mathrm{Re}\left[\frac{A_{ref}}{A_{in}}\right] = \mathrm{Re}[R] = \frac{M_b^2 - M_a^2}{M_b^2 + M_a^2} \quad \text{and} \quad \mathrm{Im}\left[\frac{A_{ref}}{A_{in}}\right] = \mathrm{Im}[R] = -\frac{2M_bM_a}{M_b^2 + M_a^2}, \tag{C.12}$$

where,

$$\begin{aligned} M_a &= \left(k_y^2 D + k_x^2 D\nu - k_{z\theta}\right)\left(-\mu_y^3 D + D\mu_y k_x^2 (2-\nu) + k_{z\theta}\mu_y - k_{zz}\right) \\ &\quad + k_{zz}\left(-\mu_y^2 D + Dk_x^2 \nu + k_{\theta\theta}\mu_y - k_{z\theta}\right), \end{aligned}$$

$$\begin{aligned} M_b &= \left(-\mu_y^2 D + Dk_x^2 \nu + k_{\theta\theta}\mu_y - k_{z\theta}\right)\left(k_y^3 D + k_y(2-\nu)Dk_x^2 + k_{z\theta}k_y\right) \\ &\quad - k_{\theta\theta}k_y\left(-\mu_y^3 D + D\mu_y k_x^2 (2-\nu) + k_{z\theta}\mu_y - k_{zz}\right), \end{aligned}$$

$$\mathrm{Re}\left[\frac{A_{e1}}{A_{in}}\right] = \mathrm{Re}[E_1] = -\frac{2M_bM_3}{M_b^2 + M_a^2} \quad \text{and} \quad \mathrm{Im}\left[\frac{A_{e1}}{A_{in}}\right] = \mathrm{Im}[E_1] = \frac{2M_3M_a}{M_b^2 + M_a^2}, \tag{C.13}$$

where $M_3 = \left(k_y^3 D + k_y(2-\nu)Dk_x^2 + k_{z\theta}k_y\right)\left(k_y^2 D + k_x^2 D\nu - k_{z\theta}\right) - k_{zz}k_{\theta\theta}k_y.$

C.6 General spring attachment including wave transmission to the adjacent system

For the case in which the plate on the left side of the edge is moving, the system of equations (C.8) can be solved to determine the amplitudes of the reflected, transmitted and evanescent field components. After some mathematical manipulation we can express the system of equations (C.8) as

$$\begin{cases} A_{ref} + A_{in} + A_{e1} - A_t - A_{e2} = 0 \\ -ik_yA_{ref} + ik_yA_{in} - \mu_yA_{e1} - ik_yA_t - \mu_yA_{e2} = 0 \\ L_1A_{ref} + L_2A_{in} + L_3A_{e1} + L_4A_t + L_5A_{e2} = 0 \\ L_6A_{ref} + L_7A_{in} + L_8A_{e1} + L_9A_t + L_{10}A_{e2} = 0 \end{cases}, \tag{C.14}$$

where,

$$L_1 = iDk_y^3 - k_{zz} + ik_y k_{z\theta}, \qquad L_2 = -iDk_y^3 - k_{zz} - ik_y k_{z\theta},$$

$$L_3 = -D\mu_y^3 - k_{zz} + \mu_y k_{z\theta}, \qquad L_4 = iDk_y^3, \qquad L_5 = -D\mu_y^3,$$

$$L_6 = Dk_y^2 - k_{z\theta} + ik_y k_{\theta\theta}, \quad L_7 = Dk_y^2 - k_{z\theta} - ik_y k_{\theta\theta},$$

$$L_8 = -D\mu_y^2 - k_{z\theta} + \mu_y k_{\theta\theta}, \quad L_9 = -Dk_y^2, \quad \text{and} \quad L_{10} = D\mu_y^2.$$

By solving this system of equations, we obtain that the amplitude of the transmitted wave as a function of the incident wave's amplitude is given by

$$\frac{A_t}{A_{in}} = T = \frac{W_1 W_2 - W_3 W_4}{W_5 W_4 + W_2 W_6}, \tag{C.15}$$

The amplitude of the evanescent field component on the left side of the spring element is given by,

$$\frac{A_{e2}}{A_{in}} = E_2 = \frac{W_3(W_5 W_4 + W_2 W_6) + W_5(W_1 W_2 - W_3 W_4)}{W_2(W_5 W_4 + W_2 W_6)}. \tag{C.16}$$

The amplitude of the evanescent field component on the right side of the spring element is,

$$\frac{A_{e1}}{A_{in}} = E_1 = \left\{ \begin{array}{c} \dfrac{(L_1 - L_2)}{(L_3 - L_1)} - \dfrac{(L_4 + L_1)}{(L_3 - L_1)}\left[\dfrac{(W_1 W_2 - W_3 W_4)}{(W_5 W_4 + W_2 W_6)}\right] \\ -\dfrac{(L_5 + L_1)}{(L_3 - L_1)}\left[\dfrac{W_3(W_5 W_4 + W_2 W_6) + W_5(W_1 W_2 - W_3 W_4)}{W_2(W_5 W_4 + W_2 W_6)}\right] \end{array} \right\}. \tag{C.17}$$

And finally the amplitude of the reflected wave as a function of the amplitude of the incident wave is expressed as

$$\frac{A_{ref}}{A_{in}} = R = \left\{ \begin{array}{c} \dfrac{(L_2 - L_3)}{(L_3 - L_1)} + \dfrac{(L_4 + L_3)}{(L_3 - L_1)}\left[\dfrac{(W_1 W_2 - W_3 W_4)}{(W_5 W_4 + W_2 W_6)}\right] \\ +\dfrac{(L_5 + L_3)}{(L_3 - L_1)}\left[\dfrac{W_3(W_5 W_4 + W_2 W_6) + W_5(W_1 W_2 - W_3 W_4)}{W_2(W_5 W_4 + W_2 W_6)}\right] \end{array} \right\}, \tag{C.18}$$

where,

$$W_1 = (L_1 - L_2)(ik_y - \mu_y) + (L_3 - L_1)i2k_y,$$

$$W_2 = (L_6 + L_{10})(ik_y - \mu_y) - (L_6 - L_8)(ik_y + \mu_y),$$

$$W_3 = (L_6 - L_7)(ik_y - \mu_y) - (L_6 - L_8)i2k_y,$$

$$W_4 = (L_3 - L_1)(ik_y + \mu_y) + (L_5 + L_1)(ik_y - \mu_y),$$

$$W_5 = (L_6 - L_8)i2k_y - (L_6 + L_9)(ik_y - \mu_y),$$

$$W_6 = (L_3 - L_1)i2k_y + (L_4 + L_1)(ik_y - \mu_y).$$

The above coefficients are equivalent to the reflection and transmission coefficients presented in ref. [55]. Expressions for k_{zz}, $k_{\theta\theta}$, $k_{z\theta}$ for the case of a general stiffener are presented in Appendix B.

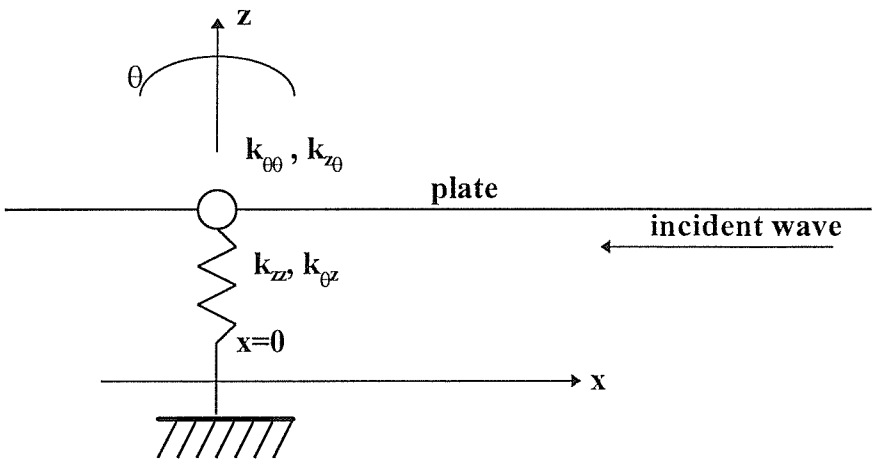

Fig. C.1 - Elastic wave incident on a general spring attachment (ref. [55]).

APPENDIX D

RESULTS OF THE INTEGRALS USED IN THE CORRELATION COEFFICIENT DERIVATION (CHAPTER 3)

- $\int_0^{\pi/2} \cos(A\cos\theta)d\theta = \frac{\pi}{2} J_0(A)$, ref. [70], (D.1)

- $\int_0^{\pi/2} \cos(A\sin\theta)\cos^{2n}\theta d\theta = \frac{\pi}{2}\frac{(2n-1)!}{A^n} J_n(A)$, n>-1/2 , ref. [70],

then for n=0 we can write that

$$\int_0^{\pi/2} \cos(A\sin\theta)d\theta = \frac{\pi}{2} J_0(A), \quad (D.2)$$

- $I = \int_0^{\pi/2} \cos(A\cos\theta)\cos(B\sin\theta)d\theta = \frac{\pi}{2} J_0\left(\sqrt{A^2+B^2}\right)$ (D.3)

Applying Jacobi's expansions in series of Bessel functions (ref. [71]) we can rewrite the integral on the left side of the above expression as

$$I = \int_0^{\pi/2} \left(J_0(A) + 2\sum_{n=1}^{\infty} (-1)^n J_{2n}(A)\cos 2n\theta \right)\left(J_0(B) + 2\sum_{n=1}^{\infty} J_{2n}(B)\cos 2n\theta \right) d\theta.$$

The cross multiplication of the two terms inside the parenthesis in the above expression result in four integrals that can be solved separately. The solution for each one of them is as follows

$$I_1 = \int_0^{\pi/2} J_0(A)J_0(B)d\theta = \frac{\pi}{2} J_0(A)J_0(B).$$

$$I_2 = J_0(A)\int_0^{\pi/2} 2\sum_{n=1}^{\infty} J_{2n}(B)\cos 2n\theta d\theta = J_0(A)2\sum_{n=1}^{\infty} J_{2n}(B)\int_0^{\pi/2} \cos 2n\theta d\theta$$

as $\int_0^{\pi/2} \cos 2n\theta d\theta = \left[\frac{\sin 2n\theta}{2n}\right]_0^{\pi/2} = 0$, then $I_2=0$.

Similar to the derivation carried out for I_2 we can show that

$$I_3 = J_0(B)\int_0^{\pi/2} 2\sum_{n=1}^{\infty}(-1)^n J_{2n}(A)\cos 2n\theta d\theta = 0.$$

$$I_4 = \int_0^{\pi/2} 4\sum_{n=1}^{\infty}(-1)^n J_{2n}(A)J_{2n}(B)\cos^2 2n\theta d\theta = 4\sum_{n=1}^{\infty}(-1)^n J_{2n}(A)J_{2n}(B)\int_0^{\pi/2}\cos^2 2n\theta d\theta$$

as $\int_0^{\pi/2}\cos^2 2n\theta d\theta = \left[\frac{\theta}{2}+\frac{\sin 4n\theta}{8n}\right]_0^{\pi/2} = \frac{\pi}{4}$, then

$$I_4 = \pi\sum_{n=1}^{\infty}(-1)^n J_{2n}(A)J_{2n}(B).$$

From the results for I_1, I_2, I_3 and I_4 we obtain that

$$I = \frac{\pi}{2}\left[J_0(A)J_0(B)+2\sum_{n=1}^{\infty}(-1)^n J_{2n}(A)J_{2n}(B)\right]. \qquad (D.4)$$

The above result can be expressed in a more convenient form if the summation theorem of Bessel functions is recalled. This theorem states that (pg. 979, ref. [70])

$$J_0(mR) = J_0(m\rho)J_0(mr)+2\sum_{k=1}^{\infty}J_k(m\rho)J_k(mr)\cos k\varphi, \qquad (D.5)$$

where $R = \sqrt{r^2+\rho^2-2r\rho\cos\varphi}$ Assuming that r and ρ are two perpendicular functions we have $\varphi=90^\circ$, $\cos\varphi=0$, $R = \sqrt{r^2+\rho^2}$ and

$$J_0(mR) = J_0(m\rho)J_0(mr)-2\sum_{k=1}^{\infty}J_k(m\rho)J_k(mr)\cos k\frac{\pi}{2}.$$

In the present work the function A represents a distance in the x-direction multiplied by a constant (k) and the function B represents a distance in the y-direction multiplied by the same constant (k). Therefore, the functions A and B are perpendicular and the above assumptions apply. Moreover, it is easy to show that for the summations involved in equation (D.4) $(-1)^n$ is equivalent to $\cos k\pi/2$, because k=2n. Therefore, equation (D.4) is equivalent to equation (D.5) and as a result

$$\frac{\pi}{2}J_0\left(\sqrt{A^2+B^2}\right) = \frac{\pi}{2}\left[J_0(A)J_0(B)+2\sum_{n=1}^{\infty}(-1)^n J_{2n}(A)J_{2n}(B)\right].$$

Finally, substituting the above result in equation (D.4) and comparing with equation (D.3) we find that

$$\int_0^{\pi/2} \cos(A\cos\theta)\cos(B\sin\theta)d\theta = \frac{\pi}{2} J_0\left(\sqrt{A^2 + B^2}\right) \qquad \text{(D.6)}$$

Equations (D.1), (D.2) and (D.6) are the basic results employed in Chapter 3 to derive closed-form expressions for the correlation coefficients.

APPENDIX E

ON THE EQUIVALENCE OF BOLOTIN'S DYNAMIC EDGE EFFECT METHOD [56] AND LANGLEY'S ELASTIC WAVE TECHNIQUE [55]

The analysis of the equivalence between the elastic wave technique employed by Langley [55] with the Bolotin's dynamic edge effect method [56] has been presented by Langley [55]. In this analysis it was concluded that both approaches are equivalent and the elastic wave technique is only a reformulation of Bolotin's method. However, the analysis presented in ref. [55] was restricted to the inner solution of Bolotin's method. In what follows an extension to that analysis is presented for the case of the inner solution (propagating waves) and for the outer solution (decaying components restricted to the vicinity of the boundaries). Reflection coefficients and Bolotin's dynamic edge effect parameters ($\sin k_x\xi_x$, $\cos k_x\xi_x$,C_x, $\sin k_y\xi_y$, $\cos k_y\xi_y$ and C_y) are then compared for various boundary conditions.

E.1 Comparison of the inner solution

The 'inner solution' assumed in Bolotin's dynamic edge effect method is given by [56]

$$W(x,y) = \sin k_x(x-\xi_x)\sin k_y(y-\xi_y)e^{i\omega t}, \tag{E.1}$$

and when trigonometric transformations are applied to (E.1) it can be expressed as

$$\begin{aligned} W(x,y) = &(\sin k_x x\cos k_x\xi_x - \cos k_x x\sin k_x\xi_x) \\ &(\sin k_y y\cos k_y\xi_y - \cos k_y y\sin k_y\xi_y)e^{i\omega t}. \end{aligned} \tag{E.2}$$

The deflection shape derived by Langley [55] using an elastic wave technique is

$$W(x,y) = 4(A_2A_4)^{1/2}\cos(k_x x+\phi_x)\cos(k_y y+\phi_y)e^{i\omega t}, \tag{E.3}$$

as $A_2 = A_1/R_L$ and $A_4 = A_1/R_B$, then

$$4(A_2A_4)^{1/2} = 4\left(\frac{A_1^2}{R_L R_B}\right)^{1/2}. \tag{E.4}$$

Substituting (E.4) in (E.3) and applying trigonometric relations to this equation we have that

$$\begin{aligned} W(x,y) = 4\left(\frac{A_1^2}{R_L R_B}\right)^{1/2} &(\cos k_x x \cos\phi_x - \sin k_x x \sin\phi_x) \\ &(\cos k_y y \cos\phi_y - \sin k_y y \sin\phi_y) e^{i\omega t}. \end{aligned} \tag{E.5}$$

From equations (E.2) and (E.5) we can write that

$$\begin{aligned} \cos\phi_x &= \sin k_x \xi_x, & \sin\phi_x &= \cos k_x \xi_x, \\ \cos\phi_y &= \sin k_y \xi_y, & \sin\phi_y &= \cos k_y \xi_y. \end{aligned} \tag{E.6}$$

From equations (30,31) of ref. [55] we have that

$$e^{i\phi_x} = (A_3/A_4)^{1/2}, \qquad e^{i\phi_y} = (A_3/A_2)^{1/2}. \tag{E.7}$$

As $A_3 = A_1/R_L R_B$, $A_2 = A_1/R_L$ and $A_4 = A_1/R_B$ then

$$e^{i\phi_x} = (1/R_L)^{1/2}, \qquad e^{i\phi_y} = (1/R_B)^{1/2}. \tag{E.8}$$

When z is complex the following mathematical relation applies (equation (3.7.27), ref. [72])

$$z^{1/2} = \left[\frac{1}{2}(r + \mathrm{Re}[z])\right]^{1/2} \pm i\left[\frac{1}{2}(r - \mathrm{Re}(z))\right]^{1/2} = u \pm iv, \tag{E.9}$$

where r is the modulus of z, 2uv=y and where the ambiguous sign is taken to be the same as the sign of y.

Substituting (E.9) in equations (E.8) and expressing the exponential functions in terms of sine and cosines we obtain

$$\begin{aligned} \cos\phi_x &= \left[\frac{1}{2}(1 + \mathrm{Re}[R_L])\right]^{1/2}, & \sin\phi_x &= \pm\left[\frac{1}{2}(1 - \mathrm{Re}[R_L])\right]^{1/2}, \\ \cos\phi_y &= \left[\frac{1}{2}(1 + \mathrm{Re}[R_B])\right]^{1/2}, & \sin\phi_y &= \pm\left[\frac{1}{2}(1 - \mathrm{Re}[R_B])\right]^{1/2}. \end{aligned} \tag{E.10}$$

As a result of (1-Re[R]) being always positive or null, the ambiguous sign in (E.10) can be taken as positive. Finally, from (E.6) and (E.10) we have that

$$\sin k_x\xi_x = \left[\frac{1}{2}\left(1+\mathrm{Re}[R_L]\right)\right]^{1/2}, \qquad \cos k_x\xi_x = \left[\frac{1}{2}\left(1-\mathrm{Re}[R_L]\right)\right]^{1/2},$$
$$\sin k_y\xi_y = \left[\frac{1}{2}\left(1+\mathrm{Re}[R_B]\right)\right]^{1/2}, \qquad \cos k_y\xi_y = \left[\frac{1}{2}\left(1-\mathrm{Re}[R_B]\right)\right]^{1/2}. \tag{E.11}$$

The above equations provide a simple relation between the parameters of Bolotin's dynamic edge effect method and the reflection coefficients of the plate boundaries.

E.2 Comparison of the outer or corrective solution

Assuming we are in the vicinity of one of the edges, a evanescent component must be added to the elastic wave representation. In this case we can write that (equation (A2), ref. [55])

$$w_1 = \left\{A_{in}\exp(-ik_x x)+A_{ref}\exp(ik_x x)+A_{el}\exp\left(\sqrt{k_x^2+2k_y^2}\,x\right)\right\}\exp(ik_y y+i\omega t). \tag{E.12}$$

The equivalent expression based on the dynamic edge effect method can be obtained from (B.1) or from ref. [56], equations (4.28) and (4.30). It is

$$w_1 = \left\{\sin k_x(x-\xi_x)+C_x\exp\left(-\sqrt{k_x^2+2k_y^2}\,x\right)\right\}\sin k_y(y-\xi_y)\cos\omega t, \tag{E.13}$$

which after some mathematical manipulation can be expressed as

$$w_1 = \left\{\sin k_x x\cos k_x\xi_x-\cos k_x x\sin k_x\xi_x+C_x\exp\left(-\sqrt{k_x^2+2k_y^2}\,x\right)\right\}\sin k_y(y-\xi_y)\cos\omega t.$$

Comparing the above expression with equation (E.12) we obtain that

$$C_x = \left[\frac{1}{2}\mathrm{Re}\left[\frac{A_{el}}{A_{in}}\right]\right]^{1/2} = \left[\frac{1}{2}\mathrm{Re}[E]\right]^{1/2}. \tag{E.14}$$

Expression (E.14) has been obtained following a similar procedure as the one used in the derivation presented in E.1. Together with equations (E.11), equation (E.14) allows the determination of the dynamic edge effect method parameters directly from the reflected and evanescent field component coefficients. Moreover, if the dynamic edge effect method is to be applied in the vicinity of a edge in which only the transmitted (A_t) and the transmitted evanescent (A_{e2}) field

components exist, it can provide a way of estimating the dynamic edge effect parameters for the indirectly driven side of a system.

E.3 Verification of the results for some boundary conditions

Expressions (E.11) and (E.14) were used to derive results for the dynamic edge effect method parameters and for the reflection and evanescent field component coefficients for various boundary conditions. These results were compared to those derived in Appendices B and C. When the result used for one typical parameter has been drawn from Appendices B or C it will be called a direct result. On the other hand, if the parameter has been obtained from the application of equations (E.11) or (E.14), then it will be called an indirect result. Direct and indirect results were compared for simply-supported, guided, clamped and free edges and they were coincident for all cases. The comparison of indirect and direct results for clamped and free edges is presented in the next two sections.

E.3.1 Clamped edges

The real part of the reflection coefficient for a left clamped edge is given by equation (C.4)

$$\mathrm{Re}[R_L] = \frac{k_y^2}{\left(k_x^2 + k_y^2\right)}. \tag{E.15}$$

Substituting (E.15) in (E.11) we can show that

$$\sin k_x \xi_x = \left[\frac{1}{2}\left(1 - \frac{k_y^2}{k_y^2 + k_x^2}\right)\right]^{1/2} = \left[\frac{1}{2}\left(\frac{k_x^2}{k_y^2 + k_x^2}\right)\right]^{1/2} = \frac{k_x}{\sqrt{2\left(k_x^2 + k_y^2\right)}}, \tag{E.16}$$

and

$$\cos k_x \xi_x = \left[\frac{1}{2}\left(1 + \frac{k_y^2}{k_y^2 + k_x^2}\right)\right]^{1/2} = \left[\frac{1}{2}\left(\frac{k_x^2 + 2k_y^2}{k_y^2 + k_x^2}\right)\right]^{1/2} = \frac{\sqrt{k_x^2 + 2k_y^2}}{\sqrt{2\left(k_x^2 + k_y^2\right)}}. \tag{E.17}$$

From equation (C.4) we have that the real part of the evanescent field component coefficient for a left clamped edge is given by

$$\mathrm{Re}[E_L] = \frac{-2k_x^2}{2\left(k_x^2 + k_y^2\right)}. \tag{E.18}$$

Substituting (E.18) in (E.14) we have that

$$C_x = \left[\frac{1}{2}\frac{2k_x^2}{2\left(k_x^2 + k_y^2\right)}\right] = \frac{k_x}{\sqrt{2\left(k_x^2 + k_y^2\right)}}. \tag{E.19}$$

The indirectly derived results (E.16), (E.17) and (E.19) agree with the directly derived results (C.4).

E.3.2 Free edges

The real part of the reflection coefficient for a free left edge is given by

$$\mathrm{Re}[R_L] = -\frac{\left(W_1^2 - W_2^2\right)}{\left(W_1^2 + W_2^2\right)}, \tag{E.20}$$

where $W_2 = k_y^3 + k_y k_x^2(2-\nu)$, $W_3 = \dfrac{k_y^2 + \nu k_x^2}{\mu_y^2 - \nu k_x^2}$ and

$$W_1 = \left(\mu_y^3 - \mu_y k_x^2(2-\nu)\right)\frac{\left(k_y^2 + \nu k_x^2\right)}{\left(\mu_y^2 - \nu k_x^2\right)}.$$

Substituting (E.20) in (E.11) we obtain that

$$\sin k_x\xi_x = \frac{W_2}{\sqrt{W_1^2 + W_2^2}}, \qquad \cos k_x\xi_x = \frac{|W_1|}{\sqrt{W_1^2 + W_2^2}}. \tag{E.21}$$

After some mathematical manipulation the above equations are shown to equal

$$\sin k_x\xi_x = \frac{\left(k_x^3 + k_x k_y^2(2-\nu)\right)\left(\mu_x^2 - \nu k_y^2\right)}{\left[\left(\mu_x^3 - \mu_x k_y^2(2-\nu)\right)^2\left(k_x^2 + \nu k_y^2\right)^2 + \left(k_x^3 + k_x k_y^2(2-\nu)\right)^2\left(\mu_x^2 - \nu k_y^2\right)^2\right]^{1/2}}, \tag{E.22}$$

$$\cos k_x\xi_x = \frac{\left(\mu_x^3 - \mu_x k_y^2(2-\nu)\right)\left(k_x^2 + \nu k_y^2\right)}{\left[\left(\mu_x^3 - \mu_x k_y^2(2-\nu)\right)^2\left(k_x^2 + \nu k_y^2\right)^2 + \left(k_x^3 + k_x k_y^2(2-\nu)\right)^2\left(\mu_x^2 - \nu k_y^2\right)^2\right]^{1/2}}. \tag{E.23}$$

The real part of the evanescent field component coefficient for a left edge can be obtained from equation (C.5),

$$\mathrm{Re}[E_L]=\frac{2\left(k_x^3+k_xk_y^2(2-\nu)\right)^2\left(\mu_x^2-\nu k_y^2\right)\left(k_x^2+\nu k_y^2\right)}{\left(\mu_x^3-\mu_xk_y^2(2-\nu)\right)^2\left(k_x^2+\nu k_y^2\right)^2+\left(k_x^3+k_xk_y^2(2-\nu)\right)^2\left(\mu_x^2-\nu k_y^2\right)^2},\quad\text{(E.24)}$$

Substituting (E.24) in (E.14) we have that

$$C_x=\left[\frac{\left(k_x^2+\nu k_y^2\right)\left(k_x^3+k_xk_y^2(2-\nu)\right)^2\left(\mu_x^2-\nu k_y^2\right)}{\left(\mu_x^3-\mu_xk_y^2(2-\nu)\right)^2\left(k_x^2+\nu k_y^2\right)^2+\left(k_x^3+k_xk_y^2(2-\nu)\right)^2\left(\mu_x^2-\nu k_y^2\right)^2}\right]^{1/2}.\quad\text{(E.25)}$$

The direct results for the dynamic edge effect method that were derived in Appendix B, equations (B.5) and (B.6) are given by

$$\cos k_x\xi_x=\frac{|W_b|}{\sqrt{W_a^2+W_b^2}},\qquad \sin k_x\xi_x=\frac{|W_a|}{\sqrt{W_a^2+W_b^2}},\qquad\text{(E.26)}$$

where,

$$W_a=-\frac{\left(\mu_x^2-\nu k_y^2\right)}{\left(k_x^2+\nu k_y^2\right)},\qquad W_b=-\frac{\left(\mu_x^3-(2-\nu)\mu_xk_y^2\right)}{\left(k_x^3+(2-\nu)k_xk_y^2\right)}.\qquad\text{(E.27)}$$

Substituting (E.27) in (E.26) and rearranging the terms we obtain exactly the same equations as (E.22) and (E.23).

The parameter C_x for the dynamic edge effect method has been derived directly in Appendix B (equation (B.7)). The result is

$$C_x=\frac{1}{\sqrt{W_a^2+W_b^2}}.\qquad\text{(E.28)}$$

Substituting equations (E.27) in (E.28) we obtain that

$$C_x=\frac{\left(k_x^2+\nu k_y^2\right)\left(k_x^3+k_xk_y^2(2-\nu)\right)}{\left[\left(\mu_x^3-\mu_xk_y^2(2-\nu)\right)^2\left(k_x^2+\nu k_y^2\right)^2+\left(k_x^3+k_xk_y^2(2-\nu)\right)^2\left(\mu_x^2-\nu k_y^2\right)^2\right]^{1/2}}.\quad\text{(E.29)}$$

Comparing equations (E.25) and (E.29) we observe that there is a slightly difference between the directly and indirectly derived C_x parameter. This difference is probably related to the omission of the term $\exp(-ik_yy)$ in equation (E.12). However, in practice, the difference between the results obtained using the present derivation is negligible. This fact is illustrated in fig. (4.28) for the case of a rectangular flat plate with all around free edges. As shown, both results are coincident and very similar to experimental ones.

APPENDIX F

DISPERSION RELATIONS FOR VARIOUS STRUCTURES

Dispersion relations for some flat structures are presented in this appendix. They are expressed as a function of frequency f and propagation angle θ.

F.1 Doubly-curved thin shell

An asymptotic expression for the natural frequencies of free oscillations of a doubly-curved thin shell that is valid under certain conditions has being derived by Bolotin [89] using the dynamic edge effect method. This expression is [89]

$$\omega^2 = \frac{D}{\rho h}\left[\left(k_x^2 + k_y^2\right)^2 + \frac{Eh}{Dr_x^2}\left(\frac{\left(k_x^2 X + k_y^2\right)^2}{\left(k_x^2 + k_y^2\right)^2}\right)\right] \qquad \text{(F.1)}$$

where $X=r_x/r_y$, $\theta=\text{arctg}\, k_y/k_x$, $D=Eh^3/12(1-\nu^2)$, ω is the frequency of the free oscillation of the shell, D is the cylindrical rigidity, ρ is the material density, h is the shell thickness, E is the Young's modulus, k_x and k_y are the wavenumbers in x and y directions, and r_x and r_y are the principal radii of curvature of the surface. The parameter X satisfies the inequalities $-1 \leq X \geq 1$. The "plane stress" ring frequencies of the shell are defined as

$$f_x = \frac{1}{2\pi r_y}\sqrt{\frac{E}{\rho}}, \qquad f_y = \frac{1}{2\pi r_x}\sqrt{\frac{E}{\rho}}, \qquad \text{(F.2)}$$

where we assume that $f_y \geq f_x$. Expressing the wavenumbers k_x and k_y as a function of the bending wavenumber k and angle θ we have that [90]

$$\omega^2 = \frac{D}{\rho h}\left[k^4 + \frac{Eh}{Dr_x^2}\left(X\cos^2\theta + \sin^2\theta\right)^2\right] \qquad \text{(F.3)}$$

where $k_x=k\cos\theta$ and $k_y=k\sin\theta$. The limits of applicability and the general behaviour of equation (F.3) have been discussed by Gol'denveizer [90]. The natural frequencies of free oscillation of the shell are strongly dependent on the ring frequencies. Operating expression (F.3) mathematically we obtain an asymptotic expression for the bending wavenumber

$$k^4 = \frac{\rho h(2\pi f)^2}{D} - \frac{Eh}{Dr_x^2}\left(X\cos^2\theta + \sin^2\theta\right)^2. \qquad \text{(F.4)}$$

The first term on the left hand side of the above equation corresponds to the bending wavenumber of an equivalent flat plate while the second term is a correction due to the shell curvature. It will only have complex solutions for $f < f_x$, complex and real solutions for $f_x \le f < f_y$ (curve marked 2 in fig. F.1) and real solutions for $f \ge f_y$ (curve marked 3 in fig. F.1). In the frequency region $f_x \le f < f_y$, the real solutions are situated in a curve delimited by the angles 0 and θ_0, where θ_0 is given by

$$\theta_0 = \frac{1}{2}\cos^{-1}\left(\frac{2\frac{f}{f_y} - (X+1)}{(X-1)}\right). \qquad \text{(F.5)}$$

In the frequency $\sqrt{2}$ times the upper ring frequency the shell bending wavenumber approaches that of the equivalent flat plate (curve marked 5 in fig. F.1).

Equation (F.4) was used to estimate the bending wavenumber of the passenger car roof in the theoretical results presented in section 4.8. In this case, for frequencies situated between the two ring frequencies, the integration in wavenumber space used in the correlation coefficient estimation was performed between 0 and θ_0, where θ_0 is given by equation (F.5). Below the lower ring frequency no integration was performed and the correlation coefficient was assumed to approach unity. Above the upper ring frequency the usual limits 0 and $\pi/2$ apply. This procedure can be applied in the estimation of correlation coefficients for all curved shells. The results presented in section 4.8 shown that a reasonable approximation of the variation of the correlation coefficient or normalised cross-power spectral density results due to the lines orientation can be obtained when equation (F.4) is employed.

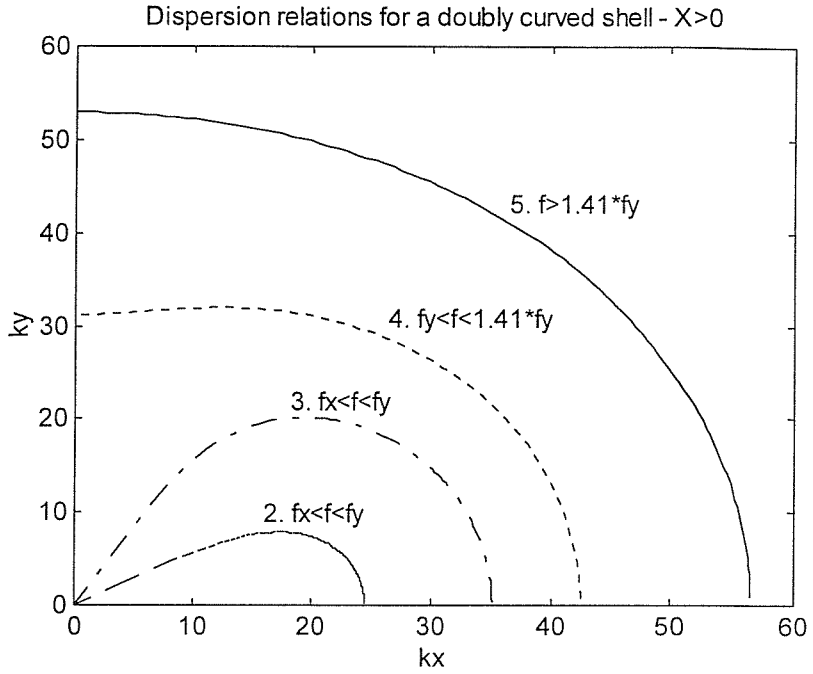

Fig. F.1 - Dispersion relations for a doubly-curved shell of positive curvature (X>0) and ring frequencies f_x = 100 Hz and f_y = 300 Hz. Frequency of oscillation: 2. f=150 Hz, 3. f=250 Hz, 4. f=350 Hz, 5. f=600 Hz

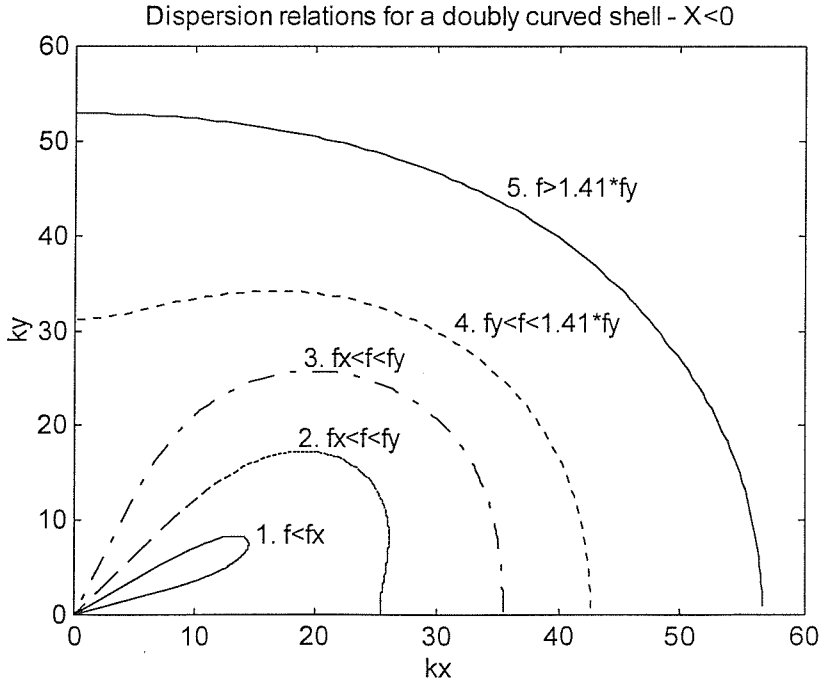

Fig. F.2 - Dispersion relations for a doubly-curved shell of negative curvature (X<0) and ring frequencies f_x = 100 Hz and f_y = 300 Hz. Frequency of oscillation: 1. f=50 Hz, 2. f=150 Hz, 3. f=250 Hz, 4. f=350 Hz, 5. f=600 Hz.

F.2 Singly-curved thin shell

The result for a singly-curved shell can be obtained directly from the doubly-curved shell one (F.2 and F.4) by setting $r_y = \infty$. Thus for a singly-curved shell we have that

$$k^4 = \frac{12(1-\nu^2)}{h^2 r^2}\left(\frac{f^2}{f_r^2} - \sin^4\theta\right) \qquad \text{(F.6)}$$

where r is the shell radius and f_r is the 'plane stress' ring frequency. In the frequency region below the ring frequency f_r the above expression gives complex and real results. The real results are situated in the curve between 0 and θ_1, where $\theta_1 = \text{acos}(f/f_y)$. The implication of the solution of this expression for regions in which $f < f_y$ have been discussed by Langley [91], who demonstrated the existence of two distinct wave types that generate out of plane displacements.

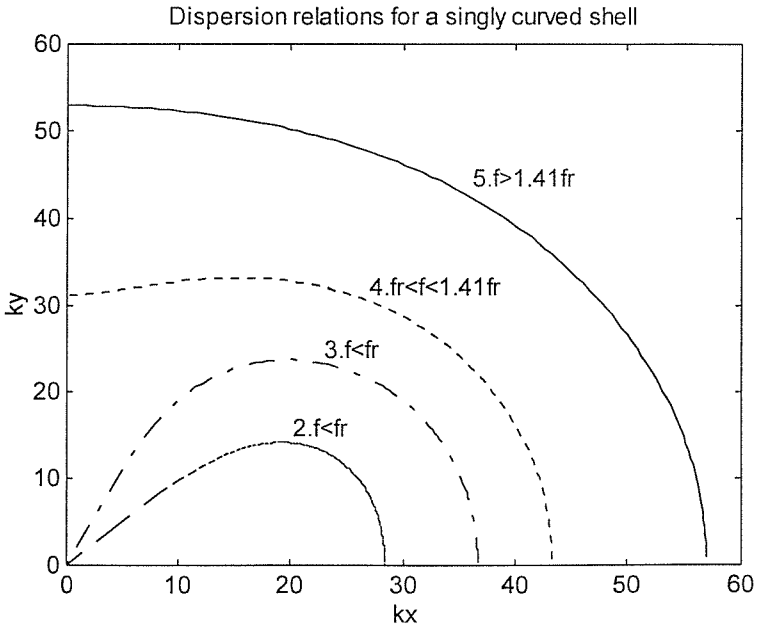

Fig. F.3 - Dispersion relations for a singly-curved shell with ring frequency f_r = 300 Hz. Frequency of oscillation: 2. f=150 Hz, 3. f=250 Hz, 4. f=350 Hz, 5. f=600 Hz

F.3 Mindlin plates: inclusion of shear deformation and rotary inertia

Mindlin plates are generally referred as plates in which shear deformation and rotary inertia are taken into account in vibration analysis. Shear deformation and rotary inertia are important for cases of thick shells and plates in which the thickness of the structure is of comparable dimension to the structure characteristic dimension. The free vibrations of Mindlin plates are governed by the following simplified equation [92]

$$D\Delta\Delta w + \rho h\frac{\partial^2 w}{\partial t^2} - \rho\left(\frac{D}{G'} + \frac{h^3}{12}\right)\Delta\frac{\partial^2 w}{\partial t^2} = 0 \qquad \text{(F.7)}$$

where G is the shear modulus, $G' = \kappa^2 G$, κ^2 is the shear coefficient, w(x,y,t) is the transverse displacement. The other terms of equation (F.7) are similar to the ones defined for equation (F.1). The natural frequency for the case of all around simply-supported edges is given by [92]

$$\omega^2 = \frac{D}{\rho h}\left(k_x^2 + k_y^2\right)^2\left[1 + \delta\left(k_x^2 + k_y^2\right)\right]^{-1}, \qquad \delta = \left(\frac{D}{G'h} + \frac{h^2}{12}\right) \qquad \text{(F.8)}$$

where the terms under brackets is the correction factor due to effects of shear deformation and rotary inertia. Substituting k_x and k_y by $k\cos\theta$ and $k\sin\theta$ in equation (F.8) and expressing the wavenumber k as a function of the frequency of oscillation we have

$$k^2 = \left[\frac{\delta\omega^2 \pm \omega\sqrt{\delta^2\omega^2 + \left(\frac{4D}{\rho h}\right)}}{\frac{2D}{\rho h}}\right] \qquad \text{(F.9)}$$

In this case the solution of the above equation will be governed by the value of the parameter δ in relation to the bending wavenumber of a flat plate without shear deformation and rotary inertia effects. The negative sign in the above equation can be discarded as it will only give complex wavenumbers.

Results from equation (F.9) for a 0.1 m thick plate are compared to the classical bending wavenumber in fig. F.4. As shown, the bending wavenumber curve

with the correction term departs from the uncorrected curve for wavenumbers higher than eight which correspond to a wavelength of 0.75 m. This observation agrees with the analysis presented in section II.3.b of ref. [38] in which it is suggested that the correction terms due to rotary inertia and shear deformation make a difference of more than 10 % if the wavelength is less than the value $\lambda = 6h$. The correction suggested in ref. [38] is also plotted in fig. F.4.

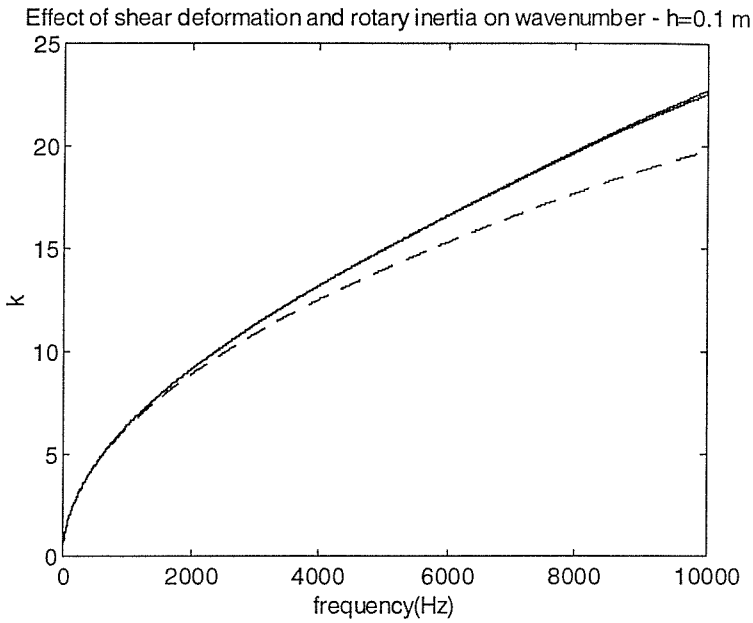

Fig. F.4 - Dispersion curve for a plate of 0.1 m thickness. —— rotary inertia and shear deformation included (eq. (F.9)); — — — classical bending wavenumber; - - - - - correction suggested in ref. [38].

APPENDIX G

AN APPROXIMATION TO THE FREQUENCY-AVERAGE RADIATION EFFICIENCY OF FLAT PLATES

In this appendix the correlation characteristics of modally-dense randomly vibrating plates are used to estimate the radiation efficiency of such structures. Comparisons are presented with well-known results from Maidanik [37] and Leppington et al. [93].

G.1 Radiation efficiency of flat plates

The time-averaged acoustic power P radiated into a half-space by a harmonically vibrating rectangular plate (area S and dimensions a,b) set in a rigid baffle is given by the Rayleigh integral representation of the induced pressure [93]

$$P = \frac{\rho_o \omega}{4\pi} \int_S \int_S v(x,y) v(x',y') \frac{\sin k_o r}{r} dS' dS, \tag{G.1}$$

where k_o denotes the acoustic wavenumber, ρ_o is the fluid mean density, v(x,y) is the normal vibration velocity of the panel, ω is the frequency of excitation and r is given by

$$r = \sqrt{(x-x')^2 + (y-y')^2}. \tag{G.2}$$

The plate radiation efficiency is defined as [19]

$$\sigma = \frac{P}{\rho_o c_o ab \langle \bar{v}_n^2 \rangle}, \tag{G.3}$$

where c_o is the fluid sound speed and the space-average value of the time-average normal vibration velocity of the panel which is defined as [19]

$$\langle \bar{v}_n^2 \rangle = \frac{1}{S} \int_S \frac{1}{T} \int_0^T v^2(x,y,t) dt dS.$$

Assuming that the plate normal displacement is given by equation (3.19'), the radiation efficiency for a single mode of vibration is then given by,

$$\sigma = \frac{\omega}{2\pi c_o} \frac{\int_S \int_S X_p(x) Y_p(y) X_p(x') Y_p(y') \frac{\sin k_o r}{r} dS' dS}{\int_S X_p^2(x) Y_p^2(y) dS}. \qquad (G.4)$$

For the case of a simply supported plate,

$$X_p(x) = \sin k_x x, \qquad Y_p(y) = \sin k_y y,$$

where k_x and k_y are the wavenumbers in x and y directions. Substituting these mode shapes in (G.4) we obtain the following expression for the modal radiation efficiency of a simply-supported plate

$$\sigma = \frac{2k_o^2}{\pi S} \int_S \int_S \sin k_x x \sin k_y y \sin k_x x' \sin k_y y' \frac{\sin k_o r}{k_o r} dS' dS. \qquad (G.5)$$

which agrees with equation (2.5) of ref. [93].

A frequency average of the radiation efficiency can then be obtained by summing the contribution from all modes that are excited in a specific frequency band. Using modal summation we can write the normal vibration velocity as

$$v(x,y) = \sum_N A_p X_p(x) Y_p(y),$$

where N controls the number of modes to be summed to obtain v(x,y). Expressing k_x and k_y in circular coordinates (k_b,θ) and assuming that all the modes are equally excited within the frequencies f_c-$\Delta f/2$ and f_c+$\Delta f/2$ we can obtain an estimate of v(x,y) for a modally-dense plate. This estimate is given by

$$v(x,y) = \frac{2}{\pi} \int_0^{\pi/2} AX(k_b,\theta,x) Y(k_b,\theta,y) d\theta, \qquad (G.6)$$

where to derive the above expression it is assumed that each individual modal wavenumber included in the discrete summation do not depart strongly from the wavenumber at the band centre frequency (k_b). Substituting (G.6) in (G.4) and neglecting the cross-modal contributions we obtain an approximate expression for the frequency-average radiation efficiency due to any type of boundary conditions

$$\sigma = \frac{\omega}{2\pi c_o} \frac{\int_S \int_S \int_0^{\pi/2} X(k_b,\theta,x)Y(k_b,\theta,y)X(k_b,\theta,x')Y(k_b,\theta,y')d\theta \frac{\sin k_o r}{r} dSdS}{\int_S \int_0^{\pi/2} X^2(k_b,\theta,x)Y^2(k_b,\theta,y)d\theta dS}, \quad (G.7)$$

where $X(k_b,\theta,x)$ and $Y(k,\theta,y)$ can be obtained from the results presented in Chapter 3.

G.2 Results for a rectangular plate

For the case of a plate which vibration field approach that of a diffuse bending wave field, equation (G.7) can be expressed as

$$\sigma = \frac{k_o^2}{2\pi S} \int_S \int_S J_o(k_b r) \frac{\sin k_o r}{k_o r} dS' dS, \quad (G.8)$$

where S is the plate area. The above representation of the frequency-average radiation efficiency is similar to the one presented in eqs. (5) and (8) of ref. [94]. As observed in [94] when the above 4-dimensional integral is reduced to a one-dimensional integral and the integration limits are extended to infinity, the well-known results for an infinite plate $\sigma = \left(1 - k_b^2 / k_o^2\right)^{-1/2}$ if $k_b \leq k_o$, and $\sigma = 0$ if $k_b > k_o$, are recovered. Results for the the radiation efficiency of a 1 cm thick rectangular plate with sides a=1.0 m and b=0.8 m computed from equation (G.8) is presented in fig. G.1. This graph is coincident with that presented in figure 2 of ref. [94]. It can also be observed in this figure that the radiation efficiency estimates for a simply-supported plate are higher than that of a diffuse vibration field, except below 40 Hz. The main reason for this is that in this frequency region the plate is behaving like a rigid piston as the first resonance frequency for this plate is estimated to be 63 Hz. Therefore, both expressions are in error in the low frequency range as a high modal density was assumed in their derivation. In the present work, the following expression (obtained from eqs. (3.15'), (3.16) and (G.7)) is used to compute the radiation efficiency of simply-supported flat plates

$$\sigma=\frac{k_o^2}{2\pi}\frac{\int_S\int_S\left[\begin{array}{l}J_0\left(k_b\sqrt{(x_1-x_2)^2+(y_1-y_2)^2}\right)J_0\left(k_b\sqrt{(x_1-x_2)^2+(y_1+y_2)^2}\right)\\-J_0\left(k_b\sqrt{(x_1+x_2)^2+(y_1-y_2)^2}\right)+J_0\left(k_b\sqrt{(x_1+x_2)^2+(y_1+y_2)^2}\right)\end{array}\right]\frac{\sin k_o r}{k_o r}dS'dS}{\int_S\left[1-J_0(2k_b x_1)-J_0(2k_b y_1)+J_0\left(2k_b\sqrt{x_1^2+y_1^2}\right)\right]dS} \quad (G.9)$$

As shown in fig. G.1 results from equation (G.9) approach that of Maidanik [37] and Leppington (eqs. (7.6), (7.7) and (7.11) from ref.[93]) for frequencies higher than 0.1 f_{crit}, where f_{crit} is the lowest coincidence frequency or, as is common terminology, the critical frequency . The critical frequency is estimated to be 1200 Hz for the plate used. The result for a diffuse vibration field (equation (G.8)) only approaches the other three in the proximity of the critical frequency and can give results almost 6 dB lower than that of equation (G.9) for $f=0.1f_{crit}$. As for regions remote from the edges the vibration field approach that of a diffuse field irrespective of the boundary conditions, the difference between simply-supported and diffuse field results clearly reflect the importance of the vibration field near the edges in controlling the plate acoustic radiation below the critical frequency.

In fig. G.2 a comparison between the asymptotic expressions derived by Leppington et al. [93] and the results presented in this work for the case of simply-supported plates is presented. When the frequency-average radiation efficiency is computed from the numerical integration of equation (2.6) of ref. [93] the curve obtained is very similar to that obtained from eq. (G.9). They only disagree for frequencies below $0.06f_{crit}$. In addition, it is worth explaining that the difference between the two results from Leppington et al. [93] as plotted in figs. G.1 and G.2 is that the dash-dotted curves in both figures represent an asymptotic estimate of equation (G.5) for cases in which the acoustic wavenumber k_o tends to infinity whereas the dashed line in fig. G.2 is obtained from a numerical integration of a 2-dimensional integral similar to equation (G.5).

The effect of the boundary conditions on the radiation of flat plates is illustrated by the results presented in fig. G.3. The Bolotin's dynamic edge effect method parameters for the case of clamped and free edges (Appendix B) are substituted in equation (G.7) and the radiation efficiency calculated. As expected, the clamped edges increase the radiation efficiency by a factor of approximately 2 in a frequency region between $0.07f_{crit}$ and f_{crit} when compared to simply-supported edges.

However, for frequencies below $0.07f_{crit}$ simply-supported plate results are higher than that of clamped plates. This agrees with the results reported by Timmel [87] and by Berry et al. [95] and they are related to the fact that low order modes (up to the (2-2) mode) are more efficient in terms of acoustic radiation for the case of simply-supported boundaries. On the other hand, the radiation efficiency of a plate with free edges is much lower than that of plates with simply-supported or clamped edges in the same frequency range. This observation is in agreement with previous analysis of sound radiation from plates with free edges [95] confirming that these plates are poor radiators of sound. Above the critical frequency the boundary conditions are unimportant to the sound radiation and the radiation efficiency approaches unity irrespective of the boundary condition.

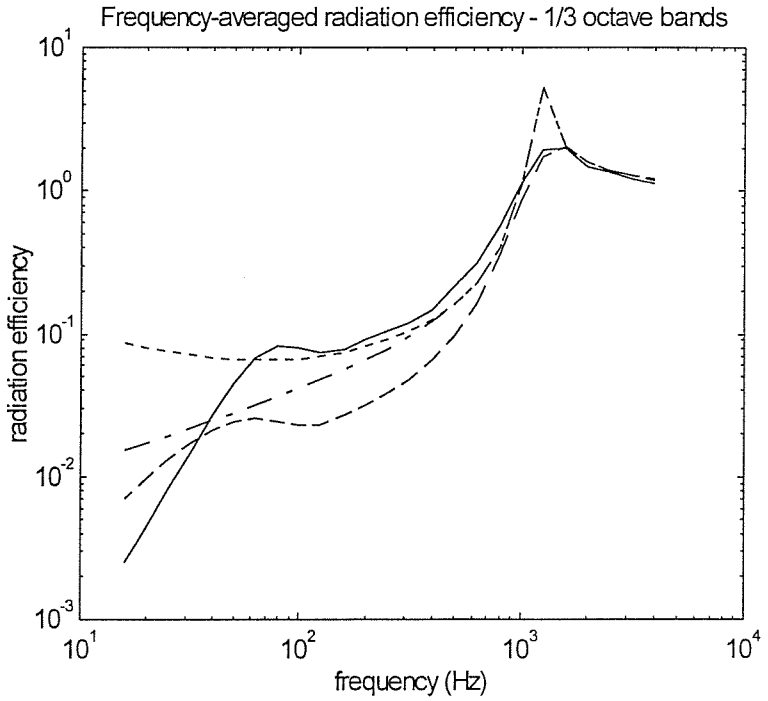

Fig. G.1 - Frequency-average radiation efficiency. 1/3 octave bands. Flat plate a=1.0 m, b=0.8 m, h=0.01 m. ——— simply-supported plate (eq. (G.9)); — — — diffuse vibration field (eq. (G.8)); – · – · – · – Leppington (eqs. (7.6),(7.7),(7.11) of ref. [93]); - - - - - Maidanik (eq. (2.39) of ref. [37]).

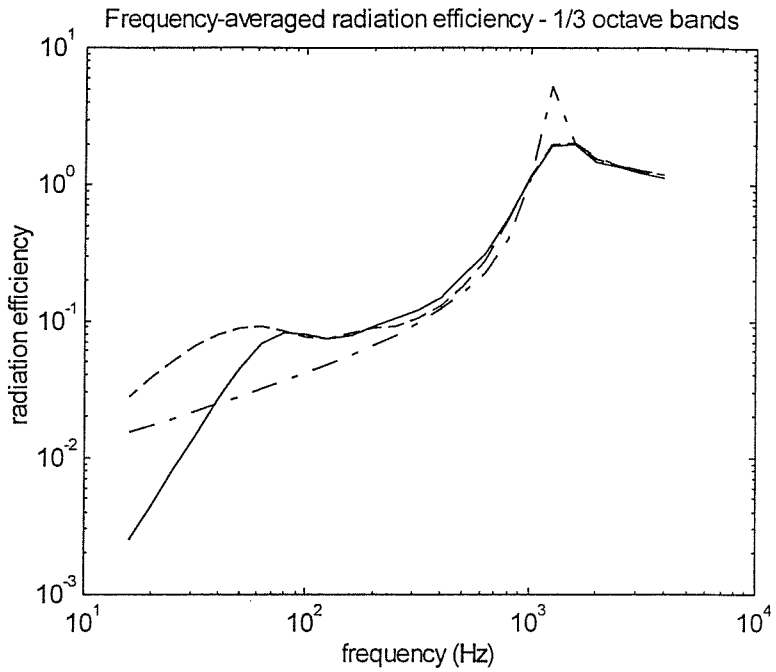

Fig. G.2 - Frequency-average radiation efficiency. 1/3 octave bands. Simply-supported flat plate a=1.0 m, b=0.8 m, h=0.01 m. ——— this work (eq. (G.9)); – · – · – · – Leppington (eqs. (7.6),(7.7),(7.11) from ref. [93]) ; — — — Leppington (numerical integration of eqs. (7.5),(2.6) from ref. [93]).

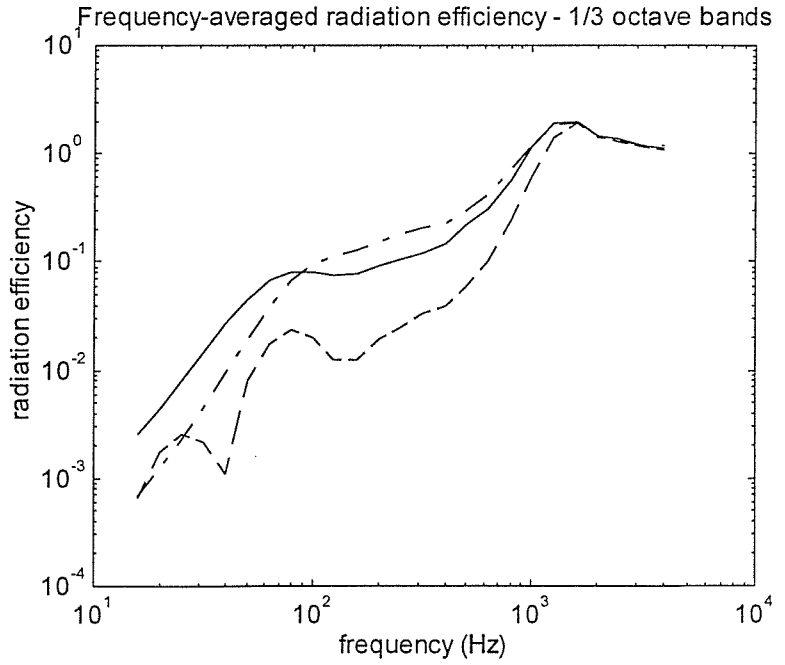

Fig. G.3 - Frequency-average radiation efficiency. 1/3 octave bands. Flat plate a=1.0 m, b=0.8 m, h=0.01 m. ——— simply-supported edges (eq. (G.9)); — — — free edges (eq. (G.7)); – · – · – · – clamped edges (eq. (G.7)).